Université de Strasbourg

UNIVERSITÉ DE STRASBOURG

École doctorale | Mathématiques, sciences de l'information et de l'ingénieur | ED 269 | Université de Strasbourg

ÉCOLE DOCTORALE MATHÉMATIQUES, SCIENCES DE L'INFORMATION ET DE L'INGÉNIEUR – ED 269
ICube : UMR 7357 CNRS - Université de Strasbourg
Le laboratoire des sciences de l'ingénieur, de l'informatique et de l'imagerie

Thèse présenté par:

Ahmed ABOTALEB

Soutenue le: **28-Nov-2024**

Pour obtenir le grade de: **Docteur en Sciences de l'université de Strasbourg**
Discipline/ Specialité: **Génie Mécanique - Mécanique des Matériaux**

Advanced modeling and optimization of the friction stir welding process: applications to Inconel 718 and high-performance alloys

THÈSE dirigée par:

M. Y. REMOND	Professeur, Université de Strasbourg
M. S. AHZI	Professeur, Université de Strasbourg

RAPPORTEURS:

M. M. EL MANSORI	Professeur, ENSAM Aix en Provence
M. H. GARMESTANI	Professeur, Georgia Institute of Technology

Examinateurs:

Mme S. TOUCHAL	Maître de Conference – HDR, Université de Strasbourg
M. M. KHRAISHEH	Professeur, Texas A&M at Qatar
M. M. AL-AZBA	Research Director, QEERI – Hamad Bin Khalifa University

Abstract

The evolution of advanced manufacturing depends on innovative and cutting-edge research activities associated with fabrication processes, materials, and product design. As most advanced manufacturing processes involve heating or generating heat during parts production, modeling heat transfer phenomena is of crucial importance. It directly affects the dimensional accuracy of the parts, their microstructure (porosity, anisotropy, etc.), mechanical properties, and surface quality. This study focuses on one of the main manufacturing processes known as friction stir welding (FSW). FSW is a recently developed solid-state joining technique that has gained popularity and efficiency in welding both similar and dissimilar metallic materials. Although FSW has shown success in joining hard-to-weld or un-weldable dissimilar materials compared to fusion welding methods, further development is required to meet industry maturity standards. Thus, having a scientific knowledge base founded on predictive models would provide significant benefits for a thorough understanding of the FSW process and its optimization. A FSW model was developed using COMSOL Multiphysics v5.3 as a 3D transient thermomechanical model that couples multiphysics including material flow and heat transfer by conduction, convection, and radiation. This model was validated using published experimental data for welding a benchmark material, 6061-T6 Aluminum, and then extended to welding Inconel 718, a nickel-based superalloy, as well as the dissimilar welding of Inconel 718 and Ti-6Al-4V alloys. Moreover, this thesis explores the optimization of FSW parameters for Inconel 718 and the dissimilar welding of Inconel 718 and Ti-6Al-4V alloys. Through a combination of parametric study followed by Taguchi analysis, ANOVA, and non-linear regression, the study identifies the influence of key process parameters: rotational speed, welding speed, axial force, shoulder diameter, pin diameter, active cooling, and induction preheating on critical performance outcomes such as workpiece temperature, microhardness, stress evolution, and grain size. The findings indicate that axial force and rotational speed are the most controlling parameters affecting the FSW process. Additionally, induction preheating significantly enhances process efficiency by reducing rotational speed and axial force requirements

while increasing welding speed, leading to improved heat dissipation and finer grain structures. Similarly, active cooling showed an improved microstructure and finer grains. Finally, precise process control strategies were proposed to optimize thermal dynamics during welding for effective workpiece thermal management. Proportional-integral-derivative (PID) and model predictive control (MPC) strategies in their single-variable and multi-variable modes proved to be successful in controlling the FSW workpiece temperature with minor differences in terms of response time and disturbance handling. The application of these strategies effectively addresses temperature control issues commonly known for causing defects associated with FSW. This approach not only advances the FSW process for Inconel 718 but also sets a precedent for applying similar methodologies to other high-performance alloys, with implications for enhancing manufacturing processes and operational scalability. This research underscores the importance of precise parameter control in the FSW of Inconel 718 and provides a predictive framework for optimizing welding conditions to achieve superior mechanical properties and structural integrity. The methodologies and results presented here contribute valuable insights for advancing the application of FSW in high-performance materials.

Résumé

L'évolution de la fabrication avancée dépend d'activités de recherche innovantes et à la pointe de la technologie associées aux processus de fabrication, aux matériaux et à la conception de produits. Étant donné que la plupart des processus de fabrication avancée impliquent le chauffage ou la génération de chaleur lors de la production de pièces, la modélisation des phénomènes de transfert de chaleur est d'une importance cruciale. Elle affecte directement la précision dimensionnelle des pièces, leur microstructure (porosité, anisotropie, etc.), leurs propriétés mécaniques et la qualité de leur surface. Cette étude se concentre sur l'un des principaux processus de fabrication connu sous le nom de soudage par friction-malaxage (FSW). Le FSW est une technique d'assemblage à l'état solide récemment développée, qui a gagné en popularité et en efficacité pour le soudage de matériaux métalliques similaires et dissemblables. Bien que le FSW ait montré un succès dans l'assemblage de matériaux dissemblables difficiles à souder ou impossibles à souder par les méthodes de soudage par fusion, un développement supplémentaire est nécessaire pour atteindre les normes de maturité industrielle. Ainsi, disposer d'une base de connaissances scientifiques fondée sur des modèles prédictifs offrirait des avantages significatifs pour une compréhension approfondie du processus FSW et son optimisation. Un modèle FSW a été développé en utilisant COMSOL Multiphysics v5.3 comme modèle thermomécanique transitoire 3D couplant des multiphysiques incluant l'écoulement de matière et le transfert de chaleur par conduction, convection et radiation. Ce modèle a été validé en utilisant des données expérimentales publiées pour le soudage d'un matériau de référence, l'aluminium 6061-T6, puis étendu au soudage de l'Inconel 718, un superalliage à base de nickel, ainsi qu'au soudage dissemblable de l'Inconel 718 et des alliages Ti-6Al-4V. De plus, cette thèse explore l'optimisation des paramètres du FSW pour l'Inconel 718 et le soudage dissemblable de l'Inconel 718 et des alliages Ti-6Al-4V. À travers une combinaison d'études paramétriques suivies d'une analyse Taguchi, d'une ANOVA et d'une régression non linéaire, l'étude identifie l'influence des principaux paramètres de processus : la vitesse de rotation, la vitesse de soudage, la force axiale, le diamètre de l'épaule, le diamètre de la broche, le refroidissement actif et le préchauffage par induction

sur les résultats de performance critiques tels que la température de la pièce, la microdureté, l'évolution des contraintes et la taille des grains. Les résultats indiquent que la force axiale et la vitesse de rotation sont les paramètres les plus contrôlants affectant le processus FSW. De plus, le préchauffage par induction améliore considérablement l'efficacité du processus en réduisant les exigences de vitesse de rotation et de force axiale tout en augmentant la vitesse de soudage, conduisant à une meilleure dissipation de la chaleur et à des structures de grains plus fins. De même, le refroidissement actif a montré une microstructure améliorée et des grains plus fins. Enfin, des stratégies précises de contrôle de processus ont été proposées pour optimiser la dynamique thermique pendant le soudage pour une gestion thermique efficace de la pièce. Les stratégies de contrôle proportionnel-intégral-dérivé (PID) et de contrôle prédictif de modèle (MPC) dans leurs modes monovariable et multivariable se sont révélées réussies pour contrôler la température de la pièce FSW avec des différences mineures en termes de temps de réponse et de gestion des perturbations. L'application de ces stratégies aborde efficacement les problèmes de contrôle de la température, connus pour causer des défauts associés au FSW. Cette approche non seulement fait progresser le processus FSW pour l'Inconel 718, mais établit également un précédent pour l'application de méthodologies similaires à d'autres alliages haute performance, avec des implications pour l'amélioration des processus de fabrication et la montée en échelle opérationnelle. Cette recherche souligne l'importance du contrôle précis des paramètres dans le FSW de l'Inconel 718 et fournit un cadre prédictif pour l'optimisation des conditions de soudage afin d'obtenir des propriétés mécaniques supérieures et une intégrité structurelle. Les méthodologies et résultats présentés ici apportent des perspectives précieuses pour l'avancement de l'application du FSW dans les matériaux haute performance.

Dedication

To my mother, the greatest mother in the world, to whom I owe everything in my life—may her soul rest in peace. To my father, the greatest mentor, supporter, and motivator. To my brother, my backbone in life's ups and downs. To my wife, the cheerful side of my world. To my children, Youssef and Hanaa, whose smiles boost my efforts. And to my sincere friends.

Acknowledgement

I extend my heartfelt gratitude to my advisors, Prof. Said and Prof. Yves, for their invaluable guidance and support throughout this research. Special thanks are also due to Dr. Mohammed Al-Azba for his assistance and collaboration. I would also like to thank the thesis monitoring committee members, Dr. João Pedro de Magalhães Correia, Dr. Daniel George, Dr. Siham Touchal, and Prof. Marwan Khraisheh, for their technical advice.

I deeply appreciate the comments and feedback from the reviewers, Prof. Hamid and Prof. El Mansori.

Additionally, I express my gratitude to Mme. Nathalie Kostmann and Mme. Nafissa for their excellent administrative support during my PhD.

For their encouragement and support, I thank my wife Nourhan, my son Youssef, my daughter Hanaa, my brother Farouk, my parents, and my friends Ahmed Al Ajji and Dr. Hicham Hamoudi.

I hope that the insights gained from this research will contribute to advancements in welding technology and inspire further studies in this field.

Table of Contents

List of Tables

List of Figures

Preface

This thesis is the culmination of extensive research conducted at ICube Laboratory, Université de Strasbourg, under the supervision of Prof. Said Ahzi and Prof. Yves Remond from 2021 to 2024. The research focuses on enhancing the friction stir welding (FSW) process for nickel-based superalloys, particularly Inconel 718. The motivation for this study stems from the critical need to improve welding processes for high-performance materials used in demanding applications such as aerospace and power generation. I embarked on this research journey with the goal of developing a comprehensive understanding of how various FSW parameters influence the welding quality and mechanical properties of Inconel 718. The study employs a rigorous methodological framework that includes finite element modeling, Taguchi analysis, ANOVA analysis, non-linear regression, and process control strategies ensuring the reliability and validity of the findings.

Chapter 1 provides a detailed literature review of friction stir welding technology with a focus on nickel-based alloys, specifically Inconel 718. This chapter includes 277 references, which have been converted into a review article. Chapter 2 summarizes the methodology for developing the finite element model that couples the thermomechanical phenomena of the FSW process, detailing the relevant equations. Additionally, the statistical equations that describe Taguchi analysis, ANOVA, and non-linear regression are presented.

Chapter 3 discusses the FSW of the benchmark material 6061-T6 aluminum alloy. After validation with published experimental data, the model was extended to the Inconel 718 alloy, including its parametric study and statistical analysis. Most of my work in Chapter 2 and Chapter 3 has been published as open access article "Ahmed Abotaleb et al.- Parametric investigation of friction stir welding of aluminum alloy and Inconel 718 using finite element analysis- Discov Mechanical Engineering 3, 37 (2024). https://doi.org/10.1007/s44245-024-00076-1 " under a Creative Commons Attribution-NonCommercial-NoDerivatives 4.0 International License.

Chapter 4 builds on the developed and validated finite element model for Inconel 718 and extends the study to the dissimilar welding of Inconel 718 and Ti-6Al-4V alloys. This chapter also incorporates a parametric study followed by statistical analysis and regression models. This chapter is based on a finalized manuscript which will be submitted for publication soon.

Finally, Chapter 5 proposes a new and cost-effective approach to workpiece thermal management through an effective control strategy, primarily utilizing PID and MPC. This chapter has been published as open access article "Ahmed Abotaleb et al.- Workpiece temperature control in friction stir welding of Inconel 718 through integrated numerical analysis and process control. Front. Control. Eng. 5:1459399. doi: 10.3389/fcteg.2024.1459399" under Creative Commons Attribution License (CC BY).

General Introduction

The advancement of manufacturing technologies is crucial for meeting the demands of modern industries, where the need for high-performance materials and efficient fabrication processes is ever-increasing. One of the notable innovations in this field is Friction Stir Welding (FSW), a solid-state joining process that has revolutionized the way materials, particularly metals and alloys, are welded. This introduction provides an overview of FSW, its process, applications, advantages, and the current state of research, particularly focusing on the welding of aluminum alloys and high-temperature materials like Inconel 718. FSW was invented at The Welding Institute (TWI) in the United Kingdom in 1991. This innovative welding technique involves the use of a non-consumable tool to join two facing workpieces without melting the material. The process leverages frictional heat generated between the rotating tool and the workpiece to soften the material, enabling the tool to stir and forge the workpieces together at temperatures below their melting points. This unique approach distinguishes FSW from conventional welding methods that rely on melting the base materials, offering several advantages such as reduced thermal distortion and enhanced mechanical properties.

The FSW process can be divided into three primary stages: penetration, probing, and withdrawal. During the penetration stage, the rotating tool is inserted into the workpieces at the joint line, generating heat through friction. This heat softens the material, allowing the tool to penetrate to the desired depth. In the probing stage, the tool traverses along the joint line, stirring and mixing the softened material to form a solid-state weld. The final stage, withdrawal, involves the removal of the tool, leaving behind a weld that solidifies upon cooling. Several key parameters influence the FSW process, including rotational speed, welding speed, axial force, shoulder diameter, and pin diameter. These parameters must be carefully controlled to achieve optimal welding conditions and produce high-quality welds. Additionally, the design of the FSW tool, which typically consists of a shoulder and a pin, plays a critical role in determining the heat generation and material flow during welding.

FSW has found extensive applications in various industries due to its ability to produce defect-free welds with superior mechanical properties. In the aerospace industry, FSW is used to join aluminum alloys for aircraft structures, as it minimizes distortion and residual stresses, which are critical for maintaining structural integrity. The automotive industry also utilizes FSW for joining lightweight materials, contributing to the development of fuel-efficient vehicles. Additionally, FSW is employed in the fabrication of ship hulls, railway carriages, and heat exchangers, demonstrating its versatility across different sectors. One of the significant advantages of FSW is its capability to weld dissimilar materials, which is particularly useful in applications requiring the combination of different material properties. For instance, FSW can join aluminum to copper or steel, enabling the integration of lightweight and high-strength components in a single assembly. This ability to join dissimilar materials opens new possibilities for innovative designs and applications.

FSW offers several advantages over traditional fusion welding methods. Firstly, because FSW operates below the melting temperature of the workpieces, it avoids many issues associated with melting and solidification, such as porosity, cracking, and distortion. This results in welds with superior mechanical properties and reduced post-weld treatment requirements. Secondly, FSW is an environmentally friendly process. It does not require the use of filler materials, flux, or shielding gases, which are commonly used in fusion welding and can have environmental and health impacts. The solid-state nature of FSW also results in lower energy consumption compared to fusion welding processes. Thirdly, FSW is highly efficient and suitable for automation. The process can be easily adapted to robotic and CNC systems, enabling high-precision and consistent welds. This makes FSW ideal for high-volume production settings where repeatability and quality are paramount.

Understanding and optimizing the FSW process parameters is crucial for achieving high-quality welds. Researchers have developed various models to simulate the heat transfer, material flow, and stress distribution during FSW. These models help predict the outcomes of different welding parameters and guide the optimization process. Thermal modeling of FSW focuses on predicting the temperature distribution within the

workpieces during welding. Accurate thermal models are essential for understanding the thermal cycles experienced by the material, which directly affect the microstructure and mechanical properties of the weld. Computational fluid dynamics (CFD) models are often used to simulate the material flow around the tool, providing insights into the formation of the weld nugget and the influence of tool geometry on material mixing. Mechanical modeling of FSW involves the simulation of stress and strain distributions during and after welding. These models help identify potential issues such as residual stresses and distortions, which can compromise the integrity of the welded structure. By understanding the mechanical behavior of the weld, researchers can optimize the process parameters to minimize defects and enhance the overall performance of the weld.

A comprehensive review of the existing literature reveals several attempts in understanding the FSW process, particularly regarding the welding of aluminum alloys and high-temperature materials like Inconel 718. Studies have explored the effects of various process parameters on the microstructure and mechanical properties of FSW joints. For instance, researchers have investigated the influence of tool design, rotational speed, welding speed, and axial force on the quality of welds. Despite the extensive research conducted, several gaps in literature remain. One of the major challenges is the comprehensive understanding of the interactions between different FSW parameters and their collective impact on the weld's microstructure and mechanical properties as well as the effect of energy and or coolant assisted FSW on the welding efficiency and the final quality of the welded workpiece. While numerous studies have explored individual parameters, the complex interplay between these variables is not yet fully understood. Additionally, there is a need for more sophisticated models that can accurately simulate these interactions and predict the outcomes of different welding conditions. Another area requiring further investigation is the welding of advanced and emerging materials using FSW. While significant progress has been made in welding aluminum alloys and some high-temperature materials, the application of FSW to newer materials, such as high-strength steels, Ti alloys and composite materials, remains underexplored. Understanding the behavior of these materials during FSW and optimizing the process parameters for their welding is crucial for expanding the applicability of FSW in various industries.

CHAPTER 1: Background, Literature Review of Friction Stir Welding Technology

1.1. Friction Stir Welding Process

The progress of advanced manufacturing hinges on pioneering and cutting-edge research related to fabrication processes, materials, and product design. Since many advanced manufacturing methods involve heating or generating heat during the creation of parts, understanding heat transfer phenomena is essential. This understanding is critical as it influences the dimensional precision of parts, their microstructure (including porosity and anisotropy), mechanical properties, and surface quality[1-3]. This study focuses on one key manufacturing process, friction stir welding (FSW). FSW is a solid-state welding technique that employs a non-consumable tool to join workpieces without reaching their melting point [4, 5]. Notably, FSW technology was developed over twenty years ago at The Welding Institute (TWI) in the UK.

FSW is a solid-state welding process that uses a non-consumable tool to join two pieces of metal or thermoplastics together. The tool is inserted into the joint between the two pieces of metal and rotated at high speeds, generating heat through friction. The heat softens the metal, and the tool is then moved along the joint, stirring and blending the metal together. The process is known as solid-state welding because the metal does not melt during the welding process, unlike traditional welding methods such as gas tungsten arc welding (GTAW) or gas metal arc welding (GMAW). FSW has several advantages over traditional welding methods, such as reduced distortion, improved mechanical properties, and the ability to weld dissimilar materials. Additionally, FSW can be used to weld materials that are difficult to weld using traditional methods, such as aluminum alloys, and it can also be used to weld thin sections.

The FSW process can be divided into three main stages: (1) penetration stage, (2) probing stage and (3) withdrawal stage. In the penetration stage, the tool is inserted into the workpiece and rotated, generating heat, and plasticizing the material. In the probing stage, the tool is moved along the joint, stirring the material and creating a solid-state weld. In the withdrawal stage, the tool is removed from the workpiece, and the weld cools and solidifies. There are different types of FSW tools, such as shouldered tools, pin tools, and

flat tools. The choice of the tool depends on the material being welded and the specific requirements of the application.

Friction serves as an effective heat source for processing metals and alloys, primarily through welding and deposition techniques. Over the last twenty years, there have been notable advancements in friction-based technologies. These methods leverage surface-generated friction to create welds or deposits and utilize the layer-by-layer construction principle of additive manufacturing. Compared to fusion-based techniques, friction stir methods offer several benefits, including low porosity, minimized distortions, and enhanced metallic properties. Additional advantages include fine-grained microstructures, high-strength components, and the absence of build volume constraints, thanks to the intense plastic deformation inherent in the process. Friction stir techniques are generally categorized into three types: welding, processing, and advanced processes[6-10].

FSW has gained popularity and efficiency in welding both similar and dissimilar metallic materials. Despite its success, further development is required to meet industry standards and deepen the understanding of the FSW process. Welding nickel-based superalloys like Inconel 718 poses significant technical challenges. Current literature indicates that successful welding of these materials necessitates high axial forces and specific process parameters, thus restricting its industrial applicability.

1.1.1. FSW Process Parameters

Friction Stir Welding/Processing is a highly intricate process that involves both material movement and plastic deformation. The outcome of the welding process is greatly impacted by a multitude of factors, including welding parameters, tool geometry, and joint design. These factors play a critical role in determining the material flow pattern and temperature distribution, which in turn have a major impact on the evolution of the microstructure of the material. In this section, we will delve into the major factors that affect the FSW/friction stir processing (FSP) process, including tool geometry, welding parameters, and joint design. These factors will be examined in detail to provide a comprehensive understanding of their impact on the FSW/FSP process and its outcome.

1.1.1.1. Tool geometry

Tool geometry is a crucial factor in the development of FSW/FSP processes. The tool geometry determines the material flow and temperature distribution, both of which have a significant impact on the microstructural evolution of the material being joined. A typical FSW tool consists of a shoulder and a pin (see Figure 1-1). The tool serves two primary functions: heating and material flow. During the initial stage of tool plunge, the heating is primarily generated by the friction between the pin and the workpiece, while additional heating is produced by the deformation of the material. The heating is at its maximum when the shoulder touches the workpiece and generates friction between the two. The relative size of the pin and shoulder is the most important design feature when it comes to heating, while other design elements have a lesser impact. The shoulder also provides confinement for the heated material. The second function of the tool is to agitate and move the material, which results in uniform microstructure and properties as well as process loads. The tool design governs these aspects, with concave shoulders and cylindrical pins with threads being the most used design features. Over time, the tool geometry has evolved significantly, with more complex features being added to alter material flow, improve mixing, and reduce process loads. This is a result of increased experience and a deeper understanding of material flow in the FSW and FSP processes.[11]

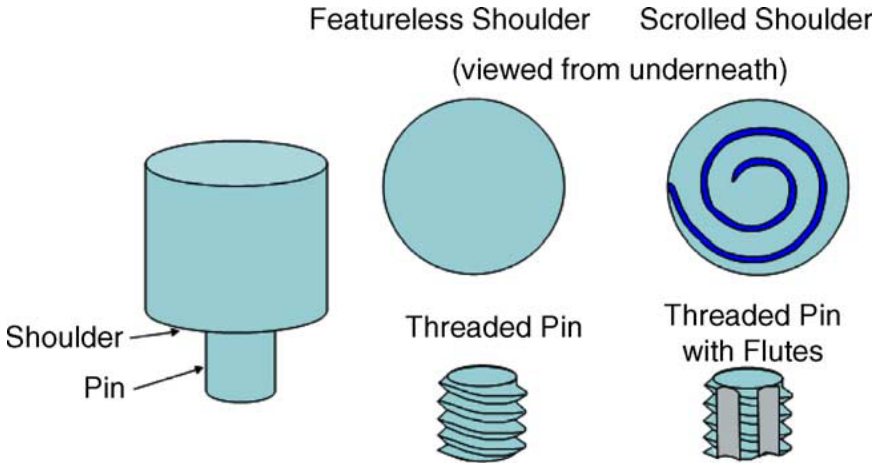

Figure 1-1: Schematic drawing of tool geometry. Reproduced with Permission from [11]. Copyright 2005 Elsevier.

The tool geometry has a major impact on the material flow during FSW. As a result, the resulting microstructure of the welded or processed parts can vary greatly depending on the tool design. To fully understand the relationship between material flow and microstructure, a systematic framework for tool design is needed. To this end, the use of computational tools, such as finite element analysis (FEA), can help visualize material flow and calculate the axial forces involved. Although some companies have reportedly engaged in internal research and development efforts in FSW and FSP, little information about these efforts and their outcomes is available in the open literature. Without proper tool information, it is challenging to generalize the microstructural development and the influence of processing parameters on the FSW and FSP process.

1.1.1.2. Welding Parameters

Two key parameters that play a significant role are the tool rotation rate, rpm (clockwise or anticlockwise) and the tool traverse speed (mm/min). The rotation of the tool causes the material to stir and mix around the rotating pin, while the translation of the tool moves the mixed material to the back of the pin to complete the welding process. The tool rotation rate affects the temperature generated by friction heating, with higher rates leading to increased heating and more intense stirring and mixing of material. However, the frictional coupling between the tool surface and workpiece governs the heating, meaning that an increase in heating with increasing tool rotation rate is not always observed. The angle of the spindle or tool tilt with respect to the workpiece surface, the insertion depth of the pin into the workpiece (also known as target depth), and the pin height are other important process parameters. A suitable tilt towards the trailing direction helps move the material efficiently, while an appropriate insertion depth of the pin ensures the production of sound welds with smooth tool shoulders. Recent developments have allowed for FSW with a 0-degree tool tilt, which is preferred for curved joints[11]. In some specific FSW processes, preheating or cooling may be necessary for effective results. When welding materials with high melting points such as steel and titanium, or high conductivity such as copper, the heat generated from friction and stirring may not be

sufficient to soften and plasticize the material. In such cases, preheating or the application of additional external heat sources can improve the material flow and broaden the process window. Conversely, for materials with lower melting points such as aluminum and magnesium, cooling can be utilized to reduce the growth of recrystallized grains and the dissolution of strengthening precipitates within and surrounding the stirred area.

1.1.1.3. Joint Design

The most used joint configurations in FSW are butt and lap joints (see Figure 1-2). In a simple square butt joint, two plates with equal thickness are placed on a backing plate and securely clamped to prevent separation of the abutting joint faces. The FSW process involves plunging a rotating tool into the joint line and traversing it along the line while keeping the tool shoulder in close contact with the plate surface, producing a weld along the abutting line. In a simple lap joint, two overlapped plates are clamped onto a backing plate, and a rotating tool is vertically inserted through the upper plate and into the lower plate, traversing along the desired direction to join the two plates. Other joint configurations can be achieved through combinations of butt and lap joints. Fillet joints, among other designs, are also possible for certain engineering applications. It is worth noting that no special preparation is required for FSW of butt and lap joints, and that two clean metal plates can be easily joined without any major surface condition considerations.

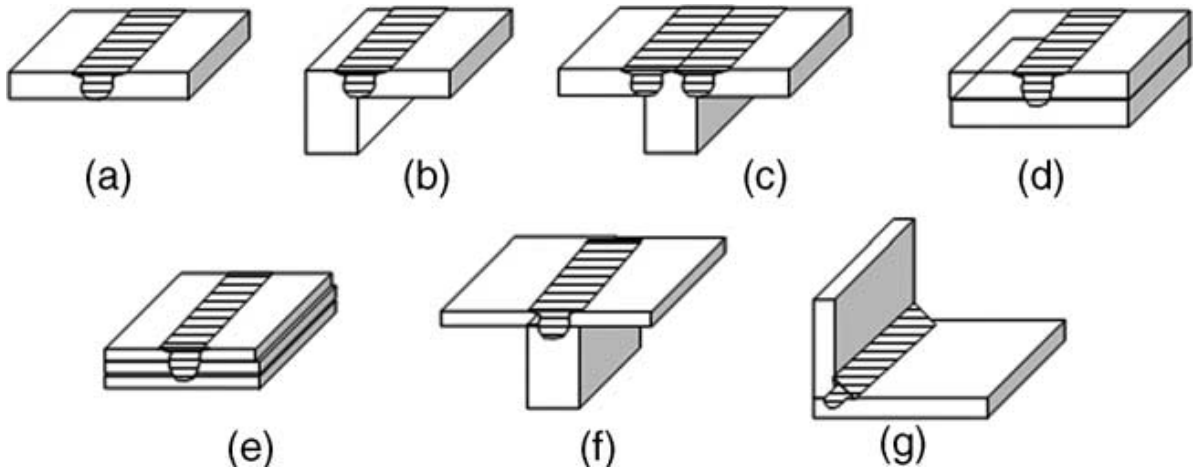

Figure 1-2: FSW type of joints: (a) square butt, (b) edge butt, (c) T butt joint, (d) lap joint, (e) multiple, (f) T lap joint, and (g) fillet joint. Reproduced with Permission from [11]. Copyright 2005 Elsevier.

1.1.2. FSW Process Dynamics

In FSW, there is a substantial amount of plastic deformation and temperature rise in and around the stirred area. This leads to a significant change in microstructure, including changes in grain size and boundary, dissolution and enlargement of precipitates, division, and movement of dispersoids, and texture. To optimize the process parameters and control the microstructure and properties of the welds, a comprehensive understanding of the mechanical and thermal processes involved is necessary. This section summarizes the current understanding of the mechanical and thermal processes that occur during FSW/FSP.

1.1.2.1. Metal Flow

To study the material flow during FSW, researchers have used various approaches such as tracer technique by marker, welding of dissimilar alloys, and computational methods including FEA. One method to track the material flow is to use a marker material as a tracer that is different from the material being welded. Different marker materials have been used. For example, Reynolds[12] and others used markers made of 5454Al-H32 and found that all welds exhibited some common flow patterns. The flow was not symmetric about the weld centerline and most of the marker material moved to a final position behind its original position. They concluded that the FSW process can be described as an in-situ extrusion process. Other researchers [13] used a faying surface tracer and a pin frozen in place to study the material flow of FSW 6061Al. They found that the material was moved around the pin in friction stir welding by two processes. First, material on the advancing side of the weld entered a zone that rotates and advances with the pin and this material was highly deformed. Second, material on the retreating side of the pin extruded between the rotational zone and the parent metal and this material exhibited low Vickers microhardness. Colligan[14] studied the material flow behavior during friction stir welding of aluminum alloys and found that material near the top of the weld moved under the influence of the shoulder rather than the threads on the pin.

Several studies have been conducted to model the material flow during FSW. These studies utilize various computational tools such as finite element models, mathematical

models, and metalworking models to understand the underlying physics of the material flow. Xu et al.[15] developed two finite element models to simulate FSW, and the simulation predictions were compared with experimental measurements. Colegrove and Shercliff [16] used a two-dimensional CFD code to model metal flow around profiled FSW tools and found that the flow behavior is significantly different from that obtained by the common assumption of material stick. Other efforts were exerted on developing a thermo-mechanical flow model that applies the principles of fluid mechanics and predicts material flow profiles, process loads, and thermal profiles.

Askari et al.[17] adapted a three-dimensional code capable of solving time-dependent equations of continuum mechanics and thermodynamics, which predicted important fields such as strain, strain rate, and temperature distribution. Stewart et al. [18] proposed two models for the FSW process, the mixed zone model and the single slip surface model. The mixed zone model assumes that the metal in the plastic zone flows in a vortex system, while the single slip surface model suggests that the principal rotational slip occurs at a contracted slip surface outside the tool-workpiece interface. Nunes[19] developed a detailed mathematical model of wiping flow transfer, which can describe tracer experiments.

Arbegast [20] suggested that the microstructure and metal flow in friction stir welding (FSW) are analogous to those observed in hot worked aluminum extrusion and forging processes. Thus, FSW can be conceptualized as a metalworking process comprising five distinct zones: preheat, initial deformation, extrusion, forging, and post-heat/cool down. In the preheat zone, the temperature increases due to the frictional heating generated by the rotating tool and the adiabatic heating from material deformation. As the tool progresses, an initial deformation zone emerges, succeeded by an extrusion zone and a forging zone. The material from the shoulder area is dragged across the joint, and behind the forging zone lies the post-heat/cool zone. Arbegast introduced a straightforward approach to model metal flow in the extrusion zone by considering mass balance, which uncovered a relationship between tool geometry, operational parameters, and the flow

stress of the materials being welded. The computed values for temperature, width of the extrusion zone, strain rate, and extrusion pressure align well with experimental findings.

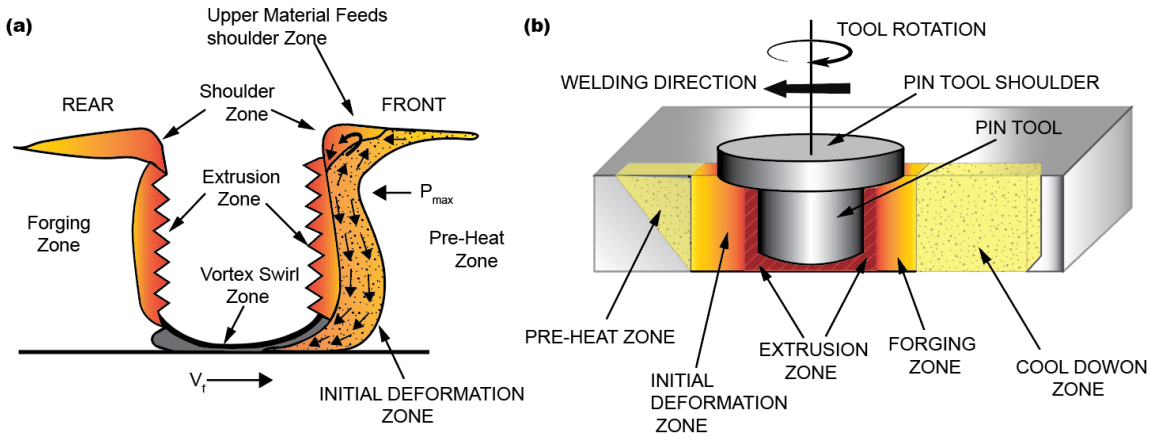

Figure 1-3. (a) Metal flow patterns and (b) metallurgical processing zones developed during FSW. Used with Permission from [20]. Copyright 2003, The Minerals, Metals & Materials Society.

1.1.2.2. Temperature Distribution

During FSW, the temperature distribution within and around the stirred zone affects the microstructure and mechanical properties of the weld. However, measuring temperature within the stirred zone is difficult due to plastic deformation caused by tool rotation and translation. Maximum temperatures have been estimated from the microstructure of the weld or recorded by embedding a thermocouple near the rotating pin. Studies on the microstructural evolution during FSW of different aluminum alloys have estimated maximum process temperatures to be between 400 and 480°C. Recently, Mahoney et al.[5] measured the temperature distribution around the stirred zone of a 7075Al-T651 plate and found that the maximum temperature near the corner between the edge of the stirred zone and the top surface exceeded 475°C. This suggests that the temperature within the stirred zone is likely above 475°C but lower than the melting point of 7075Al because no material melting was observed in the weld.

Tang et al.[19] attempted to measure the heat input and temperature distribution during friction stir welding by embedding thermocouples in 6061Al-T6 aluminum plates. They

found that the maximum peak temperature was at the weld center and decreased as the distance from the weld centerline increased. The temperature distribution within the stirred zone was relatively uniform and increasing the tool rotation rate and weld pressure increased the weld temperature. The shoulder of the tool generated more heat during FSW than the pin. The thermocouples placed at equal distances from the weld seam on opposite sides of the weld showed no significant differences in temperature. Furthermore, Arbegast and Hartley[21] conducted a study on the impact of FSW parameters on temperature. They found that the maximum temperature was greatly influenced by the rotation rate while the rate of heating was significantly affected by the traverse speed, for a given tool geometry and depth of penetration. They also noted that the temperature was slightly higher on the advancing side of the joint, where the tangential velocity vector was in the same direction as the forward velocity vector.

To summarize, the thermal profiles during FSW are influenced by many factors, including the maximum temperature rise within the weld zone, the tool shoulder, the ratio of tool rotation rate to traverse speed, and the top surface of the weld zone. Theoretical models have been proposed, but they do not fully integrate all the contributions of frictional heating and adiabatic heating. In addition, some studies indicate that the frictional condition changes from "stick" to "stick/slip" with increasing tool rotation rates, and this needs to be considered in theoretical and computational modeling of heat generation.

1.1.3. Microstructural Evolution

During the FSW/FSP process, the stirred zone experiences intense plastic deformation and high-temperature exposure, resulting in recrystallization and texture development. This also causes precipitating dissolution and coarsening in and around the stirred zone. The changes in microstructure have been studied by different researchers, and three zones have been identified - stirred (nugget) zone, thermo-mechanically affected zone (TMAZ), and heat-affected zone (HAZ). These microstructural changes have a significant impact on the post-weld mechanical properties.

1.1.3.1. Nugget Zone

The intensive plastic deformation and frictional heating that occur during FSW/FSP produce a fine-grained recrystallized microstructure within the stirred zone. This region is often called the nugget zone or the dynamically recrystallized zone (DXZ). Some researchers have observed an onion ring structure in the nugget zone under certain FSW/FSP conditions. The interior of the recrystallized grains generally has a low dislocation density, although some investigators have reported that the small, recrystallized grains of the nugget zone contain a high density of sub-boundaries, subgrains, and dislocations. The interface between the recrystallized nugget zone and the parent metal is relatively diffuse on the retreating side of the tool but quite sharp on the advancing side of the tool.

The shape of the nugget zone in friction stir welding (FSW) and friction stir processing (FSP) depends on various factors such as processing parameters, tool geometry, temperature of the workpiece, and thermal conductivity of the material. Nugget zone can be classified into basin-shaped and elliptical-shaped. Basin-shaped nugget zone widens near the upper surface and elliptical-shaped nugget zone is observed by FSW at higher tool rotation rates. Nugget shape can be changed by changing the processing parameters with the same tool geometry. The size of the nugget zone was found to be slightly larger than the pin diameter, except at the bottom of the weld where the pin tapered to a hemispherical termination. As the pin diameter increases, the nugget shape becomes more rounded with a maximum diameter in the middle of the weld.

It is widely recognized that the formation of fine and evenly shaped grains in the nugget zone is due to dynamic recrystallization during FSW/FSP. This process is affected by various factors such as FSW/FSP parameters, tool geometry, workpiece composition, workpiece temperature, vertical pressure, and active cooling. These factors can have a significant impact on the size of the recrystallized grains in the FSW/FSP materials. The effects of various processing parameters on the microstructure of FSW/FSP aluminum alloys have been studied[22]. Reduction in starting temperature of workpiece from 30 to -30 °C with liquid nitrogen cooling resulted in a decrease in the peak temperature from

330 to 140 °C at a location 10 mm away from the weld centerline, thereby leading to a reduction in the grain size from 10 to 0.8 mm in FSW 2024Al. Reducing the tool rotation speed or the ratio of tool rotation speed to traverse speed has been shown to decrease the recrystallized grain size in FSW and FSP of aluminum alloys. Research on FSP 1050Al and 7075Al-T651 suggests that the peak temperature during the FSW/FSP thermal cycle is the primary factor influencing recrystallized grain size. Additionally, there appears to be an optimal combination of tool rotation speed and traverse speed that produces the finest grain size for a specific aluminum alloy, given the same tool geometry and workpiece temperature. The grain size within the weld zone generally increases near the top of the weld zone and decreases with distance from the weld-zone centerline.

Different mechanisms were proposed[23-26] for dynamic recrystallization process in aluminum alloys, including discontinuous dynamic recrystallization (DDRX), continuous dynamic recrystallization (CDRX), and geometric dynamic recrystallization (GDRX). While aluminum alloys typically do not undergo DDRX, it is observed in alloys with large secondary phases. On the other hand, CDRX has been studied in commercial superplastic aluminum alloys and two-phase stainless steels, with several proposed mechanisms such as subgrain growth, lattice rotation associated with sliding, and lattice rotation associated with slip. In terms of the dynamic nucleation process in the nugget zone of FSW aluminum alloys, CDRX, DDRX, GDRX, and DRX in the adiabatic shear bands have been proposed as possible mechanisms. Recent experimental observations suggest that DDRX is the operative mechanism for recrystallization during FSW/FSP of aluminum alloys, with recrystallized grains in the nugget zone significantly smaller than pre-existing sub-grains in the parent alloy.

The texture of FSW materials can affect properties such as strength, ductility, formability, and corrosion resistance. FSW material consists of different zones, each with its own thermo-mechanical history. The nugget region in FSW has sub-domains and can contain different microstructural variations depending on tool rotation rate and traverse speed. Texture studies[27] of FSW aluminum alloys have been conducted using orientation imaging microscopy (OIM) to obtain texture information and grain boundary

misorientation distribution data. The nugget region of FSW welds predominantly consists of high-angle grain boundaries, but micro-texture analysis shows a complex texture pattern. During FSW, the material undergoes intense shearing and dynamic recrystallization concurrently, which can affect the final texture. The deformation under the shoulder of the tool after the pin has passed can significantly influence the final texture.

1.1.3.2. Thermomechanical Affected Zone

The FSW/FSP process produces a thermo-mechanically affected zone (TMAZ) between the parent material and the nugget zone, which is unique to this process. The TMAZ is characterized by a highly deformed structure, and the elongated grains of the parent metal are deformed in an upward flowing pattern around the nugget zone. Although the TMAZ undergoes plastic deformation, recrystallization does not occur in this zone due to insufficient deformation strain. However, high-temperature exposure during FSW/FSP causes some precipitates to dissolve in the TMAZ, which depends on the thermal cycle experienced by TMAZ. Additionally, the grains in the TMAZ usually contain a high density of sub-boundaries.

1.1.3.3. Heat Affected Zone

Beyond TMAZ is the heat-affected zone (HAZ) that undergoes only a thermal cycle and retains the same grain structure as the parent material. However, HAZ experiences significant effects on the precipitate structure due to thermal exposure above 250 °C for Aluminum alloys[5]. FSW results in coarsening of the strengthening precipitates and a widening of the precipitate-free zone (PFZ) in the HAZ. This observation is also reported for different alloys by various studies[28, 29].

1.1.4. Properties

1.1.4.1. Residual Stress

Fusion welding generates high residual stresses due to heat and constraint, whereas FSW welds are believed to have low residual stresses. However, the rigid clamping used in FSW can result in the generation of longitudinal and transverse stresses that impede weld

nugget contraction and heat-affected zone during cooling. Residual stress is important in determining the post-weld mechanical properties, especially fatigue properties. Recent studies[30-32] using X-ray diffraction, neutron diffraction, and high-energy synchrotron radiation showed that the longitudinal residual stresses in FSW are always higher than the transverse ones, with an 'M'-like distribution across the weld. The longitudinal residual stresses were tensile, and the transverse residual stresses were compressive, and both exhibited 'M'-like distributions. The residual stress magnitudes are significantly lower than those observed in fusion welding and lower than the yield stress of the aluminum alloys used in FSW. Residual stress reduction results in a significant reduction in distortion and improvement in mechanical properties of FSW components.

1.1.4.2. Hardness

Several studies[33-35] discussed the impact of the FSW technique on the hardness profile of two types of aluminum alloys. Heat-treatable (precipitation-hardenable) alloys and non-heat-treatable (solid-solution-hardened) alloys were used to carry out the study. It was noted that FSW technique led to a softened region in precipitation-hardened aluminum alloys due to coarsening and dissolution of strengthening precipitates during the thermal cycle. Hardness profile was found to be dependent on the precipitate distribution rather than grain size in the weld. The mechanical properties of precipitation-hardened aluminum alloys depend mainly on the density of needle-shaped precipitates and slightly on the density of rod-shaped precipitates. In contrast, solid-solution-hardened aluminum alloys showed no softening effect in the welds, and their hardness profile mainly depended on dislocation density, as strain hardening is the dominant hardening mechanism. Microstructural factors governing the hardness in FSW of solid-solution-hardened aluminum alloys include the dispersion strengthening due to the distribution of small particles.

1.1.4.3. Mechanical Properties

1.1.4.3.1 Strength and Ductility

The effect of FSW on the tensile properties of aluminum alloys, specifically 7075Al-T651 and 6063-T5 have been reported in the literature[5, 33, 36]. It was found that FSW

resulted in a reduction in strength in the weld nugget, but elongation remained unaffected. This reduction in strength was attributed to the reduction in pre-existing dislocations and the elimination of very fine hardening precipitates. Post-weld aging treatment resulted in the recovery of a large portion of the yield strength in the nugget, but at the expense of ultimate strength and ductility. When tested in the transverse orientation, a significant reduction in both strength and ductility was observed compared to unwelded parent metal. The low-strength Heat Affected Zone is most susceptible to fracture, resulting in low strength and ductility along the transverse orientation of the weld. Post-weld aging treatment improved the strength and ductility of the weld. However, the solution heat-treatment produced the most desirable results. It was also found that the strain of the as-welded weld was localized in a region away from the weld centerline, resulting in final fracture with low strength and ductility.

1.1.4.3.2 Fatigue

Fatigue properties are crucial in many applications, so it is important to understand the fatigue behavior of FSW welds. Studies[36, 37] have been conducted on the S-N and fatigue crack propagation behavior of FSW welds in the past few years. The fatigue strength of FSW welds was lower than that of the base metal, and the surface quality of the FSW welds had a significant effect on their fatigue strength. FSW welds have finer and more uniform microstructures, leading to better properties compared to laser and MIG welds. The impact of FSW parameters on fatigue strength is complex, and no consistent pattern has been identified to date. However, applying low plasticity burnishing (LPB) post-FSW can improve the fatigue life of FSW joints. Achieving compressive residual stresses at the surface and a high-quality surface finish is crucial for optimal fatigue properties. Corrosion products on the surface may influence the initiation of fatigue cracks, and the effect of FSW on corrosion further complicates the corrosion-fatigue interaction. Despite these complexities, the fatigue performance of FSW aluminum alloys has shown very promising results. In recent years, numerous studies have been conducted to assess the influence of FSW on the behavior of fatigue crack propagation.

1.1.4.3.3 Fractural Toughness

The welding process can produce flaws in structures that can affect their performance. Inspection codes provide standards for the acceptability of welds, and non-acceptable flaws must be repaired before the structure is put into service. FSW is a newer technique that generally produces defect-free welds, but there is no established code for FSW yet. Fracture behavior is an important consideration for evaluating the suitability of FSW for various applications. Fracture toughness is commonly used to evaluate the fracture behavior of FSW, with the crack tip intensity factors (K) and the J integral or the crack opening displacement (CTOD) being commonly used parameters. Studies[38, 39] have been conducted to evaluate the fracture toughness of FSW, and the results suggest that FSW can produce welds with higher or comparable fracture toughness to the base material, depending on the alloy chemistry and FSW parameters. The fine grain size and small particles in the nugget zone tend to enhance the fracture toughness, while the widened partially melted zone (PFZ) and coarsened particles in the heat-affected zone (HAZ) tend to reduce it.

1.2. Recent Efforts in Modelling the FSW Process

Accurately predicting the quality of a friction stir welding (FSW) process requires a thorough understanding of the influencing variables. However, due to the process's complexity, gathering all necessary information during FSW can be challenging[40, 41]. Finite element (FE) modeling serves as an effective tool to reduce the need for extensive initial experimental trials and assists in optimizing welding parameters[42, 43]. Simulating FSW through FE, which involves plastic deformation, heat flow, material flow, and friction, is complex and requires addressing nonlinear thermomechanical processes[44]. Recent advancements in various modeling approaches, including computational fluid dynamics (CFD), Arbitrary Lagrangian-Eulerian (ALE), and Coupled Eulerian-Lagrangian (CEL), have improved the simulation of FSW processes.

The CFD approach models FSW by treating the workpieces as a non-Newtonian fluid and analyzing the thermomechanical behavior using energy, momentum, and mass conservation equations[45]. Seidel and Reynolds developed a 2D thermal model based on fluid mechanics to examine material flow in FSW joints. Their model represented the

FSW process as a steady-state, laminar flow of a non-Newtonian fluid past a rotating circular cylinder that mimicked the FSW tool pin. Their findings indicated that the material flow was asymmetric about the welding centerline and involved significant vertical mixing. However, the model had discrepancies compared to experimental results, mainly due to the absence of the tool shoulder, which is crucial for the mixing process.

Colegrove and Shercliff [46, 47] conducted a comprehensive study on how material moves during the process of FSW by using various tool shapes. They used 2D and 3D models and presented a unique modeling approach that involved slip boundary conditions. This slip model revealed that the material flow was different with different tool shapes, which was not noticeable in the traditional stick model. Zhang et al.[48] developed a three-dimensional computational fluid dynamics model to study the friction and heat generated by plastic deformation during friction stir welding. The model used an advanced interfacial friction model to understand the relationship between the heat generated at the interface between the welding tool and the workpiece. They discovered that both sticking and sliding occur at different parts of the interface, which has a major impact on the way heat is generated and distributed. Hasan[49] employed a combination of a single-phase flow and a two-phase flow (volume of fluid method) model to forecast the temperature and the formation of surface flash, respectively. The results showed that the temperature predictions were accurate, and the use of the two-phase flow model provided a more realistic representation of surface formation. Zhai et al.[50] conducted a numerical simulation using CFD to examine how the tool tilt angle affects heat generation and material flow in friction stir welding. The findings showed that increasing the tool tilt angle from 0 degrees to 2.5 degrees resulted in higher heat being generated in the workpiece, helping to keep the flow of material in the nugget zone and reducing flash formation. Studies have shown that the CFD approach can effectively simulate FSW. However, one of the limitations of this method is that it does not consider material hardening and elasticity, only rigid-viscoplastic material behavior is considered.

The FSW simulation can also be done using the Arbitrary Lagrangian-Eulerian (ALE) method, which includes an adaptive re-meshing technique. This approach adjusts the

computational mesh as needed to optimize its shape and handle significant deformation without causing excessive mesh distortion during the simulation. This makes the ALE-based FSW simulation more efficient, as it can be completed within a reasonable amount of time, and helps overcome convergence issues, loss of accuracy, and extended computation time that can occur with highly distorted elements during FSW[51, 52]. Schmidt and Hattel[53] created a 3D finite element model to investigate the formation of defects in welded joints during friction stir welding. The model was based on the Johnson-Cook flow stress model and included adaptive boundary conditions and Coulomb's law of friction to define the contact forces between the tool and plate surfaces. The results showed that the cooling rate greatly affects the formation of defects in the welded joint, with a higher cooling rate leading to faulty material deposition behind the tool pin. Deng and Xu[54] used a 2D finite element model via ABAQUS to simulate the movement of material around the tool pin during FSW. They considered two different models for the interaction between the tool pin and workpiece (constant rate slip and modified Coulomb's friction models) and found little difference in the material flow simulation and post-weld marker positions. They noted that the study had some limitations due to computational limitations and a lack of experimental data.

Zhang et al.[55, 56] conducted further research to determine how different welding parameters affected the material flow and residual stresses in AA 6061-T6 FSW joints. They used 2D and 3D models and analyzed the material flow by tracking tracer particles. Their findings revealed that the material flow differed between the advancing side and retreating side, and the residual stress along the length of the joint increased as the traverse speed increased. Zhang[57] compared the classical and modified Coulomb's contact models to understand their impact on the thermal-mechanical process in FSW. The results indicated that both models generated similar outcomes at lower rotation speeds. However, when using the classical Coulomb friction law at higher tool rotation speeds, the simulation failed because of an increase in the dynamic impact of the welding tool. Dialami et al.[58-60] conducted a systematic investigation of the behavior of material flow and the formation of defects during FSW using a 3D ALE model. They created an improved friction model (modified Norton's friction law) to provide a more accurate

thermomechanical response by considering the impact of uneven pressure distribution under the tool shoulder. The study found that the welding parameters have a significant effect on defect formation in FSW joints. The comparison of numerical and experimental results showed that the proposed friction model improved the ability to predict results. Andrade et al.[61, 62] conducted research to find out how the strain rate, torque, and welding temperatures change during friction stir welding of aluminum alloys under different welding conditions and tool dimensions. They found that the rotational speed and size of the tool were the main factors that impacted the torque and temperature. The numerical model they used was successful in predicting the strain-rate gradients and heat generation in the stirred area with good accuracy. Despite these successes, the authors[63] noted that one of the challenges of using the ALE approach is choosing the right movement between the welded material and the mesh to avoid excessive mesh distortion.

Recently, a new simulation method called Coupled Eulerian-Lagrangian (CEL) was created to tackle problems involving large deformations. It was implemented in the software ABAQUS and uses an explicit time integration formulation. This approach automatically tracks and calculates the interface between the welded material and the FSW tool based on Benson's contact mixture theory[64]. This method is useful for simulating applications with large deformations and complex tool shapes without needing to fit the Eulerian mesh to the tool's geometry. Recently, Al-Badour et al.[65] used a 3D local model based on the Coupled Eulerian-Lagrangian approach to study FSW of AA 6061-T6 aluminum alloy. This model considers adiabatic heat effects and predicts volumetric defects and the forces and torque on the welding tool. The material behavior and tool-workpiece interaction were described using Johnson-Cook constitutive and Coulomb's frictional contact models, respectively. The model was found to accurately predict the shape of the plasticized zone and the formation of defects in the weldment. However, there was a discrepancy between the model and experimental results for force and torque. Tongne et al. [63] used the CEL method to study the formation of "kissing bonds" and "banded structures" in a 2D model. The results of their experiments and simulations showed that the shape of the tool pin had a greater impact on the formation of banded structures than the friction conditions. On the other hand, Chauhan et al.[66]

used also the CEL method to develop a 3D model to predict defects that occur during FSW. They found that the length and tilt angle of the tool pin greatly impacted the formation of defects in the joint. Their model was successful in predicting the formation of tunnel defects for various welding conditions.

Su et al.[67] utilized the Coupled Eulerian-Lagrangian method to study the heat distribution and flow of materials during friction stir welding of titanium alloys in T-joints. The findings revealed that the stirring zone had a higher concentration of temperature in the form of a circular truncated cone, due to titanium alloys having lower thermal conductivity than aluminum alloys. The material on the top and bottom surfaces of the weld mainly came from the skin and stringer materials, respectively. Akbari et al.[68] created a 3D model to predict how materials mix in the stirring zone during FSW of dissimilar metals. The model was able to accurately predict the mixing process at the interface but had difficulty estimating the shape of the stirring zone. Recently, Wang et al.[69] developed an analytical model using the Hill-Bower similarity relationship to study the constant stick-slip fraction in the steady-state and its relationship to the welding process. The results from their analytical model were validated with simulations, experimental work, and a CEL model. They concluded that the CEL-based finite element simulations provide more reliable results than the CFD model. In conclusion, based on the analyzed studies, the CEL approach is a more efficient way of modeling the multi-physics and severe plastic deformation involved in FSW compared to the CFD and AEL modeling techniques. Although progress has been made in using the CEL approach to model material flow and defect formation in FSW, further efforts are needed to model the heat generation and residual stresses using a real industrial FSW tool with a complicated shape.

FSP is valued for refining sheet metal grain structures, yet accurate predictive models are lacking. Experimental research dominates FSP studies, with limited modeling efforts[70]. Nassar and Khraisheh[71] have studied the application of CFD to model material flow and heat generation during FSP of AZ31B magnesium alloy, with a focus on potential local melting phenomena. By incorporating the latent heat of fusion and considering

liquid formation effects on viscosity and friction, the model provides insights into temperature evolution. Findings indicate that increasing rotational speed elevates temperature in the stirring region, with a slight decrease observed with higher translational speed. As liquid phase forms, temperature rise rate diminishes, stabilizing below the liquidus temperature at high rotational speeds. The formation of a semi-molten layer around the tool potentially reduces the shearing required for microstructure refinement. Aljoaba et al.[72] have investigated the usage of coolants to control grain growth during FSP. Two CFD models are developed with and without coolant application. They analyze process parameters' effects on temperature, strain rate, and material flow, correlating them with the Zener-Holloman parameter to predict grain size distribution. Results, validated against experiments, demonstrate the efficacy of coolants in controlling grain growth in Mg AZ31B-O alloy during FSP. Albakri at al.[73] have explored FSP with an internally cooled tool to manage heat during processing. Using a 3D CFD model, the impact of rapid tool cooling on temperature and flow stress distribution is investigated for AZ31B Mg alloy. By estimating grain size and hardness using Zener-Holloman and Hall-Petch relationships, the study demonstrates that internally cooled FSP tools effectively control temperatures, leading to improved mechanical properties and prolonged tool life. Aljoaba et al.[74] have developed a 3D CFD model to simulate FSP, analyzing temperature, strain rate, and material flow. Correlations were established to predict grain size distribution. Darras and Khraisheh[75] have introduced an analytical model predicting strain rate distribution and deformation zones in FSP, considering various process parameters. It incorporates tool effects and interfacial conditions, successfully predicting deformation zone shapes and strain rate values in line with reported literature results.

1.3. FSW of Al Alloys

FSW is mainly used on iron or aluminium and specifically for systems that requires relatively high weld strength. This technology can weld iron, aluminium, magnesium, copper, and titanium alloys, mild and stainless steel and more recently polymers[76]. In addition, welding of dissimilar metals. Moreover, Friction Stir Processing (FSP)

originates from the FSW process and was developed by Mishra et al.[5]. It is mainly used to achieve certain enhancement in mechanical properties and for microstructure refinement.

Aluminum alloys are a popular alternative to steel in various applications due to their lightweight, rust-resistant surface with a chromium coating, high strength, and good electrical conductivity. They are divided into two categories, wrought, and cast aluminum, and further subcategorized based on the main alloying elements, ranging from 1xx to 6xx series. The 2XXX series, with copper as the main alloying element, is strengthened through solution heat treatment. AA2024, also known as the aircraft alloy, is well-regarded for its strength and fatigue resistance and is commonly used to make structural parts in aircraft. The strength of aluminum composites can be increased by adding nano-ZrB2 reinforcements, resulting in super plasticity in the processed FSP composites, which display better super plasticity than cast parts[77-80].

The 3XXX series of aluminum alloys contains manganese as the main ingredient, resulting in moderate strength and good workability. These alloys are commonly used in heat exchangers, cooking utensils, radiators, piping systems, and more. The 4XXX series contains silicon, which lowers the melting point of aluminum to prevent brittleness. However, silicon is used as a filler in welding the 6XXX series. The 5XXX series contains magnesium, which provides good weldability, high corrosion resistance, and moderate to high strength. These alloys are applied in marine structures, buildings, storage tanks, pressure vessels, and other dynamic loading applications. The addition of TiO_2 nanoparticles to the base alloy improved hardness and tensile strength. FSW processing of AA5754 material resulted in smaller grain size and reduced friction heating[81-83].

The 6xx series aluminum alloys, which have Si and Mg as the main components, are known for their high corrosion resistance and moderate strength, making them ideal for use in lightweight truck and marine ship frames[84, 85]. The addition of Cu improves the material properties such as hardness and yield strength and is therefore used in the automotive and construction industries. The addition of 4.5% Cu and 10% SiC to AA6061 composite processed by FSW increases joint strength by 96% when operated at high

rotational speeds. Corrosion is a common issue in non-lithium-containing alloys, and anodization of sheet metal alloys improves specific mechanical properties in AA6061 alloys[86]. The 7XXX series, with Zn as the primary alloying element and Mg for added strength, contains heat-treatable alloys like AA7050 and AA7075, which are widely used and improve formability when subjected to high temperatures[87].

1.4. FSW of Inconel 718

Nowadays, industries are incorporating advanced and innovative materials in their products. Ceramic materials have exceptional resistance to environmental deterioration; however, they have low fracture toughness and poor performance under tensile stress conditions, making them unsuitable for most structural applications. On the other hand, refractory metal alloys have outstanding high-temperature strength but low oxidation resistance. Therefore, nickel-based superalloys have been preferred for structural applications at elevated temperatures due to their strong high-temperature mechanical characteristics and excellent environmental resilience.

Nickel-based superalloys, containing a combination of heavy refractory and lightweight elements, are utilized in demanding environments such as high temperatures and corrosive conditions due to their exceptional mechanical properties including high fracture toughness, tensile strength, and yield strength. The aerospace and power generation industries specifically require high-quality welded joints for gas turbines, leading to ongoing efforts globally to optimize process parameters and techniques to further enhance the properties of these alloys[88]. Additional strength is provided to the Ni alloys by alloying elements such as chromium, titanium, aluminum, cobalt, iron, niobium, molybdenum, tungsten, and tantalum. However, joining these alloys presents challenges due to their complex composition and properties[89]. Interest in Nickel alloys for the oil industry is rising, especially in subsea engineering where effective welding of high-strength materials is crucial. FSW offers a promising alternative for combining materials while maintaining or improving their properties. This is particularly relevant for Corrosion-Resistant Alloys used in deep-water hydrocarbon extraction. Previous research has mainly focused on FSW of Inconel series alloys like 600, 625, and 718[90]. Nickel

alloys are extensively used in petroleum industry's pre-salt reservoirs. The selection of materials for pipelines in such environments, facing high pressures and corrosive substances like NaCl, and H_2S is critical. Nickel alloys, with their corrosion-resistant properties, are increasingly favored for pipeline protection, particularly in rigid clad pipes comprising an API-5L steel with a Ni superalloy inner layer.

The success and cost-effectiveness of components made from Ni-based superalloys depends on their ability to be joined with similar and dissimilar materials. The conventional methods of manufacturing, refurbishing, and repairing Inconel 718 and other nickel superalloys include arc welding, electron beam welding, and laser welding. Fusion-welding processes commonly used for Ni-based superalloys often lead to various issues such as segregation, porosity, and embrittlement. FSW, being a solid-state joining process with lower heat input, presents a promising alternative to fusion welding, offering defect-free welds and improved mechanical properties. Additionally, solid-state cladding processes based on FSW can further enhance pipeline fabrication. Though the application of FSW to high-temperature Ni alloys is still under research, it holds significant potential for cost reduction in pipeline welding projects[91]. On the other hand, welding titanium and nickel-based alloys, crucial for aerospace components, has long posed challenges due to their exceptional properties. These alloys exhibit high dynamic shear strength and increased strain hardening, complicating the solid-state welding process. Common issues include inadequate penetration, microfissures in the HAZ, strength reduction in the HAZ, and subpar mechanical properties in the weld fusion zone (FZ). Various welding techniques encounter these difficulties when working with nickel-based superalloys[92]. Therefore, investigating the application of FSW on these alloys is essential to understand its impact on mechanical as well as corrosion properties.

Inconel 718 is a nickel-chromium-molybdenum alloy that is designed for high strength and corrosion resistance at high temperatures. It is also known as Nicrofer 5219, Superimphy 718, Haynes 718, and Udimet 718. It is often used in applications that require high strength and corrosion resistance at temperatures up to 704°C [93-95], such as in the aerospace and power industries. It can also be used in applications that require high

strength and corrosion resistance in a wide range of temperatures, including cryogenic temperatures. Inconel 718 has good weldability and is often used in welding applications. It also has excellent fatigue strength and is often used in applications that require high strength and fatigue resistance. It is a precipitation-hardened alloy, which means that it is strengthened through a heat treatment process known as precipitation hardening. This heat treatment allows Inconel 718 to maintain its strength and corrosion resistance at high temperatures.

Inconel 718 is suitable for temperatures ranging from -220°C to 700°C. Its applications span across various industries including aerospace, industrial gas turbine engines, and cryogenic tankages, where it is used for components like rocket casings, rings, and sheet metal parts. Specifically, it serves as a prime material for aircraft and gas turbine disc manufacturing, owing to its precisely balanced chemistry with over 20 controlled elements[96] (See Table 1-1 for chemical compositions). It stands out as a prevalent nickel-based alloy in aerospace applications due to its exceptional machinability and weldability compared to other superalloys.

Nickel-based alloys generally exhibit high yield (700–1200 MPa) and tensile (900–1600 MPa) strength at room temperature[97], retaining these properties across a broad temperature range (up to 600–800 °C). Consequently, they find extensive use in the hot sections of jet engines. The mechanical properties of Nickel-based superalloys, such as Inconel 718, are influenced by strengthening phases like γ'' and γ' (See Table 1-2 for mechanical properties). These phases, with specific compositions, enhance high-temperature strength. However, at temperatures above 750°C, the dissolution of the γ' phase can affect mechanical properties. Although Inconel 718, with its lower Aluminum and Titanium content, experiences fewer cracks., while it is resistant to strain age cracking, it remains susceptible to intergranular cracking. The presence of other phases like δ, carbide, laves, and sigma can also impact the mechanical properties of welded joints. Furthermore, variations in heat treatment cycles induce changes in the microstructure of Inconel 718[98, 99].

The welding of Inconel 718 is challenged by the formation of laves phases, solidification cracking, and liquation cracking. These phases, particularly rich in Nb, significantly affect the alloy's mechanical behavior and impact toughness, especially in the weld zone[100]. Inconel 718's resistance to cracking is attributed to its low Aluminum and Titanium content[101]. However, the presence of Nb contributes to solidification and liquation cracking in the fusion zone and heat-affected zone[102]. The γ phase provides solid solution strengthening, while the δ phase reduces ductility. Controlling laves phase formation, which causes liquation cracking, can be achieved through welding techniques that involve low heat input and faster cooling rates, such as electron beam and laser beam welding. Techniques like GTAW use filler materials with lower Nb content to mitigate cracking issues. Nb segregation at grain boundaries at high temperatures affects stability, weakens grain boundaries, and impacts mechanical properties. Micro-segregation of Nb-rich phases contributes to the formation of laves phases, influencing stability[103].

Iturbe et al.[104] explored the rheological properties of Inconel 718 across various temperatures and strain rates relevant to machining processes. It delineated two distinct behavior regimes based on temperature, with a critical threshold identified at 700°C (See Table 1-3 for physical properties). The flow stress curves were correlated with microstructural features and microhardness measurements for each regime. Utilizing this experimental data, an empirical model was devised, integrating strain softening and the interaction between temperature and strain rate. This model, an extension of the Johnson-Cook framework, was tailored for Finite Element Method (FEM) simulations involving Inconel 718, facilitating more accurate machining predictions.

Ni	Fe	Cr	Nb	Mo	Mn	Ti	Al	Si	C
Bal.	19	18.8	5.5	3.1	0.6	0.9	0.6	0.1	0.05

Table 1-1: Chemical compositions of Inconel 718 (in wt%)[105]

Tensile Strength (MPa)	0.2% Yield strength (MPa)	Elongation (%)	Hardness (HV)
948	455	65	260

Table 1-2: Mechanical properties of Inconel 718[105]

Density, g/cm^3	Melting range, °C	Coefficient of thermal expansion, 10^{-6}/K (at 538°C)	Thermal conductivity at RT, W/m•K	Electrical resistivity, 10^{-8} Ω/m
8.22	1260–1335	14.4	11.4	1250

Table 1-3: Physical properties of Inconel 718 [106]

Inconel 718 is a complicated alloy that has good weldability, but its welds often experience various cracking issues, such as solidification cracking, heat-affected-zone liquation cracking, ductility dip cracking, and strain age cracking[107, 108]. There are many factors that contribute to these cracking problems, such as alloy chemistry, processing methods, process variables, and weld design. Since the 1980s, efforts have been made to overcome these cracking issues through advancements in alloy design and processing, but further improvements are still necessary. FSW has been shown to be a feasible method for welding nickel-base superalloys, but more research is needed in this area[90, 109, 110].

FSW is an innovative technique that achieves coalescence through heat generated by mechanically induced sliding motion and pressure between surfaces. It offers superior mechanical properties compared to traditional arc welding methods. However, its application to nickel-based alloys is restricted due to limited tool material availability. The process parameters primarily include tool rotational speed and transversal speed. Mechanical properties like microhardness and tensile strength serve as crucial process responses. Moreover, FSW offer advantages over fusion welding methods by eliminating issues like porosity, shrinkage cracks, segregation, and grain coarsening.

To manufacture Inconel 718 alloys, recent methods have included fusion welding processes like carbon dioxide and Nd–YAG lasers and electron beam welding[111-113]. However, using fusion welding with Inconel 718 brings issues like boron/niobium segregation, Laves phase formation, and liquation cracking in weld or heat-affected zones due to high heat input[114]. Thus, adopting FSW with lower heat inputs in the solid state is crucial to address these challenges.

In recent years, researchers have been focused on developing accurate models for predicting the microstructure and mechanical properties of friction stir welded Inconel 718. One area of focus has been on developing models that can predict the HAZ and the thermo-mechanically affected zone (TMAZ) of the weld. These models can help predict the microstructure and mechanical properties of the weld and the surrounding material, which is important for optimizing the welding process and ensuring the quality of the welded joint. Another area of research has been on the effect of different welding parameters on the microstructure and mechanical properties of the weld. Researchers have been studying how variables such as welding speed, rotational speed, and axial force affect the microstructure and mechanical properties of the weld. Additionally, scientists have been working on developing models that can predict the residual stress and distortion in the welded joint, which is important for ensuring the stability of the structure[115]. Finally, researchers have been investigating the effect of post-weld heat treatment on the microstructure and mechanical properties of the welded joint, which can improve the properties of the welded joint.

There have been limited studies in the literature on friction stir welding and friction stir processing of Inconel 718 alloy. So far, successful results have only been achieved at low tool rotations (100-500 rpm) and slow welding speeds (30-150 mm/min) with high axial loads (>35kN)[90, 110, 116-119]. These conditions limit the industrial use of FSW for Inconel 718 and raise questions about its economic viability. Despite these challenges, there have been promising outcomes with these narrow process parameters, including welds with greatly refined grain structures, smaller recrystallized grains, and increased microhardness compared to the base metal[118, 119]. However, the main technical

challenge remains in achieving successful FSW welds under a wider range of process parameters.

An experimental study was conducted by Song and Nakata[118], where a sample of Inconel 718 alloy was successfully subjected to FSW without any defects. The sample dimensions were 150mm×32.5mm×2mm. The welding was conducted using a WC-Co tool which had a 15mm shoulder diameter, 6mm probe diameter, and 1.8mm length. To ensure a sound weld, the tool was tilted 3◦ forward from the vertical and argon gas was used to prevent surface oxidation during welding. The FSW process was conducted with a tool rotation speed of 200 rpm, a tool normal force of 39.2×10^3 N, and a traveling speed of 150 mm/min. The FSW process caused grain refinement in the stir zone, reducing the grain size from an average of 10μm in the base material to 1-3μm, with dynamic recrystallization accompanying the process. This refinement contributed to a significant improvement in the microhardness, which increased from 273Hv in the base material to 352Hv in the stir zone, and the tensile strength, which increased from 886MPa to 1135MPa in the stir zone, causing fracture in the base material at the joint. The mechanical properties of the FSW joint were further enhanced by post-heat treatment, as it resulted in the formation of precipitates such as MC carbides and intermetallic phases at elevated temperatures. The post-heat-treated specimen showed a significant increase of approximately 40% in microhardness distribution and more than 30% in tensile strength compared to the FSW joint. These improvements in mechanical properties were attributed to the formation of precipitates during post-heat treatment, indicating that Inconel 718 alloy could exhibit better mechanical properties if post-heat treatment is performed after FSW.

Ye et al.[109] used tungsten carbide tools to conduct FSW on a 2 mm thick sheet of Inconel 600 alloy. The study reported defect-free joints with improved properties, demonstrating the feasibility of using FSW to join nickel-based alloys. Sato et al.[120] also achieved defect-free friction stir welds in Inconel 600 alloy by using a polycrystalline cubic boron nitride tool. The welds exhibited better mechanical properties than the base material due to a fine grain structure in the stir zone. Song and Nakata[118, 121] explored

FSW of Inconel 625 and 718 alloys using WC-Co tool material to join 2 mm thickness sheets. The studies reported that the application of FSW led to enhanced mechanical properties of the welds, such as microhardness and tensile strength, due to grain refinement. Although Inconel 600 alloy is easier to weld due to its relatively low yield strength, most studies have focused on it rather than the high yield strength Inconel 718 alloy.

Another experimental trial was attempted by Ahmed et al.[110], where 4 mm thick Inconel 718 alloy was welded using a silicon nitride tool. FSW has improved the mechanical properties of the material by refining the grain size and inducing precipitation in the nugget (NG) region. The hardness in the NG region has increased compared to the base material, and the tensile properties of the FSW joints remain in the annealed properties range of the alloy. FSW has also significantly reduced the grain size across the transverse cross-section of the NG region. Additionally, there is a notable change in grain size along the thickness of the weld in the NG region from about 5 mm near the top to 2 mm near the base of the NG region. Increasing the FSW transverse speed has led to more reduction in grain size and improved hardness values.

Experimental tests have shown that Inconel 718 behaves differently above and below the critical temperature of 700°C. Below this temperature, the mechanical properties of Inconel 718 are less sensitive to temperature changes, with only a 20% decrease in mechanical properties observed between 21°C and 700°C. However, above 700°C, the mechanical properties decrease significantly with increasing temperature. As a result, it is possible to predict the thermal softening of Inconel 718 below 700°C using a constant Johnson-Cook temperature sensitivity parameter m. However, above 700°C, the m parameter should vary with temperature. These results suggest that careful consideration of temperature and its effects on Inconel 718 is necessary when designing high-temperature applications that require this material[104]. Further studies are needed to fully understand the behavior of Inconel 718 at high temperatures and to develop accurate predictive models that account for these effects. Therefore, more efforts are needed to study the friction stir welding process of Inconel 718 with the aim of producing high-

quality welds under optimized process parameters, such as high tool rotations, fast welding speeds, and lower axial loads.

1.4.1. Tool Selection

FSW, originally designed for Al alloys, has evolved to be used with Ni, steel, and Ti alloys due to the availability of more durable tools. However, tool wear and the high cost of tools remain barriers to its widespread application, particularly for high melting-temperature materials. When applied to Ni alloys, FSW encounters increased tool wear due to the high process forces, limiting welding speed. The effectiveness of tool materials remains a significant challenge in extending the use of FSW to high plasticizing-temperature materials like Ni-based alloys[122].

Polycrystalline cubic boron nitride (PcBN) is a favored material for FSW tools due to its high strength, hardness, and stability at elevated temperatures. Its interaction with the weld metal results in smooth weld surfaces[11]. Tungsten carbide-based tools, known for their toughness and hardness, are prone to fracture under impact and vibratory loads during FSW[123]. To enhance ductility, Tungsten carbide (WC) is often combined with a Cobalt (Co) binder phase, resulting in a composite material less prone to failure. W–25 wt-% Re alloy, commonly used for FSW tools, experiences significant wear compared to PcBN[124]. The addition of rhenium reduces the ductile-to-brittle transition temperature, affecting tool performance. While W-Re or W-La alloys are more cost-effective than PcBN, they suffer from increased wear due to lower high-temperature strength and hardness.

High temperatures during FSW result in tool wear, impacting weld penetration depth and microstructure, thus influencing weld strength. This wear and consumption of superalloy tools like WC-Co, PcBN, Si_3N_4, and ceramics also escalate manufacturing costs[125]. Table 1-4 below outlines the key properties of various tool materials utilized in FSW. Understanding these characteristics is crucial as both the base material and the tool interact during the process, aiding in making informed choices.

Property	Unit	polycrystalline cubic boron nitride (PcBN)[126, 127]	WC[126]	W-25 wt-% Re	WC–Co
Coefficient of friction	–	0.10–0.15	0.20	-	-
Coefficient of thermal expansion	10^{-6}/°C	4.6–4.9	4.9–5.1	4.48 @ 500°C[128]	4.9 – 5.1[129]
Thermal conductivity	W/m•K	100–250	95	55–65[130]	76–95[129]
Compressive strength	N/mm^2	2700–3500	6200	-	3000–5300[131]
Fracture toughness	$MPa•m^{-1/2}$	3.5–6.7	11	52.5 @ 600°C[129]	8.9–10.6[132]
Hardness	Vickers	2600–3500	1300–1600	-	1700–2200[128]

Table 1-4: FSW tool material properties

Inconel 718 alloy exhibits significant high-temperature strength, implying a robust mechanical interaction with the tool surface during FSW. This interaction can lead to wear particle introduction or diffusion of certain elements from the tool material into the weld. Several studies investigated banded structures in friction stir welded Inconel alloys 625 and 718, revealing the presence of Tungsten through EDS analysis, attributed to wear from the WC–Co tool. However, EDS did not detect Cobalt, and SEM investigations failed to find any particles[120]. A study conducted by Song and Nakata[118] with the support of the SEM and EDS analyses they managed to compare the band zone with the normal stir zone, revealing distinct differences. In the band zone, located at the center of the stir zone with a width of 5 μm, tungsten elements primarily from the tool were detected. However, in the normal stir zone, such tool elements were absent. These findings align with previous studies on materials with high melting points[119, 121, 133].

Hence, it is inferred that the band structure resulted from tool wear induced by the increased friction load during FSW. Table 1-5 summarizes the tool specifications used in FSW of Inconel 718, with WC-CO being the predominant tool material. The shoulder diameter varies between 20-25 mm, while the pin diameter ranges from 5-7 mm, set at an angle of 2-3 degrees for welding plates with thicknesses ranging from 2-4 mm.

Tool material	**Tilt angle (deg)**	**Shoulder diameter (mm)**	**Pin diameter (mm)**	**Workpiece thickness (mm)**	**Reference**
Tungsten carbide with cobalt	2	20	5	3	[105]
Tungsten carbide with cobalt	3	15	6	2	[118]
Silicon nitride (Si_3N_4)	2	20	7	4	[110]
Tungsten carbide with cobalt	2	25	5	3	[134]
Tungsten carbide with cobalt	2	25	5	3	[135]
Tungsten carbide with cobalt	2	25	5	3	[136]
Tungsten carbide with cobalt	2	25	5	3	[137]

Table 1-5: Tool specifications for FSW of Inconel 718

1.4.2. Parameters Selection

FSW of Inconel 718 alloy has been relatively underexplored in literature, with only a few authors addressing this application. Key process variables such as axial load, temperature, tool rotational speed, and welding speed are interconnected and play crucial roles. Table 1-6 below summarizes the main parameters used for successful FSW of Inconel 718 alloy, highlighting relatively low tool rotational speeds and associated welding speeds. Grain refinement, leading to enhanced mechanical properties, was consistently observed in FSW joints. While process parameters for Al alloys are well-established, those for Ni alloys vary, often involving lower tool rotational speeds. Most FSW trials on Ni alloys have been conducted at specific research institutes, yielding consistent results across the literature[88, 105, 134-136, 138]. Increasing the heat input in friction stir welding can be achieved by decreasing the tool's transverse speed and increasing its rotation speed. This leads to grain refinement in the fusion zone post-welding, resulting in enhanced impact properties. Based on the published literature, the process parameters for successful welding of Inconel 718 typically range from 200-600 RPM for rotational speed, 30-140 mm/min for welding speed, and 30-39 kN for axial force.

Rotational speed (RPM)	Welding speed (mm/min)	Axial force (kN)	Reference
300	70 -140	30	[105]
1600	-	150	[139]
200	150	39.2	[118]
400	30-80	12.6-14.5	[110]
300	90	-	[134]
300	90-140	33	[135]
300-600	40-140	33	[136]

Table 1-6: Process parameters for FSW of Inconel 718

1.4.3. Performance Parameters

FSW trials typically evaluate welding parameters to achieve optimal microstructure, defect-free welds, and prevent undesirable features. It's crucial to test friction stir welds to ensure structural integrity. Mechanical properties, often assessed through tensile testing, grain size and/or microhardness, generally retain or even improve the base material's strength, making FSW advantageous for Ni alloys. However, it's important to note that the microstructure across a friction stir weld may not be uniformly distributed[140], leading to localized variations in mechanical properties within welded joints. Asymmetric mechanical properties, for instance, can occur in Al alloy friction stir welds due to asymmetric material flow, severe plastic deformation, and thermal cycling during the process[141].

FSW has successfully produced joints in Ni alloy 718, known for its superior strength among Ni-based alloys [110, 118]. Post-weld heat treatment has proven effective in enhancing the properties of friction stir welded Ni alloys 718 by facilitating the formation of carbides and intermetallic phases (γ″)[118]. This treatment, acting akin to an aging treatment over a prolonged duration, significantly enhances the mechanical properties of FSWed Ni alloys.

The microstructural alterations observed in FSW of Ni alloys were largely influenced by the intense deformation processes and subsequent recrystallization. Tensile testing revealed fractures occurring in the base metal after plastic deformation, indicating that the ultimate tensile strength (UTS) of the welded joint surpassed that of the base metal. As depicted in Table 1-7, all friction stir welded Ni joints exhibited enhanced mechanical properties (UTS and/or microhardness), primarily due to the achieved grain refinement.

Song and Nakata[118] have reported the microhardness distribution of both the FSWed joint and the joint after post-heat treatment, compared to the as-friction-stir-welded condition. The base material exhibited a Vickers hardness (Hv) ranging from 265 to 285 Hv, averaging 273 Hv. Conversely, the stir zone displayed significantly higher microhardness, ranging from 335 to 370 Hv, averaging 352 Hv, attributable to grain refinement. Following post-heat treatment, all joint positions showed a notable increase

in microhardness, with the stir zone reaching 525 Hv (490–540 Hv), surpassing the as-friction-stir-welded condition. This enhancement is attributed to the combined effects of grain refinement and precipitate formation resulting from the post-heat treatment in the stir zone. Moreover, Song and Nakata have reported the effects as well of FSW on the UTS, where tensile-tested specimens showed distinct fracture patterns: the base material elongated across its length before fracturing at the center, while both friction-stir-welded and post-heat-treated joints showed preferential elongation before fracture. Notably, the stir zone specimen also displayed elongation and fracture. In terms of tensile properties, the base material initially exhibited an UTS of 886 MPa with 52% elongation. FSW slightly increased UTS but decreased elongation compared to the base material. The transversely welded materials showed a UTS of 961 MPa with 32% elongation, while the stir zone exhibited a significantly higher UTS of 1135 MPa with 28% elongation. Post-heat treatment notably increased strength, resulting in a UTS of 1426 MPa with 16% elongation. Moreover, the post-heat-treated stir zone specimen displayed a higher UTS of 1570 MPa with 15% elongation compared to the heat-treated FSW joint.

Raj et al.[134] has FSWed Inconel 718 and his study showed that, the tensile testing results reveal a lower UTS, higher yield strength, and lower elongation compared to the base material (BM). Moreover, a generalized fracture morphology of the welded tensile specimen was found, occurring in the middle part of the welded region due to the lower tensile strength of this region compared to the BM. The fracture morphology is characteristic of ductile fracture, with the presence of microdimples. The Vickers hardness was obtained on the cross-section at 1.5 mm, where the hardness of the stir zone reaches a peak of 256 HV, representing a 60% increase compared to the base material. During a single pass of the tool in welding Inconel alloy, a tool wear of 0.7 mm was observed. Considering these results, it is suggested to use an additional heat source, such as hybrid FSW, for joining Inconel 718 alloy plates. In general, Inconel 718 alloy possesses a low stacking fault energy characteristic of FCC metals. Compared to materials with higher stacking fault energies like Al alloys, these materials tend to readily undergo dynamic recrystallization, albeit resisting dislocation rearrangement via dynamic recovery. Consequently, materials with low stacking fault energies facilitate the

formation of recrystallization nuclei more readily. Moreover, severe deformation during FSW accompanied by higher dislocation densities significantly promotes the formation of dense recrystallization nuclei. Consequently, grain refinement through FSW occurs concurrently, with recrystallization nuclei formed at both grains and grain boundaries with elevated dislocation densities.

Sanjay and Pankaj[135] have studied the FSW and induction preheated FSW of Inconel 718. They concluded that, the hardness in the SZ was consistently higher than the BM due to fine-grained microstructures and precipitates. TMAZ exhibited lower hardness than SZ, attributed to coarser grains induced by thermal cycling during welding. The hardness in SZ increased with traverse speed, reflecting microstructure variations. Compared to conventional FSW, induction-assisted FSW showed slightly decreased hardness, likely due to microstructure changes. Microhardness decreased with higher preheating temperatures but increased with lower temperatures and higher traverse speeds. On the other hand, tensile-tested specimens showed fracture patterns related to welding parameters, with I-FSW exhibiting better elongation. Weld strength and elongation varied with welding parameters and preheating conditions, with excess heat generation adversely affecting strength. SEM analysis of fractured surfaces confirmed dominant fracture modes and ductility. Tool wear in FSW affects costs; induction preheating reduced wear by reducing axial force and improving material thermo-plasticization.

Sanjay et al.[136] have studied the FSW of Inconel 718 with a tungsten carbide tool, investigating the impact of key parameters like rotational and traverse speed on thermal history, axial force, and mechanical and microstructural properties of welded samples. Optimal parameters for a sound weld joint were identified as 300 rpm and traverse speed of 1.5 mm/sec. Sound welds exhibited a joint efficiency of 100.2% and impact toughness of 84.5% compared to the base material. Grain refinement occurred in both the SZ and TMAZ with lower rotational speed and increased traverse speed, leading to improved mechanical properties such as tensile strength, impact toughness, and Vickers hardness. XRD analysis confirmed the presence of tungsten and cobalt particles in the weld zone,

indicating tool wear during FSW. SEM and TEM investigations revealed refined grain and secondary phases in the SZ of sound weld samples, likely enhancing weld strength.

Saha and Biswas[137] have conducted a dynamic explicit nonlinear finite element (FE) simulations to analyze temperature and residual stress distribution during the FSW process of Inconel 718 alloy. Using ABAQUS explicit software, the computational modeling incorporated features like arbitrary Lagrangian-Eulerian formulation, adaptive meshing, mesh sensitivity analysis, and mass scaling to develop a reliable and computationally efficient FE model. A finite sliding property defined the interaction between the tool bottom surface and the plate upper surface, while tool-workpiece contact was established using a Coulomb friction model with a temperature-dependent friction coefficient value. Additionally, a small experimental validation was conducted to confirm the numerically obtained thermal profiles. Results revealed similar temperature profiles across the workpiece, albeit with slightly higher temperatures observed on the advancing side. The mechanical response of the Inconel plates was also analyzed.

Ultimate Tensile Strength of Base Material (MPa)	Ultimate Tensile Strength of FSWed (MPa)	Microhardness of Base material (Hv)	Microhardness of Welded joint (Hv)	Reference
886	1135	265	335	[118]
-	823	230	260	[110]
-	-	160	256	[134]
749	740	250	370	[135]
749	740	250	350	[136]

Table 1-7: Mechanical properties of FSWed Inconel 718 alloys.

1.4.4. Microstructure Evolution

The microstructure of highly alloyed Ni alloys is intricate, influenced by various constituents like γ′ and γ″ phases, carbides, borides, and topologically close-packed phases, which can form during heat treatment or service exposure[142]. FSW involves rapid thermal cycles, impacting the microstructure of welded parts. Each Ni alloy possesses a unique microstructure, largely dictated by its chemical composition. Understanding the temperature range during FSW is crucial for assessing microstructural changes and subsequent mechanical properties. Experimentally determined temperature variations primarily depend on alloy composition and welding parameters. While temperatures within the SZ[119] may locally exceed those measured on the plate's back, they remain below the alloys' melting points due to the solid-state process. The rapid heating and cooling rates in FSW may lead to non-equilibrium microstructures, not accounted for in traditional Time-Temperature-Transformation (TTT) diagrams, which do not consider the thermo-mechanical aspect of FSW.

Few studies have highlighted the significance of precipitation in enhancing mechanical properties like hardness, strength, and creep rupture life on Ni-based superalloys. They have shown the effectiveness of precipitations such as gamma double prime (γ″) in grains and $M_{23}C_6$ carbides in grain boundaries for this purpose. However, investigations into precipitations in FSWed Inconel 718 alloys have been scarce until now[118, 121].

The friction stir welded joint of Inconel 718 alloy reveals three distinct regions: the BM, the TMAZ, and the SZ [118]. The BM exhibits coarser grains and intragranular MC carbides (NbC) compared to the refined grains and carbides observed in the SZ. The TMAZ, although less defined, is characterized by deformed grains at the interface between the BM and the weld. Unlike fusion welding, where significant grain growth occurs in the HAZ[142], FSW of Ni-base alloys typically shows no distinct HAZ due to lower process temperatures and good temperature stability. Microstructural features in FSW Ni alloys primarily result from plastic deformation, grain refinement, and occasionally, secondary microstructural constituents.

Song and Nakata[118] have studied the microstructures of the FSWed Inconel 718 alloy. Initially, the base material contained grains sized 5-20 μm, along with annealing twins

and MC carbides distributed within the grains and grain boundaries, respectively. In contrast, the stir zone exhibited finer grains, ranging 1-3 μm, with similarly refined MC carbides. Deformed grains were observed in the TMAZ at the interface between the base material and stir zone, while HAZs were absent due to the absence of grain growth. Moreover, they checked the TEM image and diffraction patterns of the stir zone after post-heat treatment ,where the image reveals evenly distributed submicron-sized grains devoid of dislocations, a result of the post-heat treatment. Within the grains and grain boundaries, intermetallic phases and MC carbides, ranging from 100 to 200 nm in size, were dispersed, identified as Ni3Nb (γ″), M6C, and M23C6 based on the diffraction patterns[118].

Ahmed et al.[110] have studied the microstructure and crystallographic texture of the FSWed inconel 718 and revealed a significant reduction in grain size from the base material to the NG, with a distinct interface between the NG region and the TMAZ. The GB map showed variations in grain size and a higher concentration of low angle boundaries at the NG/TMAZ interface and within the NG. on the other hand, the NG region exhibits a weak texture, indicating a random orientation of grains, as evident from the pole figures (PFs). In contrast, the base material displays a strong deformation texture, as observed from the PFs[110]. This differs from the strong textures typically found in aluminum and steel alloys post-FSW. Moreover, High-resolution EBSD maps were used to analyze grain size variation across the NG. The grain size sharply decreased from around 5 μm near the top to about 2 μm near the base of the NG. This reduction is attributed to temperature changes during FSW caused by the shoulder and tapering of the tool. Even though the weld thickness is only 4 mm, the reduction in grain size over 1.5 mm is significant[110], exceeding typical FSW processes. Using a stationary shoulder FSW tool may result in more uniform temperature distribution and grain size.

Raj et al.[134] has FSWed Inconel 718 employing a traverse speed of 90 mm/min and a constant rotational speed of 300 rpm. Welding at this speed resulted in a smooth weld without surface defects. Partial penetration of the tool up to 2.01 mm from the top surface produced a sound weld, except for a section 0.84 mm from the bottom butt surface, where

inadequate welding occurred. The stir zone, located near the weld center, showed defect-free characteristics. On the other hand, the optical micrographs of the BM, SZ, and TMAZ showed that, the TMAZ exhibited a slightly larger grain structure than the SZ. FSW generated the SZ due to frictional heat and severe plastic deformation of the BM, resulting in a fine equiaxed grain structure with an average size of 18 μm. Conversely, the BM displayed a coarse grain structure with an average size of 48 μm. The FSW process induced recovery, recrystallization, and static grain growth, leading to a distinct flow pattern and interface structure between the TMAZ and SZ.

Sanjay and Pankaj[135] have studied the FSW and induction preheated FSW of Inconel 718. They have examined the cross-sectional macrostructure of the FSWed joints. Nugget zones in all optical macrographs exhibit basin shapes due to the tool pin's tapered form. Full-penetration welds were achieved at both traverse speeds (90 and 140 mm/min) with induction preheating, while conventional FSW showed incomplete penetration. Defects such as wormholes were observed in conventional FSW at high traverse speeds, possibly due to inadequate heat input. However, these defects were absent with induction preheating. Grain refinement and carbide distribution were analyzed in the stir zone, with induction preheating resulting in finer grains and a uniform carbide distribution compared to conventional FSW. TEM images and SAD patterns confirmed the presence of precipitates and carbide particles in both conventional and induction preheated FSW, with induction preheating resulting in smaller carbide particles and reduced dislocation densities.

1.4.5. Defects of the Friction Stir Welded Inconel 718

The superior quality of FSW joints makes it a preferred manufacturing process for various materials[143]. Notably, FSWed Al alloys exhibit fewer weld defects compared to conventional arc welding methods. However, improper thermal cycles during FSW, such as excessive or insufficient heat input, can lead to defects like lack of penetration, surface grooves, excessive flash, or surface galling[144]. Porosity may also occur in some cases. Defects often occur on the advancing side due to higher tangential velocity. Limited data is available on FSW of Ni alloys, with current research focusing on defects found in alloys

718. In fact, a common issue known as lack of penetration, or "kissing bond," often arises in FSWed of Ni alloys process, as evidenced by several studies[90]. Tool wear progression during the welding process can exacerbate this defect. Optimizing process parameters does not guarantee elimination of this weld root defect. Hence, effective control and reduction of tool wear are imperative for producing high-quality friction stir welded Ni joints.

Porosity, commonly associated with traditional fusion welding, occurs when gases like H_2, O_2, and/or N_2 are absorbed into the weld metal and become trapped upon solidification, resulting in various forms of porosity such as surface-breaking pores or wormholes[145]. N_2 is believed to be the culprit for porosity formation in Ni alloys. Surprisingly, even in FSW, which is a solid-state process, attempts to optimize welds can lead to porosity formation if welding parameters are not adequately adjusted[146]. It was found that porosity in the stir zone of Inconel alloys during FSW, attributed to excessive heat input at high tool speeds. Although rare, local melting may occur, causing porosity when temperatures exceed the alloy's melting point. Properly selected process parameters can prevent porosity formation, ensuring a homogeneous stir zone without defects[147].

Song and Nakata[118] have successfully friction-stir-welded Inconel 718 alloy and it showed a defect-free surface at a welding speed of 150 mm/min. Despite penetrating 1.7 mm from the top without weld zone defects, a band structure was observed at the stir zone's center. These results are consistent with prior studies on Inconel 600 and Inconel 625[119, 121]. The temperature hysteresis curve during FSW revealed a maximum temperature of around 740 °C in the stir zone rear side, cooling to 100 °C within 30 s.

1.4.6. Corrosion Resistance of the Friction Stir Welded Inconel 718

Alloy 718, a robust Ni-based alloy, showcases commendable mechanical strength and corrosion resistance within a wide temperature range[148]. While it typically outperforms alloy 625 in mechanical properties, the corrosion resistance comparison can vary. The pitting resistance equivalency number (PREN) serves as a useful tool for material selection, with higher PREN values suggesting better corrosion resistance[149]. However, the estimation may not fully reflect real-world conditions, especially in friction

stir welds of Nickel alloys. Determining critical pitting temperature (CPT) through standardized tests is essential for assessing corrosion resistance in specific environments[150]. For offshore applications, a minimum CPT of 40°C[150] is typically accepted. Notably, FSW alters material microstructure, potentially affecting CPT values. Preliminary studies on FSWed corrosion-resistant alloys indicate promising results, highlighting the importance of optimized properties like UTS, yield strength, corrosion resistance, PREN, and CPT values based on alloy composition. Nickel's role in pitting corrosion initiation is relatively minor, as demonstrated by examples like alloy 600, emphasizing the multifaceted considerations in alloy selection for challenging environments.

The corrosion resistance of FSW joints in Al alloys is typically assessed through various methods[151], but similar evaluations for FSW Ni joints are lacking, particularly concerning the top surface. Evaluating the top surface is crucial as it directly interacts with the environment, affecting corrosion, wear, fatigue, and residual stresses. Preliminary assessments of FSWed Inconel 625 showed no significant corrosion changes[152]. However, further studies should examine carbide and intermetallic precipitation effects on ductility and corrosion properties in FSWed Ni alloys[153]. Corrosion behavior analysis of FSWed alloy 600 revealed lower resistance in the SZ and HAZ due to chromium depletion, with intergranular corrosion predominantly observed in the BM. Understanding the impact of thermo-mechanical processing during solid-state welding on corrosion resistance is vital for applications involving Ni-base alloys.

1.5. FSW of Ti Alloys

Titanium and its alloys are widely used in various industrial sectors such as chemical, aeronautical, aerospace, and nuclear applications due to their exceptional corrosion resistance and high specific strength[154, 155]. Among these alloys, Ti-6Al-4V stands out as a commonly used two-phase titanium alloy, favored for applications in aero-engines, biomedical surgical instruments, and chemical processing plants due to its corrosion resistance and strength[156]. Advancing industrial applications of titanium alloys present significant challenges, particularly concerning mechanical and

metallurgical requirements. These alloys are prone to atmospheric contamination at elevated temperatures, leading to joint embrittlement due to oxygen, hydrogen, and nitrogen absorption. Furthermore, welding titanium alloys using fusion welding processes results in issues like residual stress formation and large deformation in joints due to high melting temperatures[157, 158]. Conventional joining processes for Ti-6Al-4V have limitations such as coarse microstructures, epitaxial growth, coarse β grains, and significant distortion with high residual stress[158]. To overcome these challenges, solid-state joining methods like diffusion bonding, friction welding, FSW, and explosive welding have been explored, as they avoid material melting. However, solid-state welding techniques face difficulties in producing quality joints for dissimilar combinations of titanium with stainless steel, aluminum[158], magnesium, etc. To address these issues, a novel approach involving the use of interlayers of aluminum, silver, copper[158], and nickel[159] has been developed to facilitate dissimilar joining and overcome associated problems. This technique offers potential solutions to the challenges encountered in traditional welding processes for titanium alloys [160].

FSW necessitates tools with exceptional strength to endure high temperatures and loads during the process, especially when working with materials like steels, titanium, Ni-based and its alloys. These tools must also exhibit excellent wear resistance to maintain their performance over time. Tool wear not only shortens the lifespan of the tool but can also impact the material flow and mechanical properties of the welds. However, manufacturing tools for FSW presents challenges due to the demanding requirements. Various materials are utilized for fabricating tools used in FSW of titanium alloys, including W-Mo, W-Re, W-1% La_2O_3, cobalt-based alloys, and molybdenum alloy tools. Each of these materials offers different properties and characteristics to meet the specific demands of the welding process[161]. Therefore, careful consideration is essential when selecting the appropriate tool material for achieving desired welding outcomes.

Several studies have investigated the use of different tools for FSW of Ti-6Al-4V alloy. Wang et al.[162] utilized tungsten-based alloy tools and observed tool wear during welding, noting degradation in the W-1.1% La_2O_3 tool due to plastic deformation, which

decreased with increasing tool pin diameter. Sivaji and Reddy[163] employed W-Mo alloy tools and found tungsten inclusions in the stir zone due to tool wear. Polycrystalline cubic boron nitride (PCBN) tools, commonly used for cutting steels and titanium alloys, have shown promise as FSW tools, as demonstrated by Zhang et al.[164] in their study on FSW of pure titanium. Despite observed tool wear, PCBN exhibited potential for FSW of pure titanium, with evidence suggesting a reaction between boron nitride (BN) and titanium. Additionally, Wu et al.[165] explored the influence of tool wear on joint properties of Ti-6Al-4V alloy, finding that higher rotation speeds led to increased tool wear, particularly at the tool plunge point. Sivaji and Reddy[163] also investigated FSW of Ti-6Al-4V alloy using PCBN tools. Edwards and Ramulu[166] reported on the shape of the tool pin and its impact on heat generation during FSW. Overall, these studies highlight the importance of tool selection and its effects on FSW processes and joint properties.

Various studies have examined the microstructural analysis of Ti-6Al-4V sheets joined using FSW with different welding parameters. FSW offers precise control w.r.t heat input by optimizing process parameters. Researchers have conducted FSW both above and below the β-transus temperature. Liu et al.[167] investigated FSW of Ti-6Al-4V sheets at a tool rotation speed of 400 rpm and welding speeds ranging from 25 to 100 mm/min, resulting in a stir zone with a bimodal microstructure. Zou et al.[168] explored the effect of FSW tool rotational speed on the mechanical and microstructural properties of Ti-6Al-4V weldments. They found that a rotational speed of 400 rpm produced a bimodal microstructure in the weld zone, while speeds of 500 or 600 rpm resulted in a lamellar microstructure. Increasing rotational speed led to larger α colony and prior β grain sizes in the weld zone. Kitamura et al.[169] studied the influence of welding temperature on the mechanical properties and microstructural characteristics of Ti-6Al-4V joints. They measured temperatures at different zones during welding and observed that the cooling rate varied with welding speed. As the cooling rate increased, the size of lamellar α β decreased when the welding temperature surpassed the β-transus temperature. Stir zone microstructure consisted of equiaxed α grains when welding temperature remained within

the β-transus temperature range. These findings underscore the importance of controlling welding parameters to achieve desired microstructural characteristics in Ti-6Al-4V joints.

The microstructural effects of FSW on alloy Ti-6Al-4V have been reported by researchers. Buffa et al.[169] and Esmaily et al.[170] observed tunnel defects and inclusions in the stir zone due to inadequate heat input. Jianqing et al.[171] investigated the impact of welding parameters on peak temperature, finding that higher rotational speed and lower traverse speed resulted in higher peak temperatures. Conversely, lower rotation rates and/or higher welding speeds led to finer prior β grains and smaller α colonies. Buffa et al.[162] developed a finite element model and simulation for FSW, validating their results with experimental findings. Edwards and Ramulu[172] introduced a novel technique for observing material flow patterns during FSW of Ti-6Al-4V by inserting refractory powder into the joint. This technique allowed for the experimental observation of material flow patterns, which were then traced using radiography or metallography techniques. These studies collectively highlight the importance of process parameters in influencing the microstructure of Ti-6Al-4V alloy during FSW.

Zhang et al.[173] conducted an evaluation of the mechanical properties of weld joints, revealing a decrease in the average hardness distribution value of the SZ with increasing tool rotational speed. Tensile tests indicated significantly lower strength and ductility in welded specimens compared to the base metal, with mechanical properties diminishing as the FSW tool rotation speed increased. Ramulu et al.[174] investigated tensile properties in various conditions, including as-welded, stress-relieved, and superplastic-formed, noting that while welded samples exhibited higher yield and tensile strength than the base metal, they displayed less elongation. Liu et al.[167] evaluated welds prepared with constant rotation speed and varying traverse speeds, observing lower hardness in the weld compared to the substrate in all conditions, with hardness lowest in the stir zone. They found that increasing welding speed led to higher stir zone hardness, attributed to dynamic recrystallization induced by frictional heat and plastic deformation. Furthermore, they reported that welding joints exhibited lower tensile strength and ductility compared to the base metal, with mechanical properties improving as welding

speed increased. Zhou et al.[168] noted a decrease in weld zone hardness with increasing tool rotation speed, attributed to microstructure coarsening due to higher heat input. Transverse tensile property results revealed less elongation and strength in the welds compared to the base metal, with weld tensile stresses decreasing as tool rotation speed increased. These findings underscore the complex interplay between welding parameters and mechanical properties in FSW processes.

The utilization of numerical modeling holds significant promise across various industrial applications, offering cost reduction benefits, aiding in tool material selection, and facilitating property evaluation under different process parameters. Schmidt et al.[175] and Chao et al.[176] explored two approaches: one based on thermal profiles and the other on finite element thermomechanical modeling, to predict welding thermal profiles. Heat generation in the thermal model arises from friction between the tool shoulder and specimens, as well as plastic deformation of the workpieces. Kamp et al.[177] and Chen C M & Kovacevic et al.[178] utilized finite element thermomechanical models to assess strain and stress distribution during FSW. Chiumenti et al.[179] adopted an ALE approach for modeling the area surrounding the pin and an Eulerian approach for the rest of the sheet material. Buffa et al.[180, 181] developed customized numerical models for FSW of aluminum and titanium alloys, providing insights into phase distribution within the weld zone. Pasta and Reynolds et al.[182] utilized numerical simulation to investigate the impact of residual stress on fatigue crack propagation in weld joints. Buffa et al.[181] further characterized weld joints using a combination of experimental data and numerical simulation, highlighting the importance of numerical modeling in understanding and optimizing FSW processes.

The literature review highlights the necessity for the development of tool materials with superior strength, wear resistance, and cost-effectiveness for FSW of titanium alloys. While existing research predominantly focuses on enhancing tool materials, there is a notable dearth of studies investigating weldment characterization, essential for comprehending titanium alloy weldability. Key insights reveal FSW conducted using diverse tool materials such as tungsten-based alloy, cobalt-based alloy, molybdenum-

based alloy, and polycrystalline cubic boron nitride tools. Additionally, titanium alloy Ti-6Al-4V, characterized as a two-phase (α+β) alloy, exhibits microstructure control potential through heat input management during welding. Notably, the microstructure of the stir zone varies depending on whether welding occurs below or above the β-transus temperature, with better mechanical properties observed in welds conducted below the β-transus temperature.

1.6. FSW of Dissimilar Materials

The use of different materials with diverse characteristics in various areas of a single manufactured component not only saves money but also enhances product quality. Several studies proposed welding technologies for dissimilar metals and alloys. While some studies have been done on FSW, most of these have only focused on material flow visualization and did not identify the optimal FSW parameters and tool geometry. The resulting welds were often unwelded, with open (void) zones and oxide inclusions at the root of plates. Weld efficiency was also observed to be reduced when hard aluminum alloys were stirred with soft aluminum alloys, and the locations of two dissimilar alloys exerted a significant effect on the material flow pattern and the resultant weld quality. However, some studies have shown promise in FSW for dissimilar aluminum alloys, with defect-free welds achieved for A356/6061Al and 2024Al/7075Al such as Lee et al.[183, 184] showed defect-free friction stir welds of A356/6061Al at a tool rotation rate of 1600 rpm, traverse speeds of 87-267 mm/min, and a tilted tool angle. Baumann et al.[185] evaluated properties of 2024Al/7075Al bi-alloy friction stir weld and successfully achieved defect-free joints with tensile strengths at 76-82% of Al base. Both studies showed that the strength of the weld zone of dissimilar alloys was consistently higher than that of the FSW base material, and hardness of the nugget zone was lower than that of the aluminum base metal due to the dissolution or coarsening of precipitates. While localized or incipient melting during FSW of aluminum alloys is possible, significant melting cannot be sustained as the liquid surface cannot support shear forces, making the FSW process self-regulating. Nevertheless, partial melting can occur and set the upper limit for the tool rotation rate.

Prakash et al.,[139] investigated the FSW of Inconel 718 with Inconel 600, focusing on the microstructural and mechanical properties of the resulting welds at room temperature. The researchers found that the processing setup was efficient and effective for creating these welds. The study's findings showed that FSW can be used to connect Inconel 718 with Inconel 600 without any significant negative consequences or adverse effects. The welds produced were free of undesired microstructural changes, and there was no evidence of significant plastic deformation or recrystallization at the interface. The welds did, however, exhibit some coarsening of grain at the sold contact. The divergent weld was characterized by a limited mechanical intermixing zone, where plastic deformation at high temperatures resulted in unique recrystallization, leading to fine equiaxed grains. This zone also showed significantly higher hardness than the surrounding areas. Overall, the Inconel 718/Inconel 600 divergent erosion welds showed significant room temperature malleable properties in an as-welded condition. However, the welds failed in the heat-affected zone of Inconel 718 due to significant grain coarsening. These findings suggest that FSW can be a useful technique for connecting Inconel 718 with Inconel 600, and that the resulting welds can exhibit desirable mechanical properties, particularly in the mechanical intermixing zone. However, careful attention must be paid to the potential for grain coarsening in the HAZ of the Inconel 718 during the welding process.

1.7. Energy Assisted-FSW

FSW has become a popular method of joining low melting point temperature materials like aluminium and its alloys. However, joining high melting point materials using conventional FSW presents various challenges, including tool wear, reduced weld efficiency, and limited welding speeds. These problems are caused by insufficient plasticization around the rotating tool pin due to low heat input[186].

In recent years, various methods have been explored to mitigate tool wear, extend tool life, and enhance weld quality for high-strength materials. Researchers primarily focus on modifying tool geometry and employing material preheating techniques. Hybrid or assisted FSW techniques have been developed to preheat materials, softening them, and reducing the downward load. Moreover, different types of auxiliary energy assistance

have been proposed, such as laser heating, induction heating, electrical arc heating, resistance heating, and heating from ultrasonic vibration mechanism[187].

Preheating before the FSW process has been found to be advantageous in several ways. Studies have shown that preheating AA 6061 aluminium alloy plates to 300 ◦C before FSW can reduce the axial load requirement by 43%[188], allowing for an increase in welding speeds. Laser preheating has also been found to improve material flow, reduce defect formation, and increase joint strength[189, 190]. The introduction of double laser source further enhances material flow, leading to a significant increase in tool service life and welding efficiency[191]. Electrical energy can also be used to assist FSW, with electrically assisted FSW joints exhibiting higher hardness and improved tensile strength. In GTAW assisted hybrid FSW of Al6061-T6 aluminium alloy and Ti–6%Al–4%V alloy plates, a strength improvement of 24% was observed, attributed to an improvement in ductility in hybrid FSW joints[192].

On the other hand, Ultrasonic vibration energy is a common form of external energy used to increase temperature during the FSW process. Researchers have investigated the use of a 20 kHz vibrational tool to reduce axial forces on the tool during ultrasonic-assisted FSW of AA6061-T6 plates[193]. Ultrasonic energy has also been proposed as a tool to enhance the capabilities of FSW, resulting in a 30% increase in strength in the case of hybrid FSW compared to conventional FSW of dissimilar Al/Mg joints[194]. Various types of auxiliary energy-assisted FSW processes have been reviewed, including induction-assisted FSW (IAFSW) processes used to join similar and dissimilar materials. In previous works, IAFSW processes have been patented and found to reduce the applied axial force by almost 50% when joining medium-strength AA 6082 T5 Al-alloy, while also increasing the welding speed[195]. Another study found that induction preheating led to sound welds at double the welding speed [135].

Applying a preheat temperature of 310 ◦C to the FSW process resulted in an increase in the strength of the Inconel 718 alloy. This increase in temperature allowed for proper intermixing of materials, yielding high-strength, defect-free joints. Additionally, IAFSW reduced the axial load on the tool by 26%[196]. A similar study conducted on carbon

steels showed a 40% increase in welding speed and a 26% decrease in maximum vertical load.

Alvarez et al.[197] produced IAFSW welds on marine steel grade A plates, where they observed a 30% reduction in plunge force at a tool rotation speed of 500 rpm and traverse speed of 50 mm/min. In another study, an improvement in tensile strength was observed while realizing IAFSW joints of difficult-to-weld AISI 410 Stainless steels[198]. They obtained a significantly higher tensile strength of 456.43 MPa at a tool rotation speed of 1200 rpm and 45 mm/min of welding speed. Finally, Mohan et al.[198] observed a high tensile strength, which was 94% of that of the base material, along with high grain refinement and reduced dislocation density on in-situ induction of dissimilar AA5052 and X12Cr13 SS joints.

Kaushik and Kumar Dwivedi [199] recently conducted a study on dissimilar aluminium-steel joints using induction heating to preheat the steel plate selectively. The improved material flow resulting from the lower flow stress level of the steel led to a strong bond and a 34% increase in ductility in the induction assisted FSW joint. However, the complex mechanisms involved in FSW and preheated FSW are difficult to study experimentally, making numerical modelling essential for gaining a deeper understanding of these processes and their impact on mechanical properties. Numerical modelling offers a cost and time-effective approach for conducting a detailed study of these constituent mechanisms.

Daftardar[200] conducted numerical simulations of laser-assisted friction stir welding and found that the necessary work to generate the same temperature as in conventional FSW was reduced, resulting in lower tool wear. The temperature in the workpiece had an inverse relationship with the distance between the tool pin center and the laser spot. In a study by Fei & Wu[201], a three-dimensional heat source model was used to investigate temperature distribution and material flow in laser-assisted FSW of Q235 steel, which showed improved fluidity and increased temperature in and around the shoulder with preheated stirring. Ahmad et al.[202] also found that tool reaction forces decreased by 55% with laser-assisted FSW of DH36 steel in their numerical analysis. These findings

suggest that the use of laser assistance in FSW can increase tool life and improve material flow.

Long & Khanna [203] demonstrated that electrically assisted FSW could reduce tool wear by generating higher temperature in both upper and lower parts of the workpiece during the plunge stage. Tiwari et al.[204] found that higher heat input led to a uniform temperature gradient along the weld thickness direction, while Pankaj et al.[205] observed that plasma-assisted FSW improved the process window and reduced the mean vertical force. Shi et al.[206] found that ultrasonic vibrations assisted FSW yielded more uniform temperature gradient and enhanced material flow, while Sabry et al.[207] observed improved strength and hardness with vibration assistance. Although ALE formulation has been used to predict thermal history and residual stress during FSW processes[208], the application of this approach to understand the thermal and mechanical behavior of preheated FSW is limited, and there is limited numerical work on induction preheated FSW of hard alloys such as Inconel 718.

Sanjay and Pankaj[105] have studied the effects of conventional and induction heating-assisted friction stir welding on dissimilar Inconel 718 and stainless steel (SS316L) alloy joints using a WC-10%Co tool. The experiment was conducted at a constant rotational speed of 300 rpm, with varying welding speeds and a preheating temperature of 300 °C in the I-FSW process, the research reveals that both FSW methods result in refined grains and improved mechanical properties. Induction heating increases particle size and enhances atomic diffusion at the interface, contributing to weld strength. Additionally, preheating and high welding speeds significantly improve joint mechanical properties, while reducing axial force and enhancing tool life.

Sanjay and Pankaj[135] have utilized a preheating system which showed promise in reducing axial load, enhancing weld quality, and prolonging tool life during FSW of high-strength materials. This study compared conventional FSW with high-frequency induction heating-assisted FSW for joining 3 mm thick Inconel 718 plates using a WC-10%Co tool. Welding parameters included a constant rotational speed of 300 rpm, traverse speeds of 90 mm/min and 140 mm/min, and preheating temperatures of 310 °C,

410 °C, and 700 °C. Results indicate that I-FSW at a low preheating temperature (310 °C) and high traverse speed (140 mm/min) produced good weld joints. Grain refinement in the weld zone, observed with and without preheating, contributed to improved mechanical properties. Induction preheating in I-FSW resulted in larger intermetallic phases and carbide particles, enhancing weld strength. The stir zone hardness increased from 250 HV to 370 HV, and the ultimate tensile strength of the I-FSW joint reached 740 MPa, representing 98.8% of the base material's strength. Additionally, preheating reduced axial force and frictional heat, improving tool life.

On the other hand, Palm et al.[209] patented laser assisted FSW and investigated its efficacy in improving tool life through workpiece softening. Sun et al.[210] successfully welded S45C steel plates using laser assisted FSW, demonstrating that laser preheating doubled welding speed compared to conventional FSW, with optimal laser positioning maximizing heat input. Similarly, Song et al.[122] found that laser-assisted FSW increased welding speed by 1.5 times for joining Inconel 600 plates, leading to improved mechanical strength due to grain refinement in the SZ.

Other preheating methods such as plasma[211], TIG[212], electrical[213], back heating[214], and heated FSW[188] have also been developed to enhance tool life and weld quality by facilitating material softening and flow, consequently reducing axial welding force and increasing welding speed. Cheon et al.[196] achieved a 26% load reduction and a 40% speed increase in carbon steel FSW using a 4 kW induction preheating source. Vijendra and Sharma[215] found that induction-assisted heating softened the base material, aiding in easier stirring during welding, with optimal parameters identified for maximum thermoplastic joining strength.

1.8. Coolant Assisted-FSW

The use of coolants in FSW has been extensively employed to achieve high-quality welded joints with fine and ultra-fine grains. This technique holds significant promise for welding various aluminum and copper alloys, which are critical in the aerospace, automotive, and electric power industries[216-224]. In coolant assisted FSW, cooling mediums are applied either by spraying them onto the weld bead and tool[216-218], or

by immersing the entire welding process into the cooling mediums[219-224]. These practices help to reduce or even eliminate the heat effects in FSW, altering the deformation temperature and cooling rate. This method has been used to weld aluminum, magnesium, copper, titanium alloys, and steels, resulting in high-strength joints with fine and ultra-fine grains [216-224]. However, the impact of forced cooling on the welded joints is multifaceted. While researchers have often highlighted the enhanced mechanical properties achieved through coolant assisted FSW, the adverse effects of forced cooling on the welding process are frequently overlooked.

1.9. Statistical Analysis in FSW

Several researchers have utilized numerical analysis techniques to optimize the FSW parameters to achieve certain mechanical properties and improve the welding quality. Elathasaran et al.[225] investigated the impact of three parameters - rotational speed, traverse speed, and axial force - on ultimate tensile strength, yield strength, and elongation. Their study utilized ANOVA analysis to demonstrate the effectiveness of the model at a 95% confidence level. Meanwhile, Zhang and Liu[226] proposed examining the welding of aluminum to high-strength steel by considering three parameters: rotational speed, tool offset, and traverse speed. Venkateshkannam et al.[227] explored the characterization of FSW welds, determining that defect-free joints were achievable using a stepped pin profile tool at 1000 rpm and 40 mm/min. Although a cylindrical threaded pin yielded smooth welds without defects, the resulting tensile strength and microhardness were inferior to those achieved with the stepped pin tool. Hasan et al.[228] optimized tool rotational speed, traverse speed, and shoulder diameter for grain size, ultimate tensile strength, and hardness using Taguchi L9 orthogonal Design of Experiment (DoE). Silva et al.[229] focused on optimizing Friction Stir Welding AA6063-T6 T-joints using Taguchi L27 orthogonal Array, with tool rotation speed, welding speed, and tool geometry as the selected parameters. They reported a joint efficiency of 56% for the tensile test, highlighting the significant role of tool rotational speed in joint mechanical properties. Sadeesh et al.[230] analyzed the FSW process concerning microstructure and tensile properties, utilizing five different tools to assess

the influence of welding and traverse speed on microstructure. They found that the shoulder-to-pin diameter ratio played a significant role in determining better mechanical properties and microstructure. Lastly, Shojaeefard et al.[231] employed an Artificial Neural Network model to establish the relationship between process parameters and mechanical properties, predicting the ultimate tensile strength and hardness of butt joints based on the ANN model.

1.10. Workpiece Temperature Control during FSW Process

FSW relies on temperature control to ensure optimal weld properties within a specific thermal process range. Initially, FSW was conducted on adapted milling machines where temperature monitoring was sporadic, leading to temperature fluctuations during welding[232]. Early attempts at temperature regulation often involved adjusting spindle speed[233]. Various techniques have been employed to measure stir zone temperature. Placing a thermocouple closer to the tool-plate interface significantly reduces system response time, enhancing control effectiveness. By regulating temperature and other welding parameters, weld quality can be preserved even in the face of external disruptions to the system[234, 235].

FSW was initially performed by setting specific parameters for depth, travel speed, and spindle rotation speed, techniques that have proven effective over time[236, 237]. However, maintaining constant input parameters during welding may result in temperature fluctuations within the weld due to transients and external disturbances. Given that FSW heavily relies on temperature control, deviations in weld temperature can adversely impact the strength and integrity of the weld. Poor temperature regulation can even render the welded piece unusable in certain instances[238].

An advancement in temperature regulation was achieved through the implementation of power control systems and enhanced system identification and tuning for controllers. Temperature regulation adopted a "cascade" method[239] power was utilized to regulate temperature within a slower outer loop, while a faster inner loop was employed to regulate power itself. Ross[240] employed spindle power and a PID controller to maintain weld temperature within a 2°C range. Both Ross and Marshall recognized FSW as primarily a

first order plus dead-time (FOPDT) system. Marshall utilized a relay feedback test to ascertain FOPDT system parameters and determined PID gains using tuning rules[241]. This approach shown to be able to uphold temperature stability within a 2°C range, achieving superior settling characteristics compared to Ross's initial efforts and demonstrating commendable disturbance rejection capabilities[236, 240]. On the other hand, Model Predictive Control (MPC) is an effective technique for multivariate control of intricate and extensive systems[242]. It relies on a system model to forecast how alterations in inputs affect output parameters and utilizes an optimizer to adjust input parameters accordingly for optimal control of outputs. MPC has a long history of successful application across various industries[243-245]. Furthermore, Cederqvist and Nielsen[246, 247] created nonlinear models to address welding issues with non-circular copper canisters, emphasizing depth and force regulation. Employing these models, they conducted simulations to explore nonlinear multiple-input multiple-output (MIMO) MPC control of depth and temperature. While their research holds substantial theoretical potential, it has mainly concentrated on process simulation to assess controllers. Other FSW models have emerged: a FOPDT model and a more intricate Hybrid Heat Source model[248, 249]. These models demonstrate satisfactory temperature forecasts, relying on spindle power and traverse speed post the initial transient phase of a weld. Given the accuracy of these temperature predictions, an MPC controller utilizing these models is anticipated to deliver effective performance, provided the gains and time constants align closely with those of the actual process[250].

1.11. Conclusion

Chapter 1 provides a comprehensive introduction to the significance of friction stir welding in the context of high-performance materials, specifically Inconel 718. The chapter outlines the research objectives, highlighting the need to optimize FSW parameters to achieve superior mechanical properties and structural integrity in welded joints. A detailed literature review reveals the current state of FSW research, identifying gaps and opportunities for further investigation. The chapter concludes by establishing the research hypothesis and objectives, setting the stage for a methodical exploration of

the effects of rotational speed, welding speed, axial force, shoulder diameter, pin diameter, coolant and energy assisted FSW on the welding performance of Inconel 718. This foundational chapter underscores the critical importance of parameter optimization in advancing the application of FSW for high-performance materials.

Chapter 1 provides a thorough literature review of FSW technology, emphasizing its significance in modern manufacturing processes. The review highlights the process's advantages, such as reduced distortion and improved mechanical properties, which make it suitable for critical applications in industries like aerospace. The chapter also outlines the various stages of the FSW process, and the types of tools used, showcasing the technique's versatility in welding different materials.

Despite the extensive research conducted, several gaps in the literature remain. One significant area that requires further investigation is the comprehensive understanding of the interactions between different FSW parameters and their collective impact on the weld's microstructure and mechanical properties. While numerous studies have explored individual parameters, the complex interplay between these variables is not yet fully understood.

Future research should focus on developing more sophisticated models that can accurately simulate these interactions. Additionally, experimental studies should aim to validate these models and provide deeper insights into optimizing FSW process parameters for different materials. Another promising area for future research is the exploration of FSW's potential in welding advanced and emerging materials, as well as its application in new industrial sectors. By addressing these research gaps, the scientific community can further enhance the efficiency and applicability of FSW technology, ensuring its continued contribution to advanced manufacturing processes.

CHAPTER 2: Methodology

2.1. Introduction

Chapter 2 delves into the methodology employed in this research, specifically the model definition and assumptions, material properties, governing equations, meshing system, and the validation of the model against published experimental data. It also provides detailed information of the materials and equations used, detailing the selection criteria for 6061-T6 Aluminum, Inconel 718, and Ti-6Al-4V as the workpiece materials. The methodology section describes the process parameters under investigation: rotational speed, welding speed, axial force, shoulder diameter, and pin diameter. Each parameter's range and levels are specified, along with the measurement techniques for the performance parameters: workpiece temperature, microhardness, stress evolution, and grain size. The chapter concludes with a discussion of the statistical analyses employed, including Taguchi analysis, ANOVA, and non-linear regression, setting the stage for a detailed analysis of the simulation data.

2.2. Finite Element Modelling

Finite element modeling plays a pivotal role in advancing manufacturing technologies by offering a robust framework to simulate and optimize complex processes with precision. In this study, COMSOL Multiphysics software serves as the cornerstone for constructing detailed finite element models and conducting simulations. By leveraging this tool, significant time and effort savings are realized, as it allows for thorough exploration of design parameters and material behaviors in a virtual environment. This capability not only enhances efficiency but also ensures the high quality of manufactured components by predicting performance metrics such as temperature distribution, stress evolution, and microstructural changes. Through meticulous modeling and simulation, insights gained pave the way for informed decision-making, optimization of process parameters, and validation against experimental data, thereby driving innovation and reliability in advanced manufacturing practices.

2.2.1. Model Definition

The impact of operational variables on temperature, material flow, and strain rate during the FSW of Aluminum alloys, Inconel 718, and the dissimilar welding of Inconel 718 and Ti-6Al-4V was explored via numerical simulation employing a 3D thermo-mechanical model crafted in COMSOL Multiphysics version 5.3. Initial validation of the model was conducted against documented experimental findings pertaining to Aluminum alloys, following which its application was extended to encompass Inconel 718. A parametric study was then conducted to optimize the process parameters and achieve high-quality friction stir welds in Inconel 718, specifically at high tool rotations, fast welding speeds, and low axial loads. After validating the Inconel 718 friction stir welds, the model was extended to the dissimilar welding of Inconel 718 and Ti-6Al-4V.

Figure 2-1 and Figure 2-2 reflect the model domain and system geometry, where the model was configured with a geometry consisting of two plates to facilitate potential investigations into dissimilar materials welding. The dimensions of the Aluminum plates are 400 by 102 by 12.7 millimeters, bordered an infinite domain in the x-direction. The tool, constructed from tungsten carbide with 10% cobalt, is rigid, with a 50-millimeter diameter flat circular bottom for the shoulder and a cylindrical pin of 6 millimeters radius, while Figure 2-2 showcasing a setup comprising two plates of Inconel 718. Each plate measures 250 by 75 by 3 millimeters and is flanked by an infinite domain in the x-direction. The tool, made of tungsten carbide with 10% cobalt, is sturdy, featuring a flat circular bottom with a 25-millimeter diameter for the shoulder and a cylindrical pin with a diameter of 5 millimeters and a depth of 2.7 millimeters.

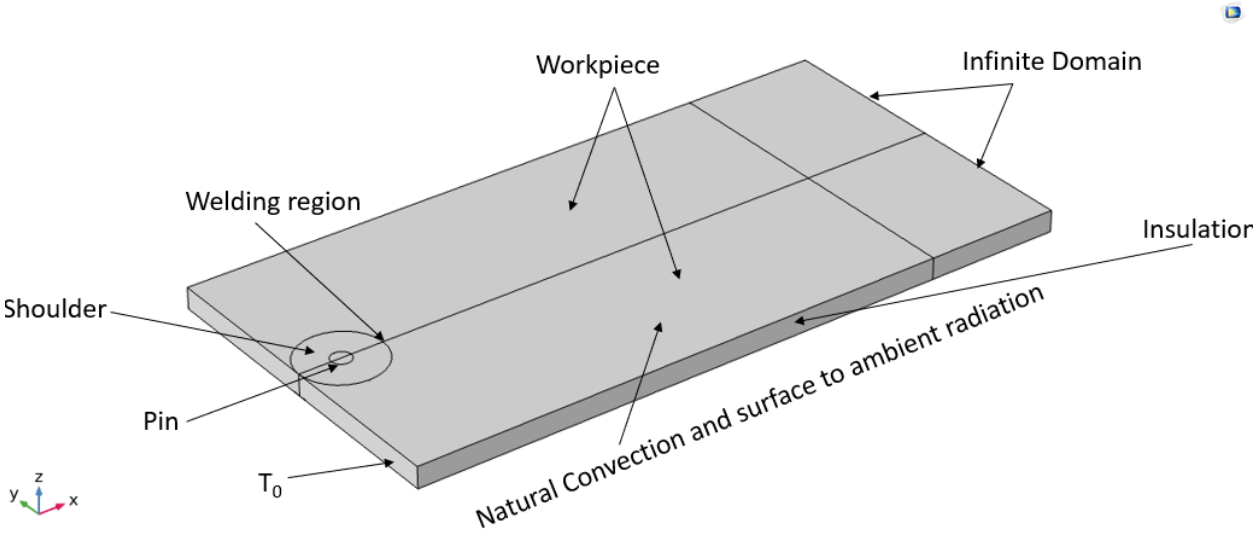

Figure 2-1:System geometry and model domain for Aluminum Alloy

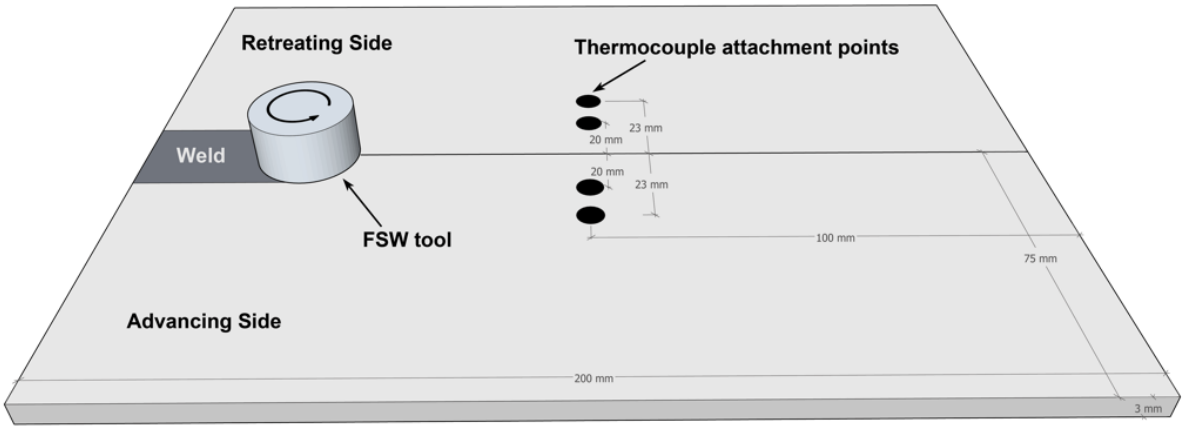

Figure 2-2:System geometry and model domain for Inconel 718 Alloy

This study presents a novel approach for simulating the tool in FSW. Rather than treating the tool as a source of heat in motion, a dynamic coordinate system fixed to the tool axis was utilized. This method employed two infinite element domains situated before and after the welding zone to simulate an infinitely long plate. The rotating tool was segmented into a pin and a shoulder, each interacting with the plate's surface.

Additionally, the model incorporates heat fluxes resulting from friction between the rotating tool and the contact surfaces, which vary based on the normal force and rotational speed. Heat fluxes from friction are disregarded if the temperature exceeds the melting point. Heat transfer within the plate occurs through surface-to-ambient radiation and convection, with the supply side assumed to maintain an ambient temperature.

The precision of simulations in FSW hinges greatly on accurately defining the workpiece properties. Throughout FSW operations, temperatures fluctuate from 25°C to slightly below the melting temperature, leading to alterations in workpiece properties with temperature variations. To ensure accuracy, pertinent thermophysical and mechanical properties of the workpiece materials (Al-T6, Inconel 718 and Ti-6Al-4V) were specified as temperature-dependent, drawing from various sources for comprehensive data[65, 139, 187, 251-255]. Moreover, apart from temperature fluctuations, the base metal undergoes intricate strains and strain rates during the welding process. To replicate the plasticity behavior of the workpiece, the Johnson-Cook constitutive model was employed. This model, an empirical viscoplastic representation, characterizes the work hardening, thermal softening, and strain rate hardening of the metal, rendering it suitable for scenarios involving high strain-rate deformations and varying temperatures. The von Mises flow stress was calculated utilizing this model.

The 3D finite element thermo-mechanical model was created using COMSOL Multiphysics software, incorporating mechanical loading from the tool. Friction stir welding is an intricate and highly dynamic process, involving coupled non-linear multiphysics challenges[187]. It encompasses intricate frictional variations, substantial plastic deformation, heat generation, tool stirring action, material flow, tool-workpiece interaction, and evolving structural dynamics. Handling the analysis in mathematical terms becomes intricate due to material non-linearity arising from plastic behavior, making it challenging to integrate[44]. Explicit models offer a way to simulate such highly non-linear and dynamic processes within short time scales more efficiently.

Employing temperature-dependent material properties for both the tool and workpiece plates allowed simultaneous calculation of thermal and mechanical results. To replicate

the process accurately, the ALE technique was utilized to prevent excessive mesh distortion during substantial material deformations occurring throughout the welding process. The ALE technique, along with adaptive meshing, maintains mesh quality by continuously regenerating the mesh, enabling it to move independently of the underlying material motion. However, this approach can compromise computation time. The cumulative heat generation during the FSW process is described by Equation (1)[187]: -

$$Q_{FSW} = Q_{friction\ between\ tool-workpiece\ interface} + Q_{plastic\ deformation} \quad (1)$$

The simulation was conducted in a system with 16 GB Intel(R) Core (TM) i7-8565U CPU @ 1.80GHz 1.99 GHz. Total time to completion was around 6.5 hrs.

2.2.2. Material Properties

The workpiece comprised Al alloy, Inconel 718, Ti-6Al-4V, with material properties falling into two main categories: thermomechanical and thermophysical properties[256]. For the temperature-dependent thermal properties like sensible heat, density, and thermal conductivity, data were sourced from previous literature[257]. Additionally, thermomechanical attributes such as expansion coefficient, Young's modulus, and Poisson's ratio were defined as temperature-dependent properties to ensure precise simulation outcomes. Capturing the material's plastic behavior during the FSW process was achieved using the Johnson-Cook plasticity model Equation (2). This model accounts for material strain hardening, strain rate, and thermal softening quotient. The Johnson-Cook model serves as one of the constitutive material models capable of delineating elastic-plastic mesh distortion under high-temperature, stress, and strain rate conditions. The flow stress σ in this model is expressed as[137]:

$$\sigma = (\mathrm{A}+\mathrm{B}\varepsilon^{n})\left[1 + C ln\left(\frac{\dot{\varepsilon}}{\dot{\varepsilon_o}}\right)\right]\left[1 - \left(\frac{T-T_o}{T_m-T_o}\right)^{m}\right] \quad (2)$$

where A, B, n, m, C, $\dot{\varepsilon_o}$ are the material constants. A is initial yield strength, B and n are stress and power coefficient of strain hardening, C is the strain rate sensitivity factor, m

is thermal softening factor. ε denotes plastic strain, $\dot{\varepsilon}$ and $\dot{\varepsilon_o}$ are strain rate and reference strain rate, respectively. T_m is the melting point temperature, T_o is the temperature around which yield stress becomes independent of temperature (See Table 2-1).

Thermal Softening for modified JC model[104]: -

- if T < 700 °C, T_o = 21 and m=2 (3)
- if T ≥ 700°C, T_o=700 and m=0.0016T+2.0031

Moreover, the Johnson-Cook dynamic failure model Equations (4) and (5),was employed to characterize the progression of damage through the material deformation stages[258]. The damage evolution, denoted by D, is contingent upon material constants d_1 - d_5, where ε_f represents the plastic strain at failure and $\Delta\varepsilon$ stands for the strain increment. These constants, d_1 - d_5, embody the failure parameters, which are established through experimental determination. The mean stress, σ^-, and equivalent stress, σ_{eq}, play roles in this model. Table 2-1, Table 2-2, Table 2-3, Table 2-4, and Table 2-5 provide an overview of the Johnson cook plasticity, damage parameters, and friction coefficient utilized in the current simulation study.

$$\varepsilon_f = \left[d_1 + d_2\, exp\left(d_3 \frac{\sigma^-}{\sigma_{eq}}\right)\right]\left[1 + d_4 ln\left(\frac{\dot{\varepsilon}}{\dot{\varepsilon_o}}\right)\right]\left[1 + d_5\left(\frac{T-T_0}{T_m-T_0}\right)\right] \quad (4)$$

$$D = \sum\left(\frac{\Delta\varepsilon}{\varepsilon_f}\right) \quad (5)$$

Material	Strain hardening			Thermal softening	Strain rate hardening		Reference
	A (MPa)	B (MPa)	n	m	C	ε^J	
Al Alloy	293.85	299.207	0.607	1.34	0.00711	1	[259]
Inconel 718	450	1700	0.65	Eq (3) [104]	0.017	1.001	[260]

Ti-6Al-4V	460	1450	1.31	0.85	0.08	1	[255]

Table 2-1: Johnson-cook model parameters

Material	d_1	d_2	d_3	d_4	d_5	T_m	T_0	Reference strain rate	Reference
Al Alloy	0.096	0.049	-3.465	0.016	1.099	660	20	0.0009	[261]
Inconel 718	0.11	0.75	-1.45	0.04	0.89	1320	20	0.001	[187, 262]
Ti-6Al-4V	-0.09	0.25	-0.5	0.014	3.87	1607	20	0.0015	[255, 263]

Table 2-2: Johnson-Cook model, Damage parameters

Temperature (°C)	Friction coefficient
25	0.6
100	0.6
200	0.6
300	0.5
400	0.4
500	0.3
600	0.2
700	0.2
800	0.2

Table 2-3: Friction coefficient as a function of temperature for Al Alloy [264]

Temperature (°C)	Friction coefficient

25	0.3
300	0.25
420	0.2
543	0.01

Table 2-4: Friction coefficient as a function of temperature for Inconel 718[137]

Temperature (°C)	Friction coefficient
25	0.46
350	0.41
700	0.36

Table 2-5: Friction coefficient as a function of temperature for Ti-6Al-4V[265]

The workpiece plates were restricted to their lower and lateral edges, preventing both translational and rotational movement to prevent distortion during the welding process. To model the interaction between the tool and workpiece, a frictional contact approach was employed. While prior studies relied on a constant friction coefficient to address the uncertain variations in friction, this research incorporated a temperature-dependent friction coefficient (see Table 2-3, Table 2-4, and Table 2-5), derived from the Coulomb friction model and Mises shear stress, as discussed in the subsequent section. The entire energy produced from the friction between the tool and workpiece was converted into heat, and it was assumed that 50%[187] of this heat transferred to the workpiece surface, accounting for losses due to heat dispersion to the tool and other undesired components in the setup. The boundary conditions applied in this finite element model are depicted in Figure 2-1. The development of the temperature field is greatly influenced by heat dissipation to the surroundings. The convection mechanism was assumed to comply with Newton's law of cooling under natural convection, as expressed in Equation (6)[266].

$$k\frac{dT}{ds} = h(T - T_{amb}) \quad (6)$$

This formula uses several variables: k represents thermal conductivity, S stands for the direction vector, h signifies the convection coefficient, and T_{amb} denotes the ambient temperature. During the FSW process, the workpiece plates are affixed to a backing plate at the base to prevent deformation caused by the force applied by the tool onto the workpiece. The interaction between the workpiece and the backing plate involves intricate changes in contact conductance influenced by multiple factors, including the vertical force exerted by the tool onto the plates, the horizontal force due to plate movement and clamping, as well as thermal and mechanical stresses. Holman[267] proposed Equation (7) to calculate the convection coefficient specifically for the interface between the workpiece and the backing plate.

$$Q_{wb} = h_{wb}(T_W - T_b) = Nu_x \frac{k}{x}(T_w - T_b) \quad (7)$$

The equation includes: -

- Q_{wb}, representing heat transfer per unit area at the workpiece-backing plate.
- h_{wb} as the heat transfer coefficient at their interface.
- Nu_x indicating the Nusselt number.
- x as the plate separation distance.
- k for thermal conductivity.
- T_w and T_b as the average temperatures of the workpiece and backing plate, respectively.

Consequently, a higher convection heat transfer coefficient of 500 W/m^2.K was allocated to the bottom surface of the plates to accommodate the intricacies in contact gap conductance. Meanwhile, the top surface and sides, exposed to ambient conditions, were assigned a heat transfer coefficient of 25 W/m^2.K.

The model accounts for heat dissipation through natural convection and surface-ambient radiation exchange with the surroundings as represented in Equations (8 & 9), where q_{wf} is the heat loss from the workpiece front surface including both the natural convection and radiation losses[268], while q_{wb} is the convection and radiation heat loss from workpiece backing plate. h_{wf}= 25 W/m^2.K and h_{wb} = 500 W/m^2.K. ϵ is the surface emissivity coefficient and σ is Stefan–Boltzmann constant 5.67 × 10^{-8} watt W/m^2.K^4.

$$q_{wf} = h_{wf}(T_o - T) + \epsilon\sigma(T_{amb}^4 - T^4) \quad (8)$$

$$q_{wb} = h_{wb}(T_o - T) + \epsilon\sigma(T_{amb}^4 - T^4) \quad (9)$$

2.2.3. Governing Equations

Heat originates mainly from the friction between the tool and workpiece, coupled with plastic deformation. FSW entails vigorous interactions between the welding tool and workpiece plates under elevated temperatures and speeds. As a result, explicit solvers are necessary for constructing the FE model, allowing the resolution of the thermomechanical challenge and examination of the intricate interactions occurring at the interface between the tool and plate[269]. A coupled dynamic explicit FE model was formulated to explore the thermal timeline and consequently compute the stresses, strains, and reaction forces during the FSW process. The temperature progression for the tool moving in the x direction throughout the process adheres to the 3D Fourier heat conduction law outlined in Equation (10)[266]. Where k_s represents the thermal conductivity in three coordinate axes, while T signifies the changing temperature field. ρ and C represent density and specific heat capacity, respectively. The variable u denotes the tool's velocity in the x direction, and Q_v stands for the heat generated due to viscous dissipation resulting from plasticity at the tool-plate interface.

$$\rho C\left(\frac{\partial T}{\partial t} + u\frac{\partial T}{\partial x}\right) + Q_v = \frac{\partial}{\partial x}\left[k_x\frac{\partial T}{\partial x}\right] + \frac{\partial}{\partial y}\left[k_y\frac{\partial T}{\partial y}\right] + \frac{\partial}{\partial z}\left[k_z\frac{\partial T}{\partial z}\right] \quad (10)$$

The mathematical representation of the dissipation rate of plastic strain energy, symbolized as q_p, is presented in Equation (11)[270], with η representing the energy dissipation fraction, while σ and $\dot{\varepsilon}$ denote flow stress and plastic strain rate, respectively.

$$q_p = \eta(\sigma \, x \, \dot{\varepsilon}) \tag{11}$$

The state of contact between the tool and workpiece was characterized using Coulomb's friction model. This model considers rigid contact pairs, neglecting internal stress. Consequently, three distinct contact states are outlined for establishing the condition of tool/workpiece contact in the FSW process, contingent on the tangential shear strength.

In FSW, the interaction between the shoulder and workpiece can result in sticking, sliding, or a combination of both conditions[271]. Depending on the friction and material properties, the workpiece may adhere to the tool (sticking) or slide against it (sliding). Both sticking and sliding contribute to heat generation and material flow during the welding process.

$$\tau_f = \delta\tau_y + (1-\delta)\mu P_n \sin\alpha \tag{12}$$

$$\tau_y = \frac{\sigma}{\sqrt{3}} \tag{13}$$

Equation (12) illustrates the Coulomb friction model, used to compute the frictional shear stress at the interface of the tool and plate[258]. Within this equation, τ_f signifies the contact shear stress, τ_y denotes the shear yield stress, while δ represents the slip rate. Specifically, δ = 1 characterizes the sliding condition, whereas δ = 0 signifies the sticking condition. Additionally, P_n stands for the normal contact pressure, and α represents the angle of the tapered pin profile adopted in this study, where α = 0 for flat surfaces. It is important to note that as the temperature rises, plastic heat generation takes precedence,

and the Von Mises criterion is utilized to define the contact shear stress, formulated in Equation (13). The friction coefficient, μ, is computed through the following equation[272]:-

$$\mu = \frac{\tau_{fb} - \tau_{fs}}{(1-\delta)P_n(1-\sin\alpha)} \tag{14}$$

$$\delta = \frac{\tau_{fs} - \tau_{fb}\sin\alpha}{(1-\sin\alpha)\tau_y} \tag{15}$$

$$\frac{dq_f}{dA} = \tau_f(\omega r - u\sin\theta) \tag{16}$$

Where τ_{fb} and τ_{fs} correspond to the contact shear stress for the bottom surfaces of the shoulder/pin and the side surface of the pin, respectively. Moreover, utilizing the aforementioned equations, the expression for the slip rate can be formulated as Equation (15)[272] :As a result, the calculation of the frictional heat energy, q_f, generated at the interface between the tool and plate, is determined by Equation (16). Within this equation, ω, r, and dA represent the angular velocity of the rotating tool, the distance of the elemental area from the tool axis, and the local elemental area of heat generation, respectively. Additionally, u stands for the welding speed, while θ denotes the angle between the direction of welding and the radius vector. Notably, the term $u\sin\theta$ becomes negligible when the tool velocity significantly surpasses the material velocity underneath.

The heat produced at the shoulder surface, $Q_{shoulder}$, can be determined using Equation (17), where R_s represents the radius of the cylindrical tool shoulder, and R_{p2} stands for the pin radius at the shoulder-pin interface. Furthermore, the heat generated, Q_{pin}, at the pin having bottom and top radii of R_{p1} and R_{p2} can be computed through Equation (18)[271]. Here, l signifies the slant height of the tapered pin. The initial portion of Equation (18) calculates the heat generation at the side surface of the pin, while the latter part estimates the heat generated at the flat pin tip.

$$Q_{Shoulder} = \int_0^{2\pi} \int_{R_{p2}}^{R_1} \omega r^2 \tau_f dr d\theta = \frac{4\pi^2}{3} \omega \tau_f \left(R_s^3 - R_{p2}^3\right) \quad (17)$$

$$Q_{pin} = \int_0^{2\pi} \int_0^{l} \omega r^2 \tau_f d\theta dz + \int_0^{2\pi} \int_0^{R_{p1}} \omega r^2 \tau_f d\theta dr = \frac{\pi}{2} \omega \tau_f l \left(R_{p1} - R_{p2}\right)^2 + \frac{2\pi}{3} \omega \tau_f R_{p1}^3 \quad (18)$$

Finally, the average grain size was calculated following Zener–Hollomon parameter[268, 273], which will subsequently be utilized to predict microhardness via the Hall-Petch relationship[268, 273]. Z is the Zener-Hollomon parameter, $\varepsilon_e^{\cdot}$ is the equivalent strain rate; Q is the activation energy; R is the ideal gas constant, and T is the temperature, d is the average grain size, and H_v is the microhardness.

$$Z = \varepsilon_e^{\cdot} exp\left(\frac{Q}{RT}\right) \quad (19)$$

$$\ln(d) = 9 - 0.27 \ln(Z) \quad (20)$$

Hall–Petch relationship (21)

$H_v = 40 + 72d^{-0.5}$

2.2.4. Model Assumptions and Boundary Conditions

- Time dependent process.
- Welding process under ambient conditions without any external heating/cooling sources.
- The shoulder moves in the X-direction without inclination.
- Workpiece and pin physical properties (Thermal conductivity, heat capacity, density, etc.) are functions of temperature.

- The system main boundary conditions are reflected in Table 2-4

Parameter	Unit	Al-T6	Ni-Inconel 718	Ti-6Al-4V
Workpiece melting temperature	°C	660	1260 - 1336	1604 - 1660
Welding speed	mm/min	30-390	50-150	50-150
Rotation Speed	RPM	50-650	100-600	100-600
Normal Force	kN	5-25	5-50	5-50
Activation energy of lattics diffusion	kJ/mol	140	320	116

Table 2-6: Process parameters for Aluminum alloy, Inconel 718 and Ti-6Al-4V.

2.2.5. Meshing System

Mesh independent studies play a crucial role in numerical simulations, especially in engineering application, as the mesh size can impact the accuracy and reliability of the results. The aim of these studies is to determine the minimum mesh size required to produce accurate and reliable results without using an excessively fine mesh, which increases computational cost and time. This is done by varying the mesh size, comparing the results with published experimental data and other numerical results, and continuing until the results converge and do not change significantly with further mesh refinement.

Table 2-7 summarizes a mesh sensitivity analysis conducted to determine the optimum number of elements required to achieve the most accurate results within an acceptable computation time for a finite element analysis that including material plasticity, adaptive mesh and sometime remeshing in the case of material melting. In this analysis, the main performance parameters including peak temperature, stress, and strain were evaluated against the number of elements and computation time for different mesh types: Coarse, Normal, Fine, Very Fine, and Extremely Fine.

As expected, increasing the number of elements improves the data quality but also significantly increases the computation time. The table shows that as the number of

elements increases from 2,532 (Coarse) to 350,000 (Extremely Fine), the computation time rises from 0.45 hours to 13 hours. The results for peak temperature, stress, and strain also become more precise with finer meshes. For instance, the peak temperature increases from 890°C for the Coarse mesh to 1108°C for the Extremely Fine mesh. Similarly, stress values decrease from 230 MPa to 92 MPa, and strain values increase from 0.075 to 0.145. Based on this study, the Very Fine mesh, with 115,000 elements and a computation time of 6.5 hours, was selected as the optimal choice with an average element quality of 0.78 (see Figure 2-3), where the main performance parameters stabilized while increasing the number of elements. It provides a good balance between accuracy and computational efficiency, delivering precise results for peak temperature, stress, and strain while keeping the computation time within a manageable range.

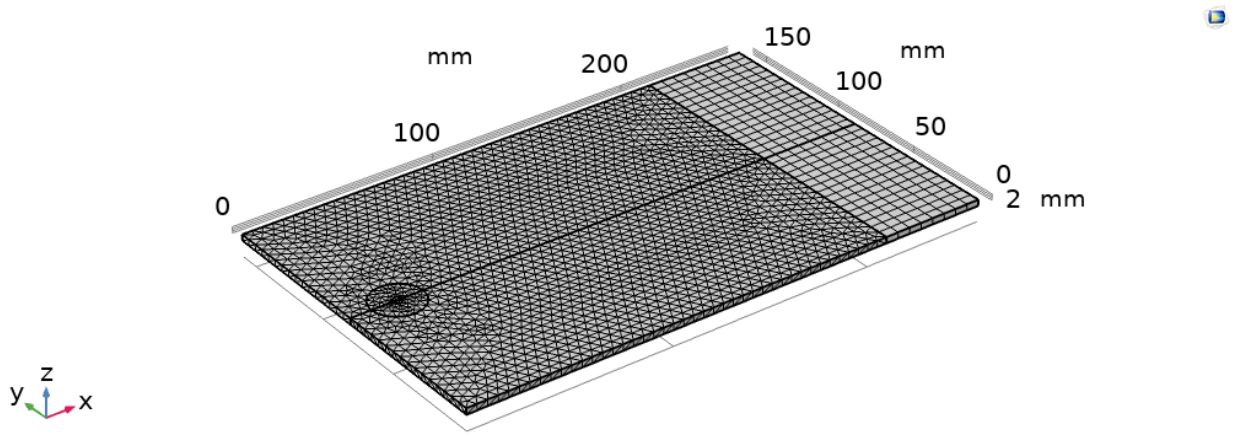

Figure 2-3: System mesh

Item	Coarse	Normal	Fine	Very Fine	Extremely Fine
CPU Time	0.45 h	0.95 h	2 h	6.5 h	13 h

No. of elements	2,532	6,595	11,795	115,000	350,000
Peak Temperature (°C)	890	989	1055	1105	1108
Stress (MPa)	230	155	101	90	92
Strain	0.075	0.11	0.138	0.144	0.145

Table 2-7: Mesh sensitivity analysis

2.2.6. Model Validation

The finite element model was verified using previously published experimental findings conducted on aluminum plates[274]. In those experiments, the temperature of the plate measured at 5 mm from the welding nugget zone was recorded as 577°C. In comparison, the temperature predicted by the developed COMSOL Multiphysics model in this study was 600°C, indicating a discrepancy of 4%. Additionally, the FE model was validated against experimental data available for Inconel 718 plates, where the plate temperature measured at a distance of 2 mm from the welding nugget zone was reported as 1059°C[187]. In contrast, the model predicted a temperature of 1105°C, demonstrating close agreement between the FE model and the published experimental results for friction stir welding (FSW).

On top of that, the finite element model underwent another verification against other experimental results[137, 187] (see Figure 2-4) conducted on Inconel 718 plates. These experiments recorded a plate temperature of 577°C at a distance of 5 mm from the welding nugget zone. Conversely, the temperature projected by the developed COMSOL Multiphysics model in this study was 600°C, indicating a 4% disparity. indicating close alignment between the FE model and published experimental outcomes for FSW.

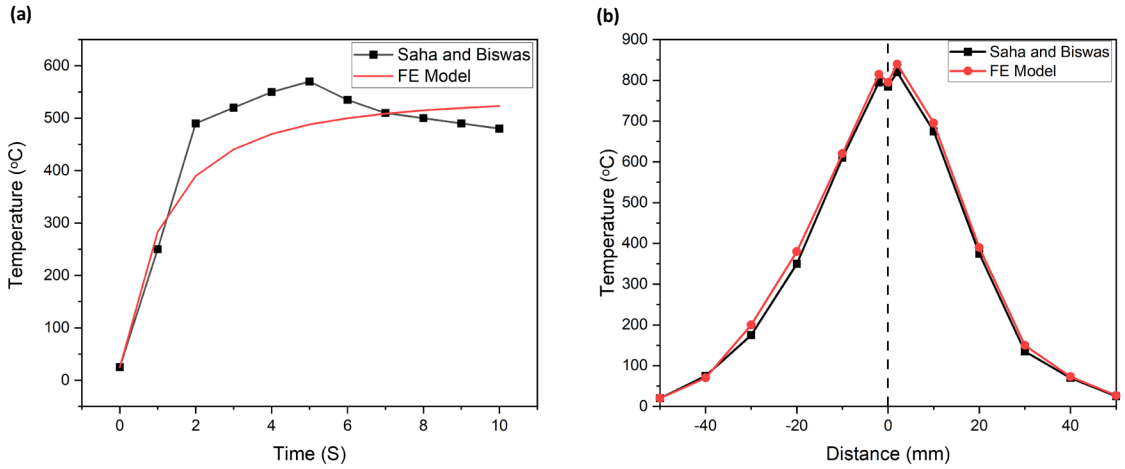

Figure 2-4: Finite element model validation against published experimental data[187]

2.3. Statistical Analysis

Taguchi analysis, one-way ANOVA and Non-linear regression analysis were used to understand the effect of the process parameters of FSW (rotational speed, axial force, welding speed, shoulder diameter, pin diameter) on the welding performance (workpiece temperature, microhardness, stress evolution and grain size.

Normality tests were conducted on all variables to assess the data distribution. The Shapiro-Wilk test, among others, was employed to verify whether the data adhered to a normal distribution. This step is essential because numerous statistical tests, such as ANOVA and regression analysis, rely on the assumption that the data is normally distributed, Shapiro-Wilk test was used per below equation

$$W = \frac{\left(\sum_{i^{-1}}^{n} a_i x_{(i)}\right)^2}{\sum_{i=1}^{n}(x_i - \bar{x}_i)^2} = \quad (22)$$

- W: Shapiro-Wilk test statistics.
- n: Number of observations in the sample.
- $x_{(i)}$: The ith ordered sample value.

• a_i : Constants generated from the means, variances, and covariances of the order statistics of a sample from the standard normal distribution. These constants depend on the sample size n.

In addition, the general Formula of Mean and standard deviation is reflected in below equations: -

$$\bar{x} = \frac{\sum_{i=1}^{n} x_i}{n} \tag{23}$$

$$\sigma = \sqrt{\frac{\sum(x - \bar{x})^2}{n - 1}} \tag{24}$$

- $\bar{x}$ is the sample mean.
- x_i are the individual sample observations.
- n is the number of observations in the sample.

2.3.1. Taguchi Analysis

Taguchi analysis[275] was employed to systematically investigate the influence of multiple process parameters on the welding performance parameters in FSW of Inconel 718. The process parameters considered were rotational speed (RPM), axial force (N), welding speed (mm/min), shoulder diameter (mm), and pin diameter (mm). The performance parameters evaluated included workpiece temperature (°C), microhardness (HV), stress evolution (MPa), and grain size (μm). An L_9 orthogonal array was selected to design the experiments, suitable for five factors at three levels each. The orthogonal array helps in studying the parameter space efficiently by minimizing the number of experiments. The levels for each factor were chosen based on preliminary experiments and literature review[275].

The Signal-to-Noise (S/N) ratio was calculated for each performance parameter to identify the optimal level of each process parameter. The S/N ratio for a response variable y with n observations is given by:

- For smaller-is-better characteristics (e.g., grain size and stress evolution):

$$S/N\ ratio = -10\log\left(\frac{1}{n}\sum_{i=1}^{n} y_i^2\right) \tag{25}$$

- For larger-is-better characteristics (e.g., microhardness):

$$S/N\ ratio = -10\log\left(\frac{1}{n}\sum_{i=1}^{n} \frac{1}{y_i^2}\right) \tag{26}$$

- For nominal-is-best characteristics (e.g., workpiece temperature within a specific range):

$$S/N\ ratio = 10\log\left(\frac{\bar{y}^2}{\frac{1}{n-1}\sum_{i=1}^{n}(y_i - \bar{y})^2}\right) \tag{27}$$

where $\bar{y}$ is the mean of the observed values.

2.3.2. One-Way ANOVA

One-Way Analysis of Variance (ANOVA) was conducted to quantify the significance of each process parameter on the welding performance parameters. The ANOVA test partitions the total variability observed in the data into components attributable to each source of variation, allowing the determination of statistically significant factors.

The ANOVA model is expressed as[276]:

$$Y_{ij} = \mu + \tau_i + \epsilon_{ij} \tag{28}$$

where:

- Y_{ij} is the response variable (e.g., workpiece temperature) for the $j-th$ observation at the $i-th$ level of a factor.
- μ is the overall mean response.
- τ_i is the effect of the $i-th$ level of the factor.
- ϵ_{ij} is the random error component.

The F-ratio was computed to test the null hypothesis that all means are equal:

$$F = \frac{MS_{between}}{MS_{within}} \tag{29}$$

where:

- $MS_{between}$ is the mean square between groups, calculated as:

$$MS_{between} = \frac{SS_{between}}{df_{between}} \tag{30}$$

- MS_{within} is the mean square within groups, calculated as:

$$MS_{within} = \frac{SS_{within}}{df_{within}} \tag{31}$$

- $SS_{between}$ is the sum of squares between groups:

$$SS_{between} = \sum_{i=1}^{k} n_i(\overline{Y}_i - \overline{Y})^2 \tag{32}$$

- SS_{within} is the sum of squares within groups:

$$SS_{within} = \sum_{i=1}^{k}\sum_{j=1}^{n_i}\left(Y_{ij} - \overline{Y}_i\right)^2 \tag{33}$$

- $df_{between}$ is the degree of freedom between groups, calculated as $k-1$ where k is the number of groups (levels of the factor).
- df_{within} is the degree of freedom within groups, calculated as $N-k$ where N is the total number of observations.

2.3.3. Regression Analysis

Non-linear regression analysis was applied to develop predictive models for the relationship between the FSW process parameters and the performance parameters. This type of regression is particularly useful when the relationship between variables is not linear, allowing for more flexibility in modeling complex behaviors[277].

The non-linear regression model can be represented as:

$$Y = f(X_1, X_2, X_3, X_4, \dots, X_k) + \epsilon \tag{34}$$

where Y is the dependent variable (e.g., workpiece temperature), $X_1, X_2, X_3, X_4, \dots, X_k$ are the independent variables (process parameters), and ϵ is the error term.

For this study, the specific form of the non-linear model used was:

$$Y = \beta_0 + \beta_1 X_1^{\alpha_1} + \beta_2 X_2^{\alpha_2} + \beta_3 X_3^{\alpha_3} + B_4 X_4^{\alpha_4} + \beta_5 X_5^{\alpha_5} + \epsilon \tag{35}$$

where:

- $\beta_0, \beta_1, \dots, \beta_5$ are the regression coefficients.
- $\alpha_1, \alpha_2, \dots, \alpha_5$ are the exponents determined through iterative fitting procedures.

The parameters of the non-linear model were estimated using the least squares method, which involves minimizing the sum of the squares of the differences between observed and predicted values:

$$minimize \sum_{i=1}^{n} \left(Y_i - \widehat{Y}_i\right)^2 \tag{36}$$

where Y_i is the observed value and $\widehat{Y}_i$ is the predicted value from the model.

2.4. Conclusions

This chapter lays the groundwork for a rigorous analysis and interpretation of results, ensuring the reliability and validity of the findings. The detailed methodology presented here is essential for gaining valuable insights into the optimization of friction stir welding processes for high-performance materials. Chapter 2 introduces a comprehensive simulation methodology tailored to investigate the impact of FSW parameters on Al-T6 alloy, Inconel 718, and Ti-6Al-4V. The setup encompasses crucial elements such as system definition, boundary conditions, material properties, governing equations, mesh selection, and a wide array of process parameters and performance metrics. This robust framework guarantees the thorough collection and analysis of data.

Furthermore, a thorough methodology was implemented to assess the effects of various process parameters on welding performance of high strength alloys. The data analysis procedure involved several key steps: First, numerical experiments were systematically conducted based on an orthogonal array for Taguchi analysis, focusing on critical performance parameters including workpiece temperature, microhardness, stress evolution, and grain size. Second, Taguchi analysis employed Signal-to-Noise (S/N) ratios for each parameter to assess process robustness and determine optimal parameter levels. Third, One-Way ANOVA was performed to statistically evaluate each parameter's significance, using F-ratios and p-values to test hypotheses and identify impactful variables. Lastly, non-linear regression models were developed for each performance metric to capture complex parameter relationships. These models were refined using the least squares method to ensure accurate fit to observed data, validated to confirm predictive reliability. Through these systematic procedures, optimal process parameters were identified, and predictive models developed to enhance quality and performance of friction stir welded joints. This comprehensive approach not only advances understanding and optimization of FSW processes but also provides valuable insights for both academic research and industrial applications.

CHAPTER 3: Simulation Results of FSW of Al-T6 and Inconel 718

3.1. Introduction

FSW is a promising technique for joining aerospace materials, including Inconel 718, due to its ability to produce high-quality welds with reduced distortion and defects. However, the microstructure and mechanical properties of Inconel 718 welds are highly dependent on the FSW process parameters. Therefore, optimizing these parameters is essential to enhance the microstructure and mechanical properties of Inconel 718 welds.

Chapter 3 presents a detailed analysis and discussion of the simulation results obtained from the FSW of Al-T6 and Inconel 718. This chapter aims to interpret the simulation data, highlighting the influence of each process parameter on performance outcomes. Additionally, it presents the results of statistical analyses, beginning with the calculation of signal-to-noise (S/N) ratios for each performance metric, followed by an assessment of the main effects of rotational speed, welding speed, axial force, shoulder diameter, and pin diameter. The chapter also explores the interactions between these parameters through ANOVA, identifying the most significant factors affecting workpiece temperature, microhardness, stress evolution, and grain size. Furthermore, non-linear regression models are developed to establish predictive equations for the performance metrics, providing a comprehensive understanding of the optimal FSW conditions for Inconel 718.

3.2. FEM Results of the FSW of Al-T6 Alloy

The 3D temperature distribution depicted in Figure 3-1 and Figure 3-2 for the aluminum plates provides insight into the heat distribution during the welding procedure. As depicted in Figure 3-1, the highest temperature, reaching 676 °C, was observed at the welding joint. Furthermore, the 2D cross-sectional perspective of the temperature distribution illustrates (see Figure 3-2) a varied heat dissipation pattern across the Al plates, ranging from below 100 up to 600 °C. These findings underscore the intricate nature of heat transfer in FSW and the significance of comprehending temperature distribution to achieve successful welds. Utilizing the temperature profile data can facilitate the optimization of the welding process and enhance the quality of the resulting welds.

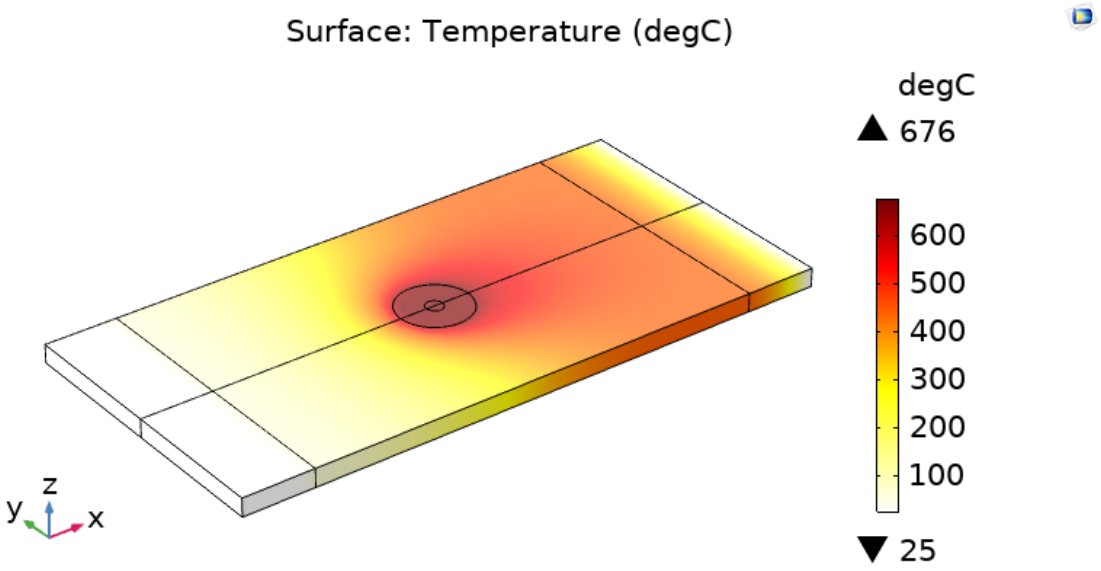

Figure 3-1: 3D Temperature profile of Al workpiece

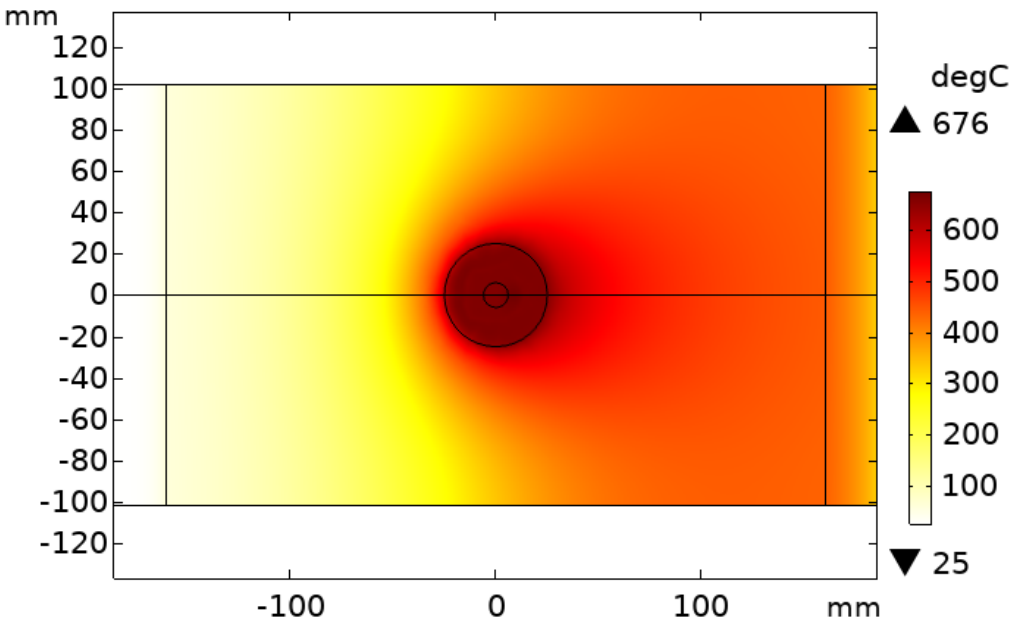

Figure 3-2: 2D Temperature profile for Al workpiece

3.2.1. Effect of Process Parameters on Welding Efficiency

In order to gain a better understanding of the effects of various process parameters on the aluminum workpiece, a comprehensive parametric study was conducted. The study

involved evaluating the impact of rotational speed (ranging from 50 rpm to 650 rpm), welding speed (varying from 0.5 mm/sec to 6.5 mm/sec), normal force (ranging from 5 kN to 25 kN), cooling velocity (with values from 0.1 m/sec to 1.1 m/sec), and cooling diameter (ranging from 0.2 inch to 1 inch). The outcomes of the study were measured using several key performance indicators, including the temperature in the x-direction, temperature in the z-direction (across the thickness of the workpiece), average grain size, and microhardness.

3.2.1.1. Axial Force

The results of the effect of normal force on various parameters were depicted in Figure 3-3. The findings showed that an increment in the normal force resulted in a heightened temperature distribution that reached its maximum at the welding nugget. Moreover, the increase in the normal force led to an increase in the average grain size and a decrease in the microhardness. A comparison between the results at normal forces of 5 kN and 25 kN revealed that temperatures increased from 260°C to 650°C, the average grain size increased from 450 µm to 2000 µm, and the hardness decreased from 43.5 to 42. These results suggest a robust relationship between the normal force, average grain size, and hardness.

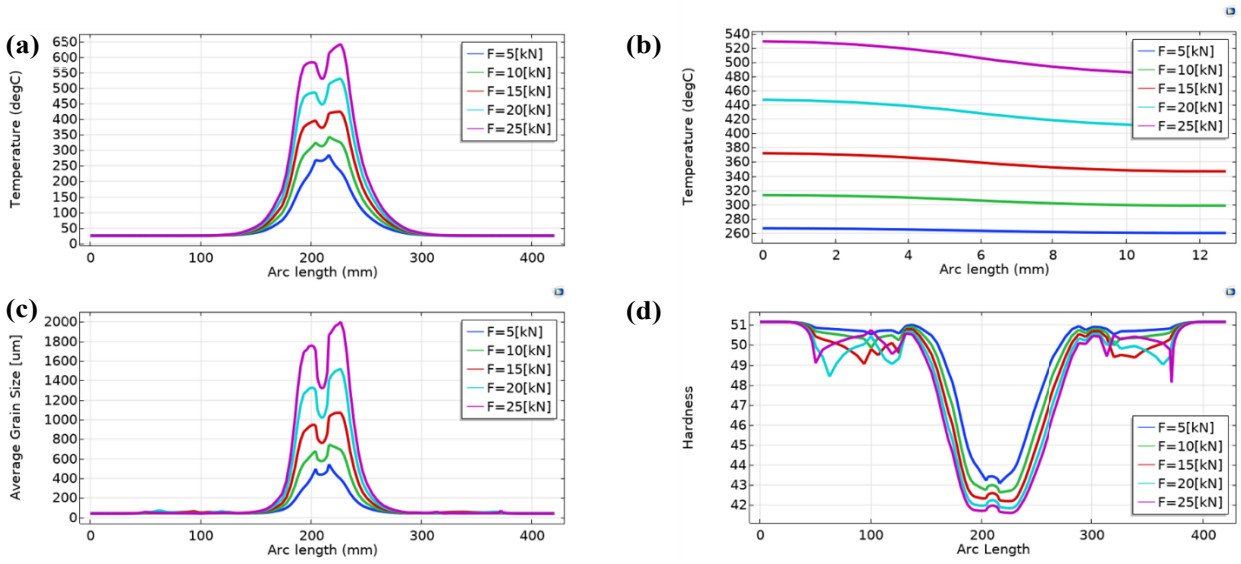

Figure 3-3: Al Workpiece, parametric analysis on normal force. a) temperature in x-direction, b) temperature in z-direction, c) average grain size, and d) hardness

3.2.1.2. Rotational Speed

The results of the effect of rotational speed on various parameters were demonstrated in Figure 3-4. The results showed that an increase in rotational speed resulted in a higher temperature distribution that reached its peak at the centerline in the welding direction and at the surface where the pin was in contact with the workpiece. Furthermore, increasing the welding speed led to an increase in average grain size, which followed an M-shaped pattern, and a corresponding decrease in hardness, which followed a w-shaped pattern. When comparing the results from a rotational speed of 50 rpm to 650 rpm, the temperatures increased from 110°C to 670°C, the average grain size increased from 200 µm to 2000 µm, and the hardness decreased from 46 to 42. These results indicate a strong correlation between the rotational speed, average grain size, and hardness. The increase in temperature and average grain size is a result of the increased energy input from the welding process, while the relative decrease in hardness is likely due to the increased grain growth and recrystallization in the material.

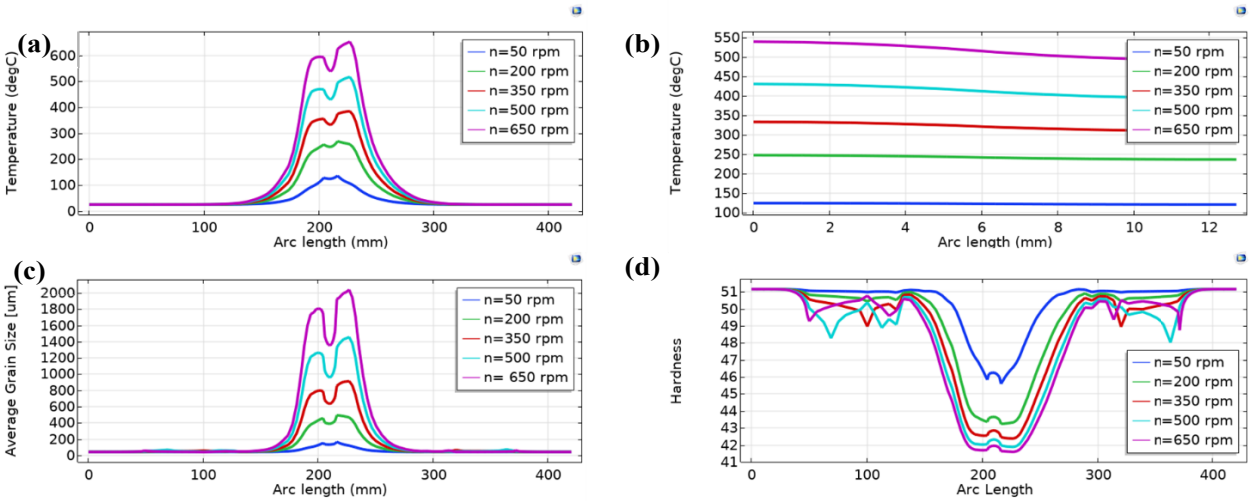

Figure 3-4: Al Workpiece, parametric analysis on rotational speed. a) temperature in x-direction, b) temperature in z-direction, c) average grain size, and d) hardness

3.2.1.3. Welding Speed

The effect of welding speed on various parameters was analyzed and the results of this analysis are shown in Figure 3-5 and demonstrate the relationship between welding speed and the temperature distribution, average grain size, and hardness. The results showed

that an increase in welding speed led to a lower peak temperature. Additionally, an increase in welding speed resulted in a decrease in the average grain size, which followed an M-shaped pattern, and a corresponding relative increase in hardness, which followed a w-shaped pattern. When comparing the results for a welding speed of 0.5 mm/sec to 6.5 mm/sec, the temperatures decreased from 670 °C to 450°C, the average grain size decreased from 2000 µm to 1000 µm, and the hardness stabilized around 42 in the welding area. These results indicate a strong correlation between welding speed, average grain size, and hardness.

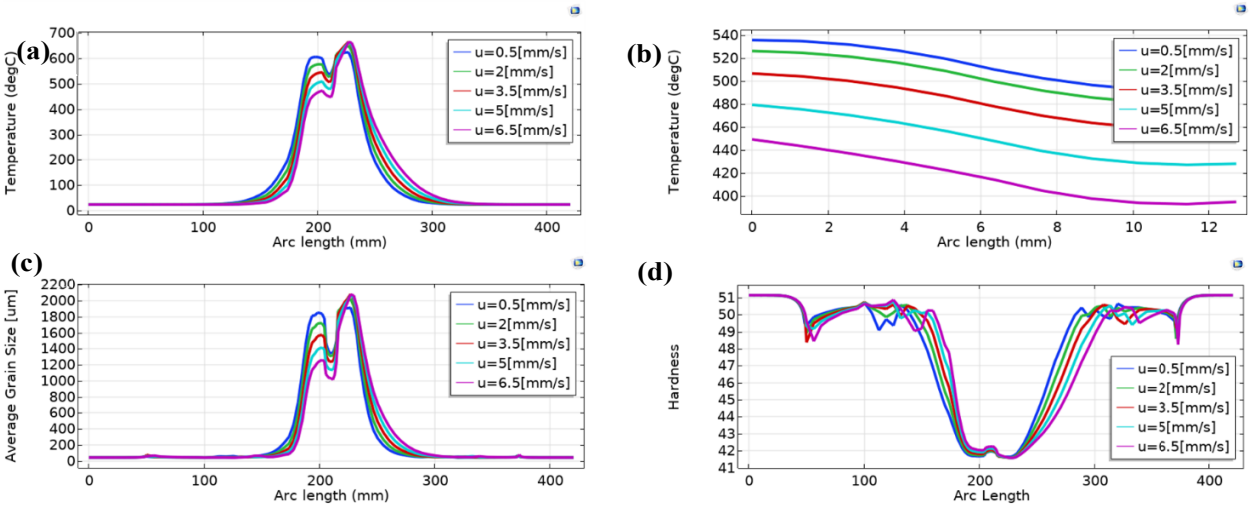

Figure 3-5: Al Workpiece, parametric analysis on welding speed. a) temperature in x-direction, b) temperature in z-direction, c) average grain size, and d) hardness

3.2.1.4. Cooling-FSW

The results of the effect of cooling velocity and cooling diameter on various parameters were presented in Figure 3-6 and Figure 3-7, respectively. In this study, cooling was performed using water with an initial temperature of 25°C, which was sprayed onto the welding area through a hose. The results showed that an increase in cooling velocity resulted in a decrease in temperature distribution, a decrease in average grain size, and an increase in microhardness. A comparison between results at cooling velocities of 0.1 m/sec and 1.1 m/sec revealed that temperatures decreased from 500°C to 300°C, average grain size decreased from 1400 µm to 600 µm, and hardness increased from 42 to 43.2. Similarly, a comparison between results at cooling diameters of 0.2 inch and 1 inch

revealed that temperatures decreased from 400°C to 300°C, average grain size decreased from 950 µm to 480 µm, and hardness increased from 42 to 43.1. These results indicate a strong correlation between the cooling parameters, average grain size, and hardness.

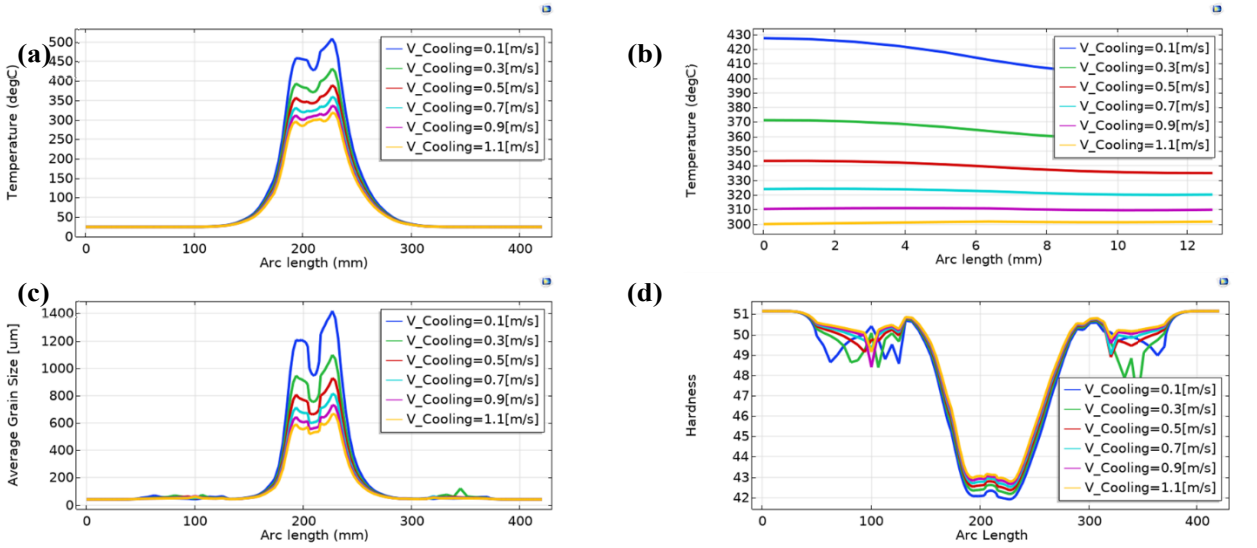

Figure 3-6: Al Workpiece, parametric analysis on cooling water velocity. a) temperature in x-direction, b) temperature in z-direction, c) average grain size, and d) hardness

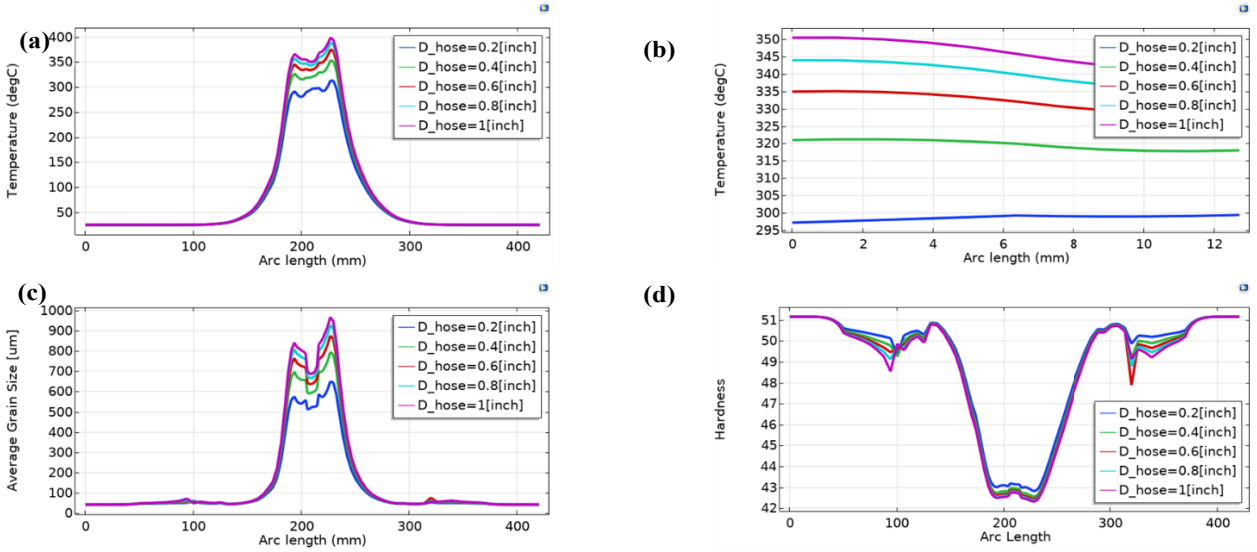

Figure 3-7: Al Workpiece, parametric analysis on cooling water hose diameter. a) temperature in x-direction, b) temperature in z-direction, c) average grain size, and d) hardness

3.3. FEM Results of the FSW of Inconel 718

The FSW process parameters used in this study are a 600 RPM rotational speed, a 90 mm/min welding speed, a 40 kN axial force, a 25 mm shoulder diameter, and a 5 mm pin diameter, without any cooling effect or preheating. The outcomes of the 3D temperature analysis for the Inconel plates are depicted in Figure 3-8. The results revealed that the highest temperature, approximately 1100°C, was concentrated within the welding regions exclusively. Further insights into the temperature distribution across the plates were gleaned from the 2D cross-sectional view, indicating a predominant concentration of maximum temperature around the welding regions with a nearly uniform spread in the x-direction as well as z-direction (across plate thickness-see subplot c). These findings illustrate a more localized temperature distribution around the welding regions in Inconel 718, leading to improved heat dissipation across the plates. This implication suggests that Inconel 718 may exhibit enhanced resistance to thermal degradation and potentially offer prolonged durability in high-temperature environments.

Figure 3-9 illustrates the 1-D temperature profiles during the FSW process of Inconel 718 Alloy, focusing on the workpiece temperature across different dimensions. Subplot (a) displays the 1D temperature profile across the workpiece, where the temperature peaks at approximately 1000°C in the welding region (around 75-85 mm) for 10 s and decreases sharply towards the edges (0 mm and 150 mm). Subplot (b) shows the 1D temperature profile along the welding line, indicating a similar peak at around 30 mm length, with the highest temperature again reaching 1000°C for 10 s and dropping to near room temperature beyond 100 mm. Subplot (c) presents the 1D temperature profile 15 mm away from the welding line, with temperatures peaking at about 650°C at 25 mm length for 10 s and declining to near 25°C beyond 100 mm. Subplot (d) illustrates the 1D temperature profile across the plate thickness, where temperatures remain constant around 900°C across most of the thickness for welding times between 2 s and 10 s, except at 0 s, where the temperature is essentially 25°C. These profiles highlight the significant thermal gradients induced by the FSW process, critical for understanding the thermal effects on the microstructure and mechanical properties of Inconel 718 Alloy.

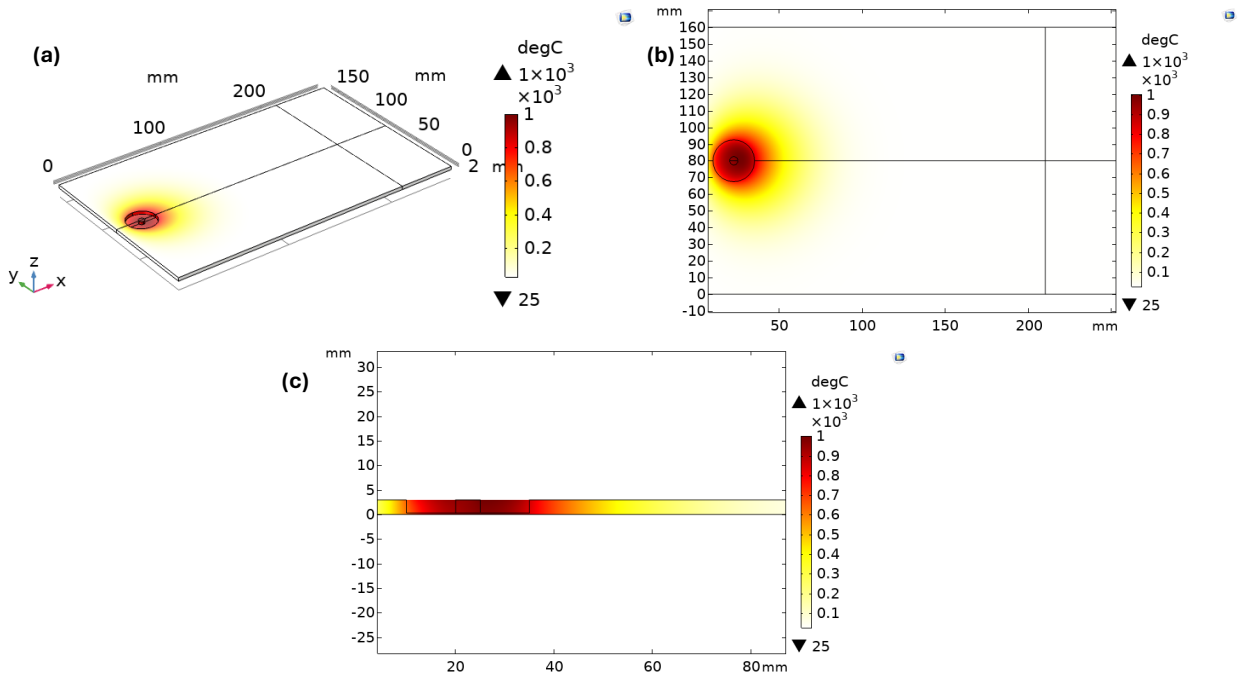

Figure 3-8: FSW of Inconel 718 alloy, a) 3D temperature profile, b)2D temperature profile, c) 2D temperature profile across plate thickness

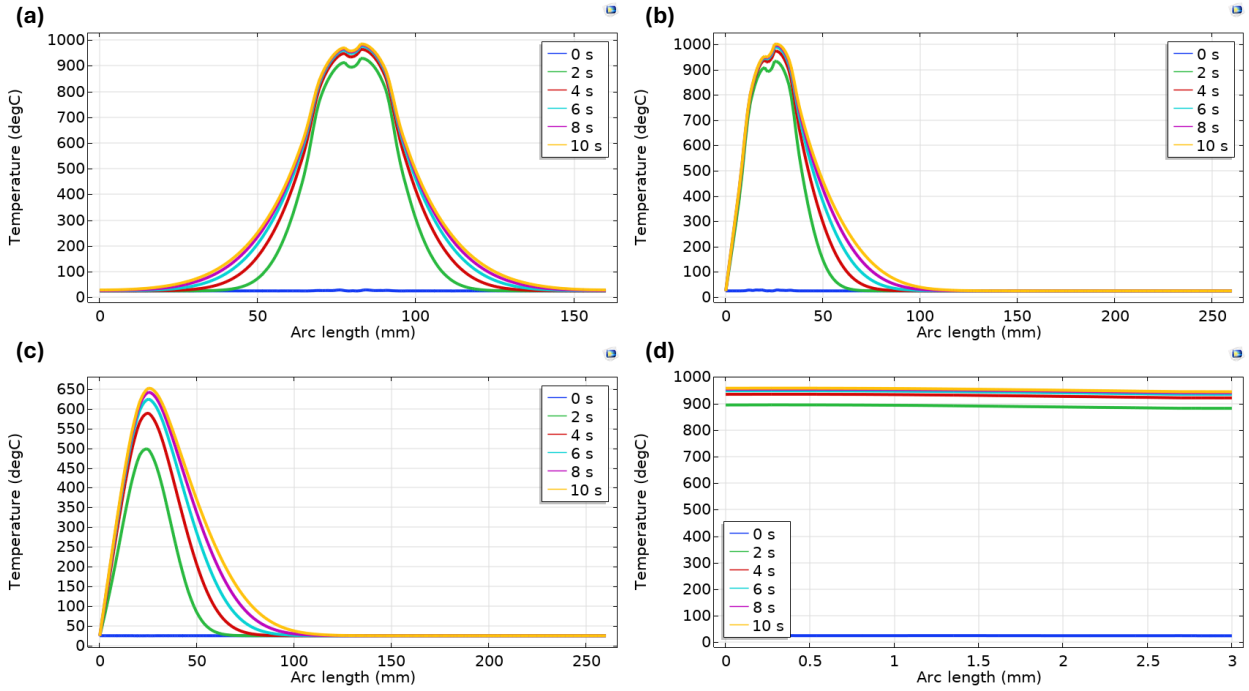

Figure 3-9: FSW of Inconel 718 alloy, a) 1D temperature profile across the nugget zone, b) 1D temperature profile across the welding line, c) 1D temperature profile at 15 mm from the welding Line, d) 1D temperature profile across the plate thickness.

On the other hand, Figure 3-10 provides a detailed analysis of the FSW process of Inconel 718 Alloy, focusing on average grain size, microhardness, and von Mises stress distribution. Subplots (a) and (b) illustrate that the average grain size increases with welding time, peaking around 50 μm at 10 s across the plates length (75-85 mm) and reaching about 6 μm at 15 mm from the welding centerline, diminishing beyond 50 mm. Subplots (c) and (d) show that hardness is highest in the welding region, peaking at approximately 415 at 10 s across the tool and around 410 units at 15 mm from the centerline, with values decreasing towards the edges. Subplots (e) and (f) depict von Mises stress, which peaks initially at about 1100 MPa at 2 s across the tool's center and around 550 MPa at 15 mm from the centerline, with stress values decreasing and spreading out as welding time increases. These findings highlight the critical changes in material properties during the FSW process, essential for optimizing welding parameters for Inconel 718 Alloy.

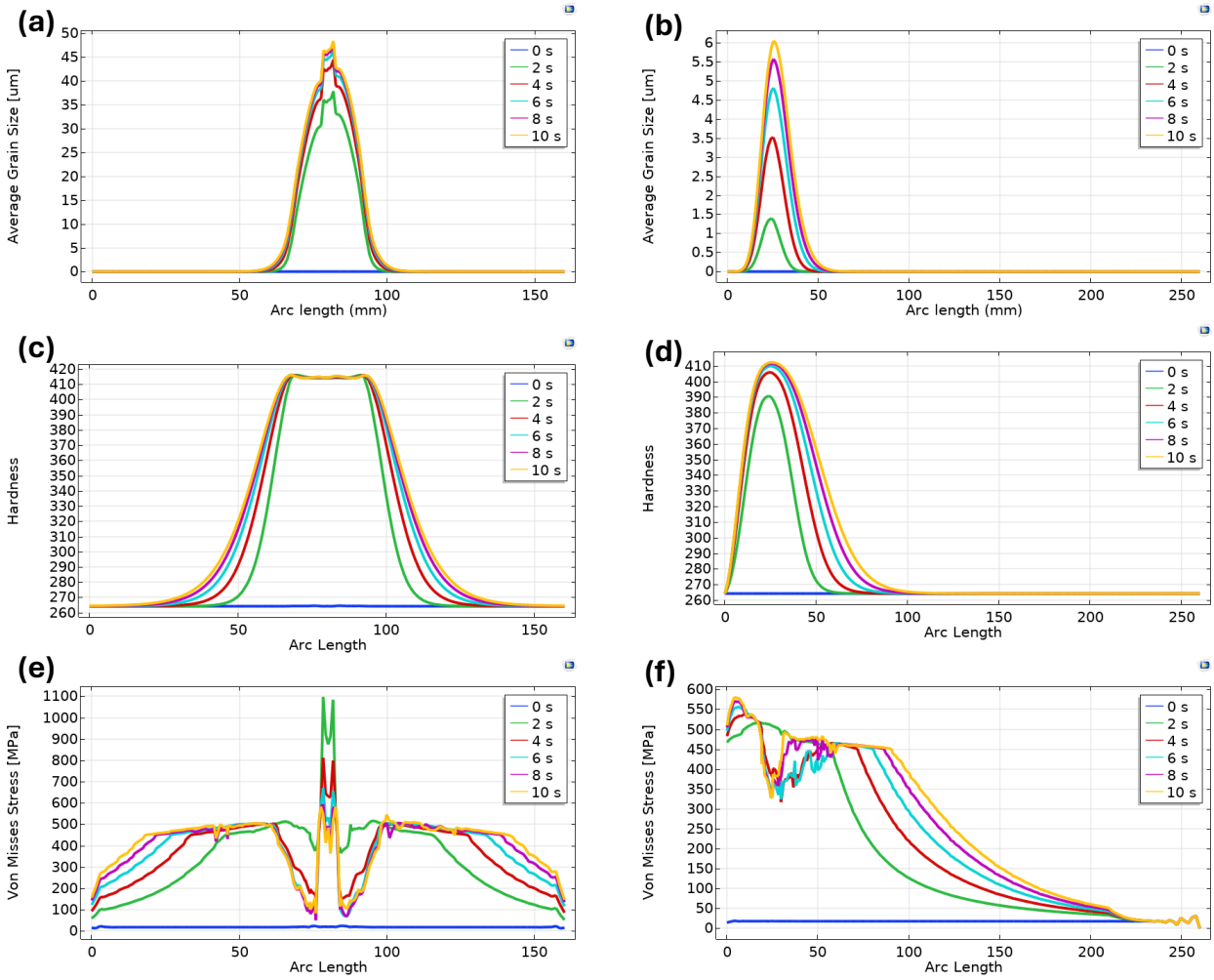

Figure 3-10: FSW of Inconel 718 alloy, a) 1D avg grain size across the nugget zone, b) 1D avg grain size at 15mm from welding centerline, c) 1D hardness across the nugget zone, d) 1D hardness at 15mm from welding centerline, e) 1D von mises stress across the nugget zone, f) 1D von mises stress at 15mm from welding centerline.

3.3.1. Effect of Process Parameters on Welding Efficiency

In this section, the effects of different process parameters, including axial force, rotational speed, welding speed, shoulder diameter, and pin diameter, as well as the effects of cooling and preheating on the workpiece thermal profile, average grain size, microhardness, and stress evolution, are discussed.

3.3.1.1. Axial Force

The FSW process parameters used in this study are a 300 RPM rotational speed, a 90 mm/min welding speed, a 5-50 kN axial force, a 25 mm shoulder diameter, and a 5 mm pin diameter, without any cooling effect or preheating. Figure 3-11 presents a parametric analysis of the FSW of Inconel 718 Alloy, focusing on the temperature profiles under varying axial forces (F_n ranging from 5 kN to 50 kN). Subplot (a) displays the 1D temperature profile across the nugget zone, showing that the temperature peaks increase with higher axial forces. For instance, at 50 kN, the peak temperature reaches approximately 900°C around the central region (75-80 mm), while at 5 kN, it peaks around 450°C. Subplot (b) illustrates the 1D temperature profile across the plate thickness, where higher axial forces consistently result in higher temperatures, with 50 kN maintaining around 850°C and 5 kN around 450°C across the thickness. Subplot (c) shows the 1D temperature profile 15 mm from the welding line, indicating that higher axial forces lead to higher temperatures at this distance as well, with 50 kN peaking at about 570°C around 25 mm length and 5 kN peaking around 250°C. These profiles underscore the significant influence of axial force on the thermal behavior during the FSW process, highlighting how increased axial force elevates the overall temperature distribution, crucial for optimizing welding parameters for Inconel 718 Alloy.

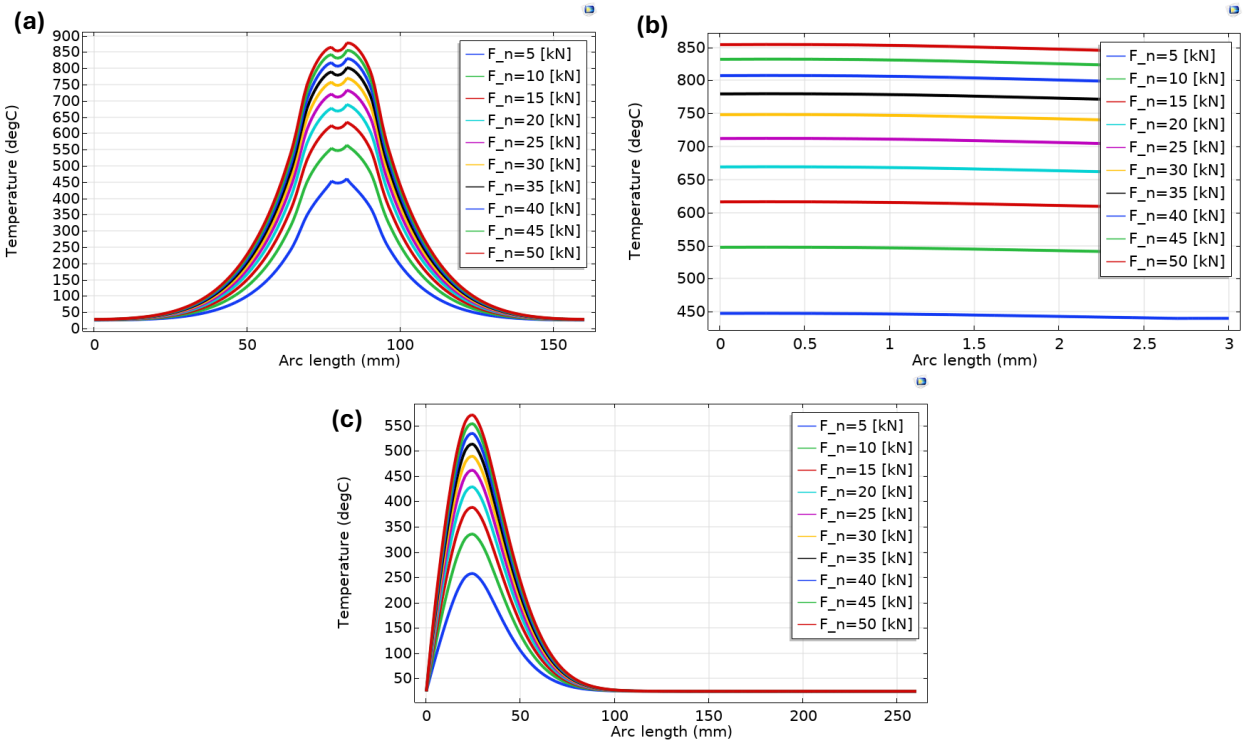

Figure 3-11: Inconel 718 workpiece, parametric analysis on axial force. a) 1D temperature profile across the nugget zone, b) 1D temperature profile across the plate thickness., c) 1D temperature profile at 15 mm from the welding line.

Moreover, Figure 3-12 provides a detailed analysis of the effect of varying axial force on average grain size, microhardness, and von Mises stress distribution. Subplots (a) and (b) illustrate that the average grain size increases with increasing axial force, peaking around 30 µm at 50 kN, while finer grains are recorded as small as 0.5 µm at 5 kN. Furthermore, grain size reaches about 3 µm at 15 mm from the welding centerline at 50 kN, while the lowest recorded grain size is less than 0.01 µm at 5 kN. Subplots (c) and (d) show that hardness is highest in the welding region, peaking at approximately 415 at axial forces higher than 20 kN, while at 15 mm from the welding centerline, it shows a gradient from 402 at 50 kN, with values decreasing to 320 units at 5 kN. Subplots (e) and (f) depict von Mises stress, which peaks at about 1100 MPa at the tool's center and around 550 MPa at 15 mm from the centerline at higher axial forces, with stress values decreasing and spreading out as axial force decreases.

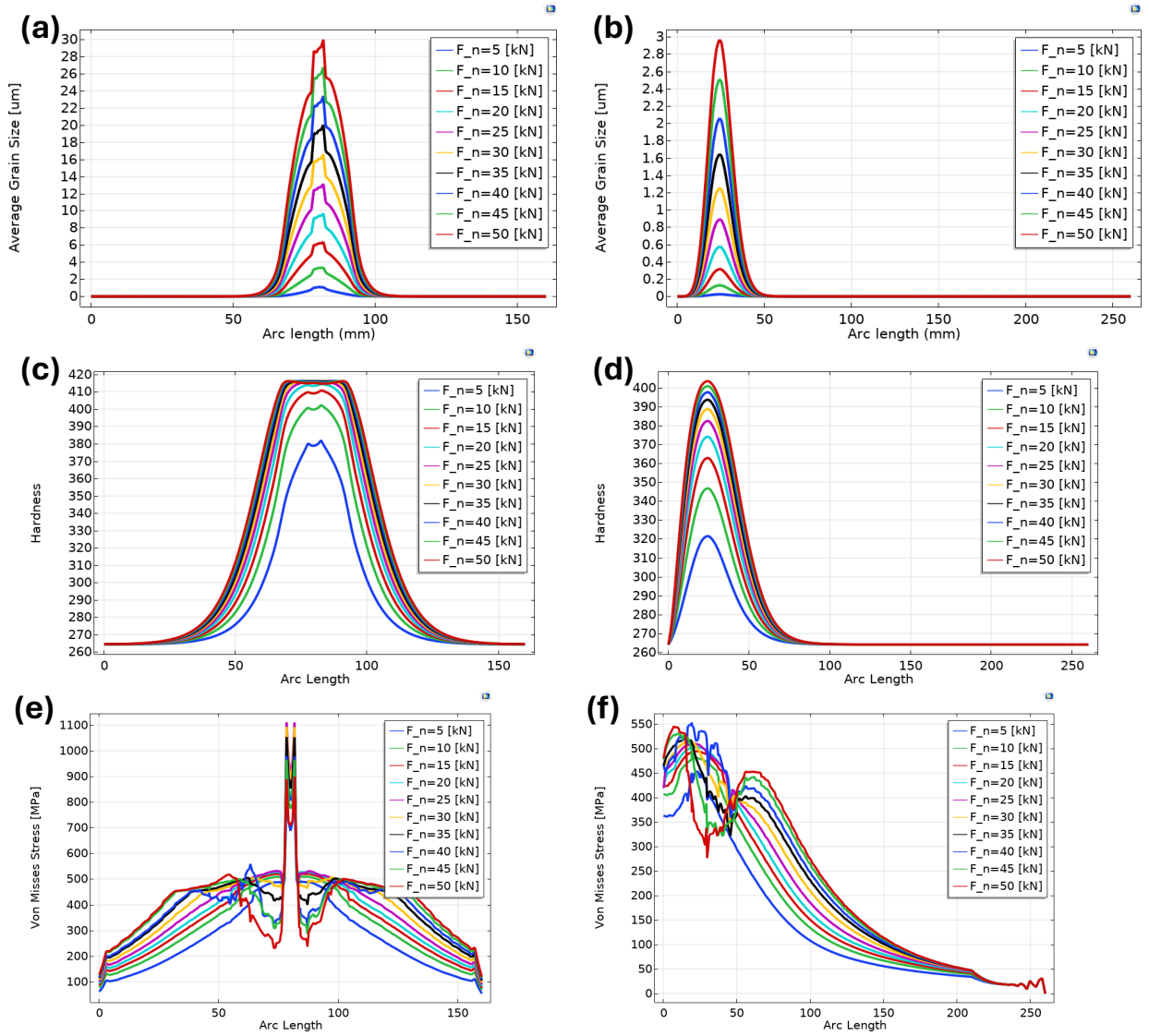

Figure 3-12: Inconel 718 workpiece, parametric analysis on axial force, a) 1D avg grain size across the nugget zone, b) 1D avg grain size at 15mm from welding centerline, c) 1D hardness across the nugget zone, d) 1D hardness at 15mm from welding centerline, e) 1D von mises stress across the nugget zone, f) 1D von mises stress at 15mm from welding centerline.

3.3.1.2. Rotational Speed

The FSW process parameters used in this study are a 100-600 RPM rotational speed, a 90 mm/min welding speed, a 27 kN axial force, a 25 mm shoulder diameter, and a 5 mm pin diameter, without any cooling effect or preheating. Figure 3-13 presents a parametric analysis of the FSW of Inconel 718 Alloy, focusing on the temperature profiles under varying rotational speeds (n ranging from 100 RPM – 600 RPM). Subplot (a) displays the

1D temperature profile across the nugget zone, showing that the temperature peaks increase with higher speeds. For instance, at 600 RPM, the peak temperature reaches approximately 900°C around the central region (75-80 mm), while at 100 RPM, it peaks around 500°C. Subplot (b) illustrates the 1D temperature profile across the plate thickness, where higher speeds consistently result in higher temperatures, with 600 RPM maintaining around 875°C and 100 RPM around 500°C across the thickness. Subplot (c) shows the 1D temperature profile 15 mm from the welding line, indicating that higher rotational speed led to higher temperatures at this distance as well, with 600RPM peaking at about 595°C around 25 mm length and 100 RPM peaking around 300°C. These profiles underscore the significant influence of rotational speed on the thermal behavior during the FSW process.

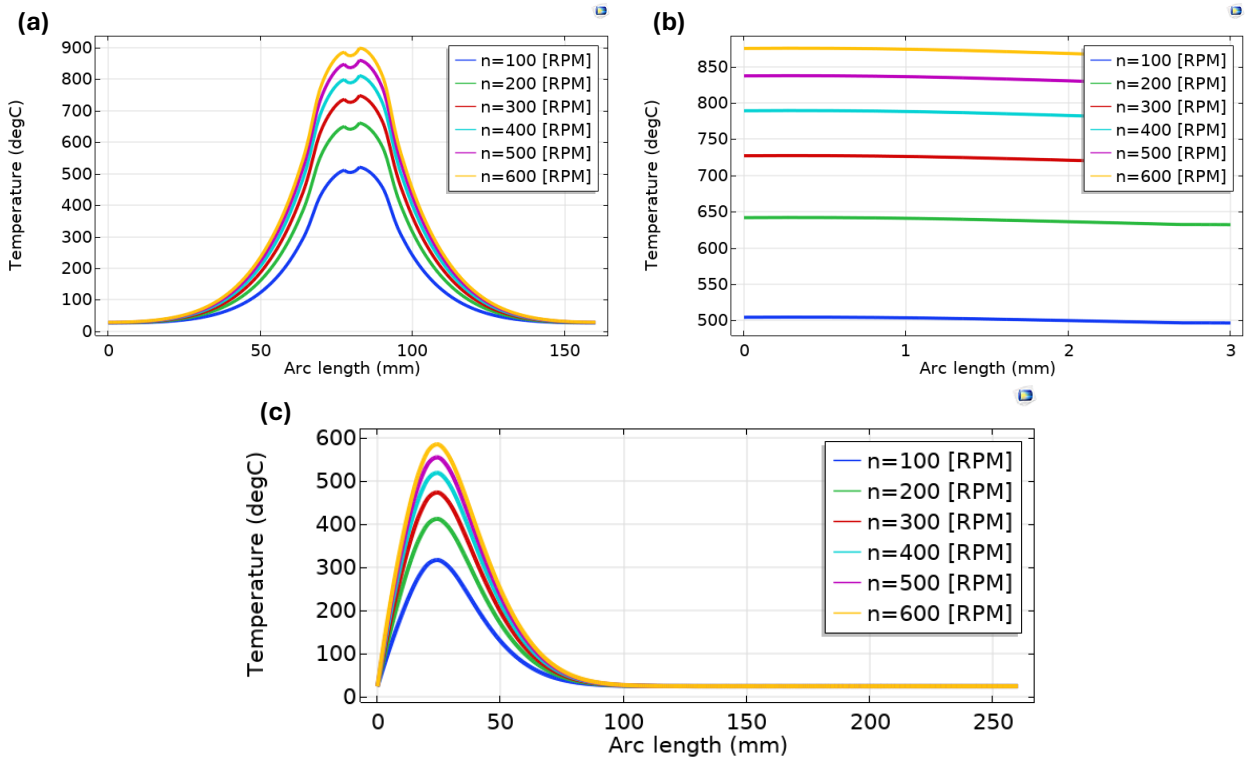

Figure 3-13: Inconel 718 workpiece, parametric analysis on rotational speed. a) 1D temperature profile across the nugget zone, b) 1D temperature profile across the plate thickness, c) 1D temperature profile at 15 mm from the welding line

Figure 3-14 provides a detailed analysis of the effect of varying rotational speed on average grain size, microhardness, and von Mises stress distribution. Subplots (a) and (b) illustrate that the average grain size increases with increasing rotational speed, peaking around 34 μm at 600 RPM, while finer grains are recorded as small as 2.5 μm at 100 RPM. Furthermore, grain size reaches about 3.4 μm at 15 mm from the welding centerline at 600 RPM, while the lowest recorded grain size is less than 0.01 μm at 100 RPM. Subplots (c) and (d) show that hardness is highest in the welding region, peaking at approximately 418 at rotational speed higher than 200 RPM, while at 15 mm from the welding centerline, it shows a gradient from 405 at 600 RPM, with values decreasing to 340 at 100 RPM. Subplots (e) and (f) depict von Mises stress, which peaks at about 1100 MPa at the tool's center and around 550 MPa at 15 mm from the centerline at higher rotational speed, with stress values decreasing and spreading out as rotational speed decreases.

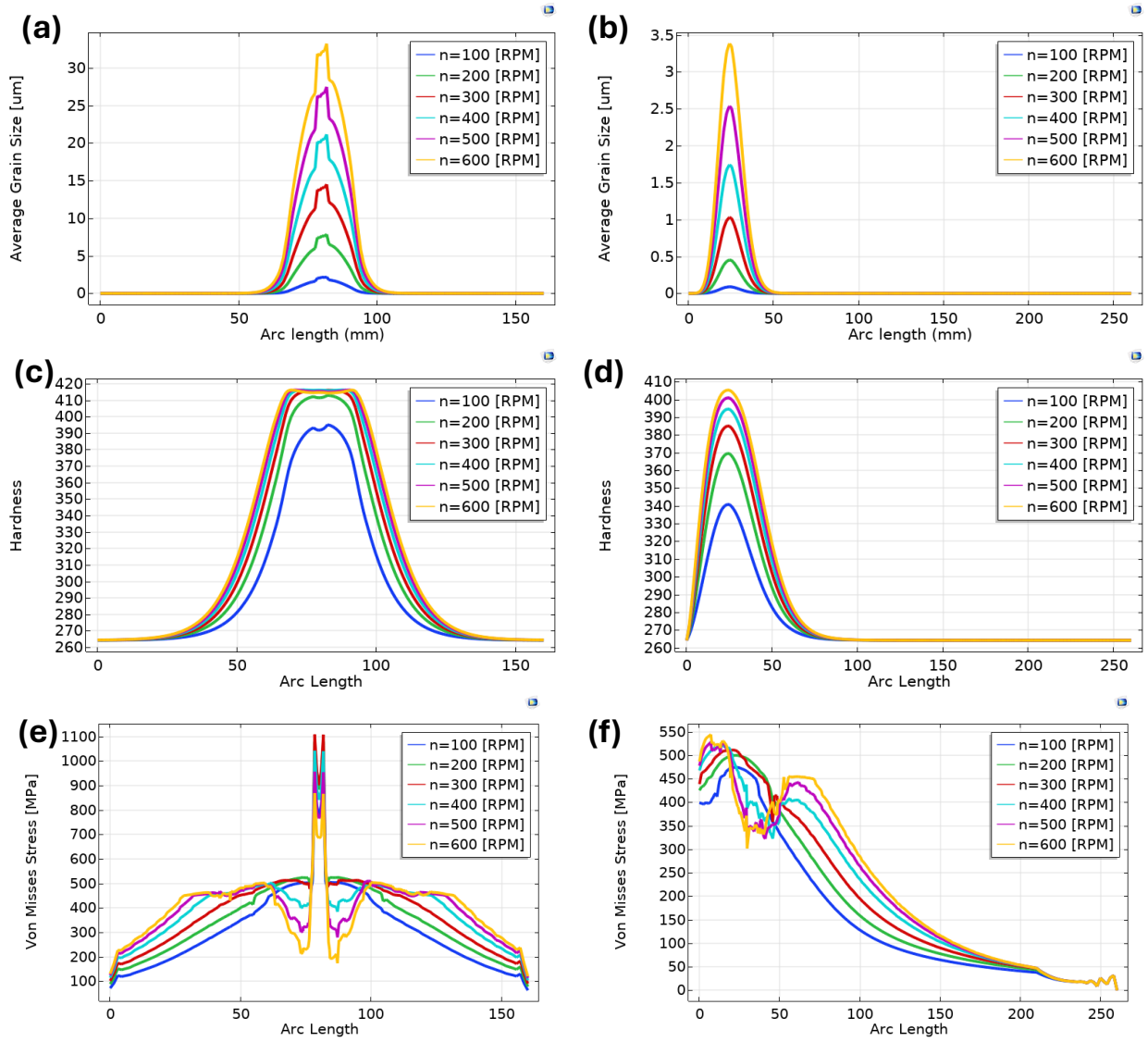

Figure 3-14: Inconel 718 workpiece, parametric analysis on rotational speed, a) 1D avg grain size across the nugget zone, b) 1D avg grain size at 15mm from welding centerline, c) 1D hardness across the nugget zone, d) 1D hardness at 15mm from welding centerline, e) 1D von mises stress across the nugget zone, f) 1D von mises stress at 15mm from welding centerline.

3.3.1.3. Welding Speed

The FSW process parameters used in this study are a 300 RPM rotational speed, a 40-160 mm/min welding speed, a 35 kN axial force, a 25 mm shoulder diameter, and a 5 mm pin diameter, without any cooling effect or preheating. Figure 3-15 reflects a parametric analysis of the FSW of Inconel 718 Alloy, focusing on the temperature profiles under varying welding speeds (u ranging from 40 mm/min to 160 mm/min). Subplot (a) displays

the 1D temperature profile across the nugget zone, showing that the temperature peaks at 800°C at all welding speeds with a slight cooling effect as the welding speed increases. This is further confirmed by Subplots (b) and (c), which show only a 30°C difference when increasing the welding speed from 40 mm/min to 160 mm/min, confirming that welding speed has a minimal effect on the thermal profile of the FSW of Inconel 718, unlike axial force and rotational speed.

Like the thermal profile, the average grain size, microhardness, and stress evolution showed minimal change with varying welding speed (see Figure 3-16). The average grain size ranges between 18 µm and 20 µm in the nugget zone, with finer grains at higher welding speeds. Hardness stabilized at 415 at all welding speeds, peaking in the welding zone. Finally, the von Mises stresses are around 1000 MPa in the nugget zone.

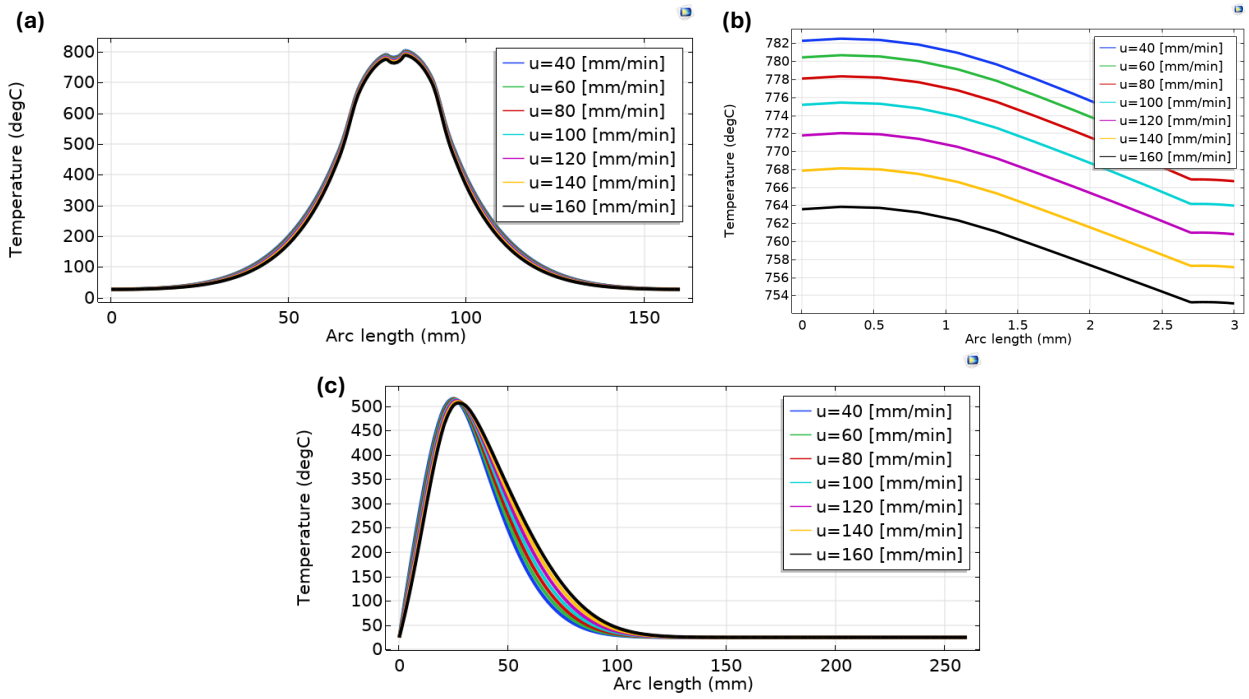

Figure 3-15: Inconel 718 workpiece, parametric analysis on welding speed. a) 1D temperature profile across the nugget zone, b) 1D temperature profile across the plate thickness, c) 1D temperature profile at 15 mm from the welding line

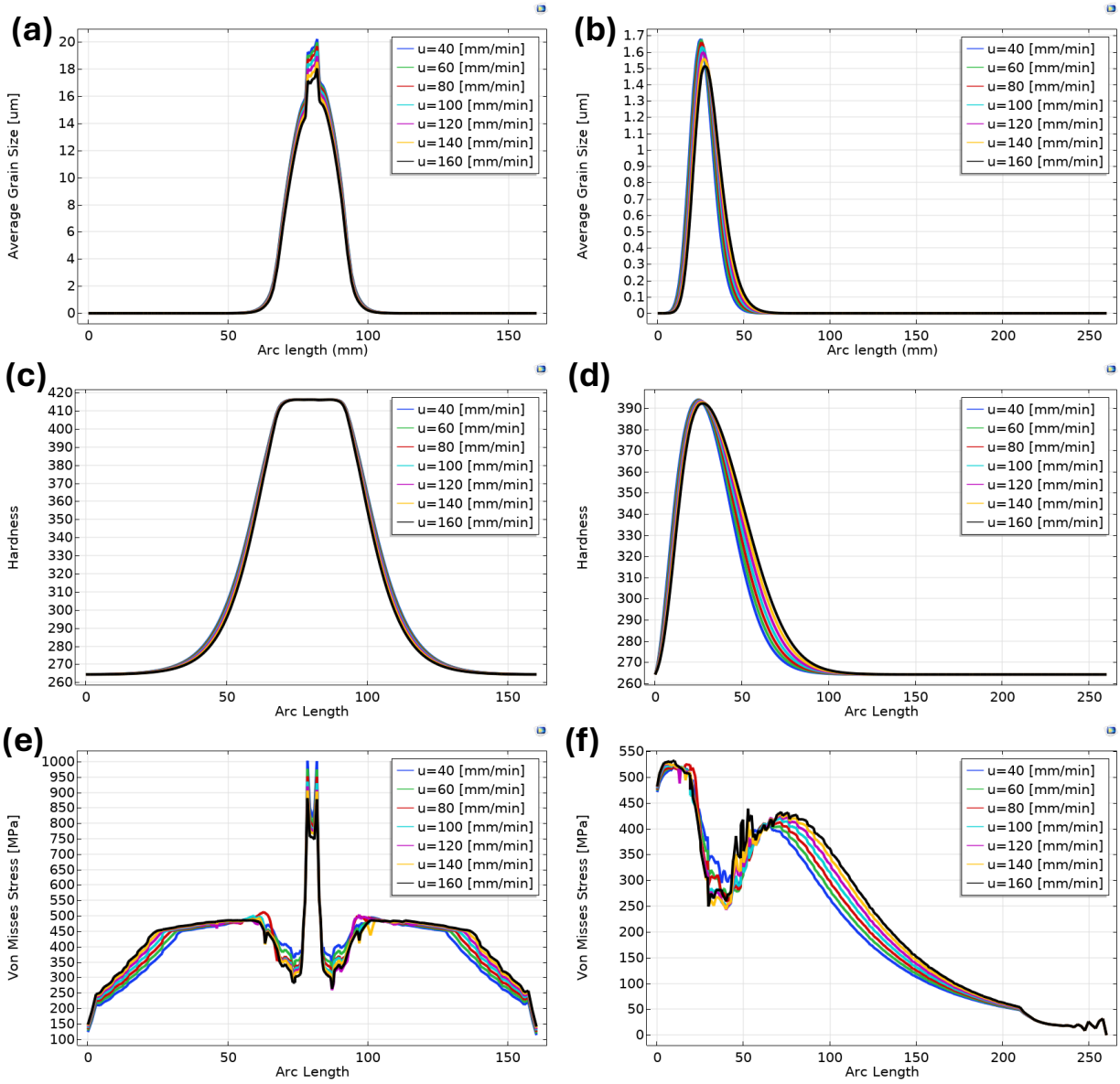

Figure 3-16: Inconel 718 workpiece, parametric analysis on welding speed, a) 1D avg grain size across the nugget zone, b) 1D avg grain size at 15mm from welding centerline, c) 1D hardness across the nugget zone, d) 1D hardness at 15mm from welding centerline, e) 1D von mises stress across the nugget zone, f) 1D von mises stress at 15mm from welding centerline.

3.3.1.4. Shoulder Diameter

The FSW process parameters used in this study are a 350 RPM rotational speed, a 90 mm/min welding speed, a 25 kN axial force, a 15-25 mm shoulder diameter, and a 5 mm pin diameter, without any cooling effect or preheating. Figure 3-17 presents a parametric analysis of the FSW of Inconel 718 Alloy, focusing on the temperature profiles under

varying shoulder diameters (ranging from 15 mm to 25 mm). Subplot (a) displays the 1D temperature profile across the nugget zone, showing that the temperature peaks decrease slightly with larger diameters at the nugget zone. For instance, at 15 mm, the peak temperature reaches approximately 820°C around the central region (75-80 mm), while at 25 mm, it peaks around 750°C. Subplot (b) illustrates the 1D temperature profile across the plate thickness, where a lower shoulder diameter consistently results in higher temperature gradients and better heat dissipation across the plate thickness, with the 15 mm diameter showing a temperature gradient of about 55°C, while the 25 mm diameter shows a gradient of around 12°C. Subplot (c) shows the 1D temperature profile 15 mm from the welding line, indicating that a lower shoulder diameter leads to better heat dissipation and lower peak temperatures at this distance, with the 25 mm diameter peaking at about 485°C around a 25 mm length and the 15 mm diameter peaking around 375°C. These profiles underscore the significant influence of shoulder diameter on the thermal behavior during the FSW process.

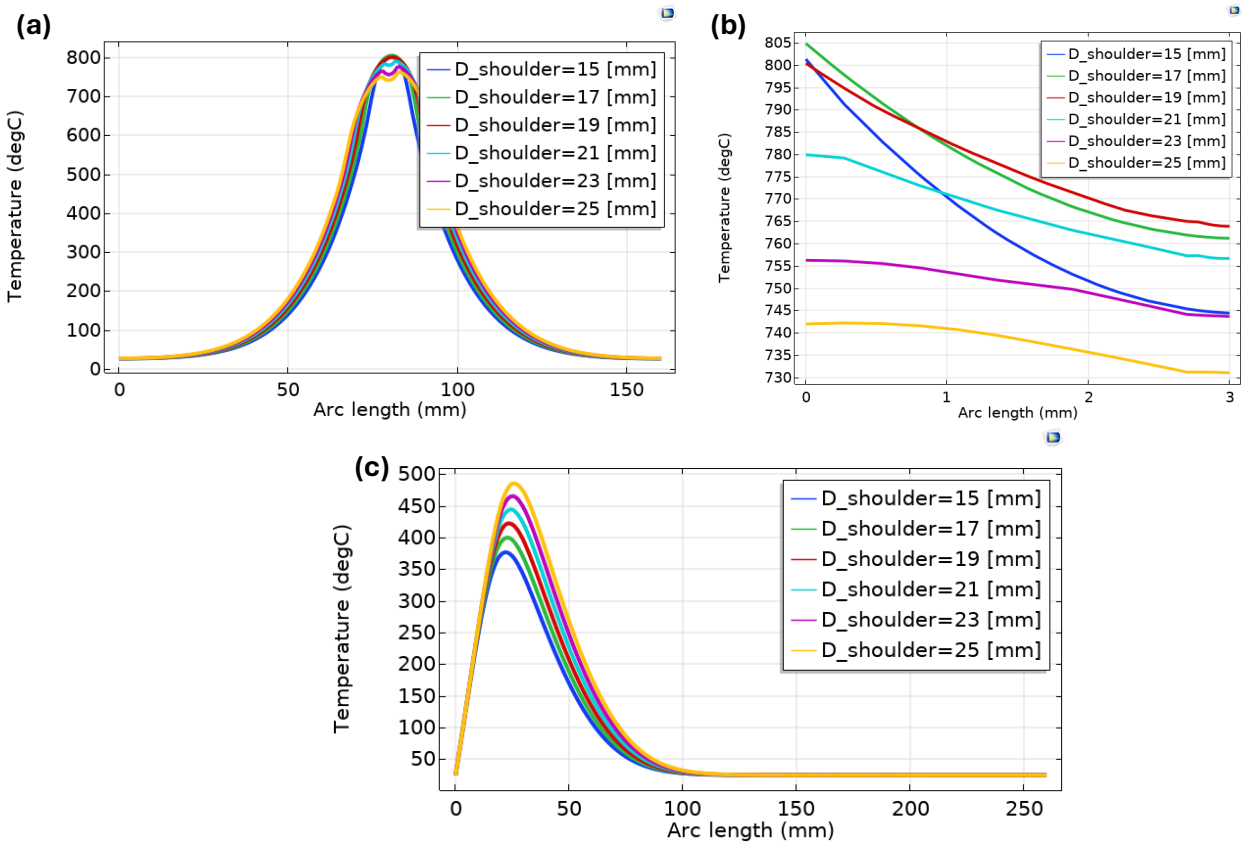

Figure 3-17: Inconel 718 workpiece, parametric analysis on shoulder diameter. a) 1D temperature profile across the nugget zone, b) 1D temperature profile across the plate thickness, c) 1D temperature profile at 15 mm from the welding line

Figure 3-18 provides a detailed analysis of the effect of varying shoulder diameter on average grain size, microhardness, and von Mises stress distribution. Subplots (a) and (b) illustrate that the average grain size at different shoulder diameter, peaking around 20 µm at 21 mm diameter, while finer grains are recorded as small as 16 µm at 25 mm diameter. Furthermore, grain size reaches about 1.2 µm at 15 mm from the welding centerline at 25 mm diameter, while the lowest recorded grain size is less than 0.3 µm at 15 mm diameter. Subplots (c) and (d) show that hardness is highest in the welding region, peaking at approximately 416 at all shoulder diameters, while at 15 mm from the welding centerline, it shows a gradient from 388 at 25 mm diameter, with values decreasing to 360 at 15 mm diameter. Subplots (e) and (f) depict von Mises stress, which peaks at about 1300 MPa at the tool's center at 21 mm diameter and around 520 MPa at 15 mm from the centerline at

higher shoulder diameter, with stress values decreasing and spreading out as shoulder diameter decreases.

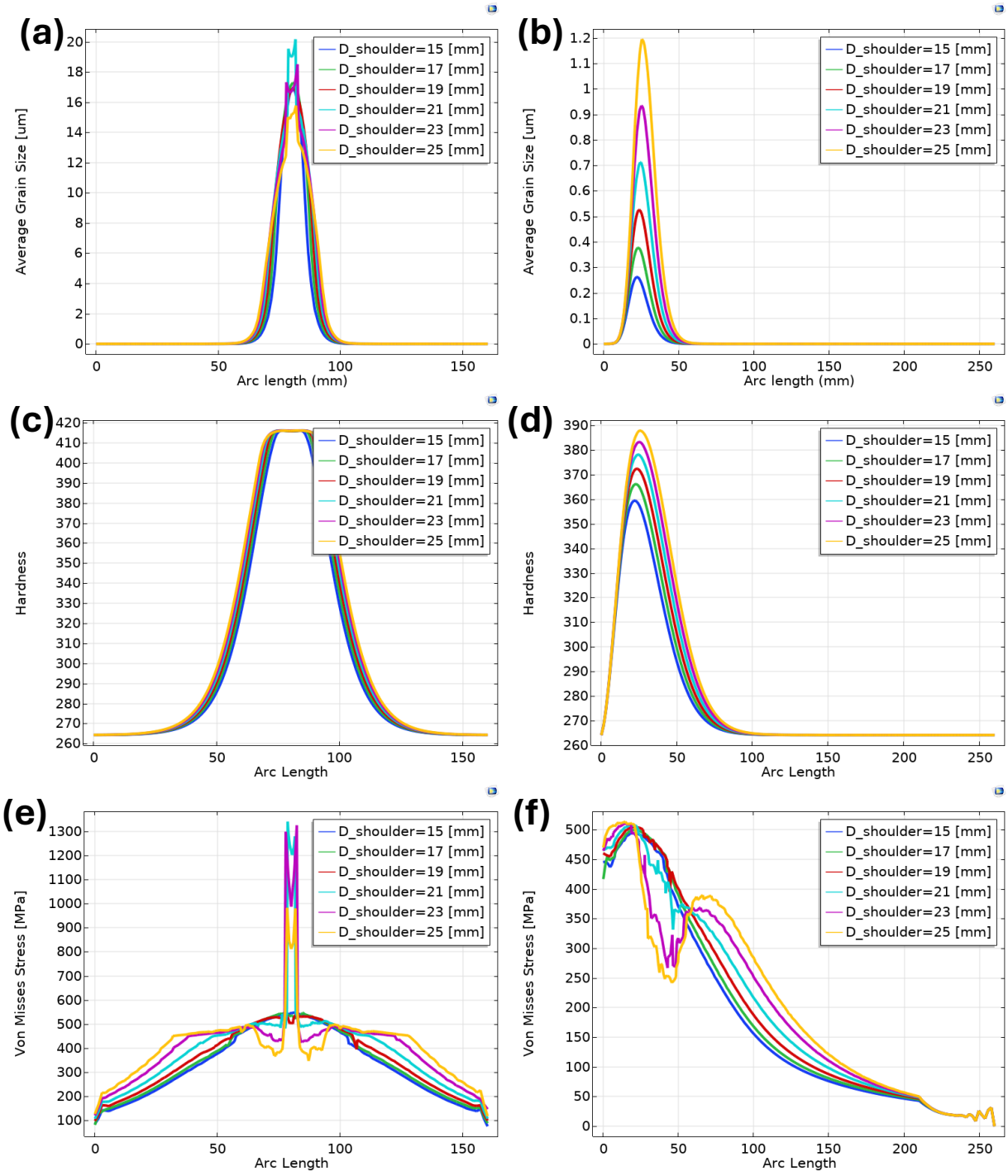

Figure 3-18: Inconel 718 workpiece, parametric analysis on shoulder diameter, a) 1D avg grain size across the nugget zone, b) 1D avg grain size at 15mm from welding centerline, c) 1D hardness across the nugget

zone, d) 1D hardness at 15mm from welding centerline, e) 1D von mises stress across the nugget zone, f) 1D von mises stress at 15mm from welding centerline.

3.3.1.5. Pin Diameter

The FSW process parameters used in this study are a 450 RPM rotational speed, a 125 mm/min welding speed, a 37 kN axial force, a 25 mm shoulder diameter, and a 4-8 mm pin diameter, without any cooling effect or preheating. Figure 3-19 presents a parametric analysis of the FSW of Inconel 718 Alloy, focusing on the temperature profiles under varying pin diameters (ranging from 4 mm to 8 mm). Subplot (a) displays the 1D temperature profile across the nugget zone, showing that the temperature peaks stabilize at the nugget zone at 900°C. Subplot (b) illustrates the 1D temperature profile across the plate thickness, where a lower pin diameter consistently results in higher temperature gradients and better heat dissipation across the plate thickness, with the 4 mm diameter showing a temperature gradient of about 16°C, while the 8 mm diameter shows a gradient of around 8°C. Subplot (c) shows the 1D temperature profile 15 mm from the welding line, indicating a peak temperature of 590°C at all pin diameters. These profiles underscore the weak influence of pin diameter on the thermal behavior during the FSW process.

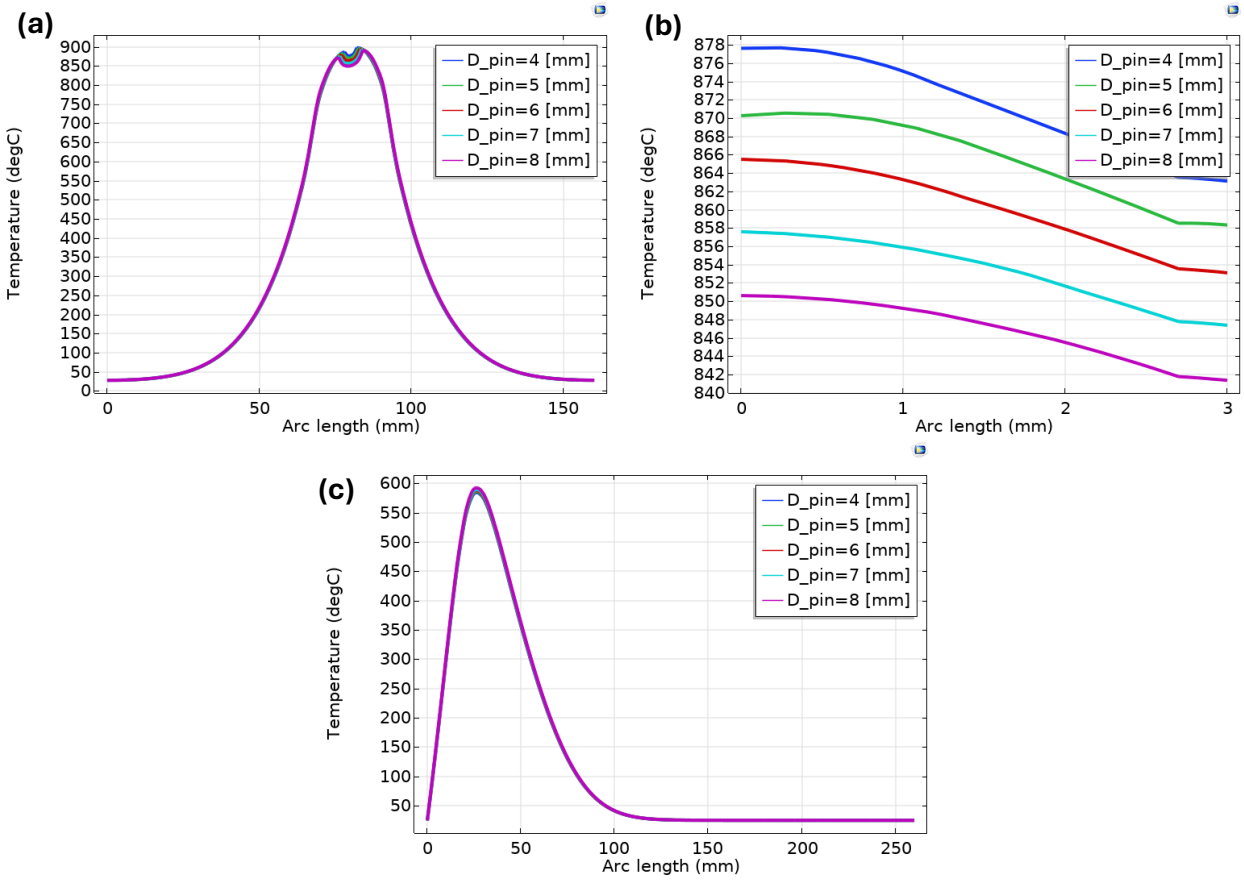

Figure 3-19: Inconel 718 workpiece, parametric analysis on pin diameter. a) 1D temperature profile across the nugget zone, b) 1D temperature profile across the plate thickness, c) 1D temperature profile at 15 mm from the welding line

Figure 3-20 provides a detailed analysis of the effect of varying pin diameter on average grain size, microhardness, and von Mises stress distribution. Subplots (a) and (b) illustrate that the average grain size at different pin diameter, peaking around 36 µm at 4 mm diameter, while finer grains are recorded as small as 28 µm at 8 mm diameter. Furthermore, grain size reaches about 3.6 µm at 15 mm from the welding centerline at all pin diameters. Subplots (c) and (d) show that hardness is highest in the welding region, peaking at approximately 414 at all pin diameters, while at 15 mm from the welding centerline, it stabilizes at 405. Subplots (e) and (f) depict von Mises stress, which peaks at about 1400 MPa at the tool's center at 4 mm pin diameter and around 555 MPa at 15 mm from the centerline at all pin diameters. It could be concluded from the above that the pin diameter has a minimal effect on the friction stir welding efficiency.

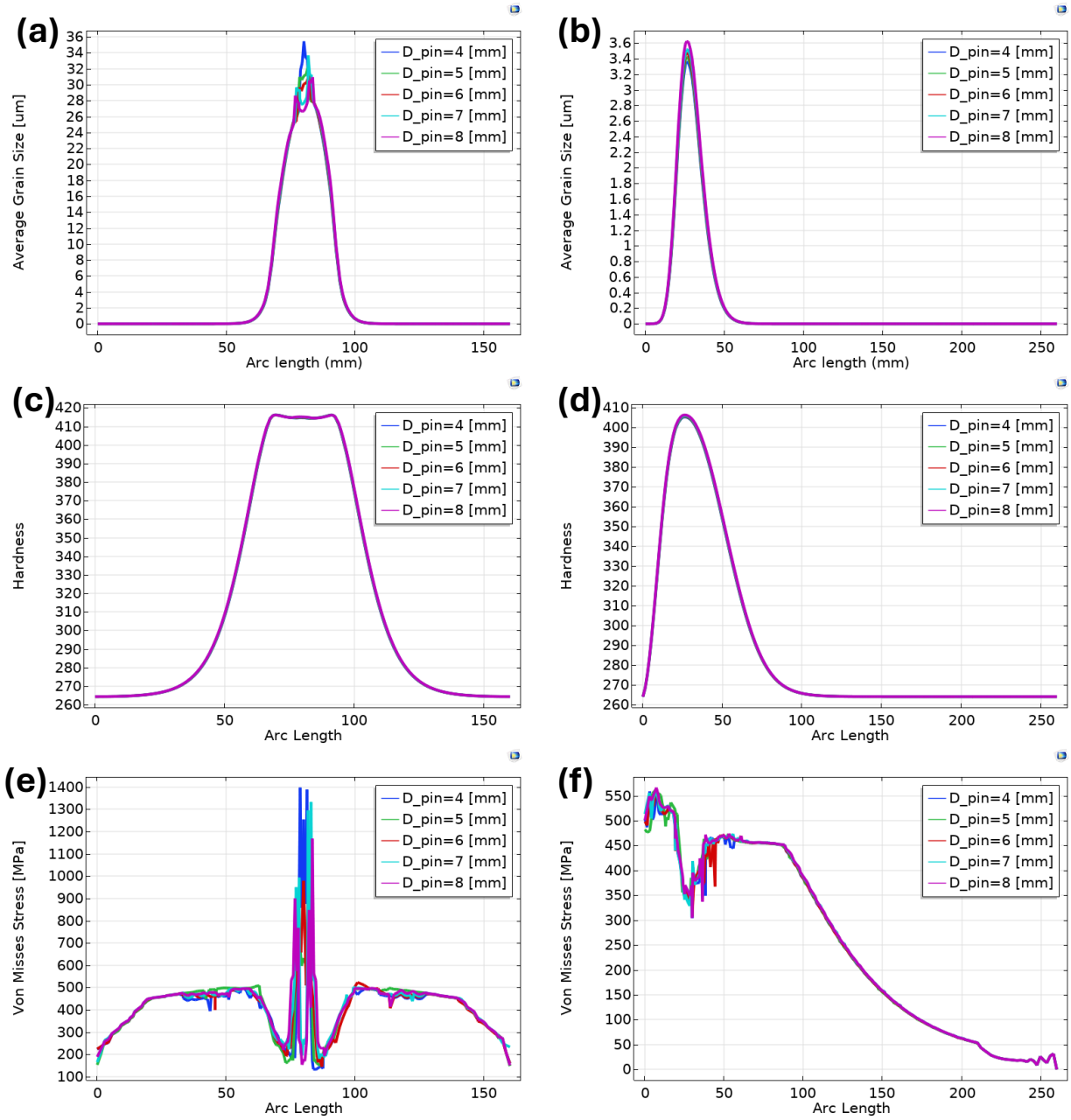

Figure 3-20: Inconel 718 workpiece, parametric analysis on pin diameter, a) 1D avg grain size across the nugget zone, b) 1D avg grain size at 15mm from welding centerline, c) 1D hardness across the nugget zone, d) 1D hardness at 15mm from welding centerline, e) 1D von mises stress across the nugget zone, f) 1D von mises stress at 15mm from welding centerline

3.3.1.6. Cooling-FSW

The FSW process parameters used in this study are a 600 RPM rotational speed, a 90 mm/min welding speed, a 35 kN axial force, a 25 mm shoulder diameter, and a 5 mm pin diameter, with active cooling effect and without preheating. Figure 3-21 presents a parametric analysis of the FSW of Inconel 718 Alloy, focusing on the temperature profiles under varying cooling water velocity (V ranging from 0.1 m/s – 1.1 m/s). Subplot (a) displays the 1D temperature profile across the nugget zone, showing that the temperature peaks decrease with higher cooling water velocity. For instance, at 0.1 m/s, the peak temperature reaches approximately 850°C around the central region (75-80 mm), while at 1.1 m/s, it peaks around 680°C. Subplot (b) illustrates the 1D temperature profile across the plate thickness, where with active cooling a constant temperature profile across the thickness was detected due to the efficient heat dissipation. Subplot (c) shows the 1D temperature profile 15 mm from the welding line, indicating that higher cooling velocity led to lower temperatures at this distance as well, with 0.1 m/s peaking at about 555°C around 25 mm length and 1.1 m/s peaking around 450°C. These profiles underscore the significant influence of active cooling on the thermal behavior during the FSW process.

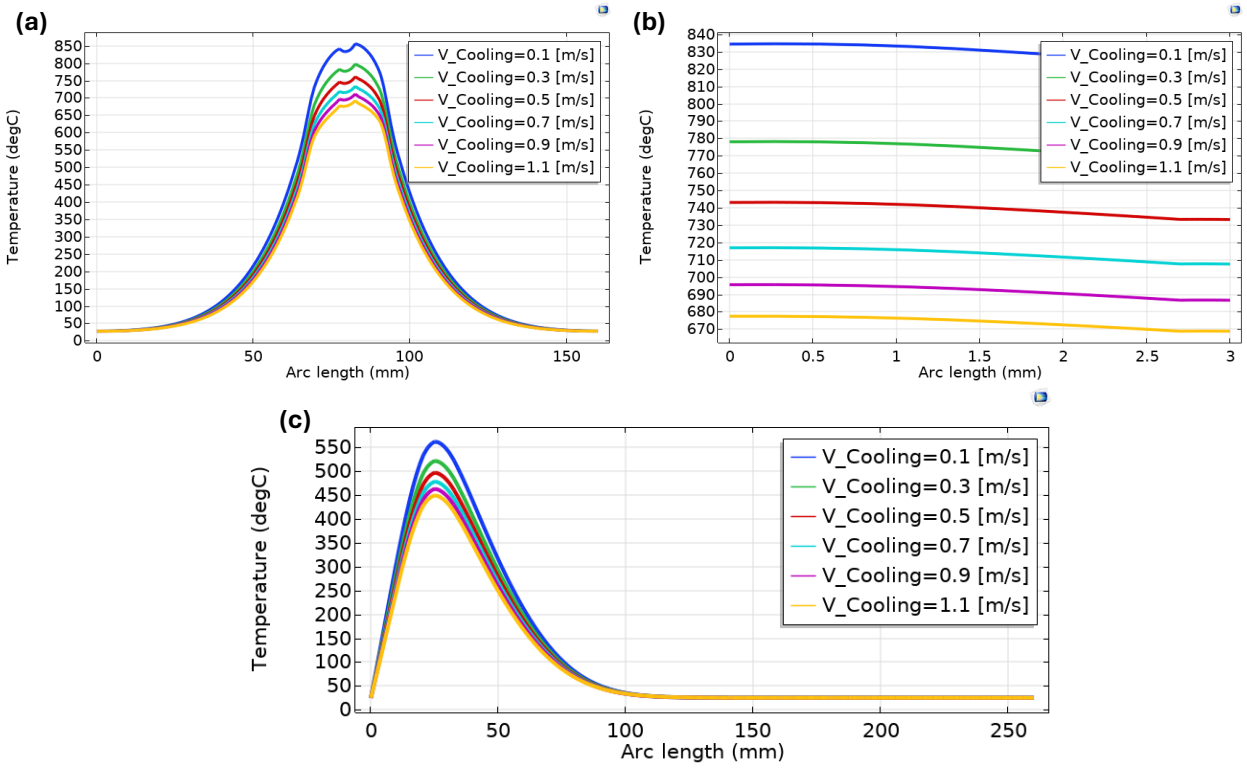

Figure 3-21: Inconel 718 workpiece, parametric analysis on cooling water velocity. a) 1D temperature profile across the nugget zone, b) 1D temperature profile across the plate thickness, c) 1D temperature profile at 15 mm from the welding line

Figure 3-22 provides a detailed analysis of the effect of varying cooling water velocity on average grain size, microhardness, and von Mises stress distribution. Subplots (a) and (b) illustrate that the average grain size decreases with increasing cooling velocity, peaking around 26 µm at 0.1 m/s, while finer grains are recorded as small as 10 µm at 1.1 m/s. Furthermore, grain size reaches about 2.7 µm at 15 mm from the welding centerline at 0.1 m/s, while the lowest recorded grain size is at 0.78 µm at 1.1 m/s. Subplots (c) and (d) show that hardness is highest in the welding region, peaking at approximately 415 at all cooling water velocities, while at 15 mm from the welding centerline, it shows a gradient from 400 at 0.1 m/s, with values decreasing to 380 at 1.1 m/s. Subplots (e) and (f) depict von Mises stress, which peaks at about 1000 MPa at the tool's center and around 550 MPa at 15 mm from the centerline at lower cooling velocities, with stress values decreasing and spreading out as cooling velocity increases as confirmed at 1.1 m/s.

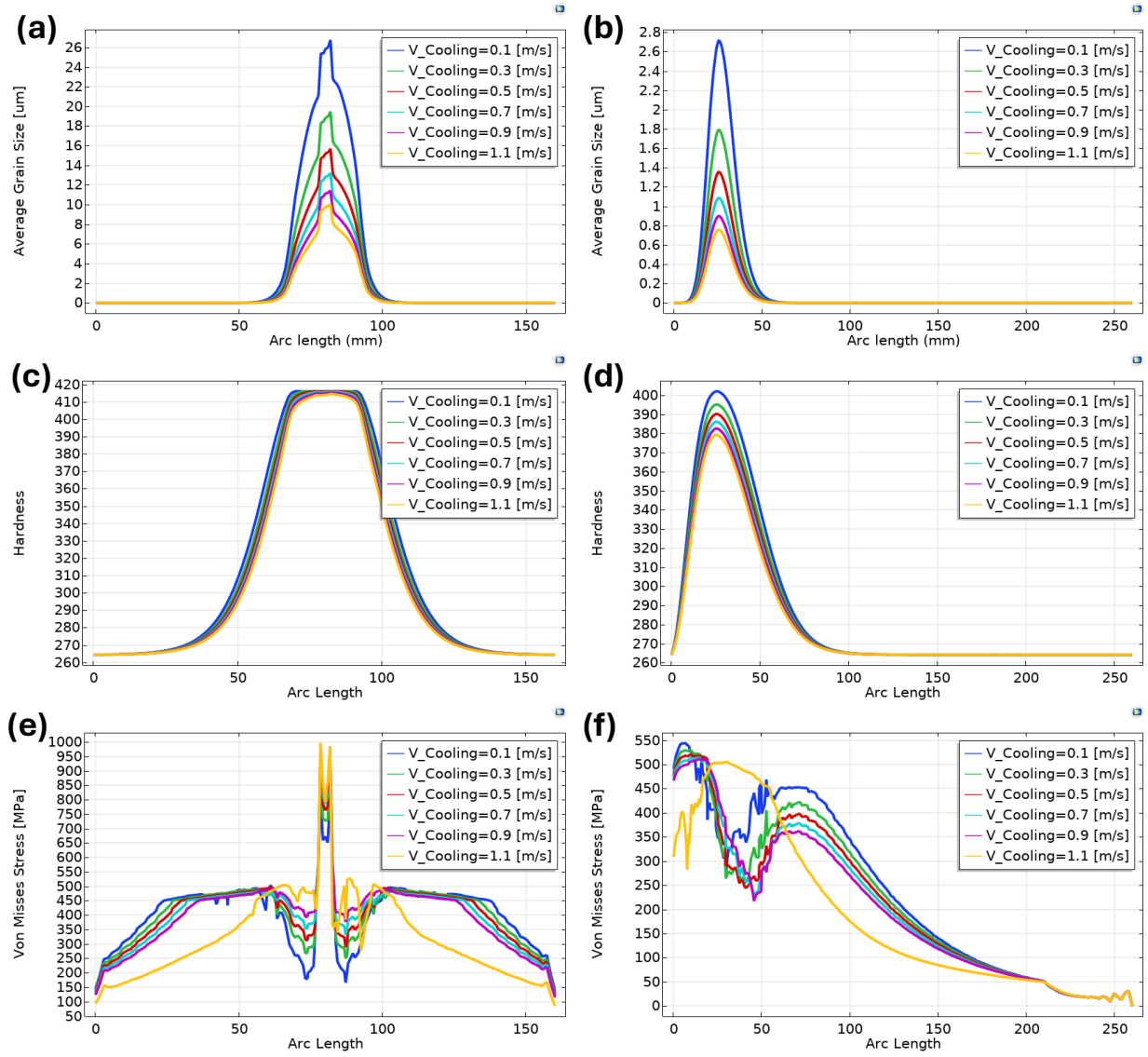

Figure 3-22: Inconel 718 workpiece, parametric analysis on cooling water velocity, a) 1D avg grain size across the nugget zone, b) 1D avg grain size at 15mm from welding centerline, c) 1D hardness across the nugget zone, d) 1D hardness at 15mm from welding centerline, e) 1D von mises stress across the nugget zone, f) 1D von mises stress at 15mm from welding centerline.

The FSW process parameters used in this study are a 600 RPM rotational speed, a 90 mm/min welding speed, a 35 kN axial force, a 25 mm shoulder diameter, and a 5 mm pin diameter, with active cooling effect and without preheating. Figure 3-23 presents a parametric analysis of the FSW of Inconel 718 Alloy, focusing on the temperature profiles under varying cooling water hose diameter (D_hose ranging from 0.2 inch – 1 inch). Subplot (a) displays the 1D temperature profile across the tool, showing that the

temperature peaks decrease with lower hose diameters. For instance, at 1 inch, the peak temperature reaches approximately 820°C, while at 0.2 inch, it peaks around 725°C. Subplot (b) illustrates the 1D temperature profile across the plate thickness, where with active cooling a constant temperature profile across the thickness was detected due to the efficient heat dissipation with nearly 10°C across the plate thickness. Subplot (c) shows the 1D temperature profile 15 mm from the welding line, indicating that lower hose diameter led to lower temperatures at this distance as well, with 1 inch peaking at about 530°C, while at 0.2 inch it is peaking around 480°C.

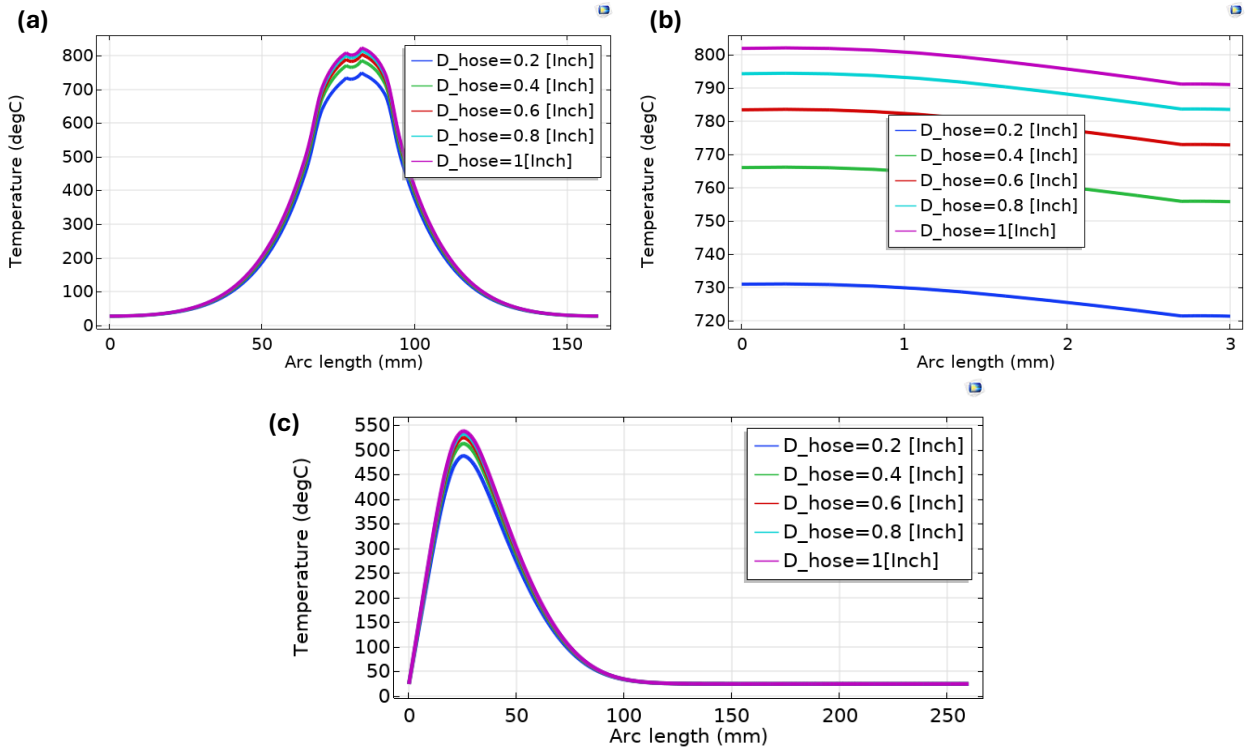

Figure 3-23: Inconel 718 workpiece, parametric analysis on cooling water hose diameter. a) 1D temperature profile across the nugget zone, b) 1D temperature profile across the plate thickness, c) 1D temperature profile at 15 mm from the welding line

Figure 3-24 provides a detailed analysis of the effect of varying cooling water velocity on average grain size, microhardness, and von Mises stress distribution. Subplots (a) and (b) illustrate that the average grain size increases with increasing cooling hose diameter, peaking around 22 µm at 1 inch, while finer grains are recorded as small as 14 µm at 0.2

inch. Furthermore, grain size reaches about 2.2 µm at 15 mm from the welding centerline at D_hose of 1 inch, while the lowest recorded grain size is at 1.2 µm at 0.2 inch. Subplots (c) and (d) show that hardness is highest in the welding region, peaking at approximately 416 at all diameters, while at 15 mm from the welding centerline, it shows a gradient from 400 at 1 inch, with values decreasing to 383 at 0.2 inch. Subplots (e) and (f) depict von Mises stress, which peaks at about 920 MPa at the tool's center and around 530 MPa at 15 mm from the centerline.

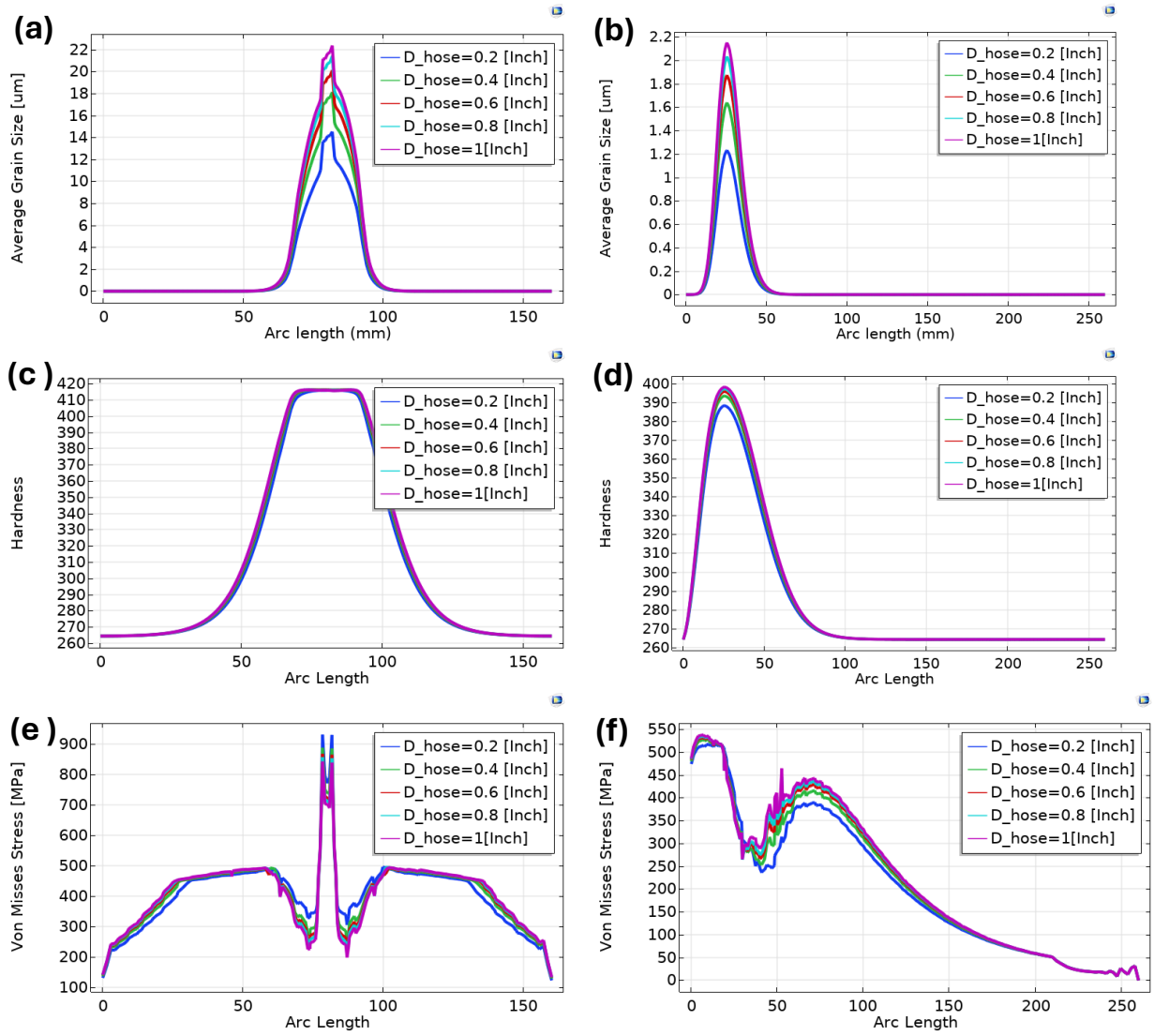

Figure 3-24: Inconel 718 workpiece, parametric analysis on cooling water hose diameter, a) 1D avg grain size across the nugget zone, b) 1D avg grain size at 15mm from welding centerline, c) 1D hardness across the nugget zone, d) 1D hardness at 15mm from welding centerline, e) 1D von mises stress across the nugget zone, f) 1D von mises stress at 15mm from welding centerline.

3.3.1.7. Induction Preheating

The FSW process parameters used in this study are a 300 RPM rotational speed, a 130 mm/min welding speed, a 20 kN axial force, a 25 mm shoulder diameter, and a 5 mm pin diameter, without any cooling effect and with induction preheating. Figure 3-25 reflects a parametric analysis of the FSW of Inconel 718 Alloy, focusing on the temperature profiles under varying induction preheating (I-FSW ranging from 0.5 kW – 2.5 kW). Subplot (a) displays the 1D temperature profile across the nugget zone, showing that the temperature peaks decrease with lower preheating. For instance, at 2.5 kW, the peak temperature reaches approximately 790°C around the nugget zone, while at 0.5 kW, it peaks around 700°C. Subplot (b) illustrates the 1D temperature profile across the plate thickness, where with induction preheating a constant temperature profile across the thickness was detected due to the mild process parameters used (relatively lower rotational speed, and lower axial force in addition to the relatively higher welding speed). Subplot (c) shows the 1D temperature profile 15 mm from the welding line, indicating clearly the preheating effect where workpiece temperature starts at 350 °C. the temperature at 2.5 kW peaking at about 550°C around 25 mm length, while at 0.5 inch it is peaking around 475°C. These profiles underscore the significant influence of preheating on the thermal behavior during the FSW process.

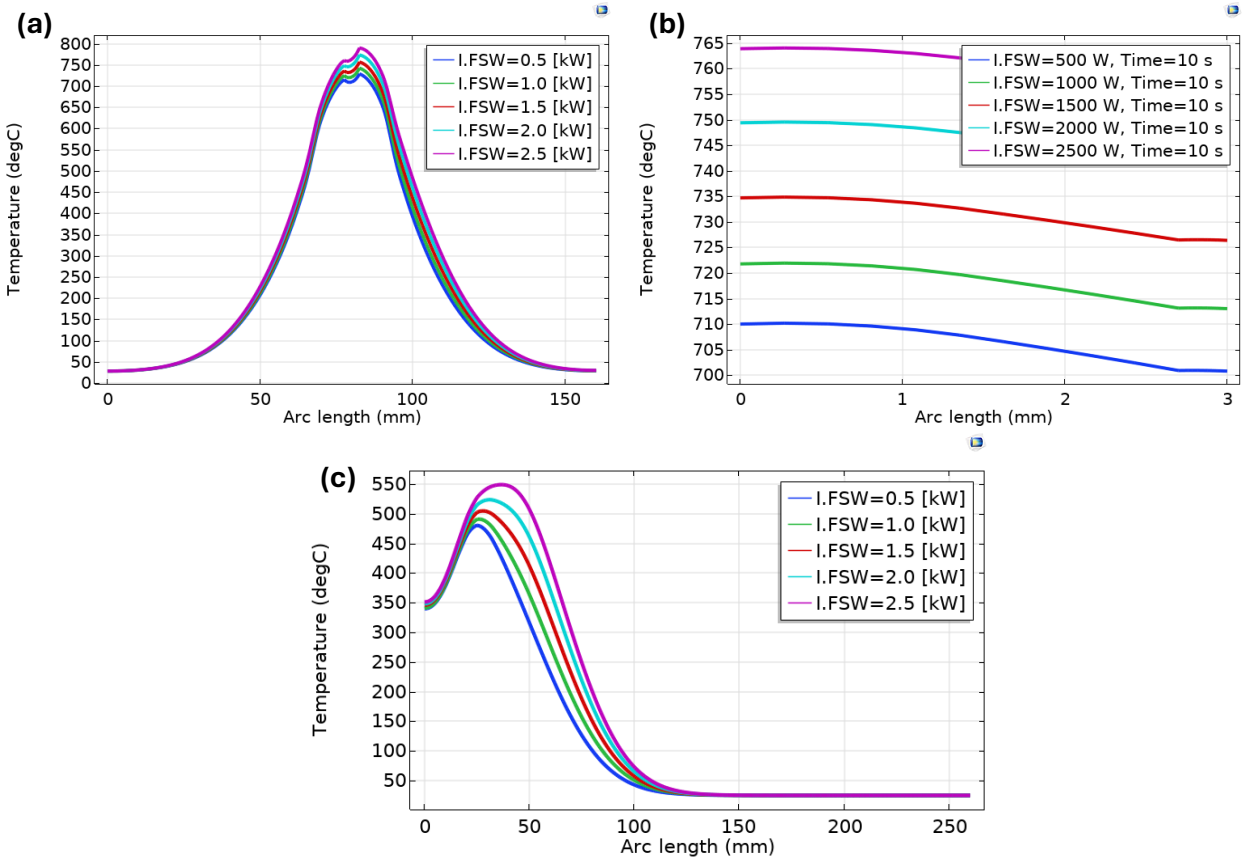

Figure 3-25: Inconel 718 workpiece, parametric analysis on induction preheating. a) 1D temperature profile across the nugget zone, b) 1D temperature profile across the plate thickness, c) 1D temperature profile at 15 mm from the welding line

Figure 3-26 provides a detailed analysis of the effect of varying preheating load on average grain size, microhardness, and von Mises stress distribution. Subplots (a) and (b) illustrate that the average grain size decreases with decreasing preheating load, peaking around 18 µm at 2.5 kW, while finer grains are recorded as small as 12.8 µm at 0.5 kW. Furthermore, grain size reaches about 2.4 µm at 15 mm from the welding centerline at 2.5 kW, while the lowest recorded grain size is at 1.1 µm at 0.5 kW. Subplots (c) and (d) show that hardness is highest in the welding region, peaking at approximately 415 at all preheating loads, while at 15 mm from the welding centerline, it shows a gradient from 400 at 2.5 kW, with values decreasing to 386 at 0.5 inch. Subplots (e) and (f) depict von Mises stress, which peaks at about 1300 MPa at the tool's center at 1.5 kW and around 600 MPa at 15 mm from the centerline at higher preheating loads, with stress values decreasing and spreading out as heating load decreases as confirmed at 1 kW.

It can be concluded that induction preheating has the most significant effect on optimizing the process parameters. It allows for a lower rotational speed and axial force while increasing the welding speed, leading to better heat dissipation, finer grain size, and lower stress evolution.

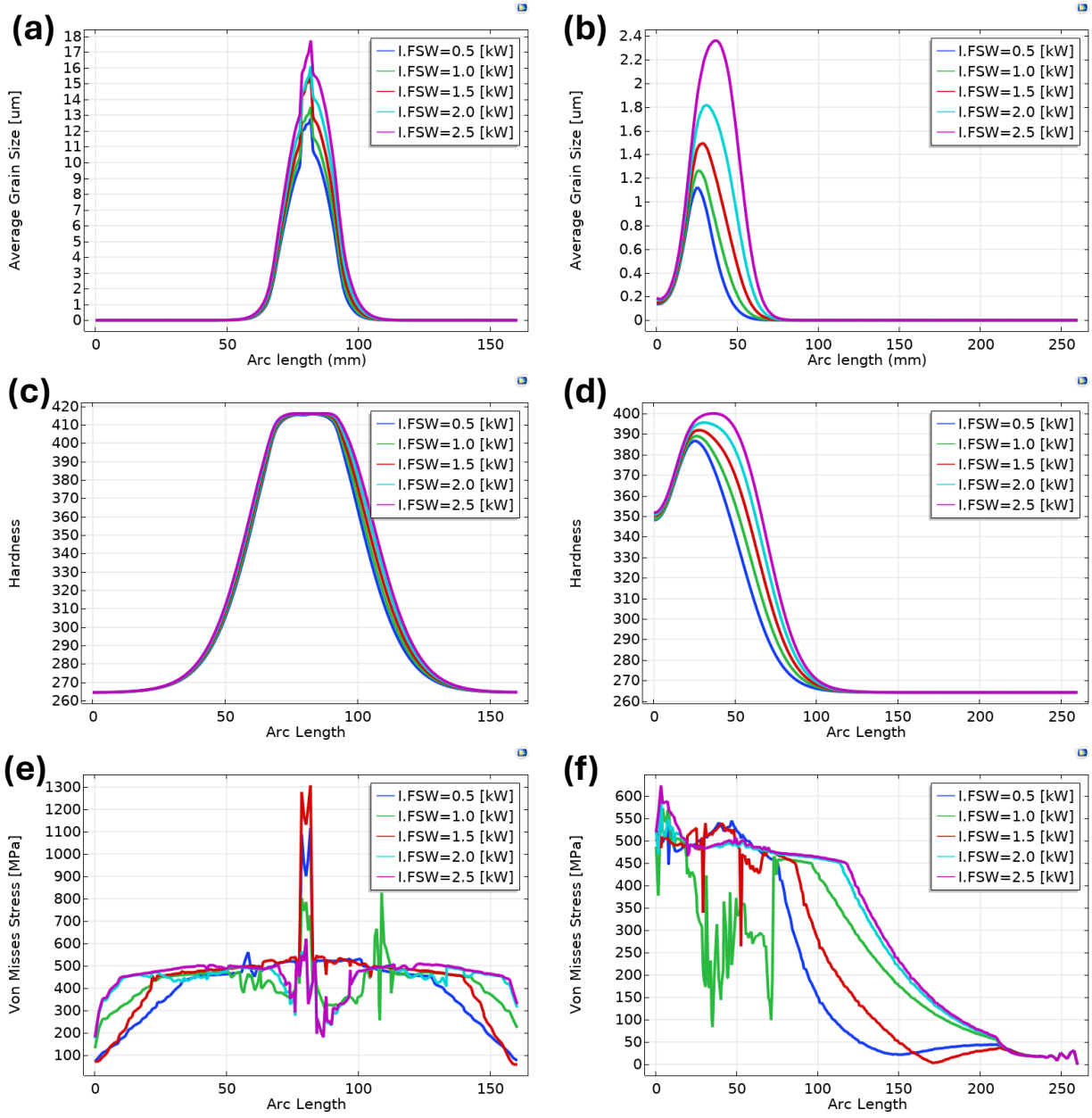

Figure 3-26: Inconel 718 workpiece, parametric analysis on induction preheating, a) 1D avg grain size across the nugget zone, b) 1D avg grain size at 15mm from welding centerline, c) 1D hardness across the nugget zone, d) 1D hardness at 15mm from welding centerline, e) 1D von mises stress across the nugget zone, f) 1D von mises stress at 15mm from welding centerline.

3.4. Results of Statistical Analysis for FSW of Inconel 718

In this section, based on the parametric analysis conducted on Inconel 718, which generated an extensive dataset, Taguchi analysis was used to identify and rank the different process parameters affecting the workpiece temperature. Following this, ANOVA analysis was utilized to understand the interaction effects of the process parameters through analysis of variance. Finally, nonlinear regression was performed to derive an equation relating the workpiece temperature to the most influential parameters, allowing for the prediction of workpiece temperature. Additionally, the post-welding performance parameters (microhardness and average grain size) were connected through equations to predict welding efficiency by measuring the workpiece temperature.

3.4.1. Taguchi Analysis

Figure 3-27 and Table 3-1 show the results of the Taguchi analysis for the friction stir welding of Inconel 718, focusing on the main effects plot for signal-to-noise (SN) ratios with a "smaller is better" criterion for workpiece temperature. The analysis evaluates five process parameters: rotational speed, welding speed, axial force, shoulder diameter, and pin diameter. The results indicate that lower rotational speeds lead to better performance, with the SN ratio decreasing significantly from 100 to 400 RPM and stabilizing thereafter. Higher welding speeds generally result in better outcomes, with the optimal range around 130 mm/min. Lower axial forces, particularly at 5 kN, show a pronounced improvement in the SN ratio, indicating lower temperatures. For shoulder diameter, larger values from 15 to 25 mm show a gradual improvement in performance. Pin diameter analysis reveals an optimal point around 5 mm, after which the SN ratio stabilizes. Overall, to achieve the lowest workpiece temperature, the optimal settings include a lower rotational speed, higher welding speed, lower axial force, larger shoulder diameter, and an optimal pin diameter around 5 mm.

Moreover, Table 3-2 and Figure 3-28 reflect the results of the Taguchi analysis for the FSW of Inconel 718, specifically focusing on the main effects plot for means with a "smaller is better" criterion for workpiece temperature. The analysis evaluates the impact

of the five process parameters mentioned before. The results show that the workpiece temperature increases with higher rotational speeds, peaking at 600 RPM, while it decreases with higher welding speeds, reaching the lowest at 150 mm/min. Lower axial forces, particularly at 5 kN, also result in lower temperatures. Additionally, a slight decrease in temperature is observed with increasing shoulder diameters from 15 to 25 mm. For pin diameter, the temperature decreases initially and then stabilizes, with the lowest temperature at 5 mm. Thus, to minimize the workpiece temperature and improve weld quality, the optimal settings would include a lower rotational speed, higher welding speed, lower axial force, larger shoulder diameter, and an optimal pin diameter.

Finally, it is worth concluding from the Taguchi analysis that the rank of the process parameters affecting the workpiece temperature, in order of significance, is axial force, rotational speed, welding speed, shoulder diameter, and pin diameter.

Level	**Rotational Speed [RPM]**	**Welding Speed [mm/min]**	**Axial Force [kN]**	**Shoulder Diameter [mm]**	**Pin Diameter [mm]**
1	-53.22	-57.16	-51.62	-57.45	-58.16
2	-55.37	-57.14	-53.74	-57.27	-56.67
3	-56.41	-57.13	-54.90	-57.10	-58.19
4	-57.04	-56.47	-55.70	-56.95	-58.20
5	-57.22	-57.10	-56.93	-56.80	-58.22
6	-58.19	-57.07	-56.37	-56.80	
7	-57.76	-58.19	-56.75		
8	-58.61	-57.03	-57.10		
9		-57.00	-58.19		
10			-58.25		
11			-57.74		
12			-57.99		
Delta	5.39	1.72	6.62	0.65	1.55
Rank	2	3	1	5	4

Table 3-1: Response table for signal to noise ratios: smaller is better

Level	Rotational Speed [RPM]	Welding Speed [mm/min]	Axial Force [kN]	Shoulder Diameter [mm]	Pin Diameter [mm]
1	458.3	721.0	381.3	745.6	809.3
2	586.6	719.8	486.2	730.3	690.6
3	671.0	718.3	556.1	716.5	811.7
4	711.6	677.9	609.3	703.8	813.0
5	726.4	716.2	703.1	692.1	814.5
6	811.8	713.7	670.5	702.3	
7	773.1	811.8	688.1		
8	853.2	710.8	715.8		
9		707.5	811.8		
10			820.8		
11			771.2		
12			793.3		
Delta	394.9	133.9	439.5	53.4	123.9
Rank	2	3	1	5	4

Table 3-2: Response table for means

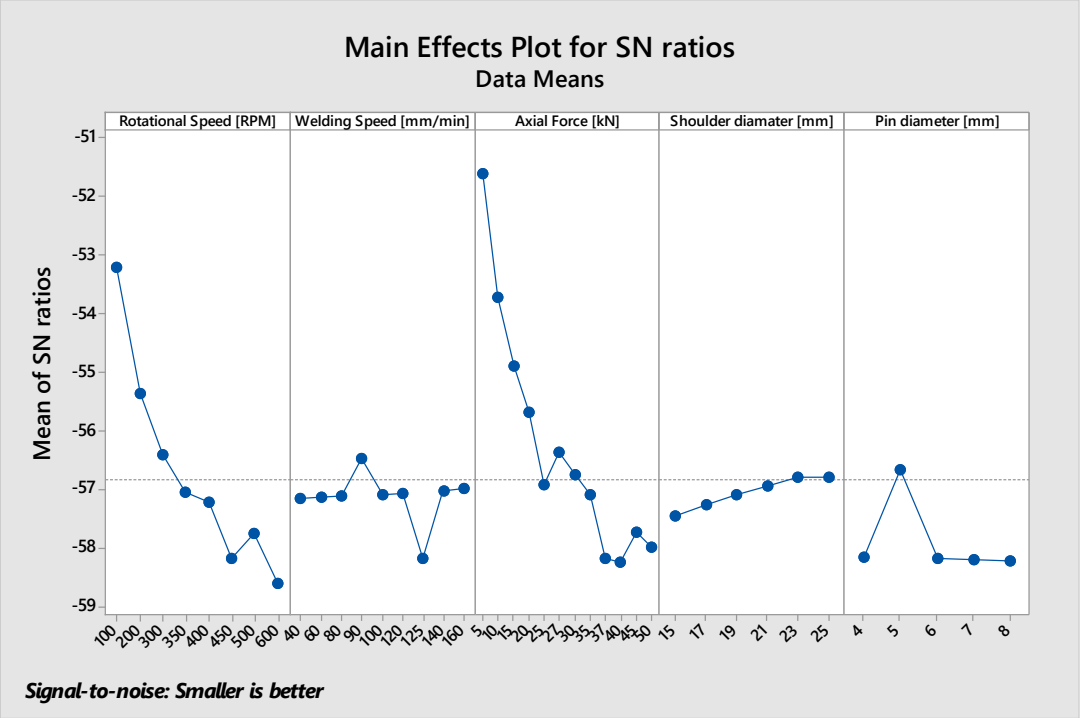

Figure 3-27: Main effects plot for SN ratios

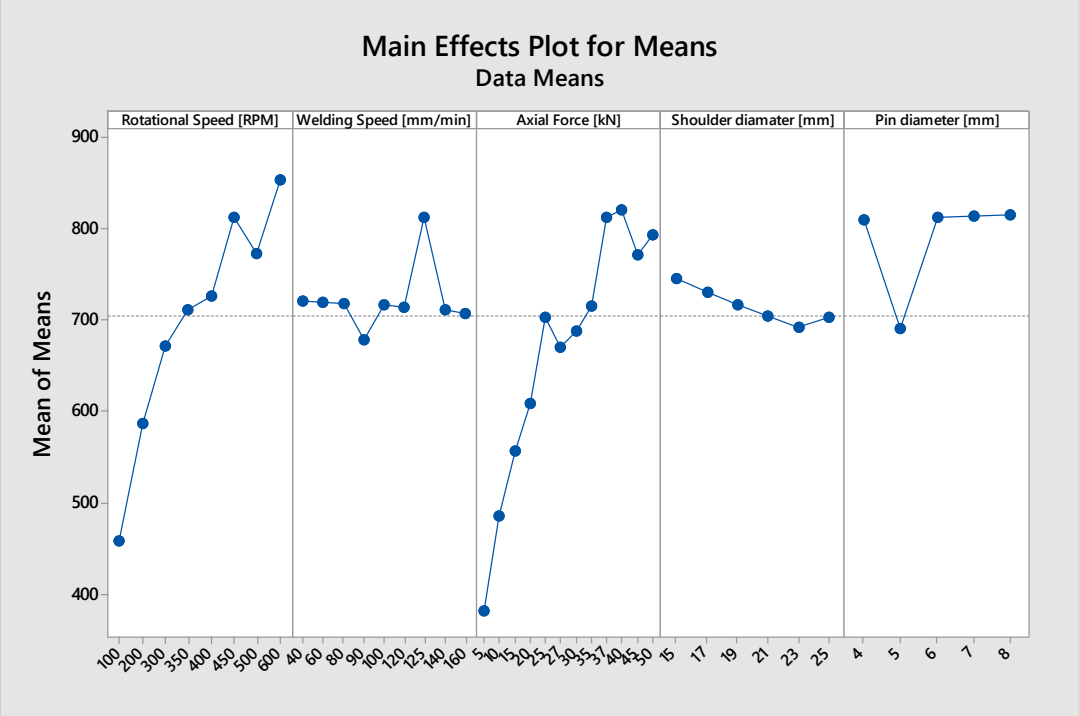

Figure 3-28:Main effects plot for means

3.4.2. One-Way ANOVA

Based on the developed finite element model, and the developed dataset from the parametric analysis while capturing the dynamic behavior of the FSW process. One-way ANOVA was used to understand the effect of these parameters on the workpiece temperature, where the Tukey Simultaneous 95% Confidence Intervals (CIs) graph from the ANOVA results provides insightful comparisons across various parameters of the FSW process (See Figure 3-29, Table 3-3, and Table 3-4). The obtained results reveal significant differences where the CIs do not cross the zero line, highlighting influential relationships between parameters such as welding speed, axial force, and rotational speed. Notably, the significant deviation in axial force across different settings suggests its critical role in influencing material deformation and joint quality during welding. Conversely, the temperature comparisons across multiple parameters (shoulder diameter, pin diameter, welding speed) mostly cross the zero line, indicating no significant differences. This suggests that temperature remains relatively stable across these variables, possibly due to effective thermal management within the tested range. Such findings are crucial for optimizing FSW parameters, where understanding the impact of axial force and rotational speeds could guide adjustments to achieve optimal weld conditions. Meanwhile, the stable temperature response across various settings supports the robustness of the process under the tested conditions.

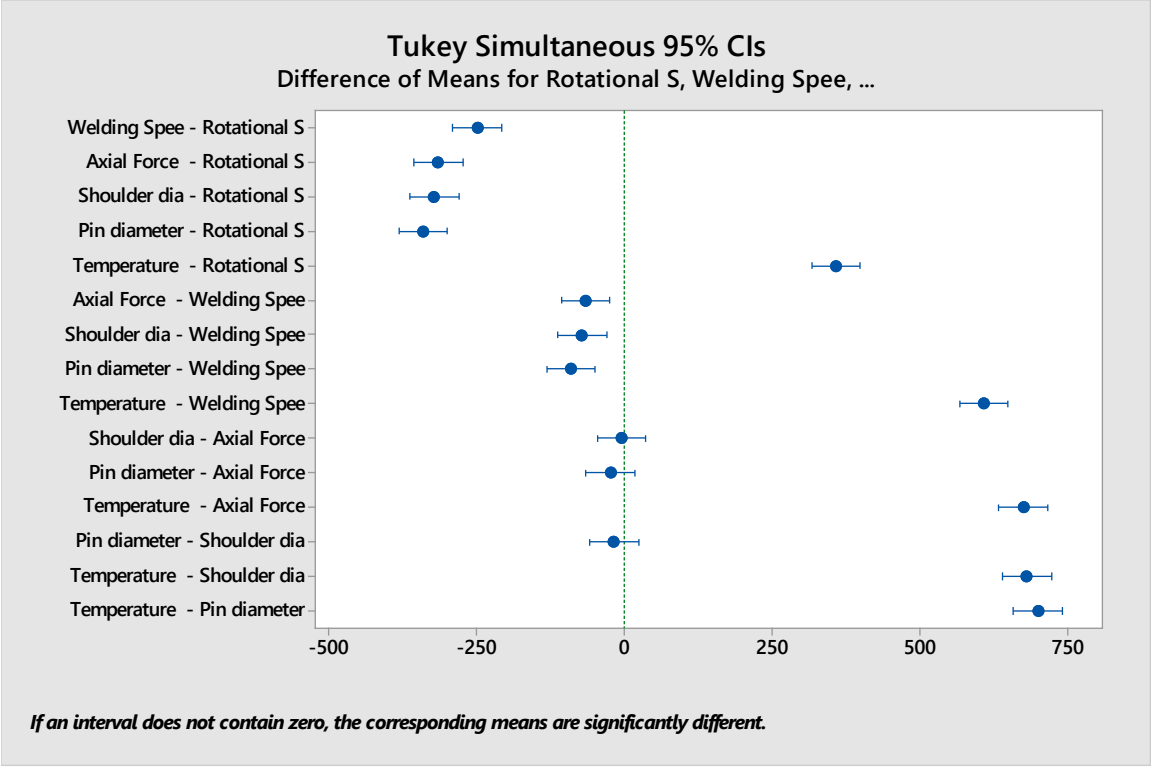

Figure 3-29: ANOVA Tukey box plot

Source	DF	Adj SS	Adj MS	F-Value	P-Value
Factor	5	13457040	2691408	741.81	0.000
Error	204	740142	3628	-	-
Total	209	14197182	-	-	-
Significance Level: 0.05					
S= 60.2341; R-sq= 94.79% R-sq(adj)= 94.66% R-sq(pred)= 94.48%					

Table 3-3: Analysis of Variance

Factor	N	Mean	Grouping
Temperature [°C]	35	704.5	A
Rotational Speed [RPM]	35	347.1	B
Welding Speed [mm/min]	35	97.00	C
Axial Force [kN]	35	30.2	D
Shoulder diameter [mm]	35	24.143	D
Pin diameter [mm]	35	5.143	D
Grouping Information Using the Tukey Method and 95% Confidence			
Means that do not share a letter are significantly different.			

Table 3-4: Tukey pairwise comparisons

3.4.3. Regression Analysis

Figure 3-30, Figure 3-31, and Figure 3-32 present the outcomes of the non-linear regression analysis for predicting workpiece temperature based on the most significant process parameters (rotational speed, axial force, and welding speed) as concluded from the Taguchi and ANOVA analysis. The non-linear regression was conducted with Minitab software. The final model equation shows temperature as a function of time (X1) in seconds, rotational speed (X2) in RPM, welding speed (X3) in mm/min, and axial force (X4) in kN, including quadratic terms and interactions:

Temperature (^{o}C) = 25.33 + 0.7829 X1 + 1.1894 X2 - 0.1388 X3 + 18.123 X4 - 0.005194 $X1^2$ - 0.00761 $X2^2$ - 0.17246 $X4^2$ - 0.000938 X2*X4.

The model building sequence chart indicates the incremental addition of terms, starting with the most significant variable, axial force (X4), followed by rotational speed (X2), their quadratic terms, and interactions, culminating in an adjusted R-squared value near 100%, reflecting a high model fit. The right-hand graphs show the incremental impact of each variable on R-squared, highlighting that axial force contributes the most significant increase (approximately 45%) in explaining temperature variance. Furthermore, the "Each X Regressed on All Other Terms" graph reveals that axial force and rotational speed are the most influential variables, contributing substantially to the model's explanatory power.

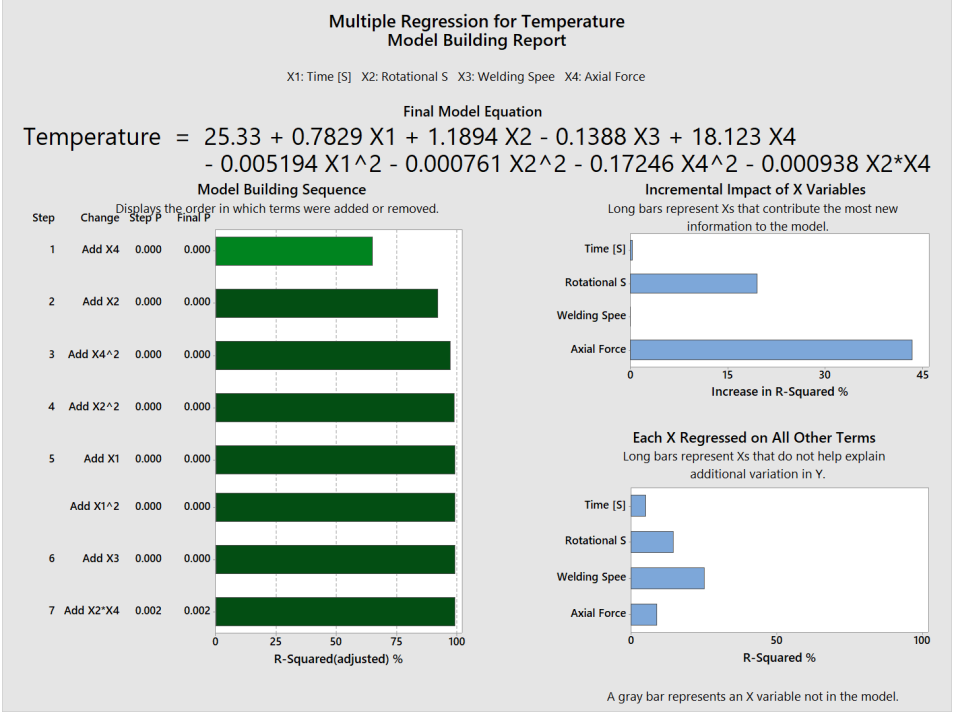

Figure 3-30: Multiple regression for temperature model building

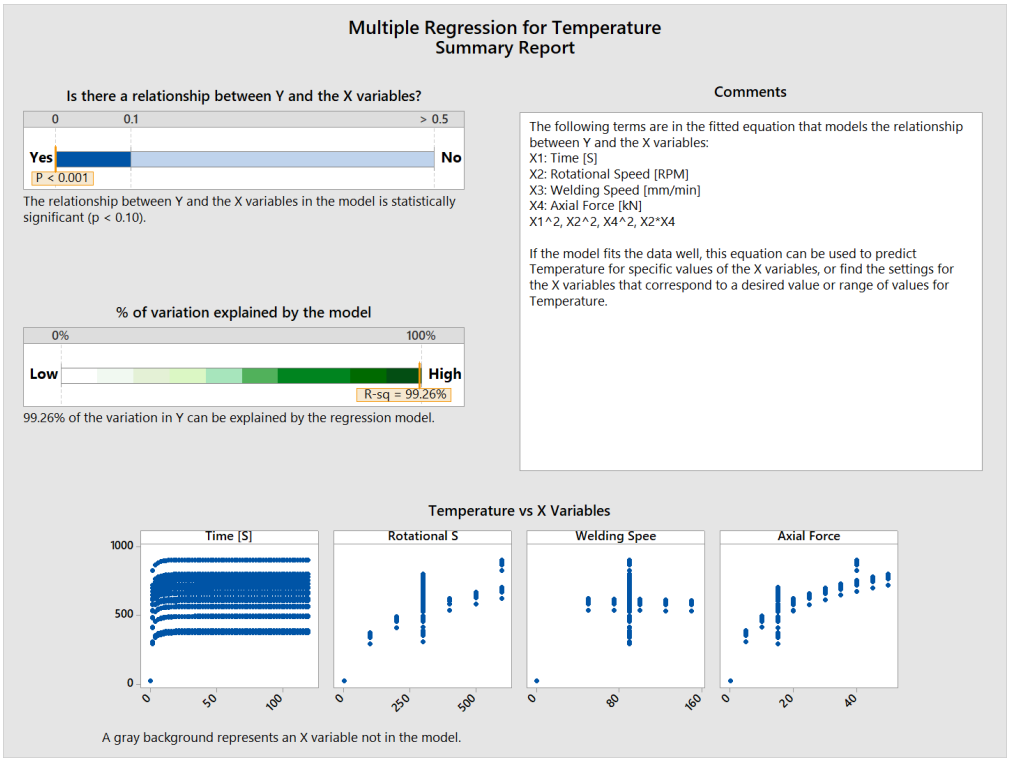

Figure 3-31: Multiple regression for temperature

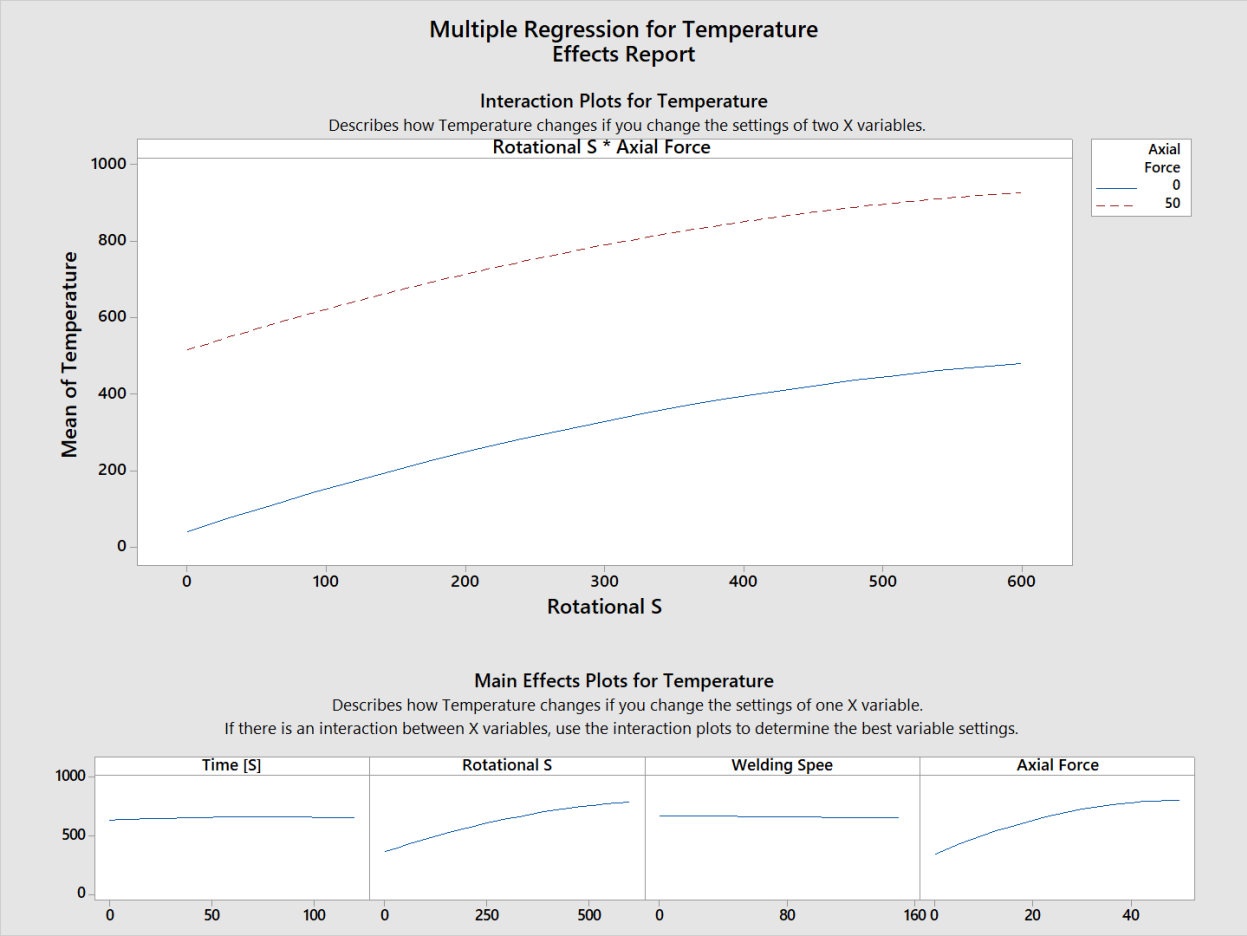

Figure 3-32: Multiple regression for temperature effects

In addition, Figure 3-33 illustrates the Multiple Regression for Temperature Prediction and Optimization report, which was generated using Minitab software to establish a relationship between workpiece temperature and the process parameters: rotational speed, axial force, and welding speed. The goal was to achieve a target temperature of 700°C. The predicted optimal settings to reach this temperature are presented, with the equation yielding a predicted Y value of 700°C within a 95% prediction interval of 675.16 to 724.84°C. Additionally, the top five alternative solutions with predicted T values closest to the optimal solution are provided, demonstrating slightly varied combinations of process parameters that still achieve a temperature near 700°C, ensuring the reliability and robustness of the model.

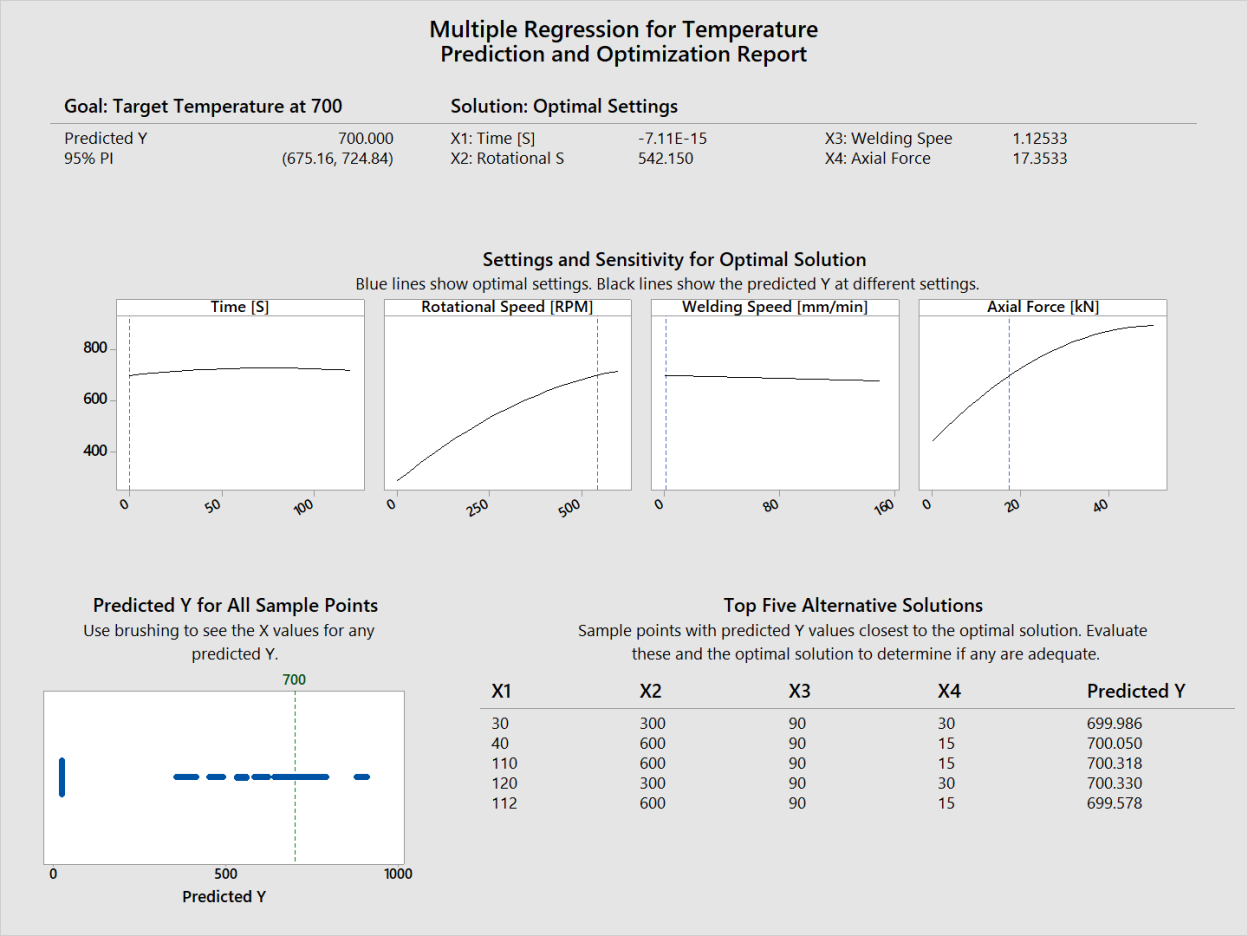

Figure 3-33: Multiple regression for temperature prediction and optimization

In FSW technology, the workpiece temperature plays a crucial role in determining both the surface quality and the mechanical properties of the welded material. Elevated temperatures during FSW facilitate the plastic deformation and material flow necessary for forming a solid-state bond, directly influencing the surface finish by reducing defects and ensuring a smoother weld seam. Additionally, the temperature affects grain size and distribution, which in turn impacts the mechanical properties such as hardness, strength, and ductility of the welded joint. Optimal temperature control ensures a balance between sufficient material mixing and minimizing thermal degradation, resulting in superior surface quality and enhanced mechanical performance of the welded material.

Figure 3-34 illustrates the results of a multiple regression analysis performed using Minitab software to explore the relationship between the average grain size (Y) in µm of a friction stir welded workpiece and its temperature (X) in °C. The analysis aimed to establish a quadratic model, yielding the equation:

$$\mathbf{Y = 16.39 - 0.09086\ X + 0.000117\ X^2}$$

The fitted line plot shows the quadratic model's curve, indicating how average grain size varies with temperature. The p-value (< 0.001) confirms that the relationship between grain size and temperature is statistically significant. The R-squared value (99.09%) demonstrates that the model explains 99.09% of the variation in average grain size, signifying a high degree of reliability. This regression model can be used to predict average grain size from temperature data, thereby aiding in the estimation of workpiece surface quality by monitoring the workpiece temperature.

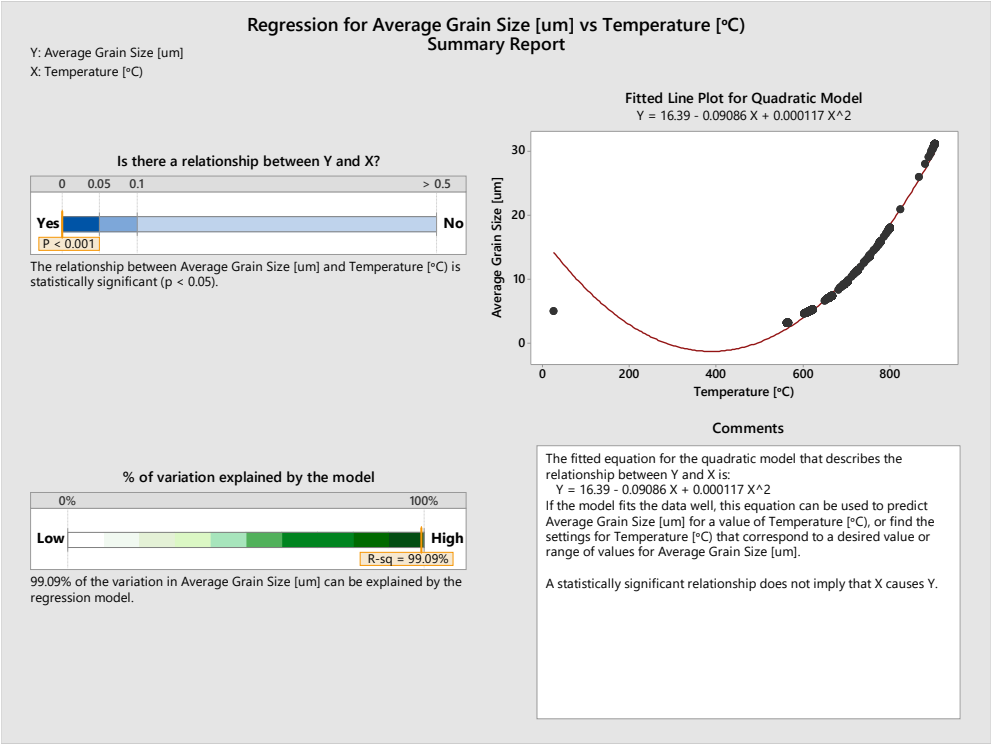

Figure 3-34: Regression analysis for average grain size vs workpiece temperature

Moreover, Figure 3-35 presents the results of a multiple regression analysis conducted using Minitab software to determine the relationship between the microhardness (Y) of a friction stir welded workpiece and its temperature (X) in °C. A quadratic model was fitted, resulting in the equation:

$$\mathbf{Y = 246.5 + 0.4079\ X - 0.000243\ X^2}$$

The fitted line plot illustrates the model's curve, showing how microhardness varies with temperature. The p-value (< 0.001) indicates a statistically significant relationship between microhardness and temperature. The R-squared value (98.70%) reveals that the model explains 98.70% of the variation in microhardness, indicating a high level of accuracy. This regression model can be utilized to predict microhardness based on temperature data, thereby assisting in the estimation of the workpiece's mechanical properties by monitoring its temperature.

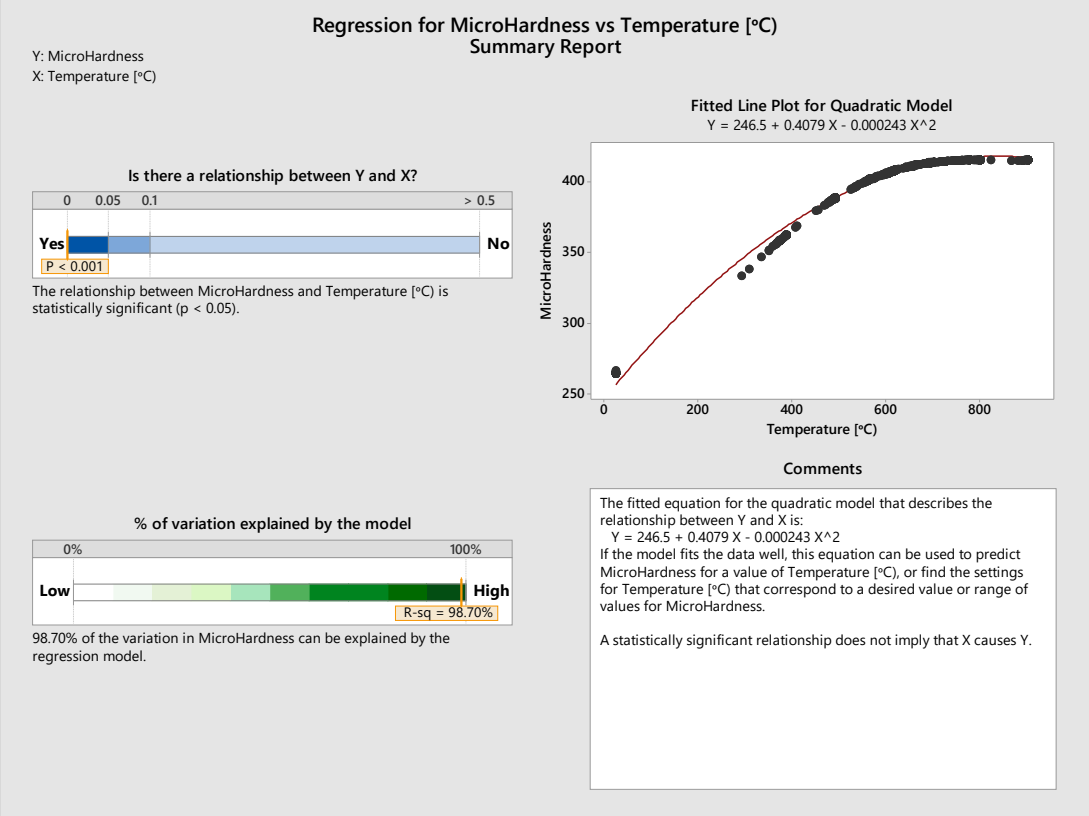

Figure 3-35: Regression analysis for microhardness vs workpiece temperature

3.5. Conclusions

Chapter 3 provides a comprehensive analysis of the simulation results, detailing the effects of various FSW parameters (axial force, rotational speed, welding speed, shoulder diameter, and pin diameter) on the performance of Al-T6 and Inconel 718, particularly focusing on workpiece temperature, grain size, microhardness, and stress evolution. The analysis revealed that lower workpiece temperatures result in finer grains, reduced stress evolution, and increased hardness. Specifically, lower axial force and rotational speed, coupled with higher welding speed and larger shoulder and pin diameters, contribute to lower workpiece temperatures and enhanced mechanical properties. It was concluded that axial force and rotational speed are the most influential parameters in the FSW process. Additionally, the study demonstrated that induction preheating significantly enhances process efficiency by reducing the required rotational speed and axial force while increasing welding speed, thereby improving heat dissipation and resulting in finer grain structures. Active cooling also contributed to improved microstructure and finer grains.

The Taguchi analysis and ANOVA highlighted the complex interactions between the parameters, emphasizing the challenges in optimizing FSW processes. The results indicated also that axial force and rotational speed are the primary factors influencing workpiece temperature, with welding speed, shoulder diameter, and pin diameter playing secondary roles. The developed non-linear regression models provided predictive capabilities, allowing for the anticipation of performance outcomes based on specific parameter settings. This chapter concludes that precise process control of FSW parameters is crucial for achieving the desired mechanical properties and structural integrity in Inconel 718 welds, thereby paving the way for practical applications and further research in this field, which is presented in Chapter 5.

CHAPTER 4: Simulation Results of Dissimilar FSW of Inconel 718 & Ti-6Al-4V

4.1. Introduction

In this section, we propose dissimilar welding of Inconel 718 and Ti-6Al-4V alloys to enhance mechanical properties and achieve a higher strength-to-weight ratio, crucial in aerospace applications. This is achieved through numerical investigations and process parameterization, including tool rotational speed, welding speeds, axial loads, pin and shoulder diameter, and the impact of cooling and induction preheating. To ensure accuracy, this study is based on the developed and validated model against existing experimental data on Inconel 718, where the model assesses dissimilar welding, focusing on temperature distribution and stress evaluation.

Additionally, data sets were created using the developed finite element model to explore the impacts of various process parameters. These parameters included axial force (5 to 50 kN), rotational speed (100 to 600 RPM), welding speed (50 to 150 mm/min), shoulder diameter (15 to 25 mm), and pin diameter (4 to 8 mm) on the workpiece's thermal profile. Furthermore, Taguchi analyses as well as one-way ANOVA were used to determine the most significant parameters affecting the FSW process. This statistical method allowed for the comparison of multiple process parameters to identify their influence on the thermal profile of the workpiece as well as the grain size distribution, microhardness and stress evolution. By analyzing the variance among different parameter levels, one-way ANOVA identified the factors with the most significant impact on the process. Subsequently, non-linear regression analysis was performed to establish a relationship between these significant parameters and the workpiece temperature. This method enabled the development of a predictive model that accurately links the influential parameters to the resulting thermal profile, offering deeper insights into optimizing the FSW process.

4.2. FEM Results of the Dissimilar FSW of Inconel 718 and Ti-6Al-4V Alloys

Figure 4-1 illustrates the model domain and system geometry, depicting a configuration with two plates: one for Inconel 718 and the other for the Ti-6Al-4V alloy. Each plate

measures 250 by 75 by 3 millimeters and is bordered by two infinite domains in the x-direction. The tool, crafted from tungsten carbide with 10% cobalt, is robust, featuring a 25-millimeter diameter flat circular bottom for the shoulder and a cylindrical pin with a 5-millimeter diameter, and 2.7 mm pin depth. Employing temperature-dependent material properties for both the tool and workpiece plates enables simultaneous calculation of thermal and mechanical outcomes. The ALE technique, coupled with adaptive meshing, maintains mesh quality during welding by preventing excessive distortion. However, this affects computation time. The simulation was conducted in a system with 16 GB Intel(R) Core (TM) i7-8565U CPU @ 1.80GHz 1.99 GHz. Total time to completion was around 3.2 h.

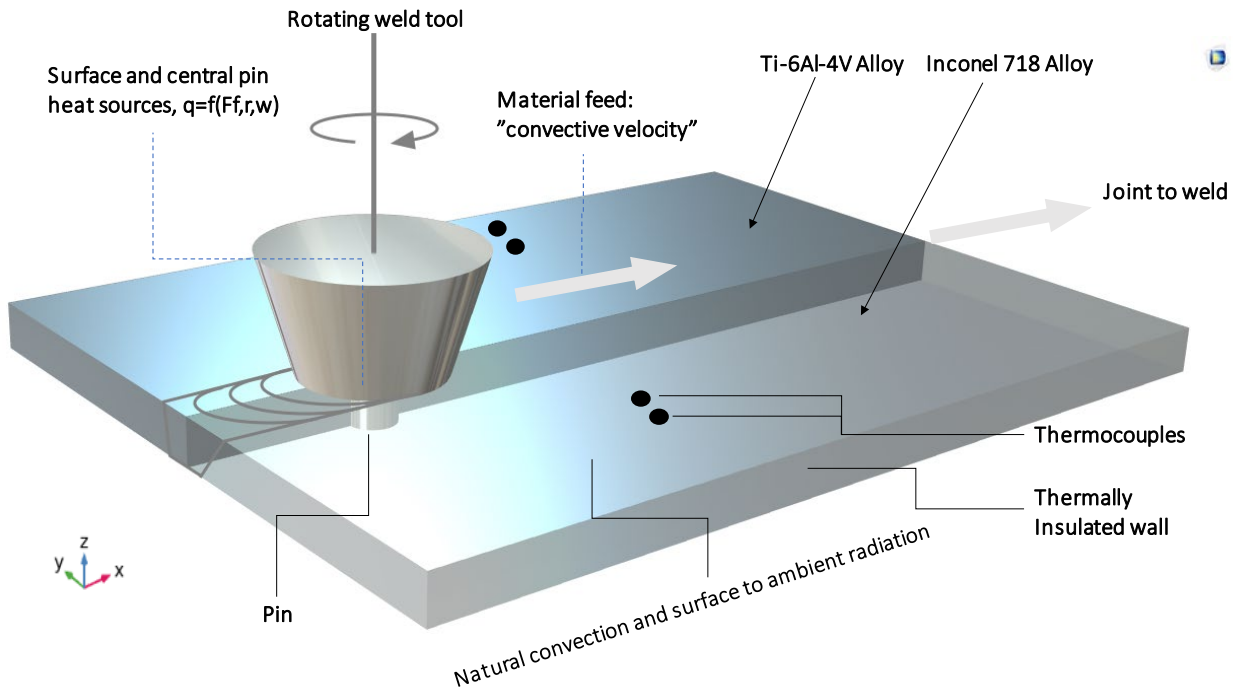

Figure 4-1:Schematic diagram of the dissimilar FSW of Inconel 718 and Ti-6Al-4V.

The FSW process parameters used in this study are a 300 RPM rotational speed, a 100 mm/min welding speed, a 40 kN axial force, a 25 mm shoulder diameter, and a 5 mm pin diameter, without any cooling effect or preheating. Figure 4-2 below illustrates the temperature profiles during the dissimilar FSW process of Inconel 718 and Ti alloy and positions relative to the welding centerline. Subplot (a) shows a 3D temperature profile

of the workpiece, with the highest temperatures concentrated around the welding tool's position at 1090 °C. Subplot (b) presents a 1D temperature distribution along the nugget zone at different time intervals, showing the peak temperature at the weld zone slightly shifted to the Ti alloy workpiece and a decrease as the distance from the welding tool increases towards the Inconel 718 side. Subplot (c) illustrates the 1D temperature profile of Inconel 718 alloy at 15mm from the welding centerline of the Inconel 718 alloy, indicating temperature changes over time with the highest temperatures near the weld at 550 °C. Subplot (d) depicts the 1D temperature profile of a Titanium alloy at 15mm from the welding centerline, showing a similar distribution pattern to that of the Inconel 718 alloy, with specific temperature values and cooling rates differing due to the different thermal properties of Titanium peaking at 500 °C. These figures provide critical insights for thermal management and process control in the FSW process.

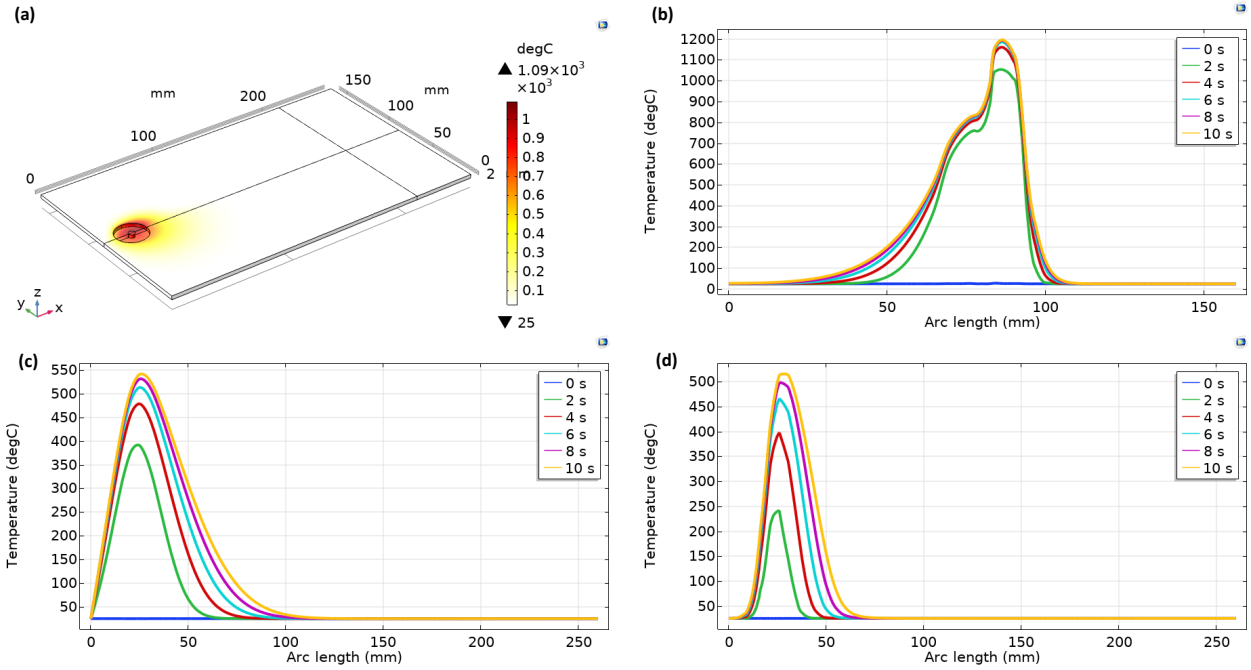

Figure 4-2: Dissimilar FSW of Inconel 718 and Ti-6Al-4V. a) 3D temperature profile, b)1D temperature across the nugget zone, c)1D temperature of Inconel 718 alloy at 15mm from welding centerline, and d)1D temperature of Ti alloy at 15mm from welding centerline

Figure 4-3 below illustrates the average grain size, hardness, and von Mises stress profiles for the dissimilar FSW of Inconel 718 and Titanium alloy, providing detailed insights into the material properties at various positions relative to the welding centerline. Subplot (a) shows the 1D average grain size across the nugget zone, highlighting the grain refinement in the weld zone over time. Subplot (b) presents the 1D average grain size of the Inconel 718 alloy at 15mm from the welding centerline, showing a peak in grain size near the weld that decreases with distance. Subplot (c) illustrates the 1D average grain size of the Titanium alloy at 15mm from the welding centerline, indicating similar trends of grain refinement. Subplot (d) displays the 1D hardness profile across the nugget zone, where the hardness peaks in the weld zone and tapers off with increasing distance from the weld, it shows a flat performance close to the Inconel side while it peaks at the other side. Subplot (e) shows the 1D hardness of the Inconel 718 alloy at 15mm from the welding centerline, reflecting variations in hardness over time. Subplot (f) presents the 1D hardness of the Titanium alloy at 15mm from the welding centerline, showing a hardness distribution like Inconel 718 but with narrower distribution across the workpiece. Subplot (g) depicts the 1D von Mises stress across the nugget zone, with the stress concentration peaking at the weld and decreasing with distance. Subplot (h) illustrates the 1D von Mises stress of the Inconel 718 alloy at 15mm from the welding centerline, showing the stress distribution over time which peaks close to the weld line up to 500 MPa and decreases with distance. Lastly, subplot (i) presents the 1D von Mises stress of the Titanium alloy at 15mm from the welding centerline, highlighting the stress profiles in the Titanium alloy, which peak close to the weld line up to 550 MPa and decreases with distance. These figures collectively provide a comprehensive understanding of the mechanical and microstructural changes occurring in dissimilar FSW of Inconel 718 and Titanium alloy.

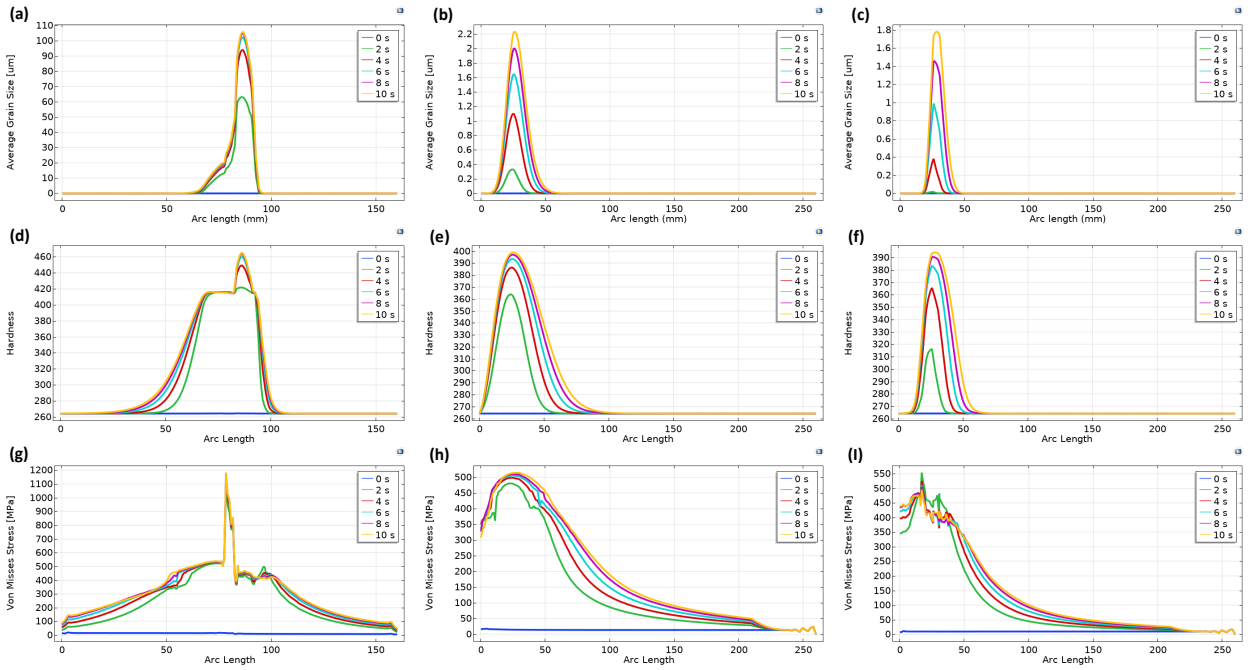

Figure 4-3: Dissimilar FSW of Inconel 718 and Ti-6Al-4V. a) 1D avg grain size across the nugget zone, b) 1D avg grain size of Inconel 718 alloy at 15mm from welding centerline , c) 1D avg grain size of Ti alloy at 15mm from welding centerline, d) 1D hardness across the nugget zone, e) 1D hardness of Inconel 718 alloy at 15mm from welding centerline, f) 1D hardness of Ti alloy at 15mm from welding centerline, g) 1D von mises stress across the nugget zone, h) 1D von mises stress of Inconel 718 alloy at 15mm from welding centerline, i)1D von mises stress of Ti alloy at 15mm from welding centerline

4.2.1. Effect of Process Parameters on Welding Efficiency

In this section, the effects of different process parameters, including axial force, rotational speed, welding speed, shoulder diameter, and pin diameter, as well as the effects of cooling and preheating on the workpiece thermal profile, average grain size, microhardness, and stress evolution, are discussed.

4.2.1.1. Axial Force

The FSW process parameters used in this study are a 300 RPM rotational speed, a 100 mm/min welding speed, a 5-50 kN axial force, a 25 mm shoulder diameter, and a 5 mm pin diameter, without any cooling effect or preheating. Figure 5 below illustrates the effect of varying axial forces from 5 to 50 kN on the temperature profiles during the dissimilar FSW process of Inconel 718 and Ti alloy, and their positions relative to the welding centerline. Figure 4-4 subplot (a) shows a 1D temperature profile of the

workpiece across the nugget zone, with the highest temperatures concentrated around the Ti alloy side at 1280°C at 50 kN, while the minimum temperature recorded is 700°C at 5 kN. Subplot (b) presents a 1D temperature distribution along the workpiece thickness (3 mm), showing a tight temperature distribution of 40°C across the plate, which ensures material homogeneity during FSW. Subplot (c) illustrates the 1D temperature profile of the Inconel 718 alloy at 15 mm from the welding centerline, indicating temperature changes from 575°C at 50 kN to 260°C at 5 kN. Subplot (d) depicts the 1D temperature profile of the titanium alloy at 15 mm from the welding centerline, showing a similar distribution pattern to that of the Inconel 718 alloy, with specific temperature values and cooling rates differing due to the different thermal properties of titanium, peaking at 530°C.

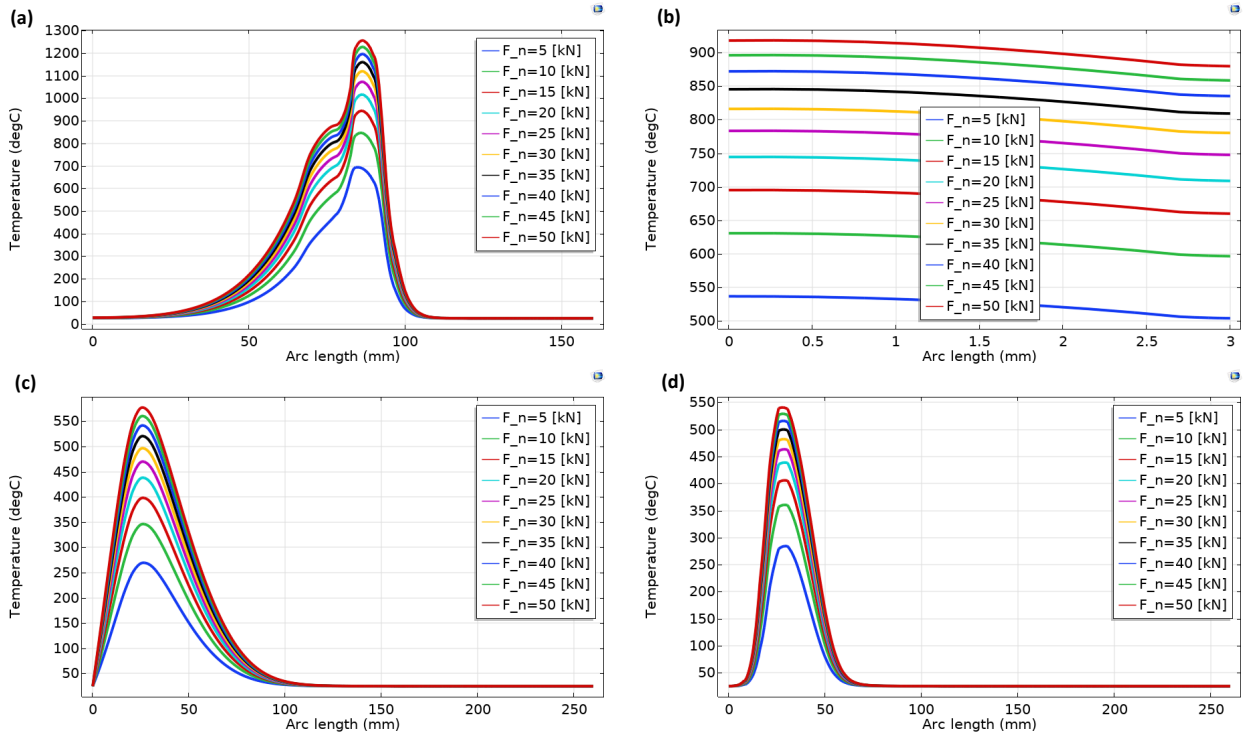

Figure 4-4: Dissimilar FSW of Inconel 718 and Ti-6Al-4V, parametric analysis on axial force, a) 1D temperature across the nugget zone, b) 1D temperature across plate thickness at welding center line, c) 1D temperature of Inconel 718 alloy at 15mm from welding centerline, d) 1D temperature of Ti alloy at 15mm from welding centerline.

Figure 4-5 below illustrate the average grain size, hardness, and von Mises stress profiles for the dissimilar FSW of Inconel 718 and Titanium alloy at various axial forces. Subplot (a) shows the 1D average grain size across the nugget zone, emphasizing grain refinement in the weld zone with lower axial force, ranging from 8 μm at 5 kN to 130 μm at 50 kN. Subplot (b) presents the 1D average grain size of the Inconel 718 alloy at 15 mm from the welding centerline, demonstrating fine grain sizes as low as 0.15 μm at 5 kN and 3.2 μm at 50 kN. Subplot (c) illustrates the 1D average grain size of the Titanium alloy at 15 mm from the welding centerline, indicating similar trends of grain refinement with finer grain size at 50 kN, reaching 2.4 μm. It can be inferred from the above that finer grain size can be achieved with lower axial force. Subplot (d) displays the 1D hardness profile across the nugget zone, where hardness peaks in the weld zone at 500 HV and tapers off with increasing distance from the weld, showing a flat performance close to the Inconel side while peaking on the other side. It is worth mentioning that the flat profile wasn't observed at 5 kN, while it exists in all the other values. Subplot (e) shows the 1D hardness of the Inconel 718 alloy at 15 mm from the welding centerline, reflecting variations in hardness with axial force, peaking at 400 HV. Subplot (f) presents the 1D hardness of the Titanium alloy at 15 mm from the welding centerline, showing a hardness distribution like Inconel 718 but with a narrower distribution across the workpiece, indicating that higher plate hardness could be achieved with higher axial force. Subplot (g) depicts the 1D von Mises stress across the nugget zone, with stress concentration peaking at the weld with 1200 MPa and decreasing with distance. Subplot (h) illustrates the 1D von Mises stress of the Inconel 718 alloy at 15 mm from the welding centerline, showing stress distribution at different axial forces, peaking close to the weld line up to 530 MPa and decreasing with distance. Lastly, Subplot (i) presents the 1D von Mises stress of the Titanium alloy at 15 mm from the welding centerline, highlighting stress profiles in the Titanium alloy, which peak close to the weld line up to 500 MPa and decrease with distance. These figures collectively provide a comprehensive understanding of the effect of axial forces on mechanical and microstructural changes occurring in dissimilar FSW of Inconel 718 and Titanium alloy.

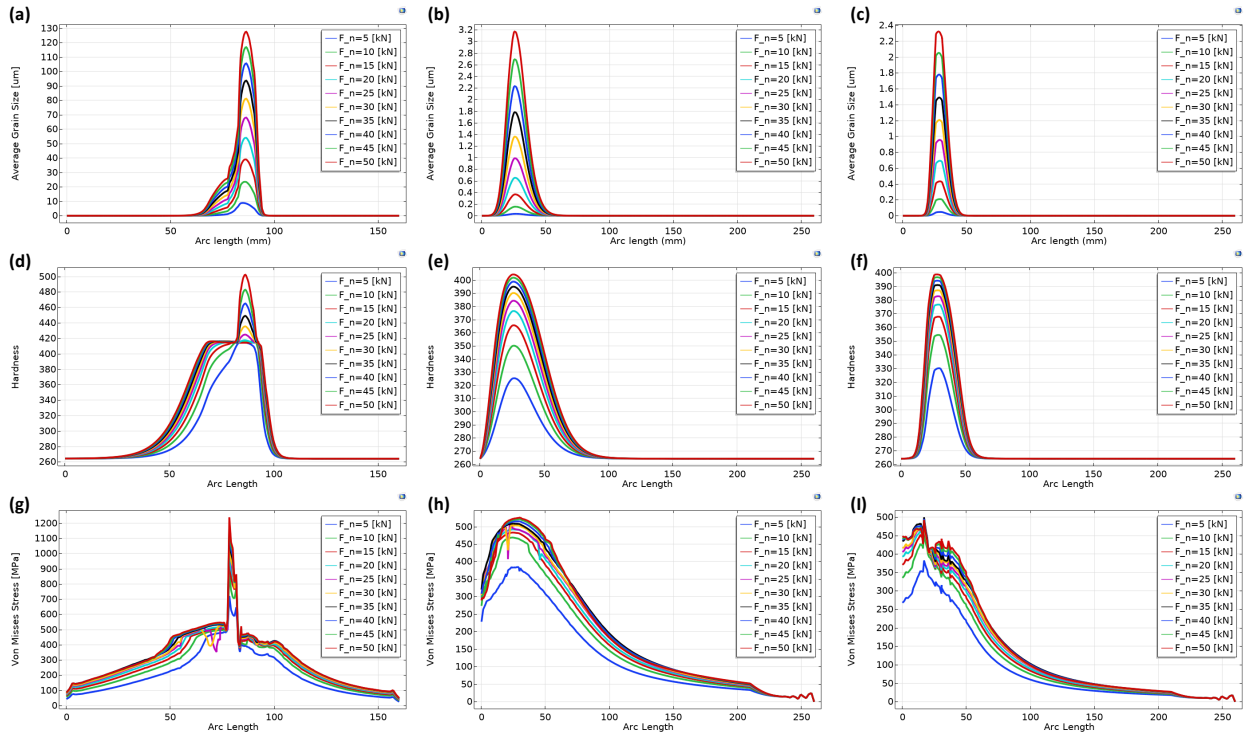

Figure 4-5: Dissimilar FSW of Inconel 718 and Ti-6Al-4V, parametric analysis on axial force, a) 1D avg grain size across the nugget zone, b) 1D avg grain size of Inconel 718 alloy at 15mm from welding centerline , c) 1D avg grain size of Ti alloy at 15mm from welding centerline, d) 1D hardness across the nugget zone, e) 1D hardness of Inconel 718 alloy at 15mm from welding centerline, f) 1D hardness of Ti alloy at 15mm from welding centerline, g) 1D von mises stress across the nugget zone, h) 1D von mises stress of Inconel 718 alloy at 15mm from welding centerline, i)1D von mises stress of Ti alloy at 15mm from welding centerline.

4.2.1.2. Rotational Speed

The FSW process parameters used in this study are a 100-600 RPM rotational speed, a 100 mm/min welding speed, a 30 kN axial force, a 25 mm shoulder diameter, and a 5 mm pin diameter, without any cooling effect or preheating. Figure 4-6 below illustrates the effect of varying rotational speeds from 100 to 600 RPM on the temperature profiles. Subplot (a) shows a 1D temperature profile of the workpiece across the nugget zone, with the highest temperatures concentrated around the Ti alloy side at 1260°C at 600 RPM, while the minimum temperature recorded is 800°C at 100 RPM. Subplot (b) presents a 1D temperature distribution along the workpiece thickness (3 mm), showing a tight temperature distribution of 40°C across the plate, which ensures material homogeneity during FSW. Subplot (c) illustrates the 1D temperature profile of the Inconel 718 alloy at

15 mm from the welding centerline, indicating temperature changes from 610°C at 600 RPM to 330 °C at 100 RPM. Subplot (d) depicts the 1D temperature profile of the titanium alloy at 15 mm from the welding centerline, showing a similar distribution pattern to that of the Inconel 718 alloy, with specific temperature values and cooling rates differing due to the different thermal properties of titanium, peaking at 580°C, while 370°C recorded as the minimum temperature at 100 RPM.

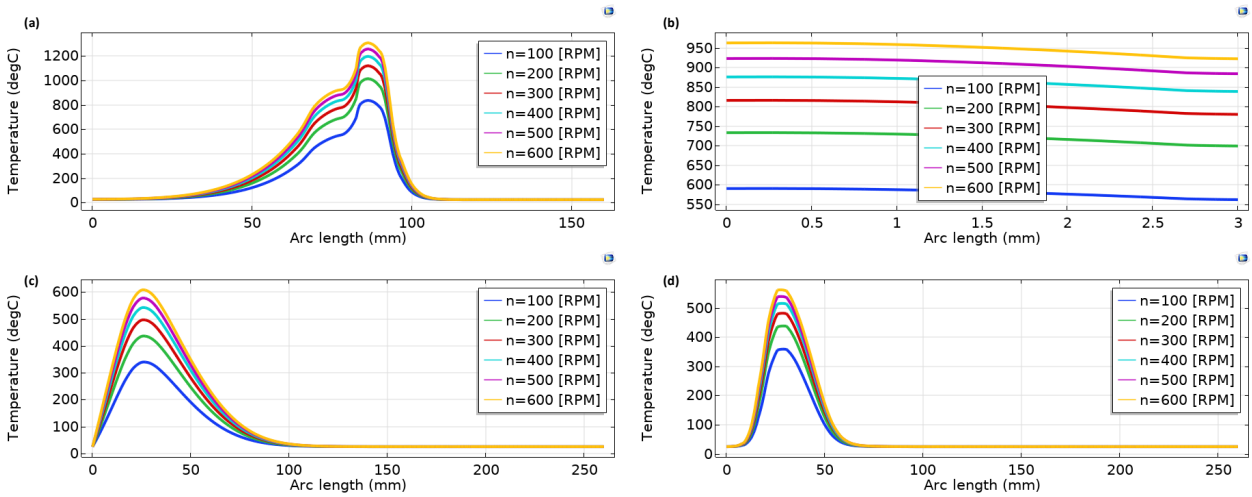

Figure 4-6: Dissimilar FSW of Inconel 718 and Ti-6Al-4V, parametric analysis on rotational speed, a) 1D temperature across the nugget zone, b) 1D temperature across plate thickness at welding center line, c) 1D temperature of Inconel 718 alloy at 15mm from welding centerline, d) 1D temperature of Ti alloy at 15mm from welding centerline.

The figures below (Figure 4-7 a-i) illustrate the average grain size, hardness, and von Mises stress profiles at various rotational speeds. Subplot (a) shows the 1D average grain size across the nugget zone, emphasizing grain refinement in the weld zone with lower rotational speed, ranging from 20 µm at 100 RPM to 150 µm at 600 RPM. Subplot (b) presents the 1D average grain size of the Inconel 718 alloy at 15 mm from the welding centerline, demonstrating fine grain sizes as low as 0.1 µm at 100 RPM and 4.2 µm at 600 RPM. Subplot (c) illustrates the 1D average grain size of the Titanium alloy at 15 mm from the welding centerline, indicating similar trends of grain refinement with finer grain size at 100 RPM, reaching 0.2 µm. It can be inferred from the above that finer grain size can be achieved with lower rotational speeds. Moreover, Subplot (d) displays the 1D hardness profile across the nugget zone, where hardness peaks in the weld zone at 550

HV and tapers off with increasing distance from the weld, showing a flat performance close to the Inconel side while peaking on the other side. It is worth mentioning that the flat profile wasn't observed at 100 RPM, while it exists in all the other values. Subplot (e) shows the 1D hardness of the Inconel 718 alloy at 15 mm from the welding centerline, reflecting variations in hardness with rotational speed, peaking at 420 HV. Subplot (f) presents the 1D hardness of the Titanium alloy at 15 mm from the welding centerline, showing a hardness distribution like Inconel 718 but with a narrower distribution across the workpiece, indicating that higher plate hardness could be achieved with higher rotational speed. Subplot (g) depicts the 1D von Mises stress across the nugget zone, with stress concentration peaking at the weld with 1200 MPa and decreasing with distance. Subplot (h) illustrates the 1D von Mises stress of the Inconel 718 alloy at 15 mm from the welding centerline, peaking close to the weld line up to 525 MPa and decreasing with distance. Lastly, Subplot (i) presents the 1D von Mises stress of the Titanium alloy at 15 mm from the welding centerline, highlighting stress profiles in the Titanium alloy, which peak close to the weld line up to 500 MPa and decrease with distance.

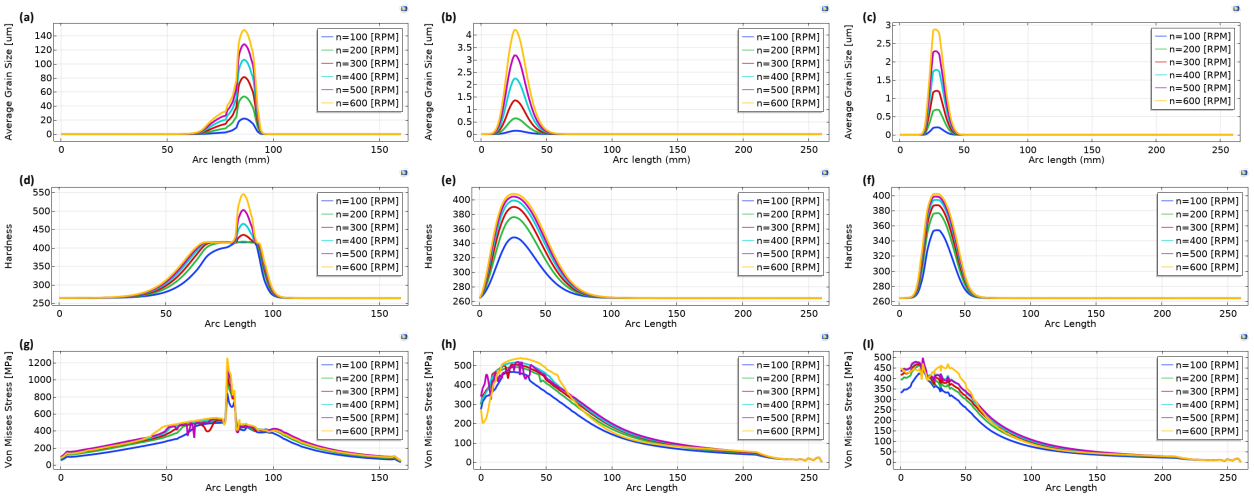

Figure 4-7: Dissimilar FSW of Inconel 718 and Ti-6Al-4V, parametric analysis on rotational speed, a) 1D avg grain size across the nugget zone, b) 1D avg grain size of Inconel 718 alloy at 15mm from welding centerline , c) 1D avg grain size of Ti alloy at 15mm from welding centerline, d) 1D hardness across the nugget zone, e) 1D hardness of Inconel 718 alloy at 15mm from welding centerline, f) 1D hardness of Ti alloy at 15mm from welding centerline, g) 1D von mises stress across the nugget zone, h) 1D von mises stress of Inconel 718 alloy at 15mm from welding centerline, i)1D von mises stress of Ti alloy at 15mm from welding centerline.

4.2.1.3. Welding Speed

The FSW process parameters used in this study are a 300 RPM rotational speed, a 40-140 mm/min welding speed, a 30 kN axial force, a 25 mm shoulder diameter, and a 5 mm pin diameter, without any cooling effect or preheating. Figure 4-8 a-d below reflect the effect of varying welding speeds from 40 to 140 mm/min on the temperature profiles. Subplot (a) shows a 1D temperature profile of the workpiece across the shoulder, with the highest temperatures concentrated around the Ti alloy side at 1150°C at 40 mm/min, while the minimum temperature recorded is 1080°C at 140 mm/min. Subplot (b) presents a 1D temperature distribution along the workpiece thickness (3 mm), showing a tight temperature distribution of 35°C across the plate thickness, which ensures material homogeneity during FSW. Subplot (c) illustrates the 1D temperature profile of the Inconel 718 alloy at 15 mm from the welding centerline, indicating almost no temperature changes with varying the welding speed peaking at 500°C, while Subplot (d) depicts the 1D temperature profile of the titanium alloy at 15 mm from the welding centerline, showing a different distribution pattern to that of the Inconel 718 alloy, with temperature ranges from 460°C at 140 mm/min up to 520°C at 40 mm/min. It could be concluded from the above that increasing the welding speed can slightly decrease the workpiece temperature.

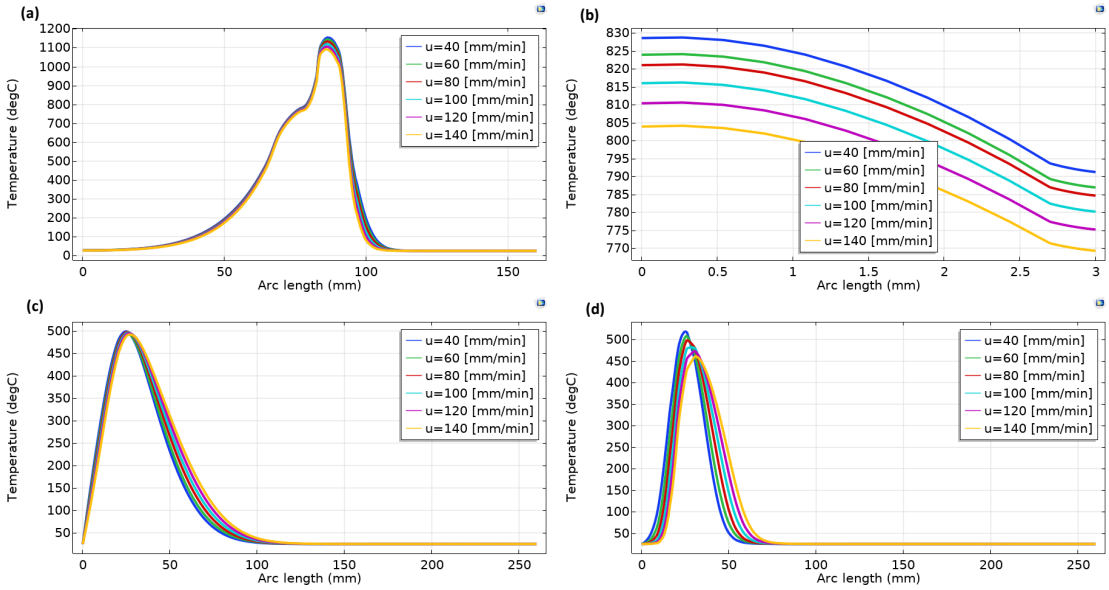

Figure 4-8: Dissimilar FSW of Inconel 718 and Ti-6Al-4V, parametric analysis on welding speed, a) 1D temperature across the nugget zone, b) 1D temperature across plate thickness at welding center line, c) 1D

temperature of Inconel 718 alloy at 15mm from welding centerline, d) 1D temperature of Ti alloy at 15mm from welding centerline.

The figures below (Figure 4-9 a-i) reflect the average grain size, hardness, and von Mises stress profiles at various welding speeds. Subplot (a) shows the 1D average grain size across the workpieces, emphasizing grain refinement in the weld zone with higher welding speed, ranging from 72 μm at 140 mm/min to 91 μm at 40 mm/min. Subplot (b) presents the 1D average grain size of the Inconel 718 alloy at 15 mm from the welding centerline, demonstrating fine grain sizes as low as 1.3 μm, while Subplot (c) illustrates the 1D average grain size of the Titanium alloy at 15 mm from the welding centerline, indicating similar trends of grain refinement with minor difference of refinement with increasing the welding speed. Subplot (d) displays the 1D hardness profile across the plates, where hardness peaks in the weld zone at 440 HV and tapers off with increasing distance from the weld, showing a flat performance close to the Inconel side while peaking on the other side. Subplot (e) shows the 1D hardness of the Inconel 718 alloy at 15 mm from the welding centerline, reflecting almost no variations in hardness with welding speed, peaking at 390 HV. Subplot (f) presents the 1D hardness of the Titanium alloy at 15 mm from the welding centerline, showing a hardness distribution like Inconel 718 but with a wider distribution across the workpiece, indicating that higher plate hardness could be achieved with lower welding speed. Subplot (g) depicts the 1D von Mises stress across the nugget zone, with stress concentration peaking at the weld with 1150 MPa and decreasing with distance. Subplot (h) illustrates the 1D von Mises stress of the Inconel 718 alloy at 15 mm from the welding centerline, peaking close to the weld line up to 520 MPa and decreasing with distance. Lastly, Subplot (i) presents the 1D von Mises stress of the Titanium alloy at 15 mm from the welding centerline, highlighting stress profiles in the Titanium alloy, which peak close to the weld line up to 500 MPa and decrease with distance.

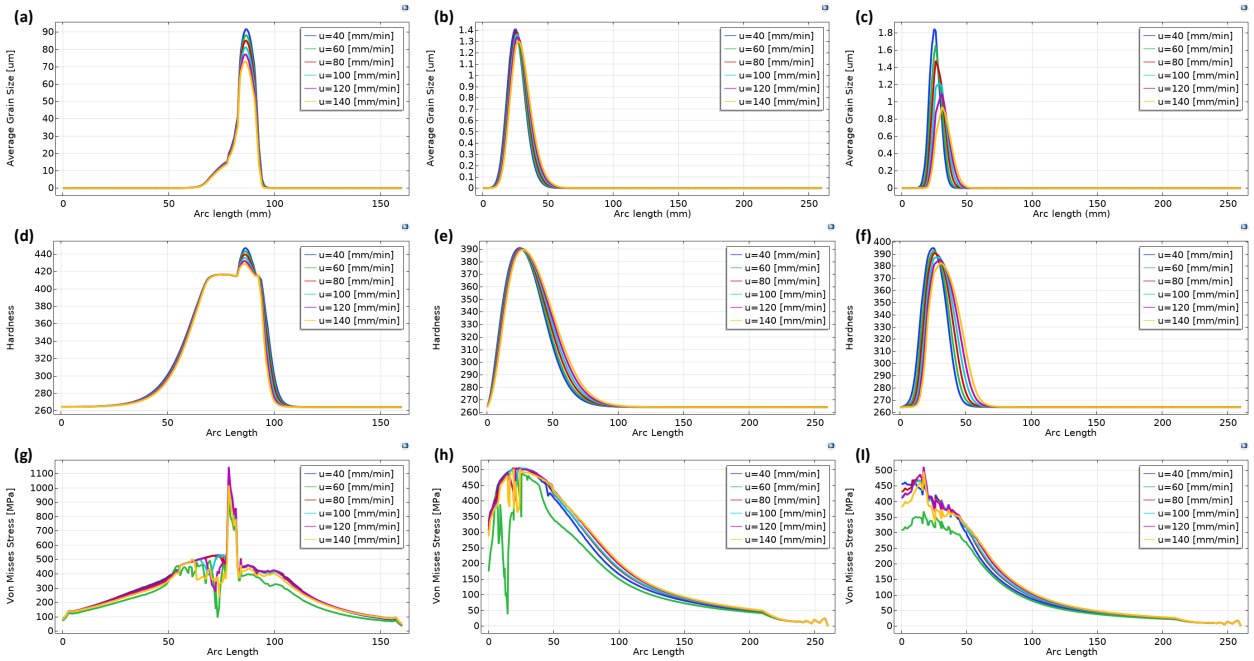

Figure 4-9: Dissimilar FSW of Inconel 718 and Ti-6Al-4V, parametric analysis on welding speed, a) 1D avg grain size across the nugget zone, b) 1D avg grain size of Inconel 718 alloy at 15mm from welding centerline , c) 1D avg grain size of Ti alloy at 15mm from welding centerline, d) 1D hardness across the nugget zone, e) 1D hardness of Inconel 718 alloy at 15mm from welding centerline, f) 1D hardness of Ti alloy at 15mm from welding centerline, g) 1D von mises stress across the nugget zone, h) 1D von mises stress of Inconel 718 alloy at 15mm from welding centerline, i)1D von mises stress of Ti alloy at 15mm from welding centerline.

4.2.1.4. Shoulder Diameter

The FSW process parameters used in this study are a 300 RPM rotational speed, a 100 mm/min welding speed, a 40 kN axial force, a 15-25 mm shoulder diameter, and a 5 mm pin diameter, without any cooling effect or preheating. Figure 4-10 reflects the effect of varying shoulder diameter from 15 to 25 mm on the temperature profiles. Subplot (a) shows a 1D temperature profile of the workpiece across the plates, with the highest temperatures concentrated around the Ti alloy side at 1350°C at 15 mm, while the minimum temperature recorded is 1180°C at 25 mm. Subplot (b) presents a 1D temperature distribution along the workpiece thickness (3 mm), showing a temperature distribution ranges from 35 °C at 25 mm up to 80 °C at 15 mm across the plate, which ensures material homogeneity during FSW. Subplot (c) illustrates the 1D temperature

profile of the Inconel 718 alloy at 15 mm from the welding centerline, indicating temperature changes from 545°C at 25 mm to 430 °C at 15 mm. Subplot (d) depicts the 1D temperature profile of the titanium alloy at 15 mm from the welding centerline, showing a similar distribution pattern to that of the Inconel 718 alloy, peaking at 510°C, while 230°C recorded as the minimum temperature at 15 mm.

On the other hand, Figure 4-11 illustrates the average grain size, hardness, and von Mises stress profiles at various shoulder diameters. Subplot (a) shows the 1D average grain size across the workpieces, emphasizing grain refinement in the weld zone with higher shoulder diameter, ranging from 110 μm at 25 mm to 165 μm at 15 mm. Subplot (b) presents the 1D average grain size of the Inconel 718 alloy at 15 mm from the welding centerline, demonstrating fine grain sizes as low as 0.5 μm at 15 mm and 2.25 μm at 25 mm. Subplot (c) illustrates the 1D average grain size of the Titanium alloy at 15 mm from the welding centerline, indicating similar trends of grain refinement with finer grain size at 15 mm, reaching 10 nm. It can be inferred from the above that finer grain size can be achieved with higher shoulder diameter at the nugget zone. However, finer grains are possible with higher shoulder diameter at the thermomechanical affected zones.

Moreover, Subplot (d) displays the 1D hardness profile across the plates, where hardness peaks in the weld zone at 590 HV and tapers off with increasing distance from the weld, showing a flat performance close to the Inconel side while peaking on the other side. Subplot (e) shows the 1D hardness of the Inconel 718 alloy at 15 mm from the welding centerline, reflecting variations in hardness with shoulder diameter, peaking at 400 HV. Subplot (f) presents the 1D hardness of the Titanium alloy at 15 mm from the welding centerline, showing a hardness distribution like Inconel 718 but with a narrower distribution across the workpiece, indicating that higher plate hardness could be achieved with higher shoulder diameter.

Furthermore, Subplot (g) depicts the 1D von Mises stress profile, where stress concentration peaking at the nugget zone with 1490 MPa and decreasing with distance. Subplot (h) illustrates the 1D von Mises stress of the Inconel 718 alloy at 15 mm from the welding centerline, peaking close to the weld line up to 515 MPa and decreasing with

distance. Lastly, Subplot (i) presents the 1D von Mises stress of the Titanium alloy at 15 mm from the welding centerline, highlighting stress profiles in the Titanium alloy, which peak close to the weld line up to 490 MPa and decrease with distance. These figures collectively provide a comprehensive understanding of the effect of shoulder diameter on mechanical and microstructural changes occurring in dissimilar FSW of Inconel 718 and Titanium alloy.

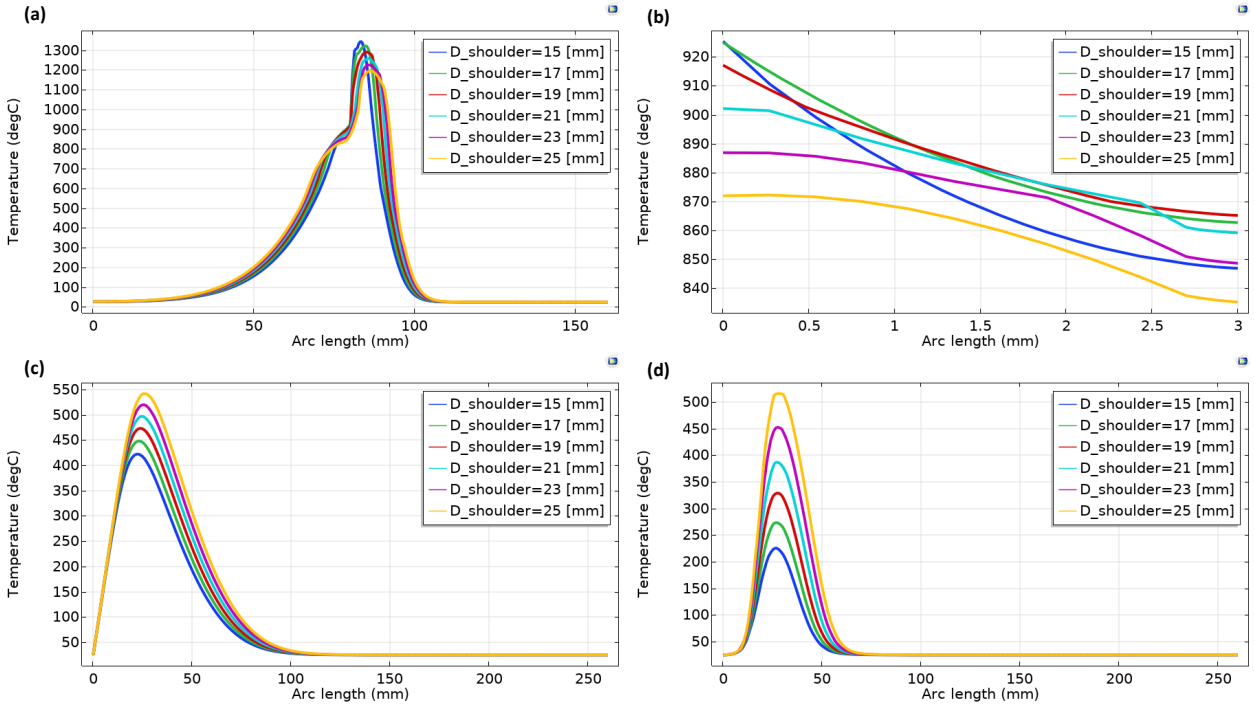

Figure 4-10: Dissimilar FSW of Inconel 718 and Ti-6Al-4V, parametric analysis on shoulder diameter, a) 1D temperature across the nugget zone, b) 1D temperature across plate thickness at welding center line, c) 1D temperature of Inconel 718 alloy at 15mm from welding centerline, d) 1D temperature of Ti alloy at 15mm from welding centerline.

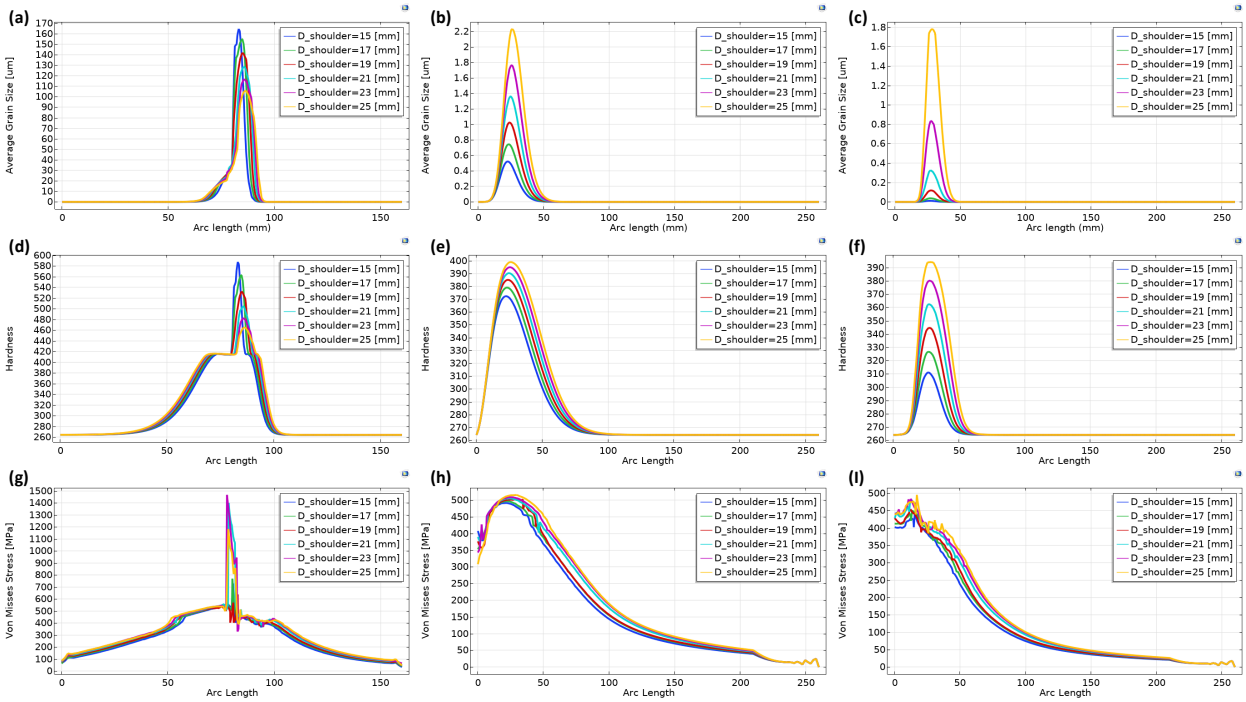

Figure 4-11: Dissimilar FSW of Inconel 718 and Ti-6Al-4V, parametric analysis on shoulder diameter, a) 1D avg grain size across the nugget zone, b) 1D avg grain size of Inconel 718 alloy at 15mm from welding centerline , c) 1D avg grain size of Ti alloy at 15mm from welding centerline, d) 1D hardness across the nugget zone, e) 1D hardness of Inconel 718 alloy at 15mm from welding centerline, f) 1D hardness of Ti alloy at 15mm from welding centerline, g) 1D von mises stress across the nugget zone, h) 1D von mises stress of Inconel 718 alloy at 15mm from welding centerline, i)1D von mises stress of Ti alloy at 15mm from welding centerline.

4.2.1.5. Pin Diameter

The FSW process parameters used in this study are a 300 RPM rotational speed, a 100 mm/min welding speed, a 40 kN axial force, a 25 mm shoulder diameter, and a 4-8 mm pin diameter, without any cooling effect or preheating. Figure 4-12 illustrates the effect of varying the pin diameter from 4 to 8 mm on the temperature profiles. Subplot (a) shows a 1D temperature profile of the workpieces across the nugget zone, with the highest temperatures concentrated around the Ti alloy side, reaching 1200°C at 4 mm, while the minimum temperature recorded is 1190°C at 8 mm. It can be concluded from subplots (a)-(d) that there is no significant difference in the thermal profile of the workpiece when varying the pin diameter. Like the thermal profile, the average grain size, microhardness, and von Mises stresses (Figure 4-13 (a)-(i)) exhibited nearly identical behavior when

varying the pin diameter from 4 to 8 mm. This further confirms that pin diameter has a minimal effect on the dissimilar friction stir welding of Inconel 718 and Ti-6Al-4V alloys.

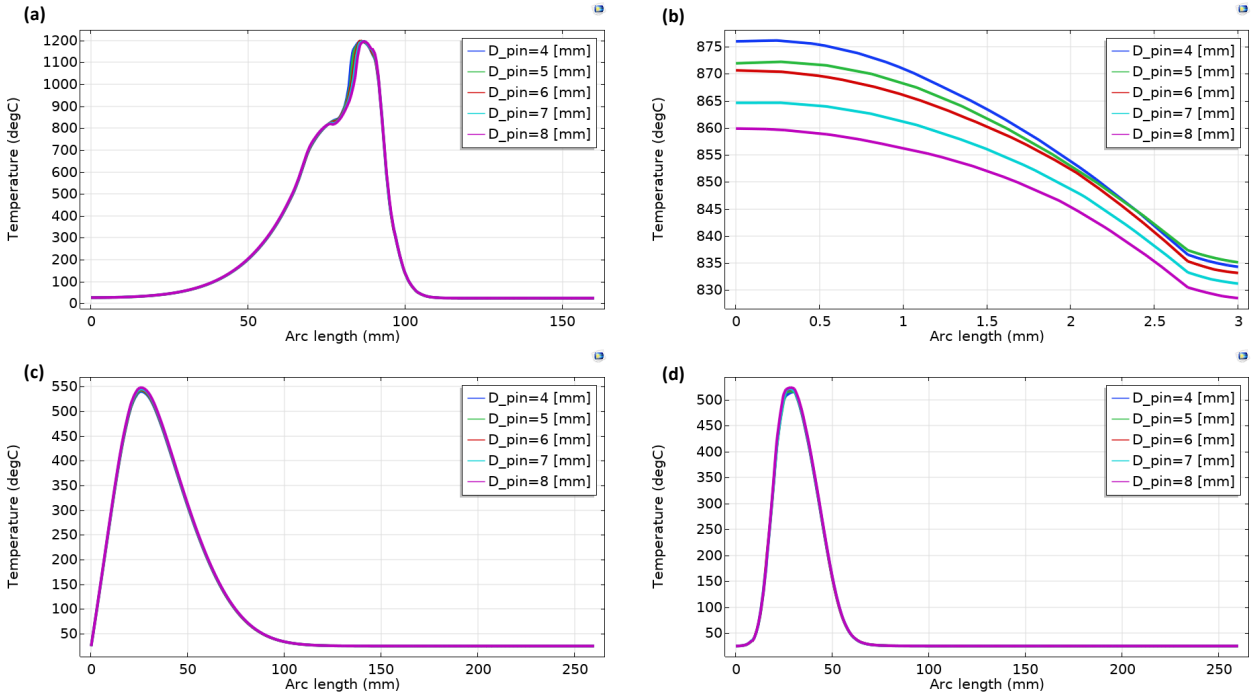

Figure 4-12: Dissimilar FSW of Inconel 718 and Ti-6Al-4V, parametric analysis on pin diameter, a) 1D temperature across the nugget zone, b) 1D temperature across plate thickness at welding center line, c) 1D temperature of Inconel 718 alloy at 15mm from welding centerline, d) 1D Temperature of Ti alloy at 15mm from welding centerline

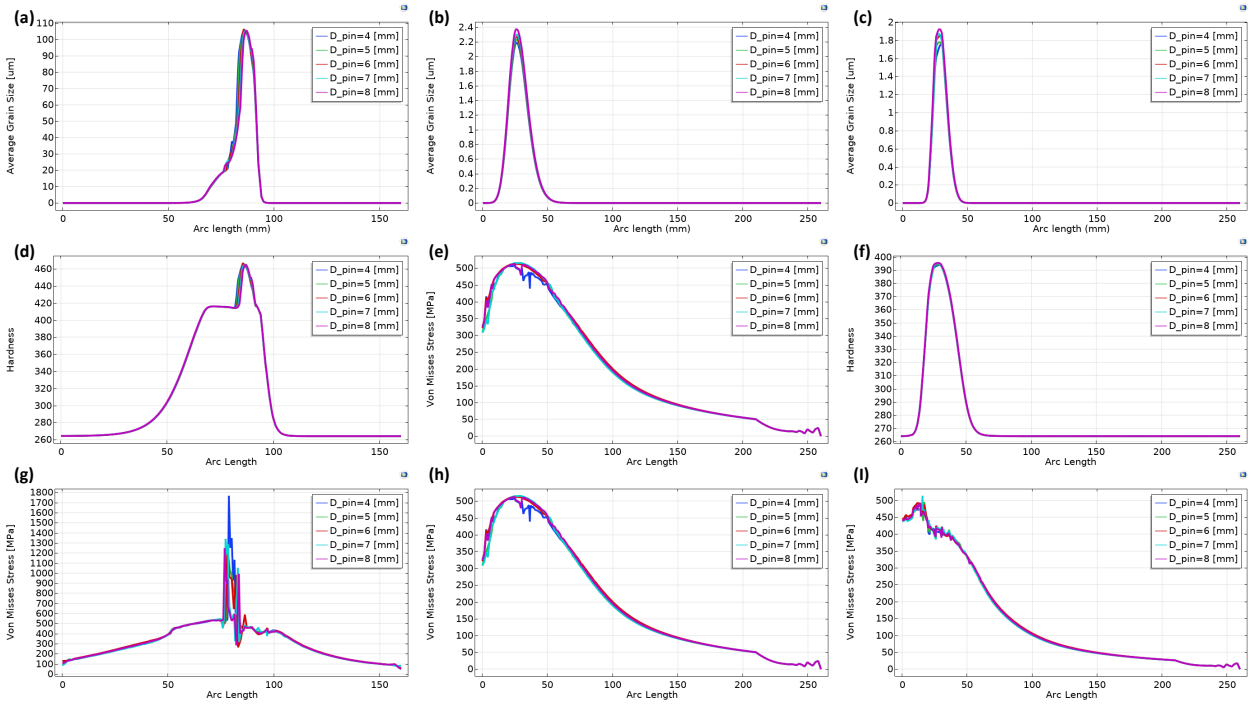

Figure 4-13: Dissimilar FSW of Inconel 718 and Ti-6Al-4V, parametric analysis on pin diameter, a) 1D avg grain size across the nugget zone, b) 1D avg grain size of Inconel 718 alloy at 15mm from welding centerline , c) 1D avg grain size of Ti alloy at 15mm from welding centerline, d) 1D hardness across the nugget zone, e) 1D hardness of Inconel 718 alloy at 15mm from welding centerline, f) 1D hardness of Ti alloy at 15mm from welding centerline, g) 1D von mises stress across the nugget zone, h) 1D von mises stress of Inconel 718 alloy at 15mm from welding centerline, i)1D von mises stress of Ti alloy at 15mm from welding centerline.

4.2.1.6. Cooling-FSW

The FSW process parameters used in this study are a 300 RPM rotational speed, a 100 mm/min welding speed, a 40 kN axial force, a 25 mm shoulder diameter, and a 5 mm pin diameter, without preheating and with cooling velocity varies from 0.1 to 1.1 m/s. Figure 4-14 reflects the effect of applying cooling water during FSW process as well as varying the cooling velocity from 0.1 to 1.1 m/s on the temperature profiles during the dissimilar FSW process of Inconel 718 and Ti alloy, and their positions relative to the welding centerline. Subplot (a) shows a 1D temperature profile of the workpieces across the nugget zone, with the highest temperatures concentrated around the Ti alloy side at 860°C at 0.1 m/s cooling water velocity, while the minimum temperature recorded is 600°C at 1.1 m/s. Subplot (b) presents a 1D temperature distribution along the workpiece thickness (3 mm), showing a tight temperature distribution of 18°C across the plate, which ensures

material homogeneity during FSW. Subplot (c) illustrates the 1D temperature profile of the Inconel 718 alloy at 15 mm from the welding centerline, indicating temperature changes from 475°C at 0.1 m/s to 360°C at 1.1 m/s. Subplot (d) depicts the 1D temperature profile of the titanium alloy at 15 mm from the welding centerline, showing a similar distribution pattern to that of the Inconel 718 alloy, with specific temperature values and cooling rates differing due to the different thermal properties of titanium, peaking at 430°C. These figures provide critical insights for thermal management and process control in the FSW process.

Furthermore, the average grain size, hardness, and von Mises stress profiles for the dissimilar FSW of Inconel 718 and Titanium alloy at various water velocities are reflected in Figure 4-15. Subplot (a) shows the 1D average grain size across the plates, emphasizing grain refinement in the weld zone with higher cooling velocity, ranging from 4 μm at 1.1 m/s to 26 μm at 0.1 m/s. Subplot (b) presents the 1D average grain size of the Inconel 718 alloy at 15 mm from the welding centerline, demonstrating fine grain sizes as low as 0.2 μm at 1.1 m/s and 1 μm at 0.1 m/s. Subplot (c) illustrates the 1D average grain size of the Titanium alloy at 15 mm from the welding centerline, indicating similar trends of grain refinement with finer grain size at 1.1 m/s, reaching 50 nm. It can be inferred from the above that finer grain size can be achieved with higher cooling rate.

Subplot (d) displays the 1D hardness profile, where hardness peaks in the weld zone at 415 HV and tapers off with increasing distance from the weld, showing a flat performance close to welding zone, where the cooling implies. It is worth mentioning that the flat profile was observed in all cooling rates. Subplot (e) shows the 1D hardness of the Inconel 718 alloy at 15 mm from the welding centerline, reflecting variations in hardness with cooling rates, peaking at 385 HV. Subplot (f) presents the 1D hardness of the Titanium alloy at 15 mm from the welding centerline, showing a hardness distribution like Inconel 718 but with a narrower distribution across the workpiece, indicating that higher plate hardness could be achieved with lower cooling velocity. Subplot (g) depicts the 1D von Mises stress across the workpieces, with stress concentration peaking at the weld with 1150 MPa and decreasing with distance. Subplot (h) illustrates the 1D von Mises stress

of the Inconel 718 alloy at 15 mm from the welding centerline, showing stress distribution at different cooling velocities, peaking close to the weld line up to 500 MPa and decreasing with distance. Lastly, Subplot (i) presents the 1D von Mises stress of the Titanium alloy at 15 mm from the welding centerline, highlighting stress profiles in the Titanium alloy, which peak close to the weld line up to 500 MPa and decrease with distance.

Moreover, Figure 4-16 illustrates the effect of varying the cooling hose diameter from 0.2 to 1 inch on the temperature profiles. Subplot (a) shows a 1D temperature profile of the workpieces across the nugget zone, with the highest temperatures concentrated around the Ti alloy side, reaching 700°C at 1 inch, while the minimum temperature recorded is 580°C at 0.2 inch. It can be concluded from subplots (a)-(d) that there is no significant difference (less than 20°C across the plate thickness and 50°C between each hose diameter) in the thermal profile of the workpiece when varying the cooling hose diameter. It could also be concluded that lower cooling hose diameter will ensure higher cooling rate, turbulence and accordingly higher heat transfer and dissipation. Like the thermal profile, the average grain size, microhardness, and von Mises stresses (Figure 4-17 (a)-(i)) exhibited nearly identical behavior when varying the cooling hose diameter from 0.2 to 1 inch. This further confirms that cooling hose diameter has a minimal effect on the dissimilar friction stir welding of Inconel 718 and Ti-6Al-4V alloys.

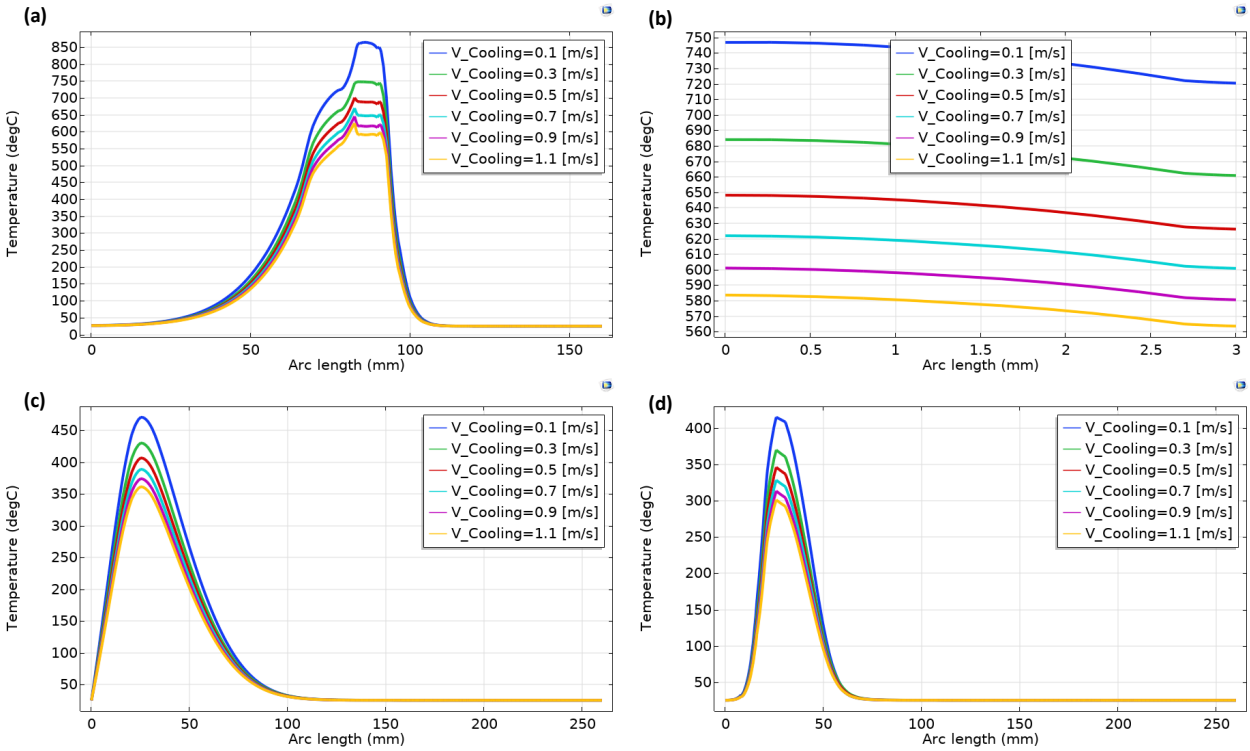

Figure 4-14: Dissimilar FSW of Inconel 718 and Ti-6Al-4V, parametric analysis on cooling water velocity, a) 1D temperature across the nugget zone, b) 1D temperature across plate thickness at welding center line, c) 1D temperature of Inconel 718 alloy at 15mm from welding centerline, d) 1D temperature of Ti alloy at 15mm from welding centerline.

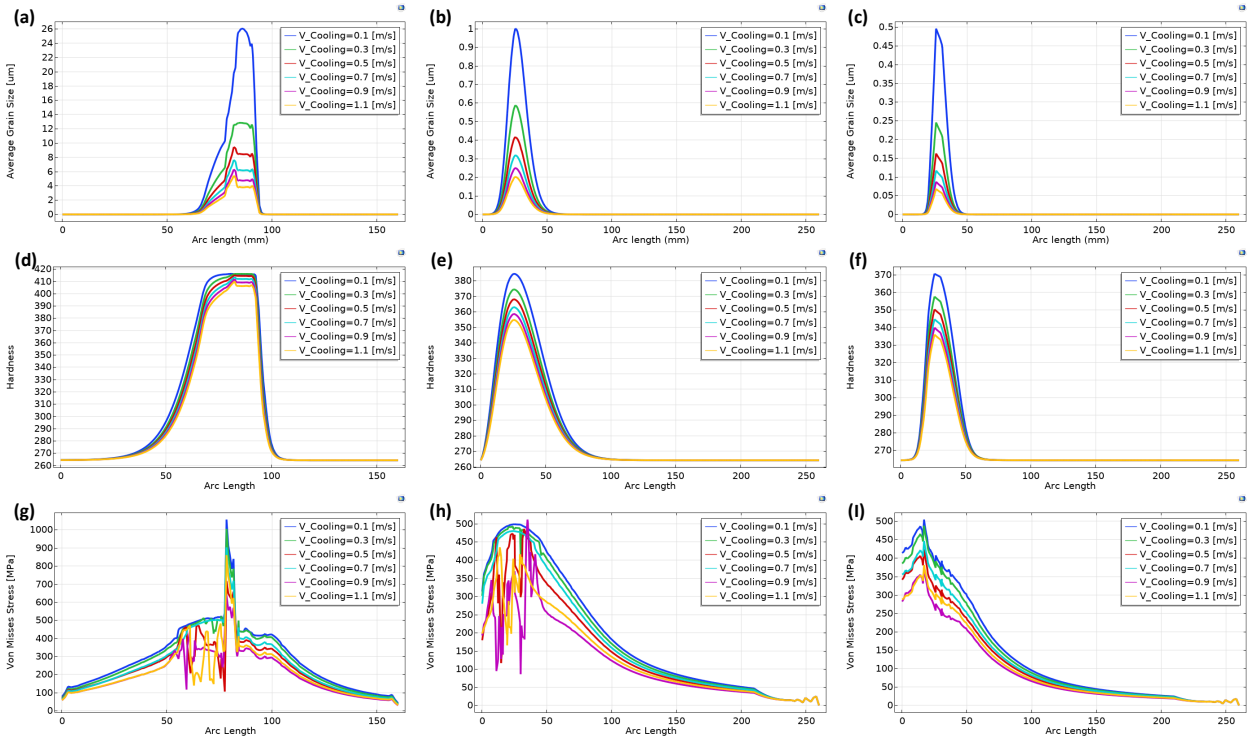

Figure 4-15: Dissimilar FSW of Inconel 718 and Ti-6Al-4V, parametric analysis on cooling water velocity, a) 1D avg grain size across the nugget zone, b) 1D avg grain size of Inconel 718 alloy at 15mm from welding centerline , c) 1D avg grain size of Ti alloy at 15mm from welding centerline, d) 1D hardness across the nugget zone, e) 1D hardness of Inconel 718 alloy at 15mm from welding centerline, f) 1D hardness of Ti alloy at 15mm from welding centerline, g) 1D von mises stress across the nugget zone, h) 1D von mises stress of Inconel 718 alloy at 15mm from welding centerline, i)1D von mises stress of Ti alloy at 15mm from welding centerline.

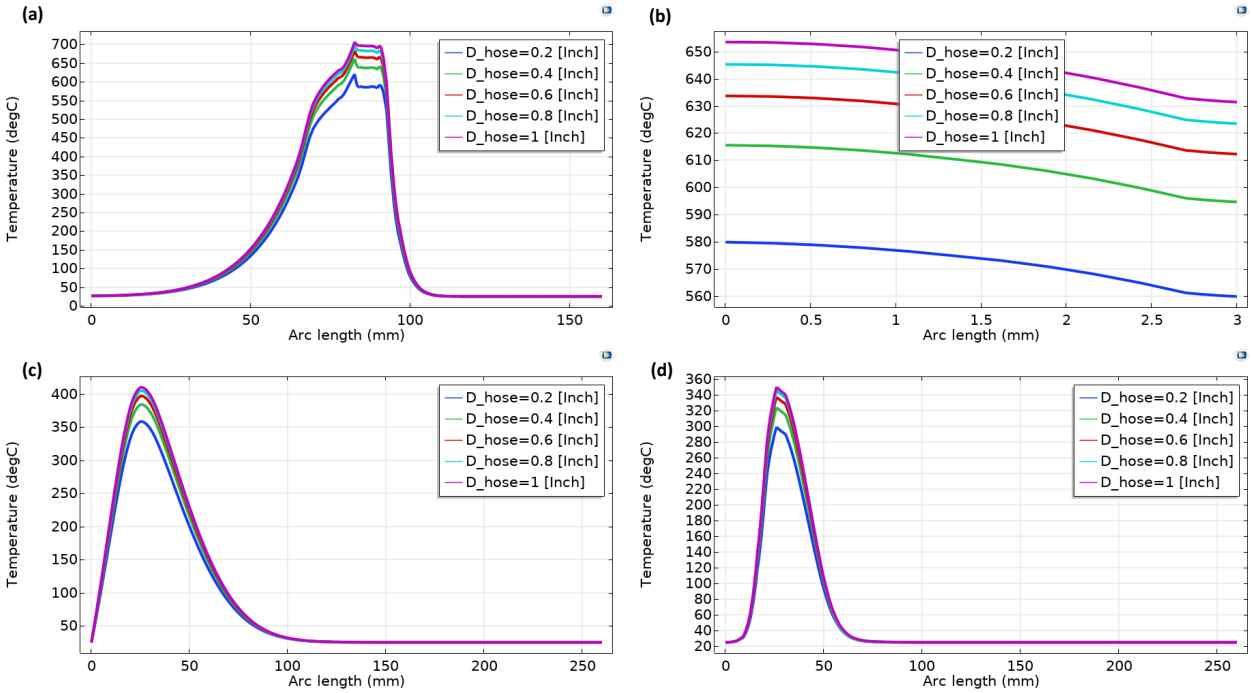

Figure 4-16: Dissimilar FSW of Inconel 718 and Ti-6Al-4V, parametric analysis on cooling water hose diameter, a) 1D temperature across the nugget zone, b) 1D temperature across plate thickness at welding center line, c) 1D temperature of Inconel 718 alloy at 15mm from welding centerline, d) 1D temperature of Ti alloy at 15mm from welding centerline.

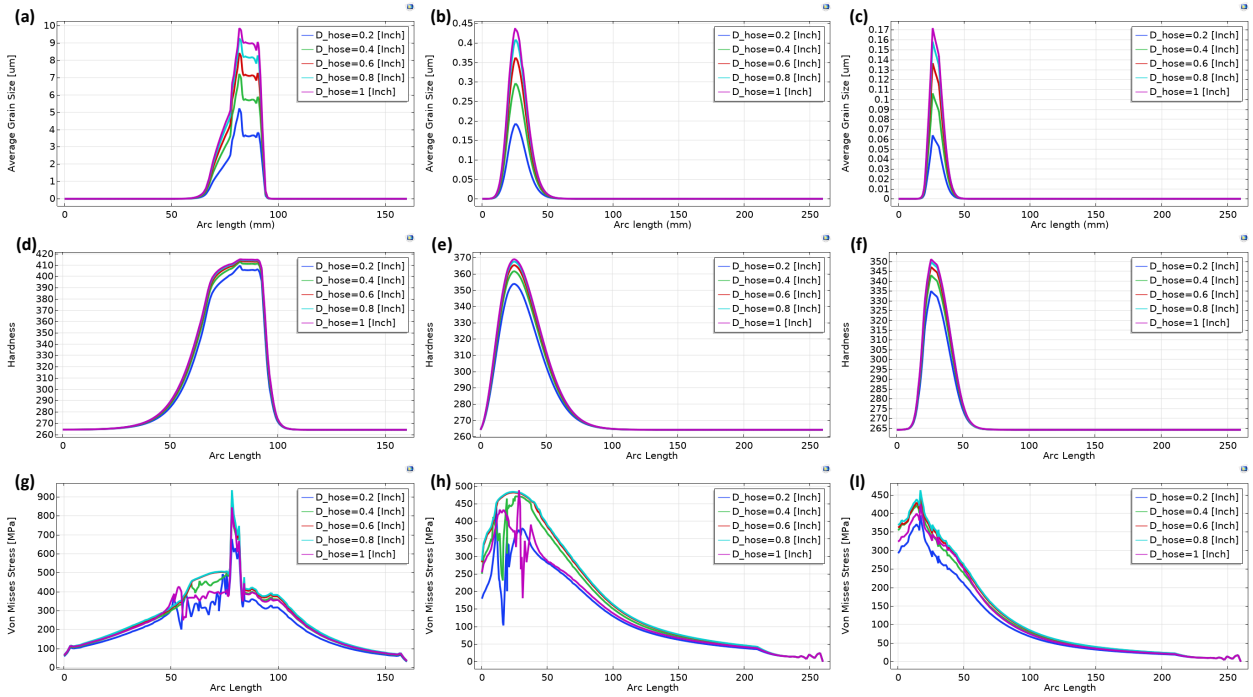

Figure 4-17: Dissimilar FSW of Inconel 718 and Ti-6Al-4V, parametric analysis on cooling water hose diameter, a) 1D avg grain size across the nugget zone, b) 1D avg grain size of Inconel 718 alloy at 15mm from welding centerline , c) 1D avg grain size of Ti alloy at 15mm from welding centerline, d) 1D hardness across the nugget zone, e) 1D hardness of Inconel 718 alloy at 15mm from welding centerline, f) 1D hardness of Ti alloy at 15mm from welding centerline, g) 1D von mises stress across the nugget zone, h) 1D von mises stress of Inconel 718 alloy at 15mm from welding centerline, i)1D von mises stress of Ti alloy at 15mm from welding centerline.

4.2.1.7. Induction Preheating

The FSW process parameters used in this study are a 300 RPM rotational speed, a 100 mm/min welding speed, a 20 kN axial force, a 25 mm shoulder diameter, and a 5 mm pin diameter, without cooling effect and with preheating load effect varies from 0.5 to 2.5 kW as induction heat assisted FSW.

Figure 4-18 illustrates the effect of applying induction preheating before the FSW process as well as varying the heating power from 0.5 to 2.5 kW on the temperature profiles during the dissimilar FSW process of Inconel 718 and Ti alloy, and their positions relative to the welding centerline. It important to note that, the purpose of applying induction preheating to the FSW process offers several benefits, including reduced tool wear due to softened material, improved weld quality through better material flow and fusion, and lower residual stresses by minimizing thermal gradients. It enhances weld penetration,

particularly in thick materials, and decreases welding forces, thus reducing the load on the equipment. This technique ensures consistent welds in dissimilar materials by balancing heat distribution and provides enhanced process control for optimal results, leading to better repeatability and reliability in industrial applications. Additionally, induction preheating allows for lower axial force and faster welding speeds, improving productivity without compromising weld quality. Overall, it significantly enhances the efficiency, quality, and durability of welded joints, especially in challenging materials (high strength alloys) and applications.

Subplot (a) shows a 1D temperature profile of the workpieces across the nugget zone, with the highest temperatures concentrated around the Ti alloy side at 1020°C. Subplot (b) presents a 1D temperature distribution along the workpiece thickness (3 mm), showing a tight temperature distribution of 35°C across the plate, which ensures material homogeneity during FSW. Subplot (c) illustrates the 1D temperature profile of the Inconel 718 alloy at 15 mm from the welding centerline, indicating temperature changes from 1110°C at 2.5 kW to 500°C at 0.5 kW. Subplot (d) depicts the 1D temperature profile of the titanium alloy at 15 mm from the welding centerline, showing a different distribution pattern to that of the Inconel 718 alloy, with specific temperature values and cooling rates differing due to the different thermal properties of titanium, peaking at 450°C.

On the other hand, Figure 4-19 illustrates the average grain size, hardness, and von Mises stress profiles for the dissimilar FSW of Inconel 718 and Titanium alloy at various induction preheating power. Subplot (a) shows the 1D average grain size across the plates, emphasizing grain refinement in the weld zone with 56 μm. Subplot (b) presents the 1D average grain size of the Inconel 718 alloy at 15 mm from the welding centerline, demonstrating fine grain sizes as low as 1 μm at 0.5 kW and 75 μm at 2.5 kW. Subplot (c) illustrates the 1D average grain size of the Titanium alloy at 15 mm from the welding centerline, indicating finer grain size than Inconel 718 plate, reaching 0.7 μm. It can be inferred from the above that finer grain size can be achieved with induction preheating.

Subplot (d) displays the 1D hardness profile, where hardness peaks in the weld zone at 420 HV and tapers off with increasing distance from the weld, showing a flat performance

close to welding zone, due to the relatively lower axial force used 20 kN compared to the reference case which was 40 kN. It is worth mentioning that the flat profile was observed in all preheating rates. Subplot (e) shows the 1D hardness of the Inconel 718 alloy at 15 mm from the welding centerline, reflecting variations in hardness with preheating rates, peaking at 440 HV at 2.5 kW. Subplot (f) presents the 1D hardness of the Titanium alloy at 15 mm from the welding centerline, showing a hardness distribution different than Inconel 718 with narrower distribution across the workpiece.

Moreover, subplot (g) depicts the 1D von Mises stress distribution across the nugget zone, with stress concentration peaking at the weld with 1200 MPa and decreasing with distance. Subplot (h) illustrates the 1D von Mises stress of the Inconel 718 alloy at 15 mm from the welding centerline, showing stress distribution at different preheating rates, peaking close to the weld line up to 620 MPa and decreasing with distance. Lastly, subplot (i) presents the 1D von Mises stress of the Titanium alloy at 15 mm from the welding centerline, highlighting stress profiles in the Titanium alloy, which peak close to the weld line up to 600 MPa and decrease with distance. These figures collectively provide a comprehensive understanding of the effect of applying induction preheating on FSW process on mechanical and microstructural changes occurring in dissimilar FSW of Inconel 718 and Titanium alloy.

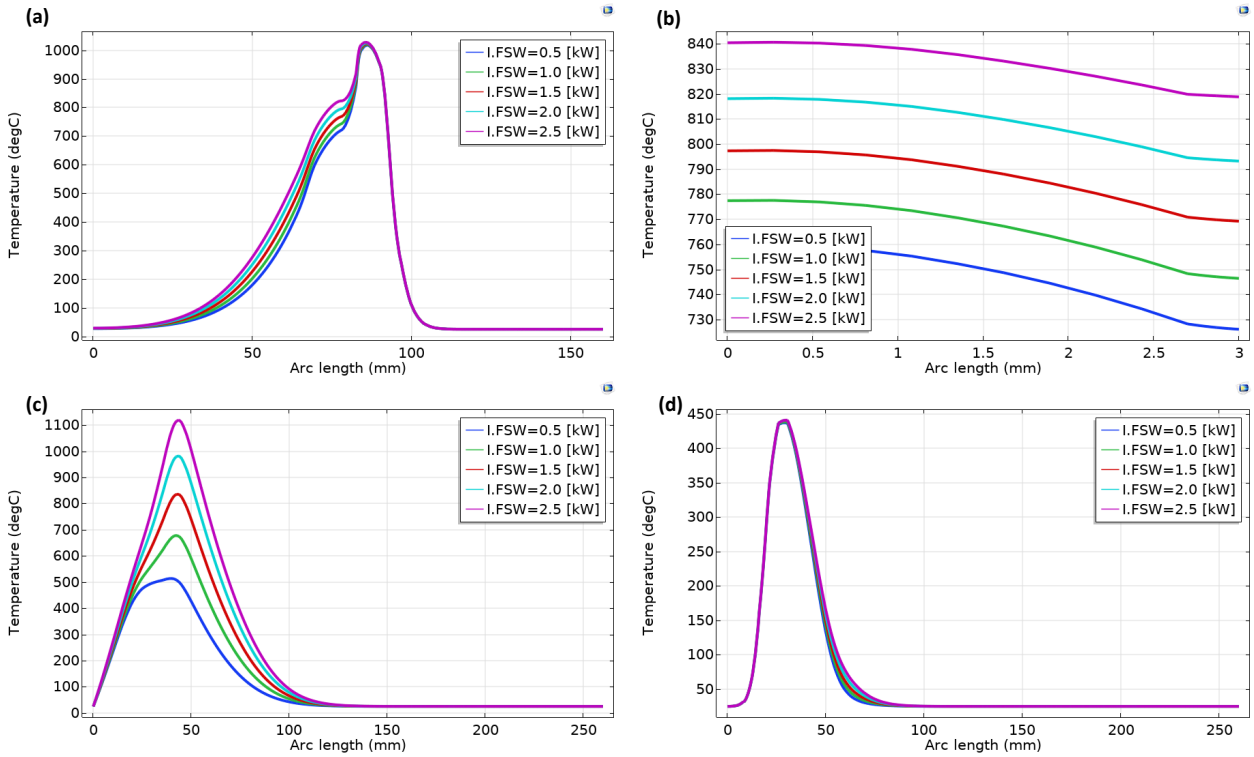

Figure 4-18: Dissimilar FSW of Inconel 718 and Ti-6Al-4V, parametric analysis on preheating load, a) 1D temperature across the nugget zone, b) 1D temperature across plate thickness at welding center line, c) 1D temperature of Inconel 718 alloy at 15mm from welding centerline, d) 1D temperature of Ti alloy at 15mm from welding centerline.

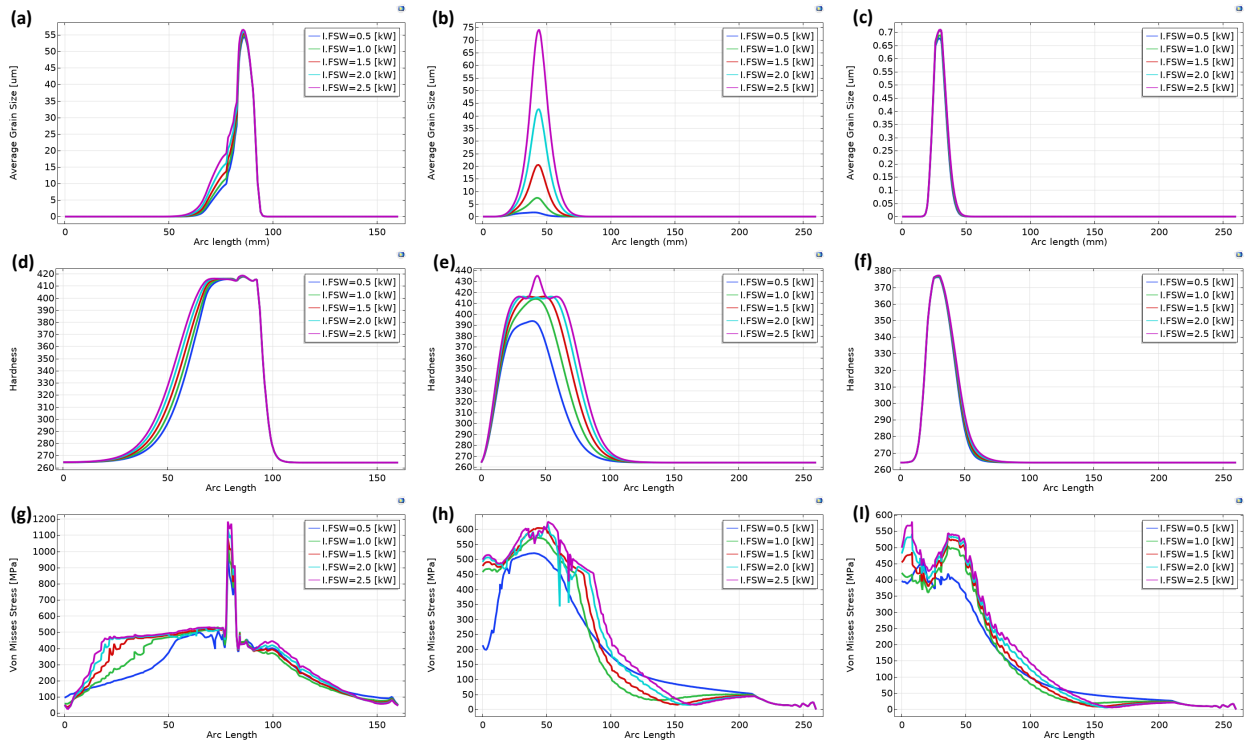

Figure 4-19: Dissimilar FSW of Inconel 718 and Ti-6Al-4V, parametric analysis on preheating load, a) 1D avg grain size across the nugget zone, b) 1D avg grain size of Inconel 718 alloy at 15mm from welding centerline , c) 1D avg grain size of Ti alloy at 15mm from welding centerline, d) 1D hardness across the nugget zone, e) 1D hardness of Inconel 718 alloy at 15mm from welding centerline, f) 1D hardness of Ti alloy at 15mm from welding centerline, g) 1D von mises stress across the nugget zone, h) 1D von mises stress of Inconel 718 alloy at 15mm from welding centerline, i)1D von mises stress of Ti alloy at 15mm from welding centerline.

4.3. Results of Statistical Analysis for the Dissimilar FSW of Inconel 718 and Ti-6Al-4V Alloys

Based on the developed finite element model, a dataset was generated by parameterizing the process parameters (rotational speed, axial force, welding speed, shoulder diameter and pin diameter) and capturing the workpiece thermal profile, grain size, hardness, and stress evolution. Taguchi, one-way ANOVA as well as regression analysis was used to understand the effect of these parameters on the welding performance. Figure 4-20, Figure 4-21, and Table 4-1 present the results of a Taguchi analysis. The mean signal-to-noise (SN) ratios as well as mean values are plotted for each parameter to identify the settings that minimize temperature variations. The analysis shows a clear downward trend in the SN ratio with decreasing rotational speed, indicating a significant impact on the

workpiece temperature. Welding speed shows minimal effect as the SN ratio remains stable across different speeds. Axial force has a strong effect, with a steep change in the SN ratio up to about 40 kN, after which it levels off. Shoulder diameter shows a moderate impact with a slight decrease in the SN ratio as it increases. Pin diameter has a negligible effect on the workpiece temperature, as indicated by minimal changes in the SN ratio. Overall, axial force and rotational speed are the most influential parameters, while welding speed, shoulder diameter, and pin diameter have lesser impacts on the workpiece temperature in FSW of dissimilar materials of high strength alloys.

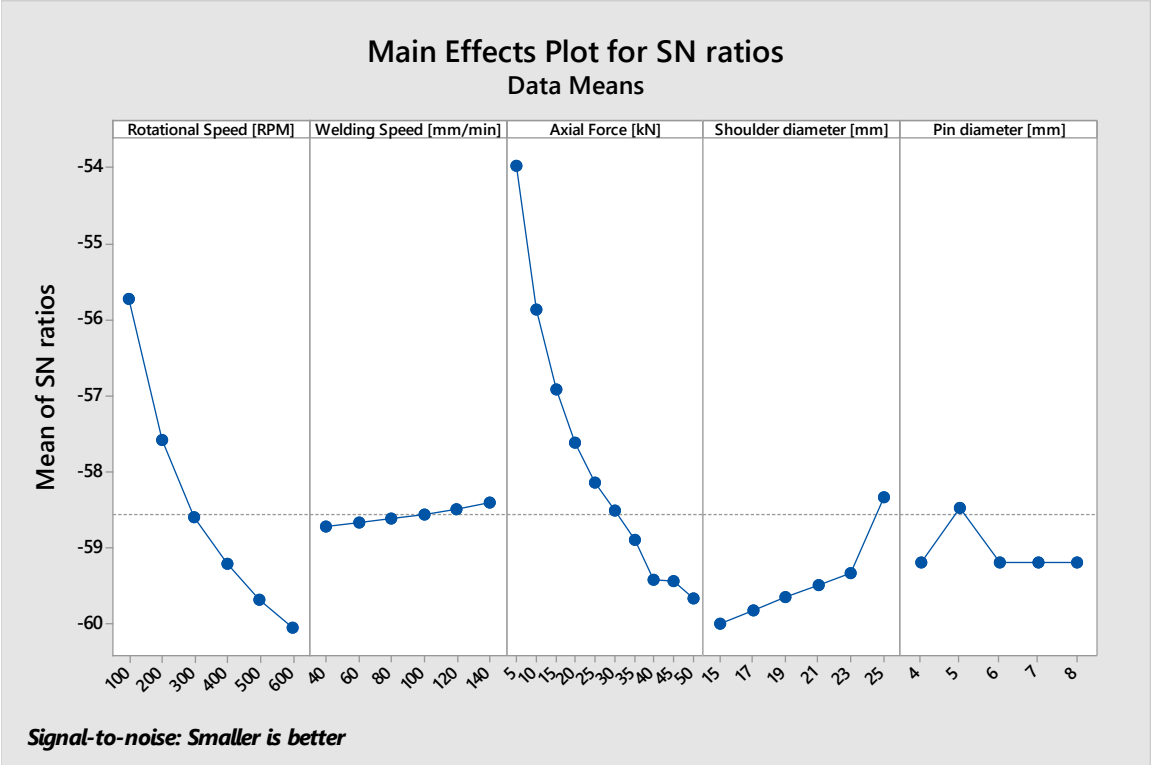

Figure 4-20: Taguchi analysis, main effects plot for SN ratios

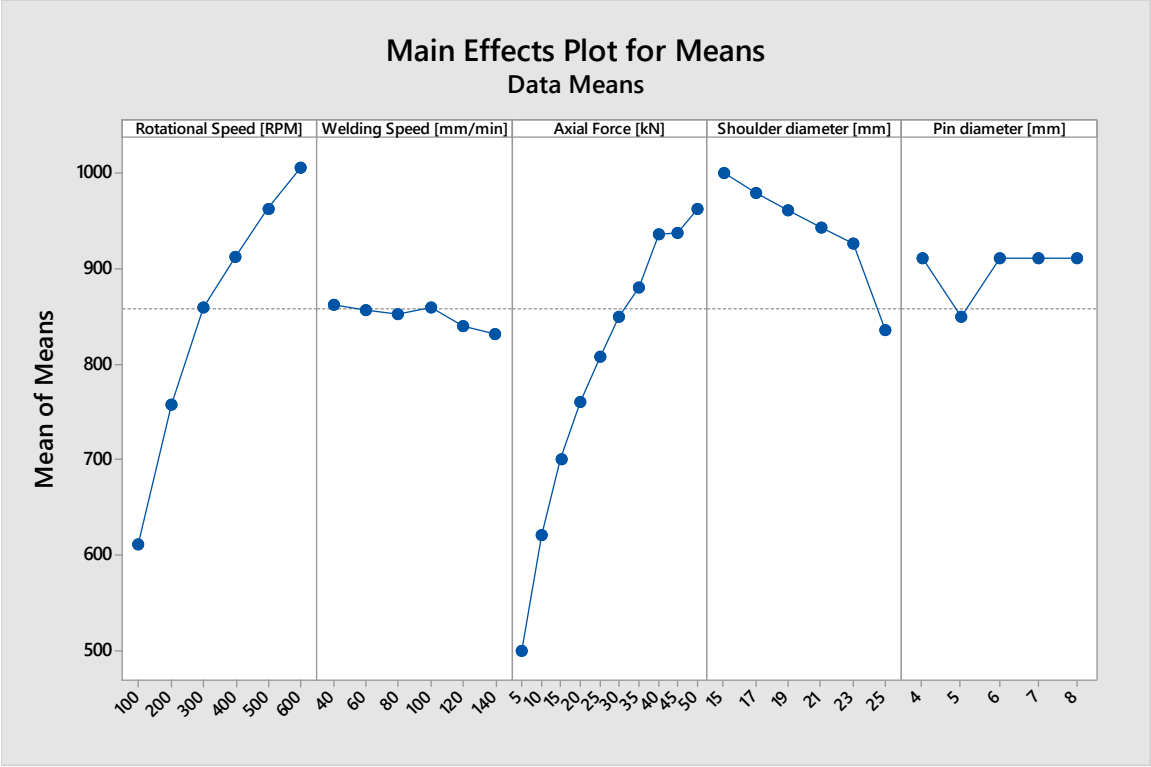

Figure 4-21: Taguchi analysis, main effects plot for means

Level	Rotational Speed [RPM]	Welding Speed [mm/min]	Axial Force [kN]	Shoulder Diameter [mm]	Pin Diameter [mm]
1	-55.72	-58.71	-53.97	-60.00	-59.19
2	-57.59	-58.66	-55.87	-59.82	-58.47
3	-58.59	-58.62	-56.91	-59.66	-59.19
4	-59.20	-58.57	-57.62	-59.49	-59.19
5	-59.67	-58.48	-58.14	-59.34	-59.20
6	-60.05	-58.40	-58.52	-58.34	
7			-58.90		
8			-59.43		

9			-59.44		
10			-59.67		
Delta	4.34	0.31	5.69	1.66	0.73
Rank	2	5	1	3	4

Table 4-1: Taguchi analysis: response table for signal to noise ratios, smaller is better

On the other hand, Table 4-2, Table 4-3, and Figure 4-22 summarize the one-way ANOVA analysis, where Tukey Simultaneous 95% Confidence Intervals (CIs) graph from the ANOVA results provides insightful comparisons across various parameters of the FSW process. The obtained results reveal significant differences where the CIs do not cross the zero line, highlighting influential relationships between parameters such as welding speed, axial force, and rotational speed. Notably, the significant deviation in axial force across different settings suggests its critical role in influencing material deformation and joint quality during welding. Conversely, the temperature comparisons across multiple parameters (shoulder diameter, pin diameter, welding speed) mostly cross the zero line, indicating no significant differences. This suggests that temperature remains relatively stable across these variables, possibly due to effective thermal management within the tested range. Such findings are crucial for optimizing FSW parameters, where understanding the impact of axial force and rotational speeds could guide adjustments to achieve optimal weld conditions. Meanwhile, the stable temperature response across various settings supports the robustness of the process under the tested conditions.

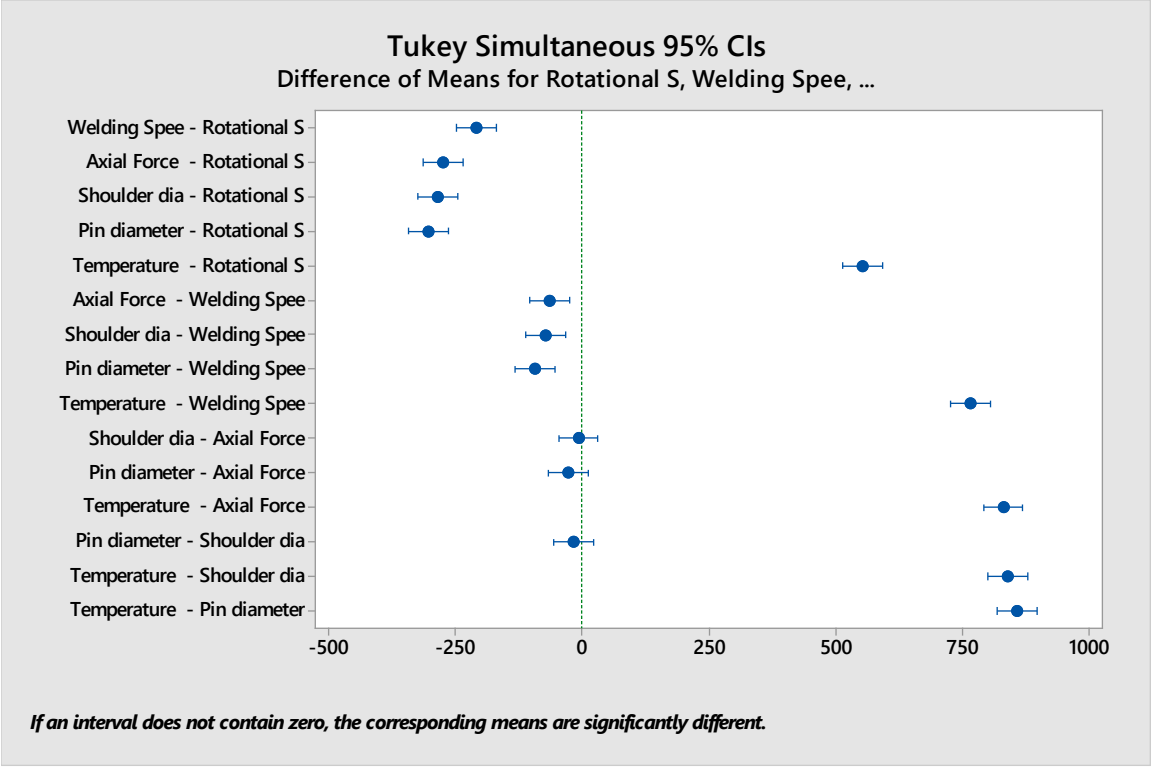

Figure 4-22: One-way ANOVA Tukey box plot

Source	DF	Adj SS	Adj MS	F-Value	P-Value
Factor	5	18848605	3769721	1193.17	0.000
Error	198	625562	3159	-	-
Total	203	19474167	-	-	-
Significance Level: 0.05					
S= 56.2086 ; R-sq= 96.79% R-sq(adj)= 96.71% R-sq(pred)= 96.59%					

Table 4-2: Analysis of Variance

Factor	N	Mean	Grouping
Temperature [°C]	34	861.9	A
Rotational Speed [RPM]	34	308.8	B
Welding Speed [mm/min]	34	98.24	C
Axial Force [kN]	34	32.79	D
Shoulder diameter [mm]	34	24.118	D
Pin diameter [mm]	34	5.147	D
Grouping Information Using the Tukey Method and 95% Confidence			
Means that do not share a letter are significantly different.			

Table 4-3: Tukey pairwise comparisons

Finally, a multiple regression analysis of the effects of the main controlling parameters namely rotational speed, and axial force on the workpiece temperature, hardness, and grain size were concluded, and the final model equations are provided below, where rotational speed (Rts in RPM), axial force (AF in kN)

- **Workpiece Temperature** (°C) = 38.4 + 1.722 Rts + 19.16 AF - 0.001385 Rts^2 - 0.169 AF^2
- **Workpiece Microhardness** (Hv) = 359.36 + 0.092 Rts + 1.0639 AF
- **Workpiece Average grain size** (μm) = 36.533 + 8.934 AF – 28.42 Rts*AF

The model building sequence (see Figure 4-23 a-c) shows the order in which terms were added, highlighting their statistical significance and the cumulative R-squared values, which reached an adjusted 96.5% for temperature, 85.8% for microhardness, and 91.4% for average grain size. The incremental impact of the variables is depicted, with axial force having the most significant effect, contributing the most to the increase in R-squared, followed by rotational speed. Each variable regressed on all other terms confirms that axial force is the predominant factor affecting the measured parameters, while rotational speed and welding speed have lesser impacts.

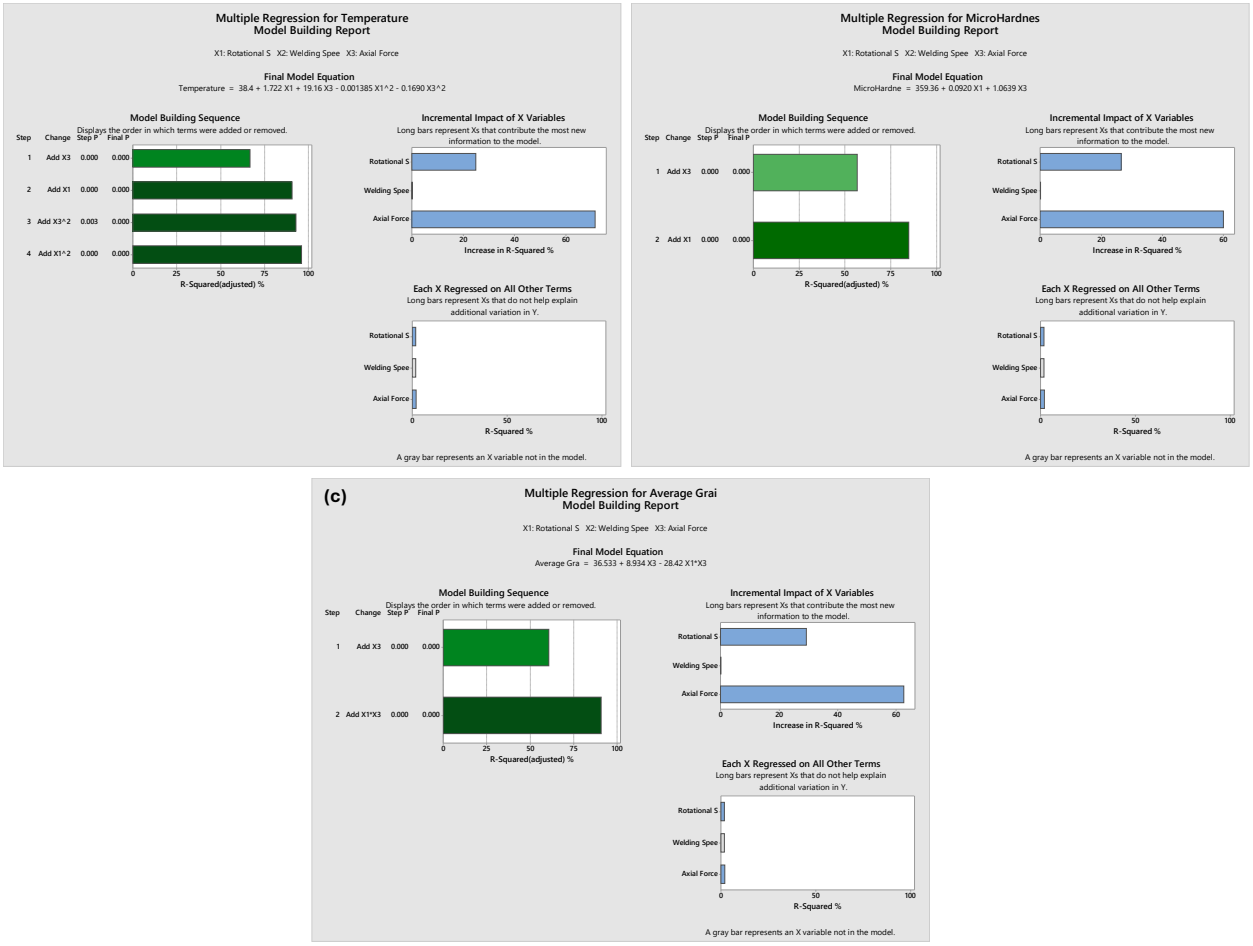

Figure 4-23: Multiple regression analysis for: a) workpiece temperature, b) workpiece microhardness and c) workpiece average grain size.

4.4. Conclusions

The comprehensive numerical analysis of FSW for dissimilar materials, specifically Inconel 718 and Ti-6Al-4V alloys, has provided significant insights into the effects of various process parameters on temperature distribution and stress evolution. The study employed a validated 3D finite element analysis (FEA) model, demonstrating its reliability in predicting the thermal and mechanical behavior of these challenging material combinations. Key findings highlight the pivotal role of rotational speed in influencing the thermal profile and grain structure of the welded joint. Higher rotational speeds were associated with increased heat generation, leading to a more uniform temperature distribution. In contrast, lower rotational speeds promoted finer grain sizes, enhancing the

mechanical properties of the weld. The axial force was found to be the predominant factor affecting residual stress distribution, with higher forces resulting in greater stress concentrations within the weld zone. These results underscore the critical importance of optimizing FSW parameters to achieve high-quality welds in dissimilar materials. By carefully balancing rotational speed, welding speed, and axial force, it is possible to minimize thermal and mechanical discrepancies, thereby improving the performance and durability of the welded joints.

This chapter provides a foundational understanding of the FSW process for dissimilar materials, with significant implications for aerospace applications. The ability to join Inconel 718 and Ti-6Al-4V alloy efficiently opens new possibilities for manufacturing high-strength, lightweight components essential for modern aerospace engineering. Future research should focus on further refining the FEA model and exploring additional material combinations to expand the applicability of FSW technology. The insights gained from this work pave the way for advancements in welding techniques, contributing to the development of more reliable and efficient joining processes for complex material systems.

CHAPTER 5: Workpiece Temperature Control in FSW of Inconel 718 Alloy

5.1. Introduction

Friction stir welding offers significant advantages over fusion welding, particularly for high-strength alloys like Inconel 718. However, achieving optimal surface quality in Inconel 718 FSW remains challenging due to its sensitivity to temperature fluctuations during welding. In this chapter, a study integrates finite element simulations, statistical analysis, and advanced control methodologies to enhance weld surface quality through adequate thermal management. Based on the high-fidelity simulations of the FSW process reported in CHAPTER 3:, a comprehensive dataset correlating process parameters (rotational speed, axial force, and welding speed) with workpiece temperature were generated. This dataset facilitated statistical analysis and parameter optimization through Analysis of variance (ANOVA) method, leading to a deeper understanding of process variables. Accordingly, a nonlinear state-space system model was subsequently developed using simulation data and the system identification toolbox in Matlab, incorporating domain-specific insights. This model was rigorously validated with an independent dataset to ensure predictive accuracy. Utilizing the validated model, tailored control strategies, including proportional-integral-derivative (PID) and model predictive control (MPC) in both single and multivariable configurations, were designed and evaluated. These control strategies excelled in maintaining welding temperatures within optimal ranges, demonstrating robustness in response times and disturbance handling. This precision in thermal management is poised to significantly refine the FSW process, enhancing both surface integrity and microstructural uniformity. The strategic implementation of these controls is anticipated to substantially improve the quality and consistency of welding outcomes.

5.2. Methodology and System Identification

The methodology followed in this study (see Figure 5-1) to perform adequate process control involves importing and preprocessing input-output data from the generated dataset to enhance relevance and accuracy. A suitable model structure is then selected based on the system's characteristics, with options including transfer functions, state-

space models, and ARX (AutoRegressive with eXogenous inputs) models available in MATLAB's toolbox. Specific data subsets are defined for model estimation, and advanced algorithms are applied to optimize the model parameters for the best fit. The model's accuracy is rigorously evaluated against a separate validation dataset to ensure it replicates the system's behavior effectively. Adjustments and refinements are made as necessary to enhance performance.

In industrial control systems, PID control and MPC are widely employed due to their ability to be finely tuned to meet specific performance criteria. These control strategies have been extensively utilized within the context of the FSW process as explained in section 1.10. PID controllers, known for their simplicity and effectiveness in a wide range of operating conditions, adjust the process based on the error between a setpoint and the process variable. On the other hand, MPC provides a more sophisticated approach by predicting future system behavior and optimizing control moves accordingly. This predictive capability makes MPC particularly valuable for managing the intricate dynamics of FSW, allowing for precise adjustments in response to the thermal and mechanical variables affecting the welding quality.

Two operational modes are considered for each control strategy to adapt to different process requirements. The first mode simplifies the control structure by using only the Rotational Speed (RtS) as the control variable, treating Axial Force (AF) and Welding Speed (WS) as disturbances. This mode focuses on controlling the rotational speed to stabilize the welding process temperature while monitoring the effects of AF and WS. The second mode expands the control framework to include RtS, AF, and WS as control variables, aiming for more robust control. This comprehensive approach ensures that all influencing factors are actively regulated, enhancing the process's adaptability and performance under varying operational conditions. Both control techniques were implemented to enhance the process stability and optimize the welding parameters, ensuring the robustness and accuracy of the FSW process.

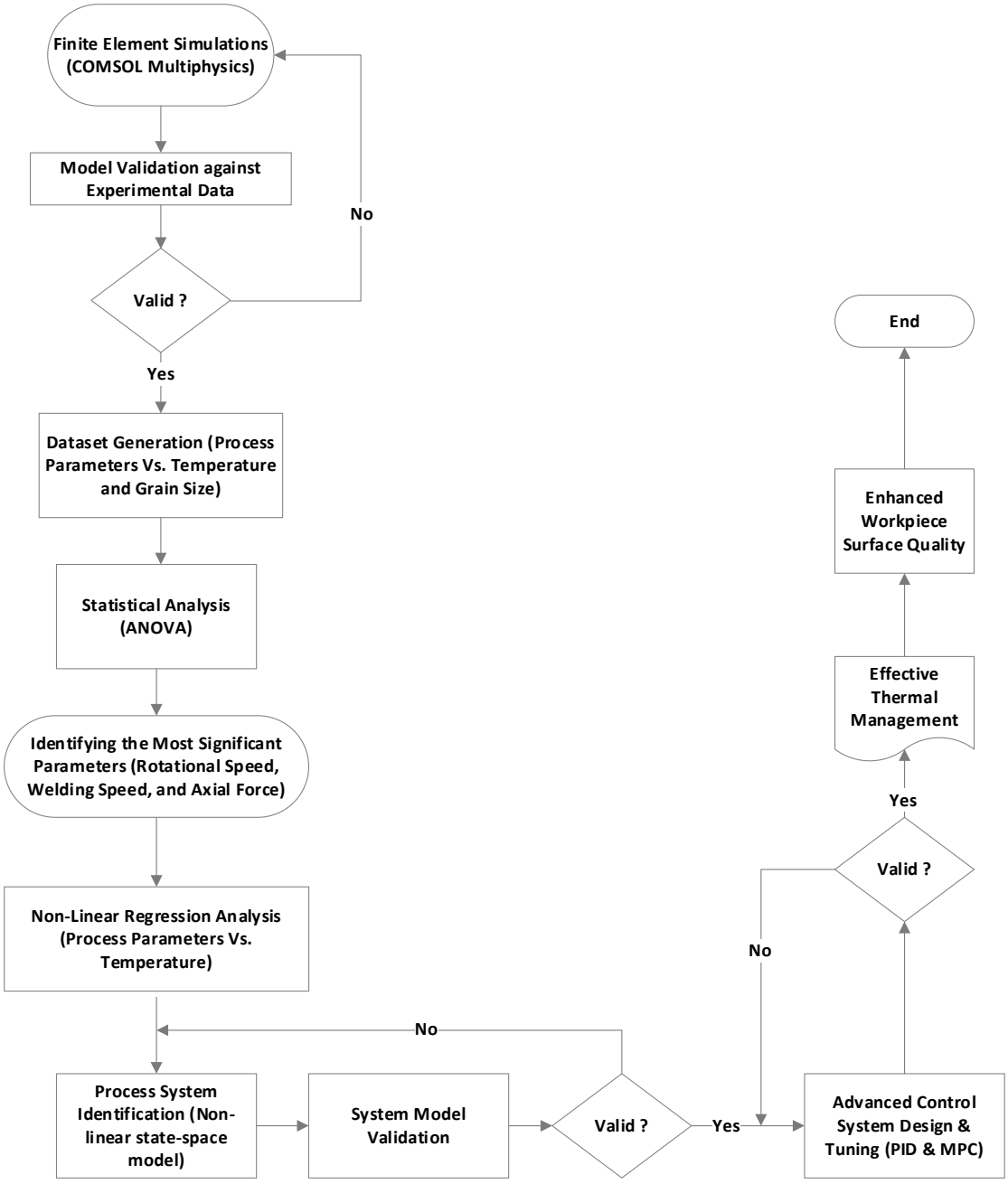

Figure 5-1: Flow chart for the developed model system

FSW is characterized by significant nonlinearities. An initial system identification was conducted using MATLAB's System Identification Toolbox, leveraging the FSW dataset generated from the COMSOL finite element model. After importing the numerical experimental data into the toolbox, a curve fitting procedure was utilized to approximate the FSW process model. Among the various tested models, it is found that the ARXQS

(Fourth-order autoregressive ARX model) and TF (Transfer Function) generate the best estimates. This is shown in Figure 5-2. It was concluded that the match of the ARXQS model output with that of numerical experimental data is 99.21% whereas that of continuous time TF has a match of 99.63% and discrete time TF has a match of 99.95%. These three have good matches but do not actually capture the real system behavior due to the inherent nonlinearities. Thus, the system identification toolbox could not give a realistic system model of the FSW. Among all the tested models, the closest fit found was the discrete time model using transfer function, which is given below, where z is discrete time domain:

$$\left[\frac{0.38248\,z^{-1}}{(1-0.6078\,z^{-1})(1+0.2544\,z^{-1})} \quad \frac{2.095\times10^{-5}\,z^{-1}}{(1-z^{-1})(1-0.1662\,z^{-1})} \quad \frac{3.7657\,z^{-1}}{(1-0.8189\,z^{-1})(1+0.1232\,z^{-1})}\right]$$

Accordingly, here the Nonlinear Model Identification and refinement is proposed, where the initial application of the system identification toolbox captured main features of the process but failed to accurately capture the whole system dynamics, necessitating a refinement of the model identification process. This was achieved by integrating expert knowledge and insights about the physical system to address accuracy issues and obtain a valid nonlinear model. Adopting this strategy, an initial nonlinear model was established, and various parameters and nonlinear elements were fine-tuned to optimize the correlation with experimental data. Multiple iterations enhanced the model's fit significantly. This refined process led to the accurate identification of a nonlinear state-space model as described below:

State equations:

$$\dot{x}_1 = -10.43\,x_1 - 12.86\,x_2 + 12.86\,u_1$$

$$\dot{x}_2 = x_1$$

$$\dot{x}_3 = (0.0011\,u_2 - 0.056)x_4$$

$$\dot{x}_4 = \frac{-12.5}{0.0011\,u_2 - 0.0555}x_3 - 11.25\,x_4 + 12.5\,u_2$$

$\dot{x}_5 = x_6$

$\dot{x}_6 = -8.75\ x_5 - 8.25x_6 + 8.75\ u_3$

Output equation:

$y = (-0.00075\ u_1 + 1.21)x_2 - x_3 + (-0.2396\ u_3 + 21.3)x_5$

Where: -

$u_1 =$ Rotational Speed

$u_2 =$ Welding Speed

$u_3 =$ Axial Force

$y =$ Temperature

$x_1, x_2, x_3, x_4, and\ x_5$ are state variables of the space-space model

The state-space model in matrix form is as follows:

System Matrix (A)

$$\mathbf{A} = \begin{bmatrix} -10.43 & -12.86 & 0 & 0 & 0 & 0 \\ 1 & 0 & 0 & 0 & 0 & 0 \\ 0 & 0 & 0 & -0.056 & 0 & 0 \\ 0 & 0 & -0.0555 & -11.25 & 0 & 0 \\ 0 & 0 & 0 & 0 & 0 & 1 \\ 0 & 0 & 0 & 0 & -8.75 & -8.25 \end{bmatrix}$$

Input Matrix (B)

$$\mathbf{B} = \begin{bmatrix} 12.86 & 0 & 0 \\ 0 & 0 & 0 \\ 0 & 0.0011 & 0 \\ 0 & 12.5 & 0 \\ 0 & 0 & 0 \\ 0 & 0 & 8.75 \end{bmatrix}$$

Output Matrix (C)

$$\mathbf{C} = \begin{bmatrix} 0 & 1.21 & -1 & 0 & 21.3 & 0 \end{bmatrix}$$

Feedthrough Matrix (D)

$$\mathbf{D} = \begin{bmatrix} -0.00075 & 0 & -0.2396 \end{bmatrix}$$

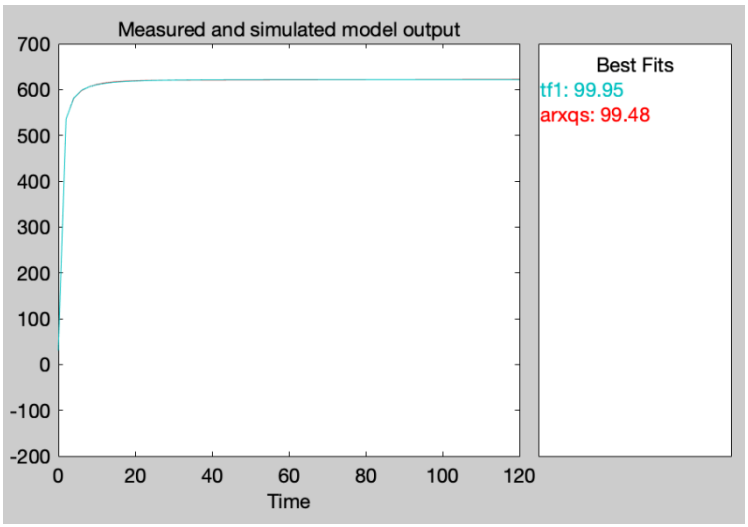

Figure 5-2: ARXQS and TF generate the best possible fit

5.3. Model Construction and Validation

The developed nonlinear model was implemented in Simulink, as depicted in Figure 5-3a and b. Figure 5-3a presents the subsystem block diagram, and subplot (b) details the internal configuration of the Simulink model. The model achieved an excellent match with the numerical experimental data, a conclusion supported by numerous simulations using varied control input values. Figure 5-4 illustrates the system's response from simulations of the nonlinear model alongside plots of experimental data for selected cases. The model was also exposed to input disturbance in the form of step change of axial force as shown in Figure 5-5. This confirms the model's ability to satisfactorily capture the underlying physical system dynamics. Having developed a satisfactory mathematical model, it is feasible to design adequate control systems that accurately track the desired reference welding temperature across different operating conditions.

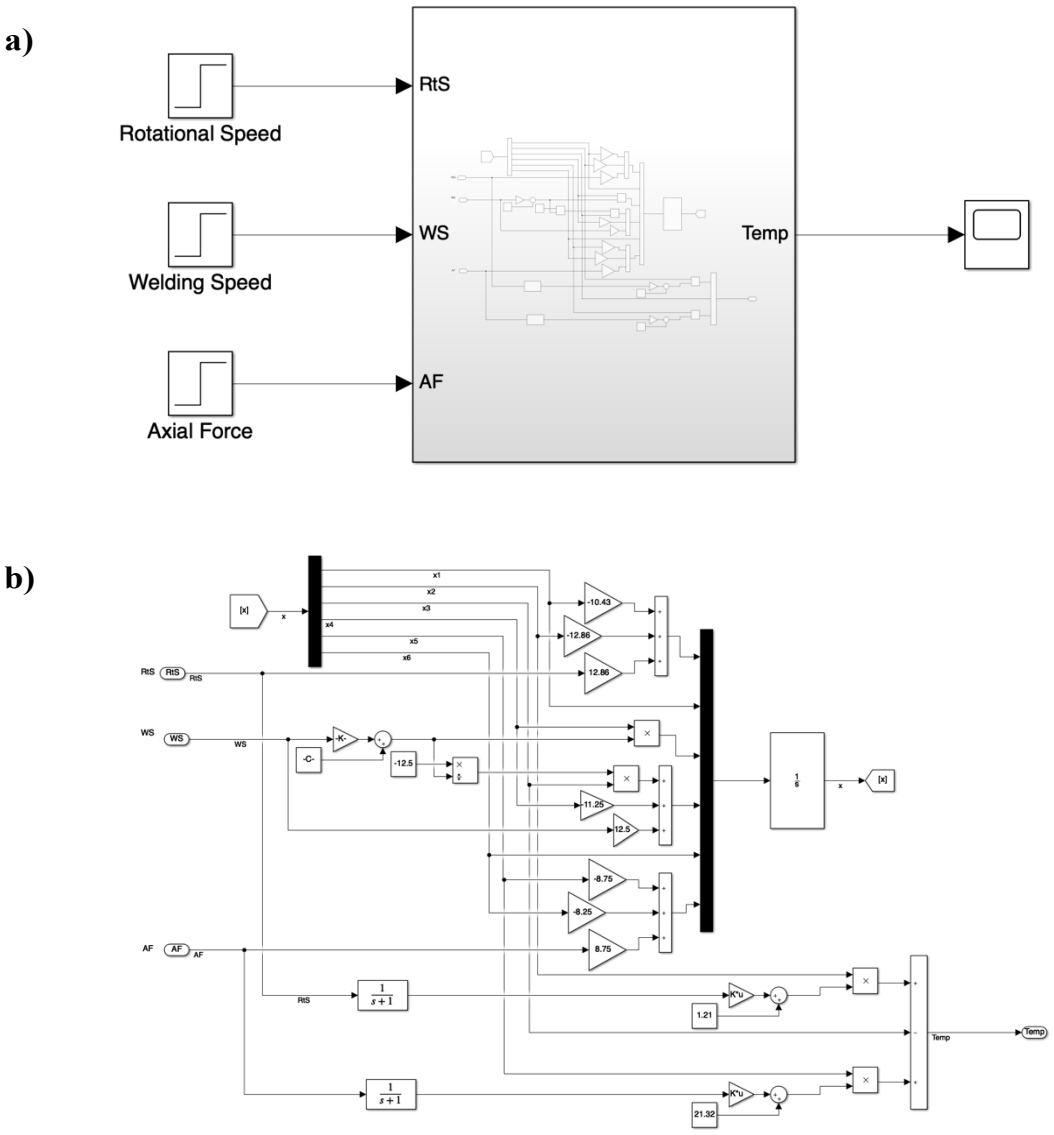

Figure 5-3: Simulink implantation of nonlinear model (a) block diagram (b) detailed description of the Simulink implementation

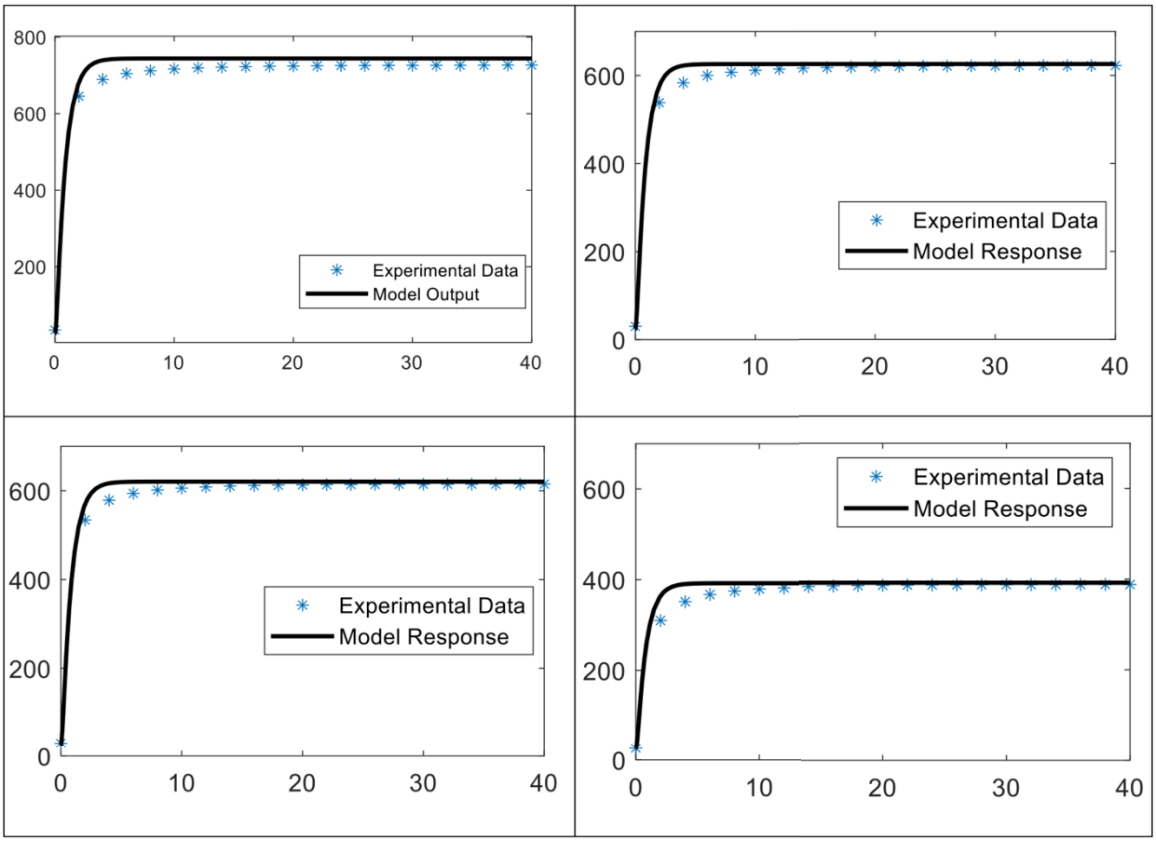

Figure 5-4: Plot of response of system and the numerical experimental data for various conditions of input signals. (a) RtS = 300 [RPM], WS = 90 [mm/min], AF = 35 [kN] (b) RtS = 400 [RPM], WS = 90 [mm/min], AF = 15 [kN](c) (b) RtS = 300 [RPM], WS = 100 [mm/min], AF = 20 [kN](d) RtS = 300 [RPM], WS = 90 [mm/min], AF = 5 [kN]

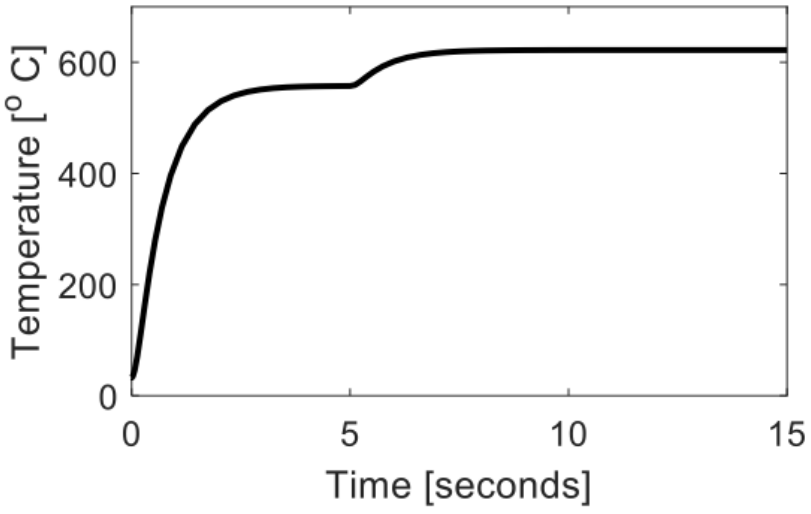

Figure 5-5: Open loop system response to increase in welding axial force

5.4. Process Control

For the purpose of FSW process control, two primary control strategies are explored: PID and MPC. Each strategy is implemented in two distinct configurations: single-variable and multi-variable control modes. In the single-variable mode, rotational speed serves as the primary control variable for adjusting the welding temperature, with axial force and welding speed treated as external disturbances. This approach focuses on straightforward control by manipulating one key variable to achieve desired temperature outcomes. The reason for selecting rotational speed is due to its significant effect on the workpiece temperature, and it is practically easier to control compared to axial force. Conversely, the multi-variable mode leverages a more comprehensive approach by simultaneously controlling multiple variables—rotational speed, axial force, and welding speed. This mode aims to optimize the control performance by adjusting several inputs in concert, allowing for a more refined and responsive control system. These configurations highlight the versatility and adaptability of PID and MPC strategies in addressing different complexities within the FSW process.

5.4.1. PID Control

PID control is one of the most widely used controllers for industrial processes. The PID controller utilizes three terms to compute the control signal sent to an actuator, these are the Proportional (P) Term, Integral (I) Term, and the Derivative (D) Term. Proportional term responds immediately to the current error value, where a larger error results in a higher output correction. Integral term addresses long-term errors by accumulating the error over time. It helps eliminate any steady-state error, where the output settles at a value different from the setpoint. Derivative term anticipates future errors by considering the rate of change of the error signal. It helps reduce oscillation and speeds up the system's response to setpoint changes. For the FSW process, two different control modes are considered to design and implement the PID controller, single variable, and multi-variable modes.

5.4.1.1. Single Variable PID Control

In the first configuration of PID control strategy, a single PID controller is designed, as indicated in the Simulink block diagram of Figure 5-6. The Rotational Speed (RtS) is taken as the control input, whereas Axial Force (AF) and Welding Speed (WS) are treated as disturbances. The initial design of the PID controller is fine-tuned using the Simulink Response Optimization Toolbox. The tuned PID controller parameters are given in Table 5-1. It is worth mentioning that the controller parameters are tuned to tackle the actuator saturation problem as well. That is, the controller ensures the performance while keeping all the variables within their defined limits.

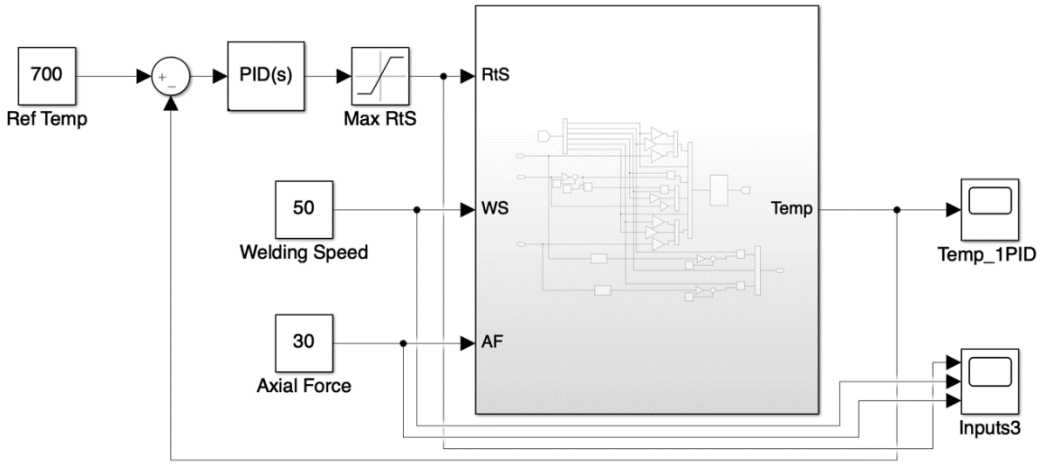

Figure 5-6: PID control for FSW process, where rotational speed is taken as control input, welding speed and axial force are treated as disturbances

Transfer function of PID control	$P + I\frac{1}{s} + D\frac{N}{1 + N\frac{1}{s}}$
P	0.4160
I	0.7053
D	0.0010

Table 5-1: Designed PID controller for FSW

The simulation results corresponding to the designed controller with the welding speed equal to 35 mm/min and Axial Force equal to 25 kN are shown in Figure 5-7. The controller successfully

stabilized the temperature at the desired value (in simulations at 700 °C). The simulations are repeated for several different values of welding speed and axial force, and it is seen that the controller successfully tracks the reference signal despite variations in AF and WS. That is, we can set AF and WS at any level and the controller will automatically adjust the RtS to achieve desired temperature. The response of the system to a step change in Axial Force at time T = 10 seconds is shown in Figure 5-8, which again shows the proficiency of the controller. One advantage of single PID controller is the freedom to choose any suitable, convenient and cost-effective values of WS and AF.

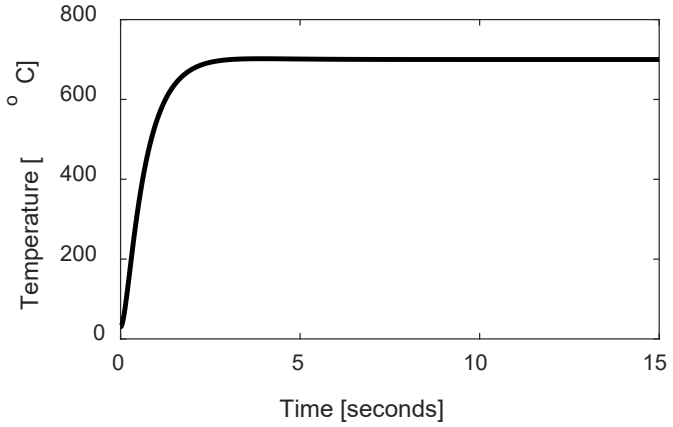

Figure 5-7: Closed-loop response of the FSW system with single PID controller

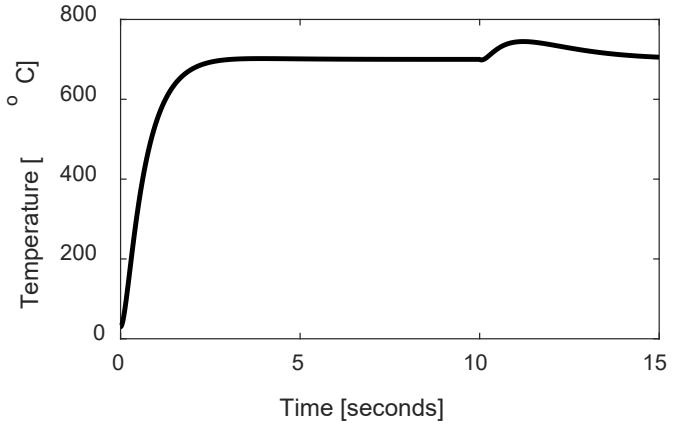

Figure 5-8: Response of closed loop system with PID control and step increase in axial force at time T = 10 seconds.

5.4.1.2. Multi Variable PID Control

In the second case, three distinct PID controllers are tuned, each controller to control each of the three process inputs, that is the RtS, WS, and AF. The Simulink block diagram corresponding to this scenario is shown in Figure 5-9. The parameters of the PID controllers are optimally tuned using the Simulink Response Optimization Toolbox, the parameters of the tuned PID controllers are given in Table 5-2 . Like the previous case of single PID controller, the problem of actuator saturation is taken care of for the three PID controllers. The simulation results corresponding to the case of three PID controllers are shown in Figure 5-10. It can be clearly seen that this design can also successfully track the reference temperature with good performance.

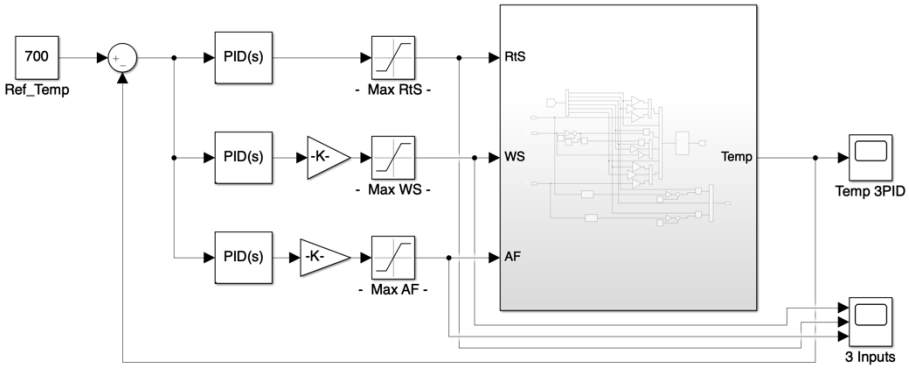

Figure 5-9: Three PID controllers with adjustable weights are designed for FSW

Transfer function of PID control	$P + I\frac{1}{s} + D\frac{N}{1 + N\frac{1}{s}}$
P	0.4160
I	0.7053
D	0.0010
Weight associated with WS	0.0977
Weight associated with AF	0.0939

Table 5-2: Parameters of designed PID controllers for FSW and weights

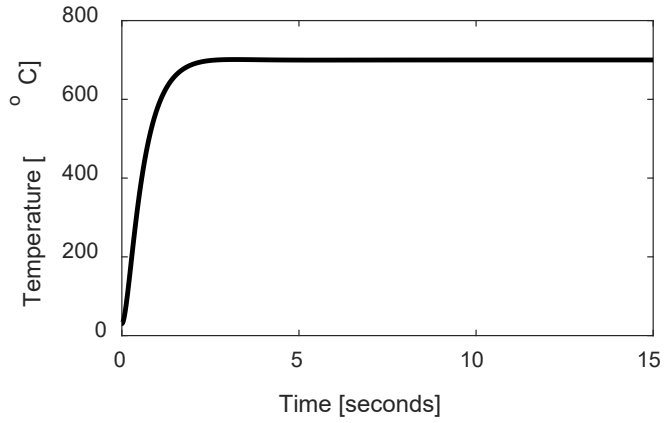

Figure 5-10: Response of FSW with three PID controllers

Compared with the case of one PID controller, the three PID controller automatically adjusts all the three control inputs (RtS, WS, and AF) to track the desired temperature, thereby, putting proportional load to all the control inputs. However, with this arrangement, we lose the freedom of manual adjustments on the AF and WS. An additional advantage in the three PID controller case is that tunable weights associated with three control inputs are also provided. These tunable weights can provide additional freedom which can be utilized to achieve some other optimization. For example, if any of the three control inputs is associated with some additional cost / energy consumption, that variable can be given more weight to achieve the desired temperature with less consumption of energy.

5.4.2. Model Predictive Control

MPC is an advanced technique used to control dynamic systems while adhering to constraints. Unlike PID controllers which focus on the present error, MPC takes a future-oriented approach. MPC relies on a mathematical model that predicts the future behavior of the system based on current state and control inputs. MPC considers a finite window of time steps into the future, called the prediction horizon. It predicts the system's response for various control actions over this horizon. MPC solves an optimization problem to determine the control sequence that minimizes a cost function while keeping the predicted system behavior within specified constraints. For the FSW process, two different strategies, like the situations in the design of PID controller, are proposed to

design and implement MPC. That is, in the first strategy, a single MPC is there to control RtS and treat AF and WS as disturbances. In the second strategy, three different MPC to adjust each of the three control inputs (RtS, WS and AF) to track the temperature.

5.4.2.1. Single Mode Predictive Control

The block diagram of a single MPC for the FSW is shown in Figure 5-11. Like the case of single PID controller, there is a freedom to choose any value of the AF and WS and the MPC will adjust the RtS to track the reference temperature. The simulation results for the case of single MPC are shown in Figure 5-12, which also confirms the successful control of the workpiece temperature at 700°C.

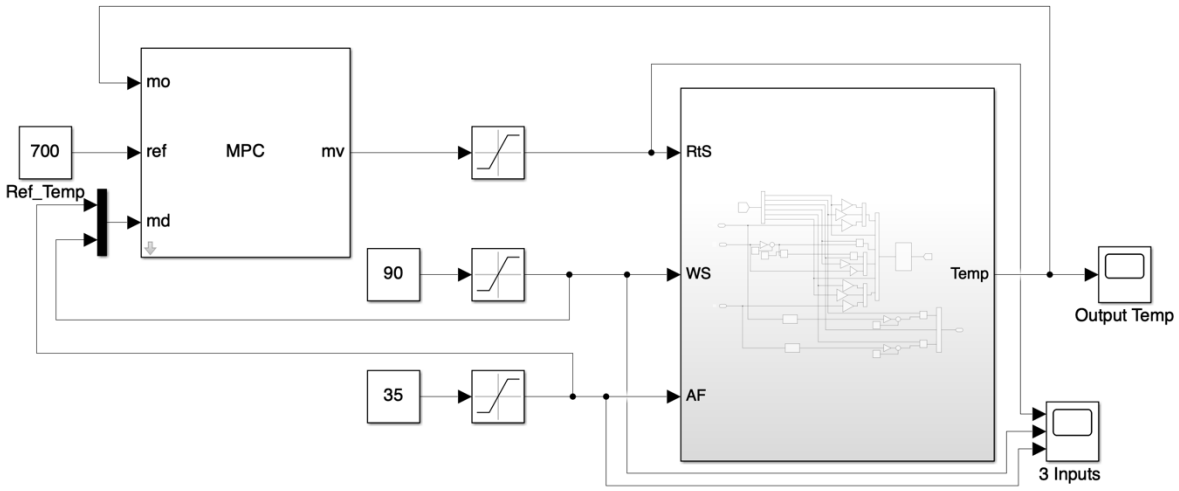

Figure 5-11: Single MPC for FSW with WS and AF considered as disturbances

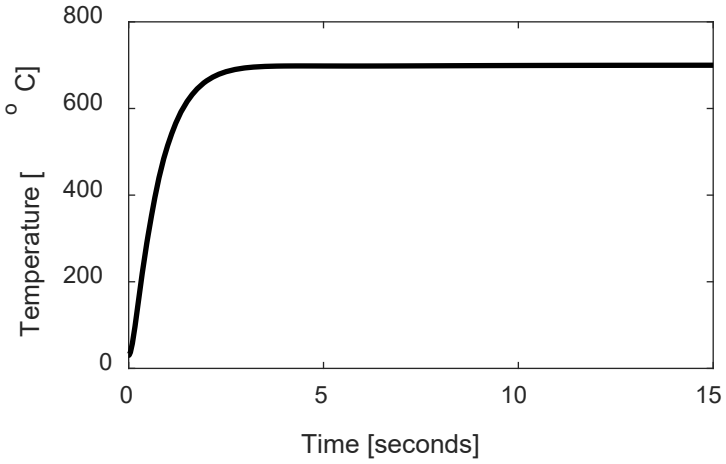

Figure 5-12: Response of FSW with single MPC

5.4.2.2. Multi-Variable Model Predictive Controllers

In the second case of MPC, where three MPC are designed to control each of the three control inputs, that is the Rotational Speed, Axial Speed and the Welding Speed. The block diagram of three MPC is shown in Figure 5-13. The MPC are designed using Simulink Model Predictive Control Toolbox. Each of the three control inputs have some saturation limits, therefore, saturation blocks are also added in the design procedure. Furthermore, two gain blocks are added to the controller against welding speed and axial force. These gain blocks are adjustable and can be utilized for some additional optimization, for example, energy / cost optimization. For the design of the MPC, the following parameters are set.

- Sampling time: 0.5 (seconds)
- Prediction Horizon: 5
- Control Horizon: 1

The simulation results for the case of three MPC is shown Figure 5-14. It can be seen from the figure that the three MPC case can also be utilized to maintain the temperature at the desired level. Furthermore, the effect of sudden disturbance in Axial Force introduced at a time of T = 10 seconds is shown in Figure 5-15. It is observed that the controller can maintain the temperature despite some bias or variation in some of the actuators.

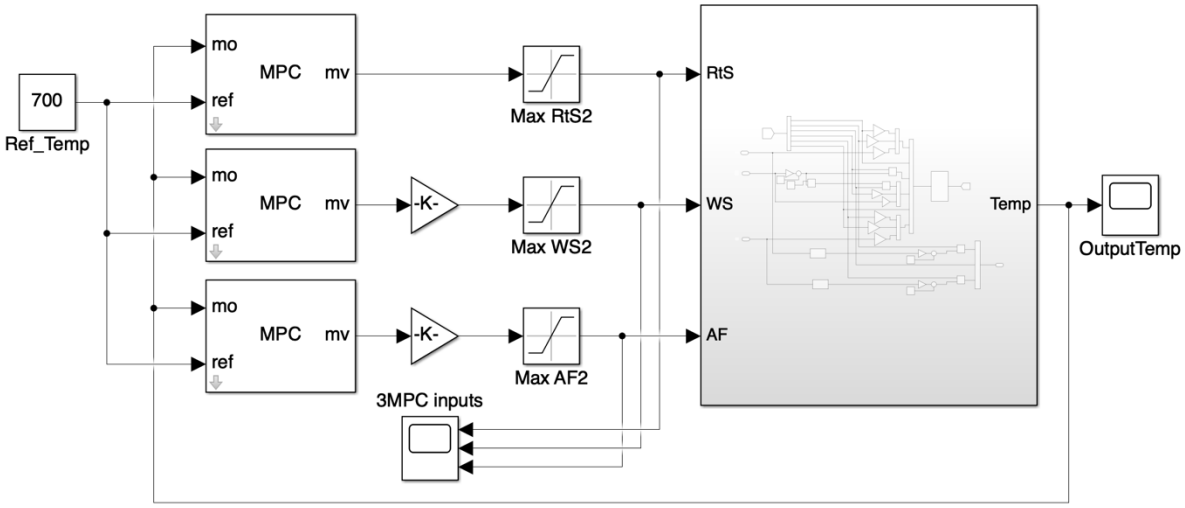

Figure 5-13: Simulink diagram of three MPC for FSW

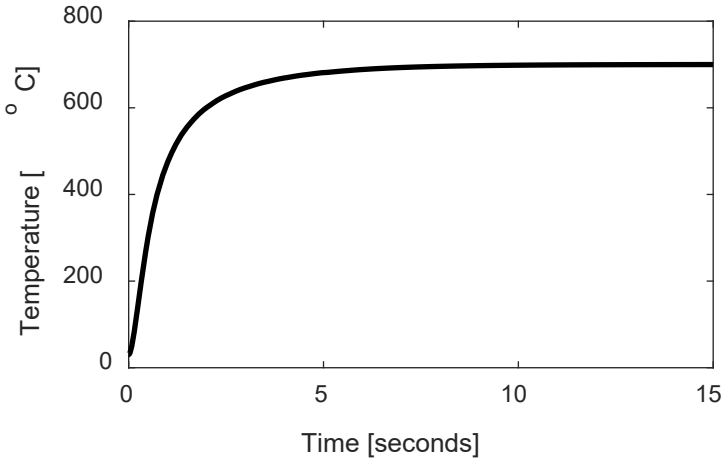

Figure 5-14: Response of closed loop system with three MPC

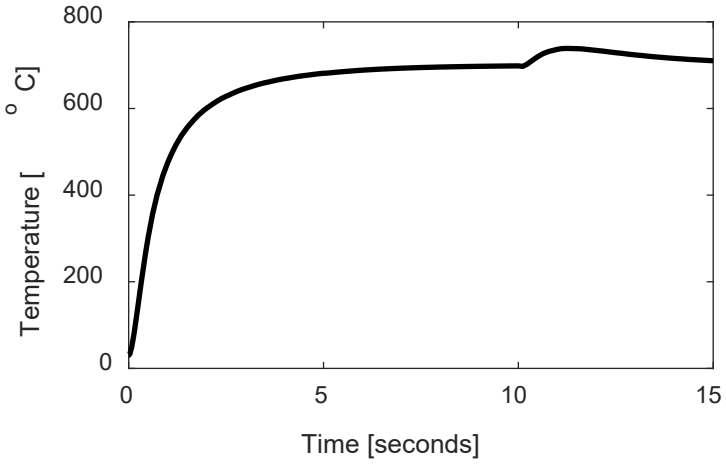

Figure 5-15: The MPC response to axial force disturbance

5.4.3. Comparison of Designed Control Systems

After exploring various control system designs, it is beneficial to compare and evaluate them to gain a comprehensive understanding of their performance, along with the advantages and disadvantages of each model. It is worth mentioning that all controllers have been tuned to give the best possible performance. Figure 5-16 below presents a comparison of the PID and MPC controllers in both their single and multi-variable control modes through a hypothetical scenario of temperature set point alteration and disturbances in axial force and welding speed.

Initially, during the transient state, all controllers exhibit similar responses, with the PID controllers (3PID followed by 1PID) responding slightly faster than their MPC counterparts, a trend that persists after the second temperature setpoint change. At the 70-second mark, when the temperature setpoint dropped by 400°C, the PID controllers maintained their faster response, but the multi-variable controllers (3PID and 3MPC) experienced noticeable undershoots, while the single-variable controllers (1PID and 1MPC) approached the new setpoint more steadily. During the axial force disturbance introduced at 85 seconds, the single-variable controllers (1PID and 1MPC) managed the disturbance more effectively, showing minimal overshot. In contrast, both multi-variable controllers (3PID and 3MPC) struggled with significant overshoots. Surprisingly, when it came to handling disturbances from welding speed at 100 seconds, the multi-variable

controllers (3PID and 3MPC) performed better, exhibiting minimal undershoot, while the single-variable controllers displayed more significant undershoot. Throughout the remainder of the test, PID controllers consistently demonstrated a faster response to changes in desired temperature, indicating their potential superiority in scenarios where speed of response is critical. Figure 5-17 illustrates the response of the four designed control systems to changes in the temperature setpoint and disturbances caused by variations in axial force and welding speed.

As observed in Figure 5-17, there are slight variations in the response of each controller to changes during steady-state conditions, which can be attributed to differences in their level of complexity and operating principles. Nonetheless, all proposed control systems demonstrate satisfactory performance in maintaining the temperature within acceptable operating limits. These observations and analysis underscore that while no single controller excels in every aspect, the choice between them can be optimized based on specific operational priorities such as response speed, stability, or disturbance handling.

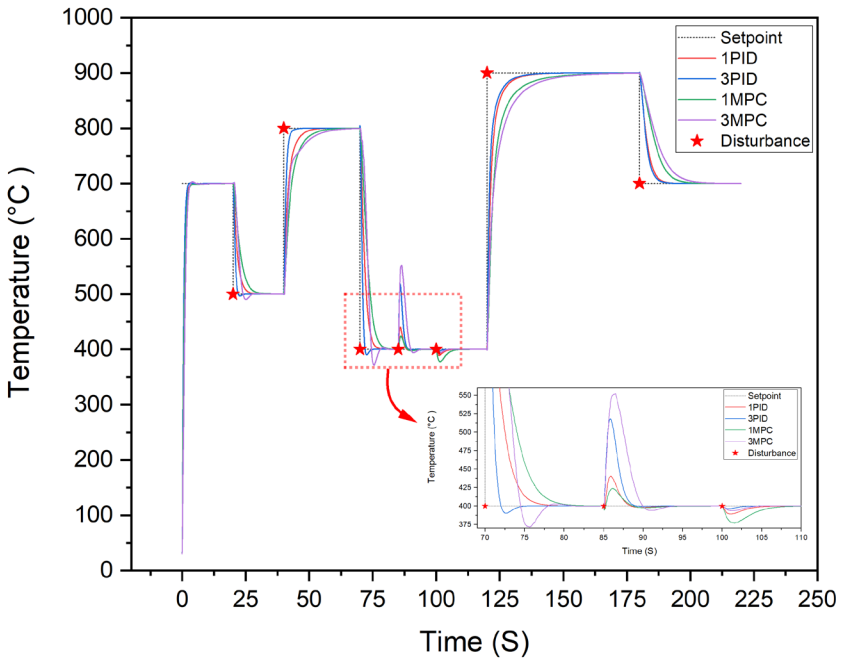

Figure 5-16: Comparison of designed control systems

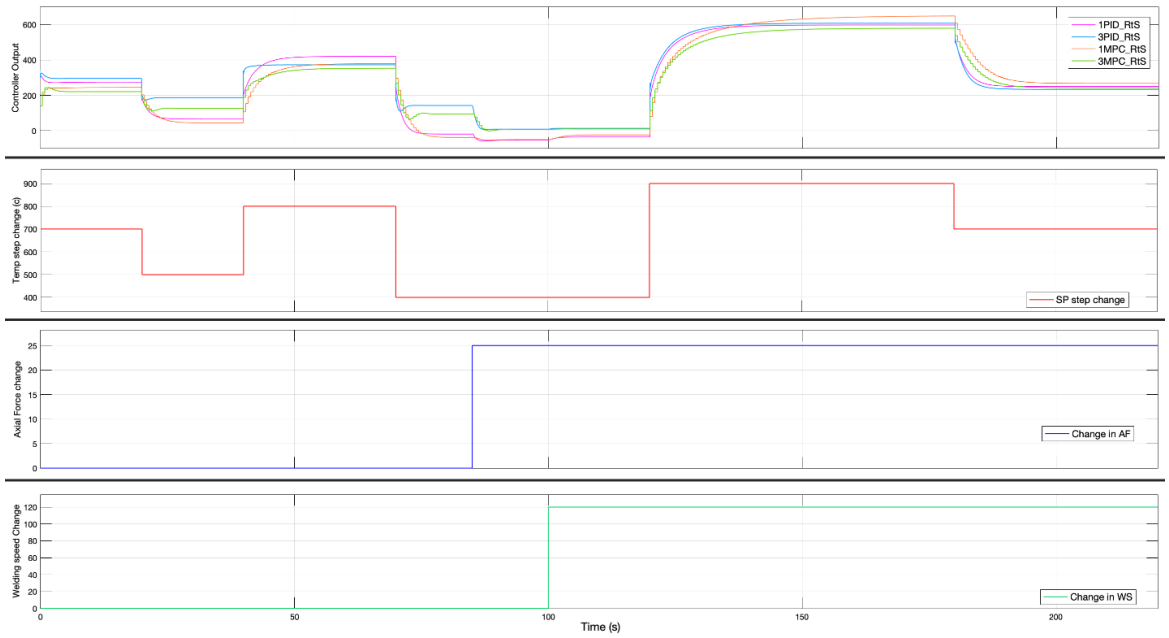

Figure 5-17: Controller output

5.5. Conclusion

This research outlines a comprehensive methodology for controlling the workpiece temperature of friction stir welds in Inconel 718 through the integration of finite element simulations, statistical analysis, and system control. Building on the robust dataset that informed the statistical optimization of process parameters. The insights gained from ANOVA guided the selection of best process parameters then the development of a nonlinear state-space model, which was validated for accuracy against a secondary dataset. The confirmed model underpinned the formulation of precise PID and MPC control strategies, optimizing thermal dynamics during welding. Both PID and MPC strategies in their single variable and multi-variable modes proved to be successful in controlling the FSW workpiece temperature with minor differences in terms of response time and disturbance handling. The application of these strategies effectively addresses temperature control issues commonly known for causing defects associated with FSW. This approach not only advances the FSW process for Inconel 718 but also sets a precedent for applying similar methodologies to other high-performance alloys, with implications for enhancing manufacturing processes and operational scalability.

Summary and General Conclusions

This thesis comprehensively investigates the optimization of Friction Stir Welding (FSW) parameters for nickel-based superalloys, specifically Inconel 718, with a focus on enhancing welding performance and mechanical properties. The research spans various analytical techniques, including finite element modeling, Taguchi analysis, ANOVA, and non-linear regression, to derive significant insights into the FSW process.

The initial chapter lays the foundation by reviewing the current state of FSW technology, particularly its application to nickel-based superalloys like Inconel 718. It underscores the challenges associated with welding high-strength materials and highlights the need for advanced thermal management strategies. The literature review, encompassing around 275 references, provides a comprehensive overview of the existing knowledge and identifies gaps that this thesis aims to address.

Chapter 2 details the development of a finite element model (FEM) that accurately simulates the thermomechanical behavior of the FSW process. The model couples thermal and mechanical phenomena to predict the temperature distribution, stress evolution, and material flow during welding. The FEM was validated using published experimental data from welding trials on 6061-T6 aluminum alloy and then extended to Inconel 718. The statistical methodologies, including Taguchi analysis and ANOVA, are presented with relevant equations, establishing a robust framework for parameter optimization.

In Chapter 3, the effects of various FSW parameters—axial force, rotational speed, welding speed, shoulder diameter, and pin diameter—on the performance of Al-T6 and Inconel 718 are analyzed. The results indicate that lower workpiece temperatures lead to finer grain structures, reduced stress evolution, and increased hardness. Specifically, lower axial force and rotational speed, combined with higher welding speed and larger shoulder and pin diameters, were found to optimize the thermal and mechanical properties of the welds. Additionally, the chapter demonstrates that axial force and rotational speed are the most influential parameters. Non-linear regression models introduced in this

chapter offer predictive capabilities, aiding in the anticipation of performance outcomes based on FSW parameter settings.

Chapter 4 extends the validated FEM to the dissimilar welding of Inconel 718 and Ti-6Al-4V alloys. The parametric study and statistical analysis reveal the intricate interactions between welding parameters and their effects on weld quality. The findings highlight the importance of precise control over process variables to achieve optimal results in dissimilar material welding. This chapter also introduces regression models that offer predictive capabilities, aiding in the anticipation of performance outcomes based on specific parameter settings.

Chapters 3 and 4 also explore innovative approaches to thermal management during FSW, focusing on induction preheating and active cooling. The introduction of these strategies significantly enhances process efficiency by allowing for lower rotational speeds and axial forces, thereby improving heat dissipation and resulting in finer grain structures. Finally, Chapter 5 proposes an alternative and cost-effective approach to thermal management through the implementation of control strategies, such as including proportional-integral-derivative (PID) and model predictive control (MPC), demonstrating their effectiveness in maintaining optimal welding temperatures and enhancing overall weld quality.

The research presented in this thesis provides valuable insights into the optimization of FSW parameters for Inconel 718. The integration of finite element modeling with statistical analysis and advanced control methodologies has led to a deeper understanding of the thermomechanical behavior of the FSW process. Key findings include:

- **Parameter Influence**: Axial force and rotational speed are the most critical parameters affecting workpiece temperature and, consequently, the mechanical properties of the welds.
- **Thermal Management**: Induction preheating, and active cooling significantly enhance weld quality by improving heat dissipation and enabling finer grain

structures. Additionally, applying an effective process control strategy successfully maintains an optimal workpiece temperature.

- **Predictive Models**: The developed non-linear regression models offer robust predictive capabilities, facilitating the anticipation of welding outcomes based on specific FSW parameter settings, primarily rotational speed.

Recommendations for Future Work

Future research should explore the following areas to further advance the understanding and application of FSW for nickel-based superalloys:

- **Extended Material Range**: Investigate the applicability of the developed models and control strategies to other high-performance alloys, including those used in aerospace and nuclear industries.
- **Real-time Monitoring**: Develop real-time monitoring and control systems that leverage predictive models to dynamically adjust welding parameters during the FSW process.
- **Scale-up Studies**: Perform scale-up studies to evaluate the feasibility of the optimized FSW parameters and control strategies in industrial applications, ensuring scalability and reproducibility.

By addressing these areas, future research can build upon the findings of this thesis, contributing to the continued advancement of FSW technology and its application to high-performance materials.

Extended Abstract in French (Résumé étendu)

Titre de la thèse: **Modélisation avancée et optimisation du procédé de soudage par friction malaxage : applications à l'Inconel 718 et aux alliages à hautes performances**

Cette thèse est le fruit d'une recherche approfondie menée au laboratoire ICube de l'Université de Strasbourg, sous la supervision du Professeur Said Ahzi et du Professeur Yves Remond, de 2021 à 2024. La recherche se concentre sur l'amélioration du processus de soudage par friction malaxage (FSW) pour les superalliages à base de nickel, en particulier l'Inconel 718. La motivation de cette étude réside dans le besoin crucial d'améliorer les processus de soudage pour les matériaux de haute performance utilisés dans des applications exigeantes telles que l'aérospatiale et la production d'énergie. J'ai entrepris ce voyage de recherche avec l'objectif de développer une compréhension globale de la manière dont divers paramètres du FSW influencent la qualité du soudage et les propriétés mécaniques de l'Inconel 718. L'étude utilise un cadre méthodologique rigoureux comprenant la modélisation par éléments finis, l'analyse Taguchi, l'analyse ANOVA, la régression non linéaire et les stratégies de contrôle des processus, garantissant la fiabilité et la validité des résultats.

Le chapitre 1 offre une revue de la littérature détaillée sur la technologie du soudage par friction malaxage, en se concentrant sur les alliages à base de nickel, en particulier l'Inconel 718. Ce chapitre comprend 277 références, qui ont été converties en un article de revue. Le chapitre 2 résume la méthodologie de développement du modèle par éléments finis qui couple les phénomènes thermomécaniques du processus FSW, détaillant les équations pertinentes. De plus, les équations statistiques décrivant l'analyse Taguchi, l'ANOVA et la régression non linéaire sont présentées.

Le chapitre 3 traite du FSW du matériau de référence en alliage d'aluminium 6061-T6. Après validation avec des données expérimentales publiées, le modèle a été étendu à

l'alliage Inconel 718, incluant son étude paramétrique et son analyse statistique. Le chapitre 4 s'appuie sur le modèle par éléments finis développé et validé pour l'Inconel 718 et étend l'étude au soudage dissemblable de l'Inconel 718 et des alliages Ti-6Al-4V. Ce chapitre inclut également une étude paramétrique suivie d'une analyse statistique et de modèles de régression. Enfin, le chapitre 5 propose une nouvelle approche économique pour la gestion thermique des pièces à usiner grâce à une stratégie de contrôle efficace, principalement en utilisant PID et MPC.

Introduction

L'avancement des technologies de fabrication est crucial pour répondre aux exigences des industries modernes, où le besoin de matériaux de haute performance et de processus de fabrication efficaces ne cesse de croître. Une des innovations notables dans ce domaine est le soudage par friction malaxage (FSW), un procédé de soudage à l'état solide qui a révolutionné la manière dont les matériaux, en particulier les métaux et les alliages, sont soudés. Cette introduction offre un aperçu du FSW, de son processus, de ses applications, de ses avantages et de l'état actuel de la recherche, en se concentrant particulièrement sur le soudage des alliages d'aluminium et des matériaux à haute température comme l'Inconel 718.

Le FSW a été inventé à The Welding Institute (TWI) au Royaume-Uni en 1991. Cette technique de soudage innovante implique l'utilisation d'un outil non consommable pour joindre deux pièces opposées sans fondre le matériau. Le processus utilise la chaleur de friction générée entre l'outil rotatif et la pièce pour adoucir le matériau, permettant à l'outil de malaxer et de forger les pièces ensemble à des températures inférieures à leur point de fusion. Cette approche unique distingue le FSW des méthodes de soudage conventionnelles qui reposent sur la fusion des matériaux de base, offrant plusieurs avantages tels qu'une distorsion thermique réduite et des propriétés mécaniques améliorées.

Le processus FSW peut être divisé en trois étapes principales : la pénétration, le malaxage et le retrait. Pendant l'étape de pénétration, l'outil rotatif est inséré dans les pièces au niveau de la ligne de joint, générant de la chaleur par friction. Cette chaleur adoucit le matériau, permettant à l'outil de pénétrer à la profondeur désirée. Dans l'étape de malaxage, l'outil se déplace le long de la ligne de joint, malaxant et mélangeant le matériau adouci pour former une soudure à l'état solide. La dernière étape, le retrait, implique le retrait de l'outil, laissant derrière lui une soudure qui se solidifie en refroidissant. Plusieurs paramètres clés influencent le processus FSW, y compris la vitesse de rotation, la vitesse de soudage, la force axiale, le diamètre de l'épaulement et le diamètre de la broche. Ces paramètres doivent être soigneusement contrôlés pour atteindre des conditions de soudage optimales et produire des soudures de haute qualité. De plus, la conception de l'outil FSW, qui comprend généralement un épaulement et une broche, joue un rôle crucial dans la détermination de la génération de chaleur et du flux de matériau pendant le soudage.

Le FSW a trouvé des applications étendues dans diverses industries en raison de sa capacité à produire des soudures sans défaut avec des propriétés mécaniques supérieures. Dans l'industrie aérospatiale, le FSW est utilisé pour assembler des alliages d'aluminium pour les structures d'avions, car il minimise la distorsion et les contraintes résiduelles, essentielles pour maintenir l'intégrité structurelle. L'industrie automobile utilise également le FSW pour assembler des matériaux légers, contribuant au développement de véhicules économes en carburant. De plus, le FSW est employé dans la fabrication de coques de navires, de wagons ferroviaires et d'échangeurs de chaleur, démontrant sa polyvalence dans différents secteurs. Un des avantages significatifs du FSW est sa capacité à souder des matériaux dissemblables, ce qui est particulièrement utile dans les applications nécessitant la combinaison de différentes propriétés de matériaux. Par exemple, le FSW peut assembler l'aluminium au cuivre ou à l'acier, permettant l'intégration de composants légers et de haute résistance dans un même assemblage. Cette capacité à assembler des matériaux dissemblables ouvre de nouvelles possibilités pour des conceptions et des applications innovantes.

Le FSW offre plusieurs avantages par rapport aux méthodes de soudage par fusion traditionnelles. Premièrement, parce que le FSW fonctionne en dessous de la température de fusion des pièces, il évite de nombreux problèmes associés à la fusion et à la solidification, tels que la porosité, la fissuration et la distorsion. Cela se traduit par des soudures avec des propriétés mécaniques supérieures et une réduction des besoins en traitements post-soudure. Deuxièmement, le FSW est un processus respectueux de l'environnement. Il ne nécessite pas l'utilisation de matériaux de remplissage, de flux ou de gaz de protection, qui sont couramment utilisés dans le soudage par fusion et peuvent avoir des impacts environnementaux et sur la santé. La nature à l'état solide du FSW entraîne également une consommation d'énergie inférieure par rapport aux processus de soudage par fusion. Troisièmement, le FSW est hautement efficace et adapté à l'automatisation. Le processus peut être facilement adapté à des systèmes robotiques et CNC, permettant des soudures de haute précision et cohérentes. Cela rend le FSW idéal pour les environnements de production en grande série où la répétabilité et la qualité sont primordiales.

Comprendre et optimiser les paramètres du processus FSW est crucial pour obtenir des soudures de haute qualité. Les chercheurs ont développé divers modèles pour simuler le transfert de chaleur, le flux de matériau et la distribution des contraintes pendant le FSW. Ces modèles aident à prédire les résultats de différents paramètres de soudage et à guider le processus d'optimisation. La modélisation thermique du FSW se concentre sur la prédiction de la distribution de la température dans les pièces pendant le soudage. Des modèles thermiques précis sont essentiels pour comprendre les cycles thermiques expérimentés par le matériau, qui affectent directement la microstructure et les propriétés mécaniques de la soudure. Les modèles de dynamique des fluides computationnelle (CFD) sont souvent utilisés pour simuler le flux de matériau autour de l'outil, fournissant des informations sur la formation du noyau de soudure et l'influence de la géométrie de l'outil sur le mélange des matériaux. La modélisation mécanique du FSW implique la simulation des distributions de contraintes et de déformations pendant et après le soudage. Ces modèles aident à identifier les problèmes potentiels tels que les contraintes résiduelles

et les distorsions, qui peuvent compromettre l'intégrité de la structure soudée. En comprenant le comportement mécanique de la soudure, les chercheurs peuvent optimiser les paramètres du processus pour minimiser les défauts et améliorer les performances globales de la soudure.

Une revue complète de la littérature existante révèle plusieurs tentatives pour comprendre le processus FSW, en particulier en ce qui concerne le soudage des alliages d'aluminium et des matériaux à haute température comme l'Inconel 718. Les études ont exploré les effets de divers paramètres de processus sur la microstructure et les propriétés mécaniques des joints FSW. Par exemple, des chercheurs ont étudié l'influence de la conception de l'outil, de la vitesse de rotation, de la vitesse de soudage et de la force axiale sur la qualité des soudures. Malgré les recherches approfondies menées, plusieurs lacunes dans la littérature subsistent. Un des principaux défis est la compréhension globale des interactions entre les différents paramètres du FSW et leur impact collectif sur la microstructure et les propriétés mécaniques de la soudure, ainsi que l'effet du FSW assisté par énergie et/ou refroidissement sur l'efficacité du soudage et la qualité finale de la pièce soudée. Alors que de nombreuses études ont exploré des paramètres individuels, l'interaction complexe entre ces variables n'est pas encore entièrement comprise. De plus, il est nécessaire de développer des modèles plus sophistiqués capables de simuler avec précision ces interactions et de prédire les résultats de différentes conditions de soudage. Un autre domaine nécessitant une investigation plus approfondie est le soudage de matériaux avancés et émergents en utilisant le FSW. Bien que des progrès significatifs aient été réalisés dans le soudage des alliages d'aluminium et de certains matériaux à haute température, l'application du FSW à de nouveaux matériaux, tels que les aciers à haute résistance, les alliages de titane et les matériaux composites, reste sous-explorée. Comprendre le comportement de ces matériaux pendant le FSW et optimiser les paramètres du processus pour leur soudage est crucial pour étendre l'applicabilité du FSW dans diverses industries.

Méthodologie

L'impact des variables opérationnelles sur la température, le flux de matériau et le taux de déformation pendant le FSW des alliages d'aluminium, de l'Inconel 718 et du soudage dissemblable de l'Inconel 718 et du Ti-6Al-4V a été exploré via une simulation numérique employant un modèle thermomécanique 3D conçu dans COMSOL Multiphysics version 5.3. La validation initiale du modèle a été effectuée par rapport aux résultats expérimentaux documentés concernant les alliages d'aluminium, après quoi son application a été étendue à l'Inconel 718. Une étude paramétrique a ensuite été menée pour optimiser les paramètres du processus et obtenir des soudures par friction malaxage de haute qualité dans l'Inconel 718, en particulier à des rotations d'outil élevées, des vitesses de soudage rapides et des charges axiales faibles. Après validation des soudures par friction malaxage de l'Inconel 718, le modèle a été étendu au soudage dissemblable de l'Inconel 718 et du Ti-6Al-4V.

Les figures 1 et 2 illustrent le domaine du modèle et la géométrie du système, où le modèle a été configuré avec une géométrie comprenant deux plaques pour faciliter les enquêtes potentielles sur le soudage de matériaux dissemblables. Les dimensions des plaques d'aluminium sont de 400 par 102 par 12,7 millimètres, bordées d'un domaine infini dans la direction x. L'outil, fabriqué en carbure de tungstène avec 10 % de cobalt, est rigide, avec un fond circulaire plat de 50 millimètres de diamètre pour l'épaulement et une broche cylindrique de 6 millimètres de rayon, tandis que la figure 2 présente une configuration comprenant deux plaques d'Inconel 718. Chaque plaque mesure 250 par 75 par 3 millimètres et est flanquée d'un domaine infini dans la direction x. L'outil, fabriqué en carbure de tungstène avec 10 % de cobalt, est robuste, avec un fond circulaire plat de 25 millimètres de diamètre pour l'épaulement et une broche cylindrique d'un diamètre de 5 millimètres et d'une profondeur de 2,7 millimètres.

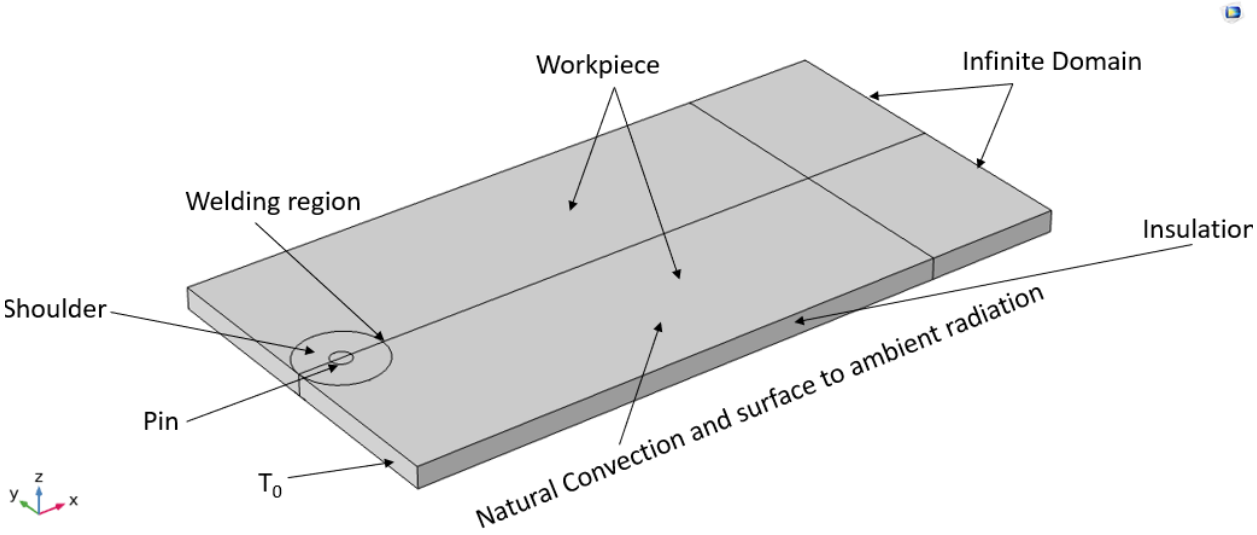

Figure 1: Géométrie du système et domaine du modèle pour l'alliage d'aluminium

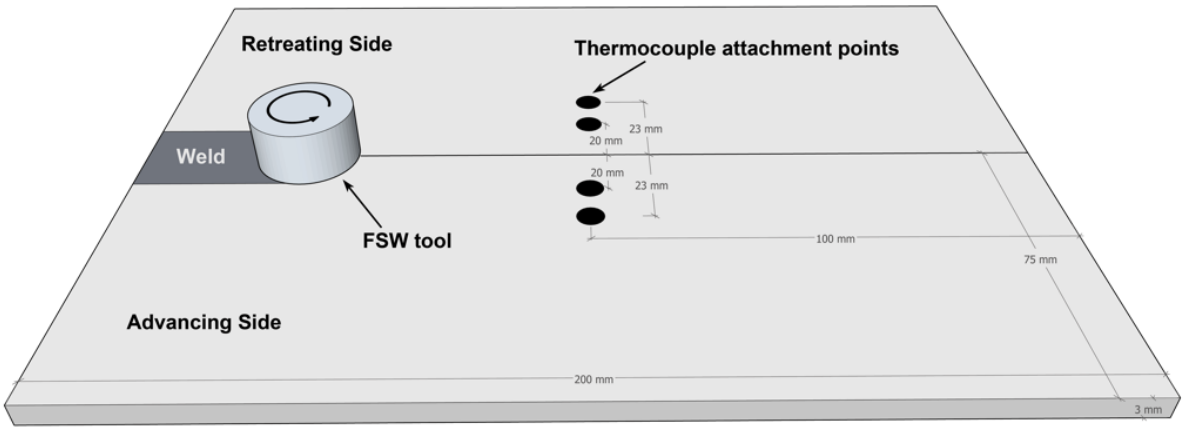

Figure 2: Géométrie du système et domaine du modèle pour l'alliage Inconel 718

Résultats FEM du FSW de l'alliage Al-T6

La distribution de température en 3D pour les plaques d'aluminium, présentée dans les Figures 3, révèle la répartition de la chaleur pendant le processus de soudage des alliages Al-T6. Elle indique la température la plus élevée au niveau du joint de soudage, atteignant 676°C, avec un schéma de dissipation de la chaleur à travers les plaques, les températures variant de moins de 100°C à 600°C. Ces résultats mettent en évidence la complexité du

transfert de chaleur dans le FSW et soulignent l'importance de comprendre la distribution de température pour obtenir des soudures réussies. L'utilisation de ces données de profil de température peut optimiser le processus de soudage et améliorer la qualité des soudures.

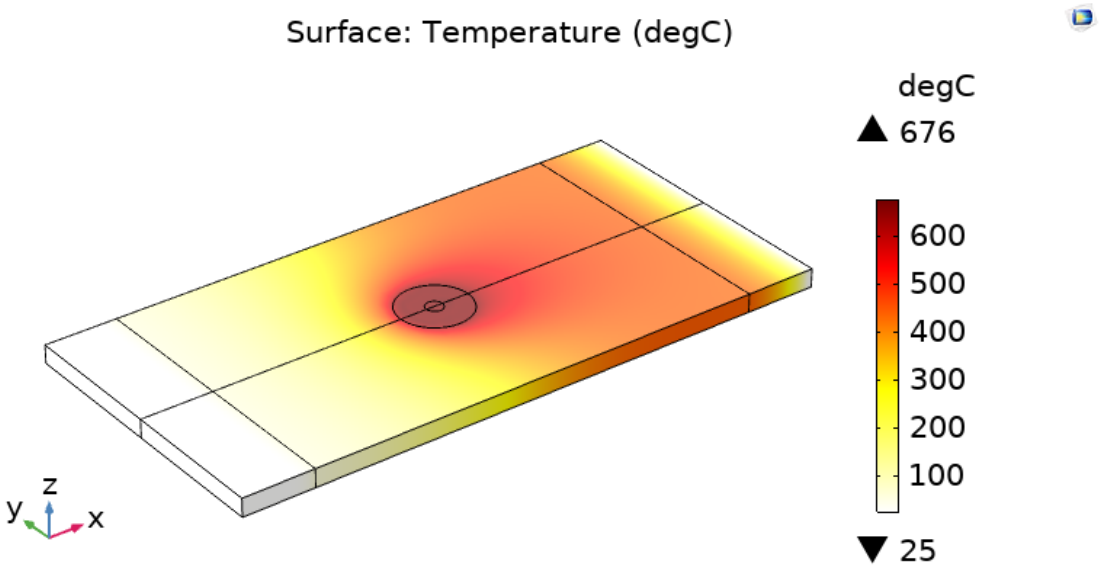

Figure 3: Profil de température en 3D de la pièce en aluminium

Une étude paramétrique complète a été menée pour comprendre les effets de divers paramètres de processus sur les pièces en aluminium. Les paramètres évalués comprenaient la vitesse de rotation (de 50 à 650 tr/min), la vitesse de soudage (de 0,5 à 6,5 mm/s), la force normale (de 5 à 25 kN), la vitesse de refroidissement (de 0,1 à 1,1 m/s) et le diamètre de refroidissement (de 0,2 à 1 pouce). Les indicateurs de performance clés étaient la température dans la direction x, la température dans la direction z (à travers l'épaisseur de la pièce), la taille moyenne des grains et la microdureté. Les résultats, illustrés dans la Figure 4, ont montré qu'une augmentation de la force normale augmentait la distribution de la température, atteignant un pic au niveau du noyau de soudure. Par exemple, avec des forces normales de 5 kN et 25 kN, les températures sont passées de 260°C à 650°C, la taille moyenne des grains a augmenté de 450 µm à 2000 µm, et la dureté a diminué de 43,5 à 42. Ces résultats indiquent une forte relation entre la force normale, la taille des grains et la dureté.

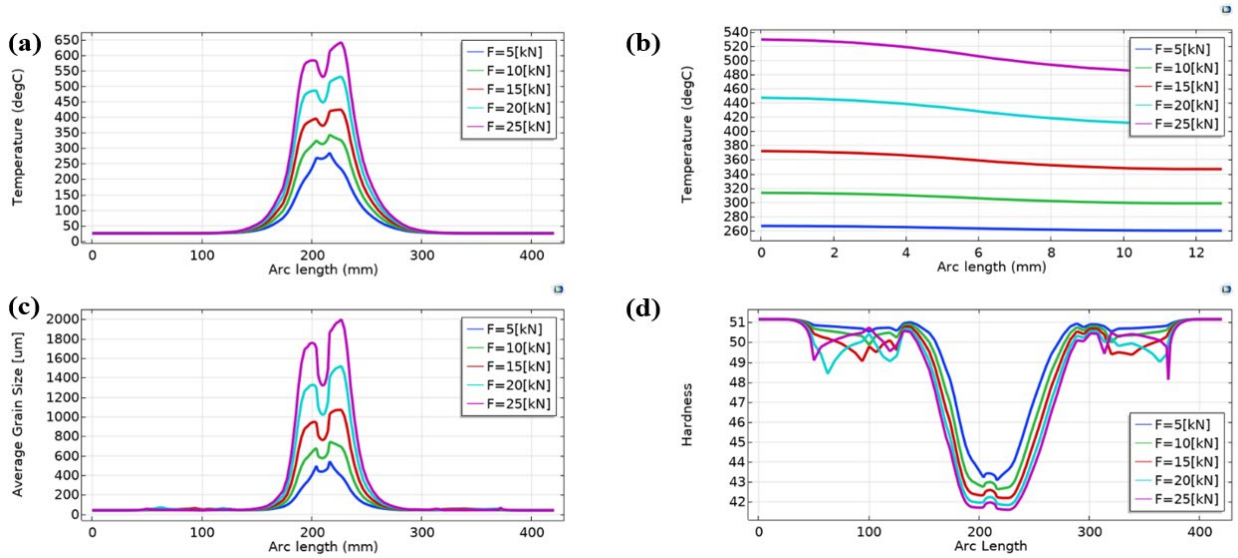

Figure 4: Pièce en aluminium, analyse paramétrique de la force normale. a) température dans la direction x, b) température dans la direction z, c) taille moyenne des grains, et d) dureté

Résultats FEM du FSW de l'Inconel 718

Les paramètres du processus FSW dans cette étude incluaient une vitesse de rotation de 600 tr/min, une vitesse de soudage de 90 mm/min, une force axiale de 40 kN, un diamètre d'épaulement de 25 mm et un diamètre de broche de 5 mm, sans refroidissement ni préchauffage. L'analyse de la température en 3D pour les plaques d'Inconel, comme montré dans la Figure 5, a révélé une température maximale d'environ 1100°C concentrée dans les zones de soudage. La vue en coupe 2D indiquait une concentration prédominante de la température maximale autour des zones de soudage avec une répartition presque uniforme dans les directions x et z. Ces résultats suggèrent que la distribution localisée de la température autour des zones de soudage de l'Inconel 718 améliore la dissipation de la chaleur, augmentant ainsi la résistance à la dégradation thermique et offrant potentiellement une plus grande durabilité dans les environnements à haute température.

La Figure 6 illustre les profils de température 1-D pendant le processus FSW de l'alliage Inconel 718. Le sous-graphique (a) montre le profil de température à travers la pièce, atteignant un pic à environ 1000°C dans la zone de soudage (75-85 mm) pendant 10

secondes et diminuant brusquement vers les bords. Le sous-graphique (b) présente le profil de température le long de la ligne de soudage, avec un pic similaire à 30 mm de longueur et des températures atteignant 1000°C pendant 10 secondes, chutant à près de la température ambiante au-delà de 100 mm. Le sous-graphique (c) affiche le profil de température à 15 mm de la ligne de soudage, atteignant un pic à environ 650°C à 25 mm de longueur pendant 10 secondes et déclinant à près de 25°C au-delà de 100 mm. Le sous-graphique (d) montre le profil de température à travers l'épaisseur de la plaque, avec des températures restant autour de 900°C pour des temps de soudage entre 2 et 10 secondes, sauf à 0 secondes où la température est de 25°C. Ces profils mettent en évidence des gradients thermiques significatifs induits par le processus FSW, cruciaux pour comprendre les effets thermiques sur la microstructure et les propriétés mécaniques de l'alliage Inconel 718.

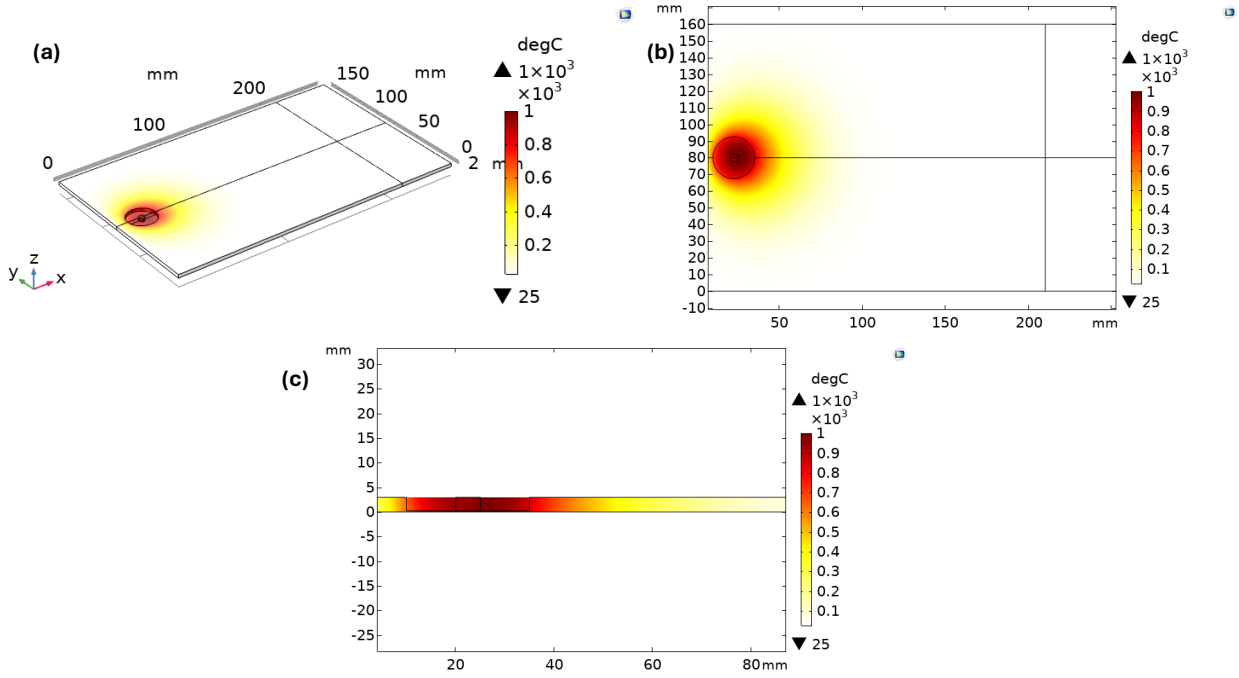

Figure 5: FSW de l'alliage Inconel 718, a) profil de température en 3D, b) profil de température en 2D, c) profil de température en 2D à travers l'épaisseur de la plaque

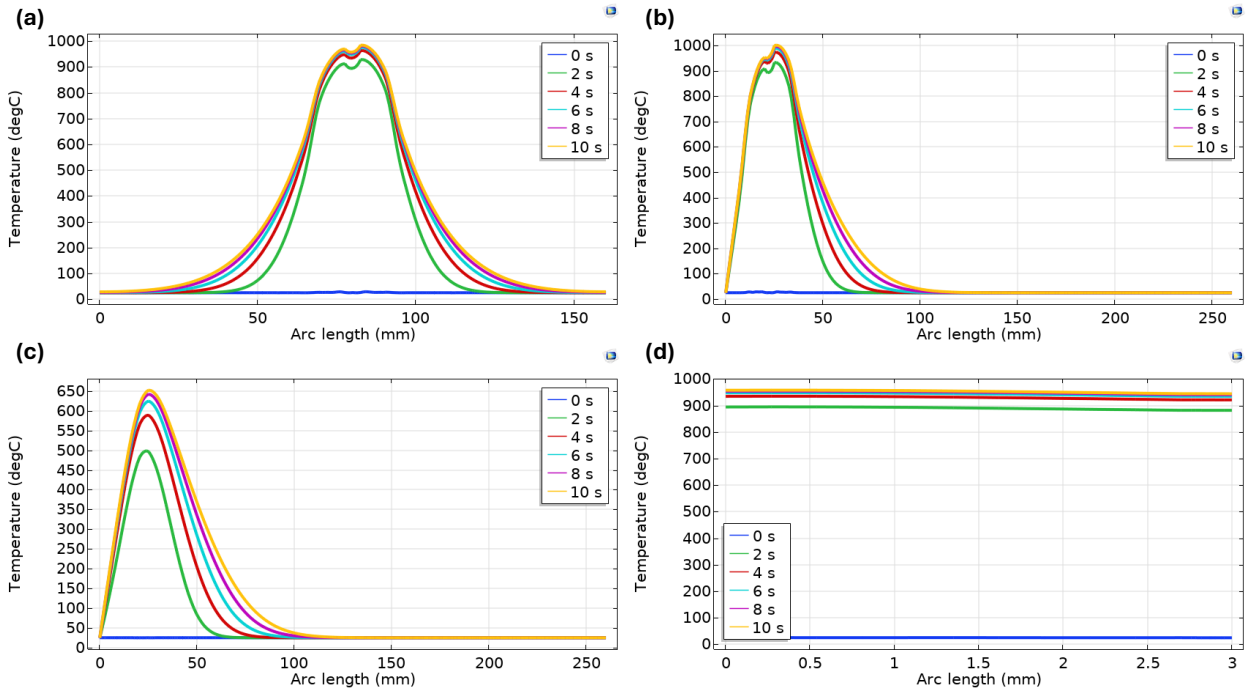

Figure 6: FSW de l'alliage Inconel 718, a) profil de température 1D à travers la zone du nugget, b) profil de température 1D à travers la ligne de soudage, c) profil de température 1D à 15 mm de la ligne de soudage, d) profil de température 1D à travers l'épaisseur de la plaque.

Dans cette section, les effets de différents paramètres de processus, y compris la force axiale, la vitesse de rotation, la vitesse de soudage, le diamètre de l'épaulement et le diamètre de la broche, ainsi que les effets du refroidissement et du préchauffage sur le profil thermique de la pièce, la taille moyenne des grains, la microdureté et l'évolution des contraintes, sont discutés.

La Figure 7 présente une analyse paramétrique du FSW de l'alliage Inconel 718, en se concentrant sur les profils de température sous différentes forces axiales (5 kN à 50 kN). Le sous-graphique (a) montre que des forces axiales plus élevées conduisent à des températures maximales plus élevées dans la zone du nugget, avec 50 kN atteignant environ 900°C et 5 kN culminant autour de 450°C. Le sous-graphique (b) indique que des forces axiales plus élevées maintiennent des températures plus élevées à travers l'épaisseur de la plaque, avec 50 kN autour de 850°C et 5 kN autour de 450°C. Le sous-

graphique (c) révèle que des forces axiales plus élevées entraînent des températures plus élevées à 15 mm de la ligne de soudage, avec 50 kN atteignant environ 570°C et 5 kN autour de 250°C. Ces profils soulignent l'impact significatif de la force axiale sur le comportement thermique pendant le FSW, montrant comment une force axiale accrue élève la distribution globale de la température, ce qui est crucial pour optimiser les paramètres de soudage de l'alliage Inconel 718.

La Figure 8 analyse en outre l'effet de la variation de la force axiale sur la taille moyenne des grains, la microdureté et la distribution des contraintes de von Mises. Les sous-graphiques (a) et (b) montrent que la taille moyenne des grains augmente avec une force axiale plus élevée, culminant autour de 30 µm à 50 kN, tandis que les grains les plus fins sont aussi petits que 0,5 µm à 5 kN. La taille des grains atteint environ 3 µm à 15 mm de la ligne centrale de soudage à 50 kN, tandis que la plus petite taille de grain enregistrée est inférieure à 0,01 µm à 5 kN. Les sous-graphiques (c) et (d) montrent que la dureté est la plus élevée dans la région de soudage, atteignant un maximum d'environ 415 à des forces axiales supérieures à 20 kN, avec un gradient de 402 à 50 kN à 320 unités à 5 kN 15 mm de la ligne centrale de soudage. Les sous-graphiques (e) et (f) représentent les contraintes de von Mises, culminant à environ 1100 MPa au centre de l'outil et autour de 550 MPa à 15 mm de la ligne centrale à des forces axiales plus élevées, les valeurs de contrainte diminuant et se propageant à mesure que la force axiale diminue.

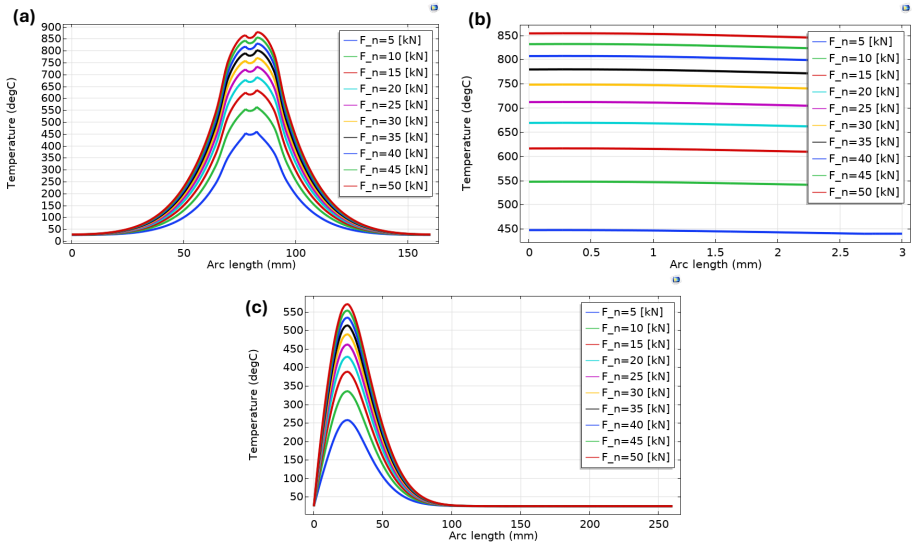

Figure 7: Pièce en Inconel 718, analyse paramétrique de la force axiale. a) Profil de température 1D à travers la zone du nugget, b) Profil de température 1D à travers l'épaisseur de la plaque, c) Profil de température 1D à 15 mm de la ligne de soudage.

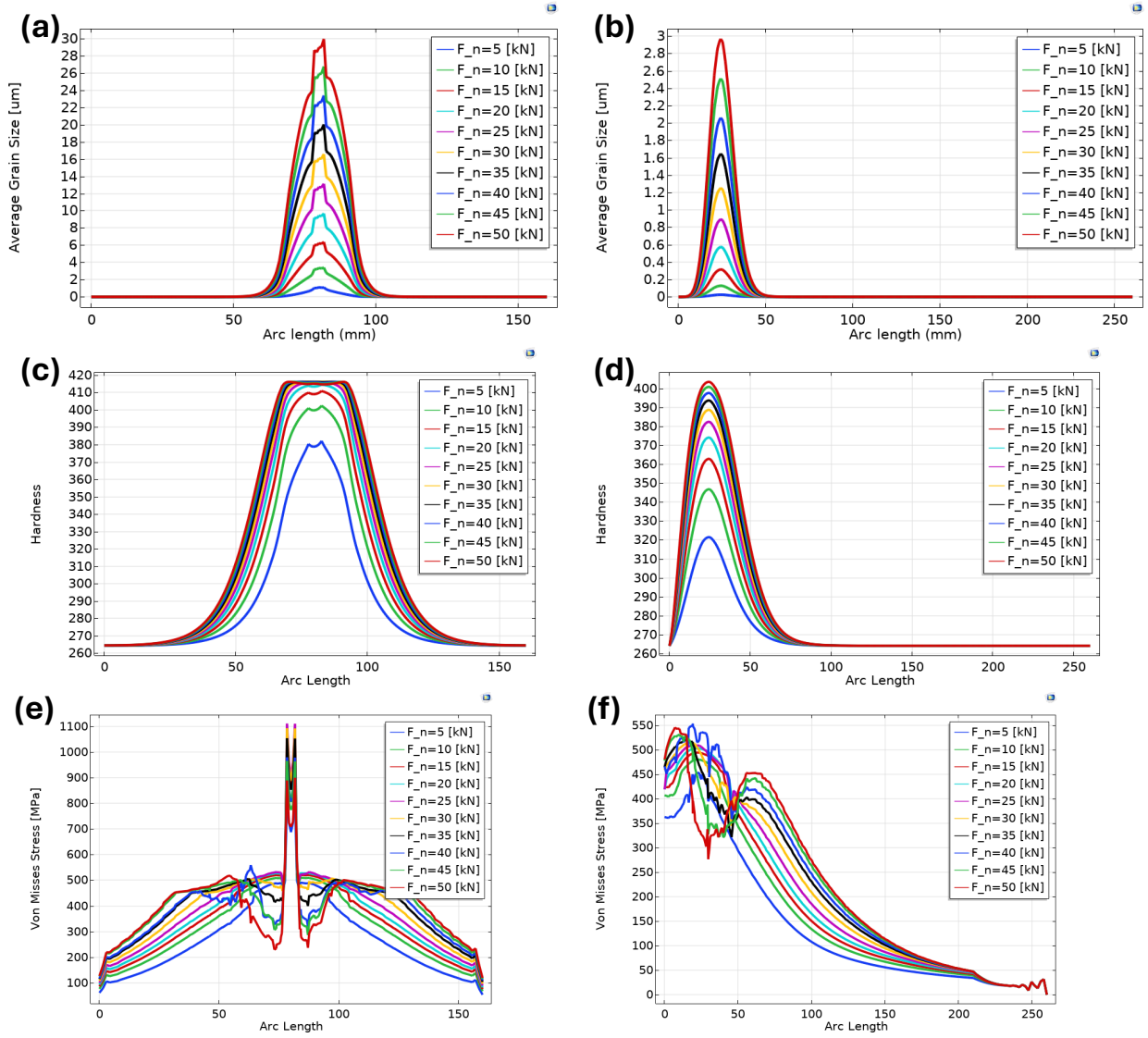

Figure 8: Pièce en Inconel 718, analyse paramétrique de la force axiale, a) Taille moyenne des grains en 1D à travers la zone du nugget, b) Taille moyenne des grains en 1D à 15 mm de la ligne centrale de soudage, c) Dureté en 1D à travers la zone du nugget, d) Dureté en 1D à 15 mm de la ligne centrale de soudage, e) Contrainte de von Mises en 1D à travers la zone du nugget, f) Contrainte de von Mises en 1D à 15 mm de la ligne centrale de soudage.

L'étude a examiné le processus FSW de l'alliage Inconel 718 avec des vitesses de rotation variables (100-600 RPM), une vitesse de soudage de 90 mm/min, une force axiale de 27 kN, un diamètre d'épaulement de 25 mm et un diamètre de broche de 5 mm, sans refroidissement ni préchauffage. La Figure 9 présente une analyse paramétrique des profils de température dans ces conditions. Le sous-graphique (a) montre que les températures maximales augmentent avec des vitesses de rotation plus élevées, atteignant environ 900°C à 600 RPM et 500°C à 100 RPM. Le sous-graphique (b) indique que des vitesses plus élevées maintiennent des températures plus élevées à travers l'épaisseur de la plaque, avec 600 RPM autour de 875°C et 100 RPM autour de 500°C. Le sous-graphique (c) révèle des températures plus élevées à 15 mm de la ligne de soudage, avec 600 RPM culminant à environ 595°C et 100 RPM autour de 300°C. Ces profils soulignent l'impact significatif de la vitesse de rotation sur le comportement thermique pendant le FSW.

La Figure 10 analyse les effets de la variation des vitesses de rotation sur la taille moyenne des grains, la microdureté et la distribution des contraintes de von Mises. Les sous-graphiques (a) et (b) montrent que la taille moyenne des grains augmente avec la vitesse de rotation, atteignant un maximum d'environ 34 μm à 600 RPM, avec des grains plus fins aussi petits que 2,5 μm à 100 RPM. La taille des grains à 15 mm de la ligne centrale de soudage atteint environ 3,4 μm à 600 RPM, avec la plus petite taille enregistrée inférieure à 0,01 μm à 100 RPM. Les sous-graphiques (c) et (d) démontrent que la dureté est la plus élevée dans la région de soudage, culminant à environ 418 à des vitesses supérieures à 200 RPM, avec un gradient de 405 à 600 RPM à 340 à 100 RPM à 15 mm de la ligne centrale. Les sous-graphiques (e) et (f) représentent la contrainte de von Mises, culminant à environ 1100 MPa au centre de l'outil et autour de 550 MPa à 15 mm de la ligne centrale à des vitesses plus élevées, les valeurs de contrainte diminuant et se propageant à mesure que la vitesse de rotation diminue.

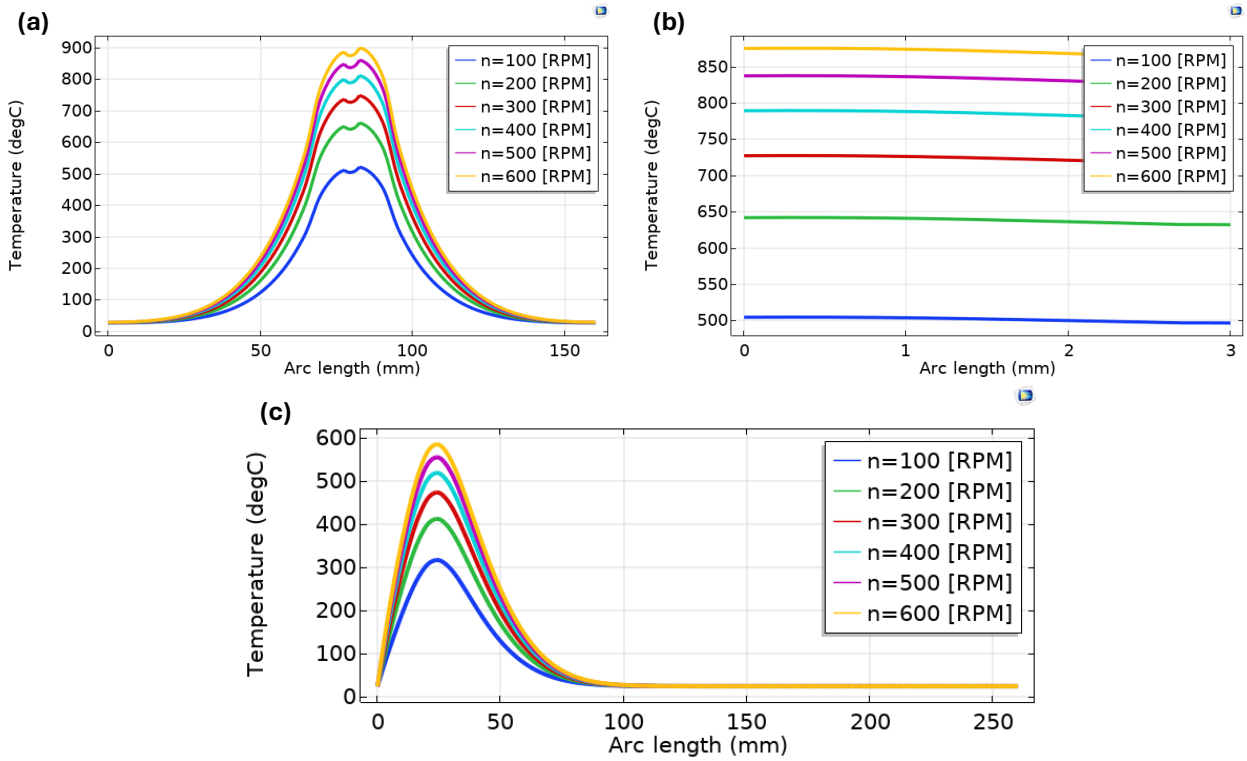

Figure 9: Pièce en Inconel 718, analyse paramétrique de la vitesse de rotation. a) Profil de température 1D à travers la zone du nugget, b) Profil de température 1D à travers l'épaisseur de la plaque, c) Profil de température 1D à 15 mm de la ligne de soudage

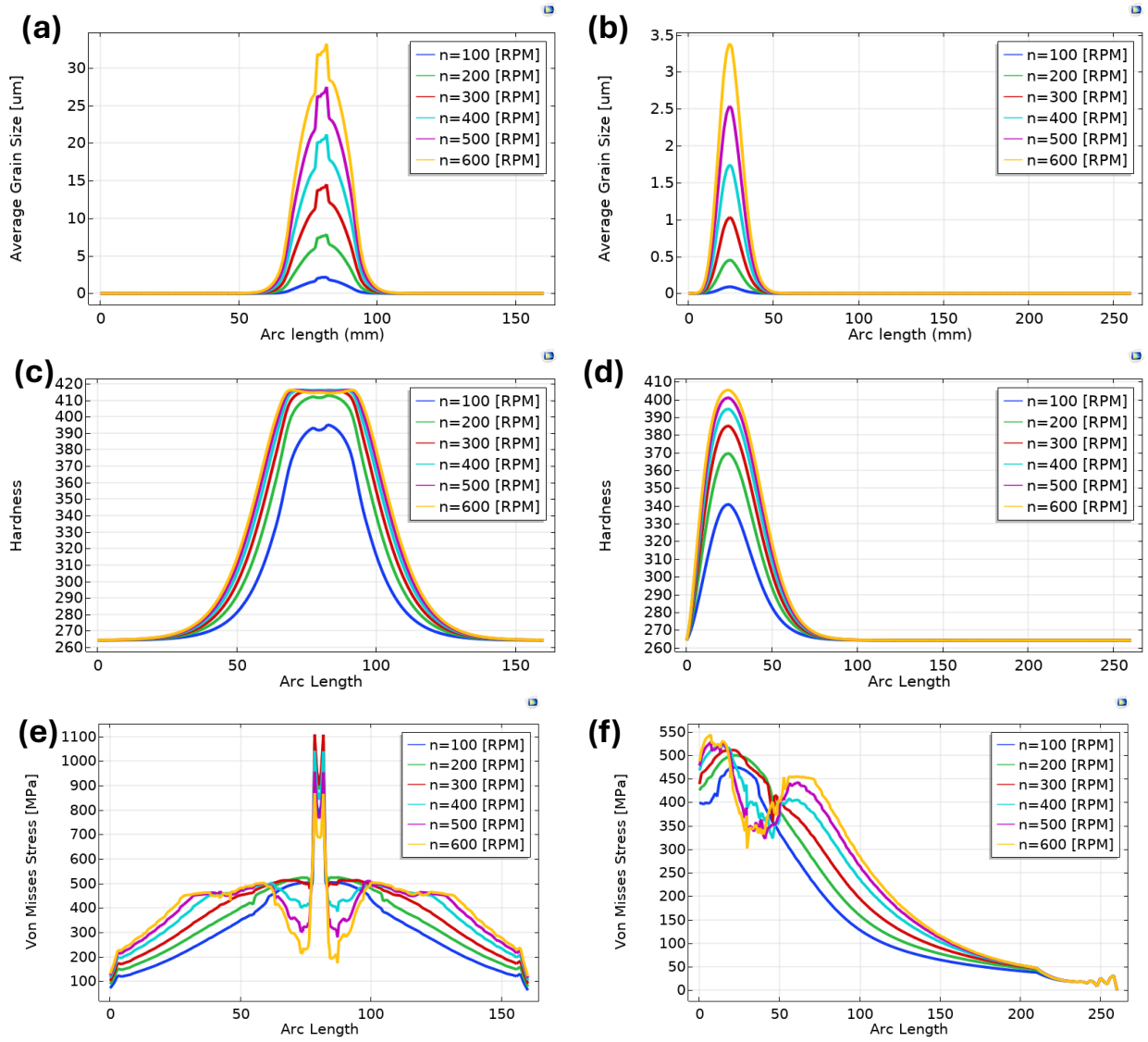

Figure 10: Pièce en Inconel 718, analyse paramétrique de la vitesse de rotation, a) Taille moyenne des grains en 1D à travers la zone du nugget, b) Taille moyenne des grains en 1D à 15 mm de la ligne centrale de soudage, c) Dureté en 1D à travers la zone du nugget, d) Dureté en 1D à 15 mm de la ligne centrale de soudage, e) Contrainte de von Mises en 1D à travers la zone du nugget, f) Contrainte de von Mises en 1D à 15 mm de la ligne centrale de soudage.

Résultats de l'analyse statistique pour le FSW de l'Inconel 718

De plus, les résultats de l'analyse de régression non linéaire pour prédire la température de la pièce en fonction des paramètres de procédé les plus significatifs (vitesse de rotation, force axiale et vitesse de soudage), tels que conclus par l'analyse Taguchi et ANOVA. La régression non linéaire a été réalisée avec le logiciel Minitab. L'équation finale du modèle montre la température en fonction du temps (X1) en secondes, de la vitesse de rotation (X2) en RPM, de la vitesse de soudage (X3) en mm/min, et de la force axiale (X4) en kN, incluant les termes quadratiques et les interactions:

- Température (°C) = 25.33 + 0.7829 X1 + 1.1894 X2 - 0.1388 X3 + 18.123 X4 - 0.005194 $X1^2$ - 0.00761 $X2^2$ - 0.17246 $X4^2$ - 0.000938 X2*X4.

De plus, la relation entre la taille moyenne des grains (Y) en µm d'une pièce soudée par friction malaxage et sa température (X) en °C. L'analyse visait à établir un modèle quadratique, donnant l'équation suivante:

- $Y = 16.39 - 0.09086 X + 0.000117 X^2$

Enfin, la relation entre la microdureté (Y) d'une pièce soudée par friction malaxage et sa température (X) en °C. Un modèle quadratique a été ajusté, résultant en l'équation suivante :

- $Y = 246.5 + 0.4079 X - 0.000243 X^2$

Résultats FEM du FSW dissemblable de l'Inconel 718 et des alliages Ti-6Al-4V

La Figure 11 illustre le domaine du modèle et la géométrie du système, qui comprend deux plaques: l'une en Inconel 718 et l'autre en alliage Ti-6Al-4V, chacune mesurant 250 par 75 par 3 millimètres, bordée par deux domaines infinis dans la direction x. L'outil, fabriqué en carbure de tungstène avec 10 % de cobalt, possède une épaule plate circulaire de 25 millimètres de diamètre et un pion cylindrique de 5 millimètres de diamètre et de 2,7 mm de profondeur. Les propriétés des matériaux dépendantes de la température pour l'outil et les plaques de la pièce permettent des calculs thermiques et mécaniques simultanés. La technique ALE, combinée à un maillage adaptatif, maintient la qualité du maillage pendant le soudage en évitant une distorsion excessive, bien qu'elle impacte le temps de calcul. La simulation a été réalisée sur un système avec un processeur Intel(R)

Core(TM) i7-8565U CPU @ 1.80GHz 1.99 GHz de 16 Go, prenant environ 3,2 heures pour se terminer.

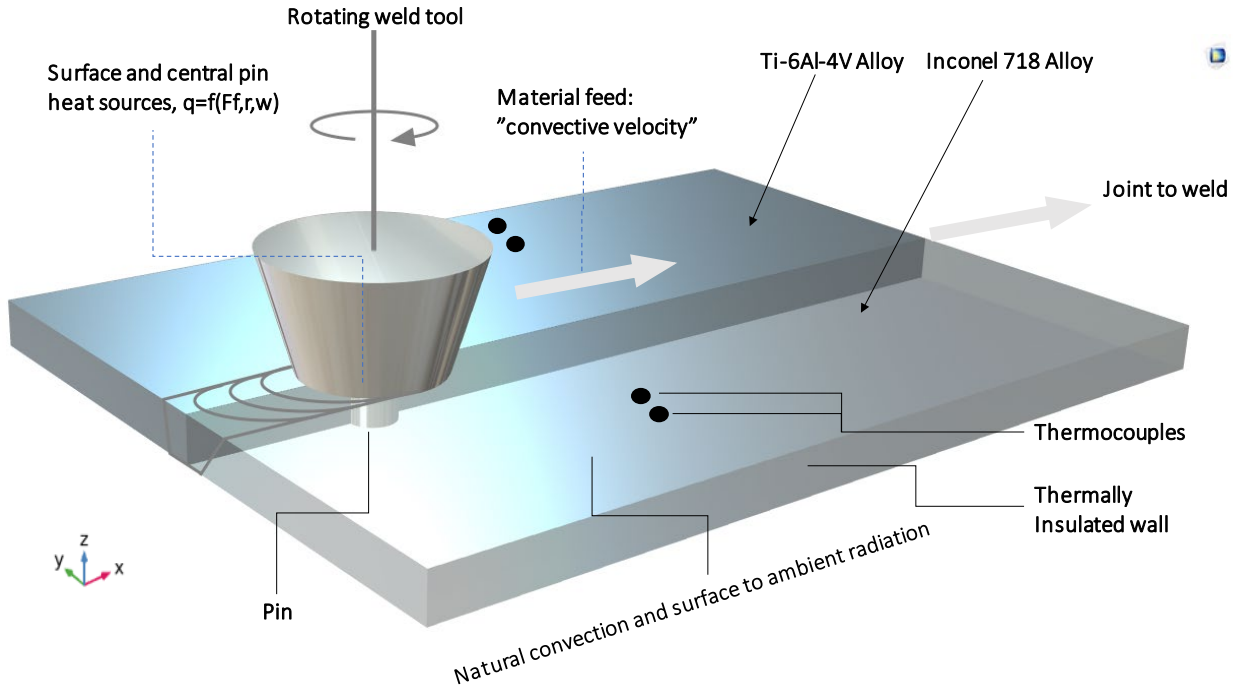

Figure 11: Schéma du diagramme de soudage par friction-malaxage (FSW) dissimilaire d'Inconel 718 et de Ti-6Al-4V.

Les paramètres de processus de FSW dans cette étude comprenaient une vitesse de rotation de 300 RPM, une vitesse de soudage de 100 mm/min, une force axiale de 40 kN, un diamètre d'épaule de 25 mm et un diamètre de broche de 5 mm, sans refroidissement ni préchauffage. La Figure 12 illustre les profils de température pendant le FSW dissimilaire d'Inconel 718 et de l'alliage de titane. Le sous-graphique (a) montre un profil de température 3D avec les températures les plus élevées autour de l'outil de soudage à 1090°C. Le sous-graphique (b) présente une distribution de température 1D le long de la zone de soudure à différents intervalles de temps, avec des températures de pointe légèrement décalées vers l'alliage de titane et diminuant vers le côté Inconel 718. Les sous-graphiques (c) et (d) affichent des profils de température 1D à 15 mm de la ligne centrale de soudage pour l'Inconel 718 et l'alliage de titane, respectivement, avec des températures de pointe près de la soudure à 550°C pour l'Inconel 718 et 500°C pour

l'alliage de titane. Ces informations sont cruciales pour la gestion thermique et le contrôle du processus de FSW.

La Figure 13 présente des profils détaillés de la taille moyenne de grain, de la dureté et de contrainte de von Mises pour le FSW dissimilaire d'Inconel 718 et d'alliage de titane. Le sous-graphique (a) montre la taille moyenne de grain 1D à travers la zone de soudure, indiquant un affinement des grains dans la zone de soudure au fil du temps. Les sous-graphiques (b) et (c) illustrent la taille moyenne de grain 1D à 15 mm de la ligne centrale de soudage pour l'Inconel 718 et l'alliage de titane, montrant des tailles de grain maximales près de la soudure diminuant avec la distance. Le sous-graphique (d) affiche la dureté 1D à travers la zone de soudure, avec des pics de dureté diminuant progressivement avec la distance. Les sous-graphiques (e) et (f) montrent la dureté 1D à 15 mm de la ligne centrale de soudage pour l'Inconel 718 et l'alliage de titane, reflétant les variations de dureté au fil du temps. Les sous-graphiques (g), (h) et (i) représentent les profils de contrainte de von Mises 1D à travers la zone de soudure et à 15 mm de la ligne centrale de soudage pour l'Inconel 718 et l'alliage de titane, mettant en évidence les concentrations de contrainte atteignant un pic près de la soudure et diminuant avec la distance. Ces figures offrent une compréhension approfondie des changements mécaniques et microstructuraux lors du FSW dissimilaire d'Inconel 718 et d'alliage de titane.

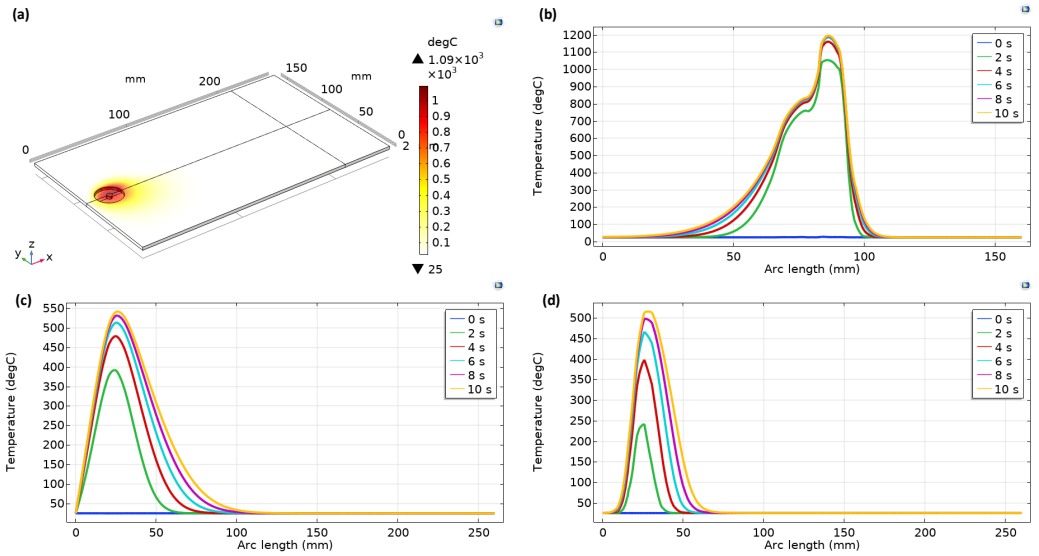

Figure 12: FSW dissimilaire d'Inconel 718 et de Ti-6Al-4V. a) Profil de température 3D, b) Température 1D à travers la zone de soudure, c) Température 1D de l'alliage Inconel 718 à 15 mm de la ligne centrale de soudage, et d) Température 1D de l'alliage Ti à 15 mm de la ligne centrale de soudage.

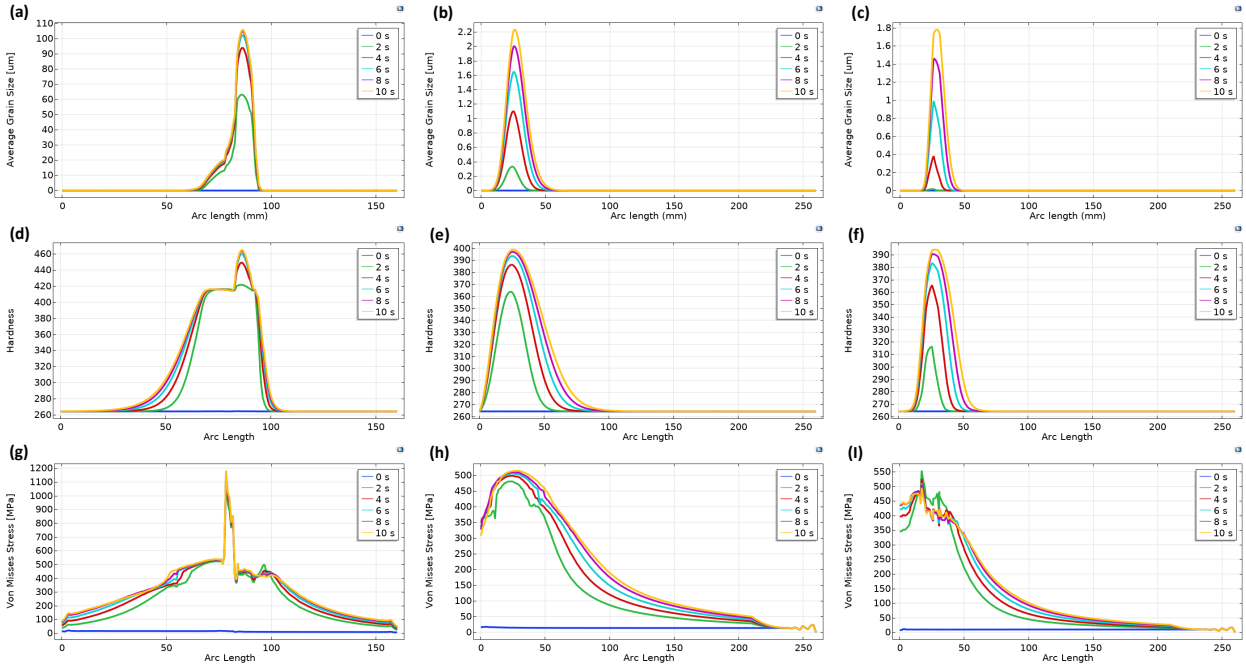

Figure 13: FSW dissimilaire d'Inconel 718 et de Ti-6Al-4V. a) Taille moyenne de grain 1D à travers la zone de soudure, b) Taille moyenne de grain 1D de l'alliage Inconel 718 à 15 mm de la ligne centrale de soudage, c) Taille moyenne de grain 1D de l'alliage Ti à 15 mm de la ligne centrale de soudage, d) Dureté 1D à travers la zone de soudure, e) Dureté 1D de l'alliage Inconel 718 à 15 mm de la ligne centrale de soudage, f) Dureté 1D de l'alliage Ti à 15 mm de la ligne centrale de soudage, g) Contrainte de von Mises 1D à travers la zone de soudure, h) Contrainte de von Mises 1D de l'alliage Inconel 718 à 15 mm de la ligne centrale de soudage, i) Contrainte de von Mises 1D de l'alliage Ti à 15 mm de la ligne centrale de soudage.

Les effets de différents paramètres de processus, y compris la force axiale, la vitesse de rotation, la vitesse de soudage, le diamètre de l'épaule et le diamètre de la broche, ainsi que les effets du refroidissement et du préchauffage sur le profil thermique de la pièce, la taille moyenne de grain, la microdureté et l'évolution des contraintes ont été étudiés. Les

principales conclusions mettent en évidence le rôle crucial de la vitesse de rotation dans l'influence du profil thermique et de la structure de grain du joint soudé. Des vitesses de rotation plus élevées ont été associées à une génération de chaleur accrue, entraînant une distribution de température plus uniforme. En revanche, des vitesses de rotation plus basses favorisaient des tailles de grain plus fines, améliorant ainsi les propriétés mécaniques du joint soudé. La force axiale s'est révélée être le facteur prédominant influençant la distribution des contraintes résiduelles, les forces plus élevées entraînant des concentrations de contrainte plus importantes dans la zone de soudure. Ces résultats soulignent l'importance critique de l'optimisation des paramètres de FSW pour obtenir des soudures de haute qualité entre matériaux différents. En équilibrant soigneusement la vitesse de rotation, la vitesse de soudage et la force axiale, il est possible de minimiser les disparités thermiques et mécaniques, améliorant ainsi les performances et la durabilité des joints soudés.

Résultats de l'analyse statistique pour le soudage par friction-malaxage (FSW) dissimilaire des alliages Inconel 718 et Ti-6Al-4V

Une analyse de régression multiple des effets des principaux paramètres de contrôle, à savoir la vitesse de rotation et la force axiale, sur la température de la pièce, la dureté et la taille moyenne de grain a été menée, et les équations du modèle final sont fournies ci-dessous, où la vitesse de rotation (Rts en RPM), la force axiale (AF en kN) sont définies comme suit :

- Température de la pièce (°C) = 38.4 + 1.722 Rts + 19.16 AF - 0.001385 Rts^2 - 0.169 AF^2
- Microdureté de la pièce (Hv) = 359.36 + 0.092 Rts + 1.0639 AF
- Taille moyenne de grain de la pièce (μm) = 36.533 + 8.934 AF – 28.42 Rts * AF

Contrôle de la température de la pièce dans le soudage par friction-malaxage (FSW) de l'alliage Inconel 718

Une étude intègre des simulations par éléments finis, une analyse statistique et des méthodologies avancées de contrôle pour améliorer la qualité de la surface du joint par

une gestion thermique efficace. Basée sur des simulations haute fidélité du processus FSW rapportées au chapitre 3, une base de données exhaustive a été créée, corrélant les paramètres de processus (vitesse de rotation, force axiale et vitesse de soudage) avec la température de la pièce. Cette base de données a facilité l'analyse statistique et l'optimisation des paramètres par la méthode de l'analyse de la variance (ANOVA), permettant une compréhension approfondie des variables de processus. Un modèle de système espace-état non linéaire a ensuite été développé à l'aide des données de simulation et de l'outil d'identification de système dans Matlab, intégrant des connaissances spécifiques au domaine. Ce modèle a été rigoureusement validé avec un jeu de données indépendant pour assurer une précision prédictive. En utilisant le modèle validé, des stratégies de contrôle sur mesure, incluant le contrôle proportionnel-intégral-dérivé (PID) et le contrôle prédictif de modèle (MPC) en configurations à une ou plusieurs variables, ont été conçues et évaluées (voir Figure 14). Ces stratégies de contrôle se sont distinguées en maintenant les températures de soudage dans des plages optimales, démontrant une robustesse en termes de temps de réponse et de gestion des perturbations. Cette précision dans la gestion thermique est en passe de raffiner considérablement le processus FSW, améliorant à la fois l'intégrité de la surface et l'uniformité microstructurale. L'implémentation stratégique de ces contrôles est prévue pour substantiellement améliorer la qualité et la cohérence des résultats de soudage.

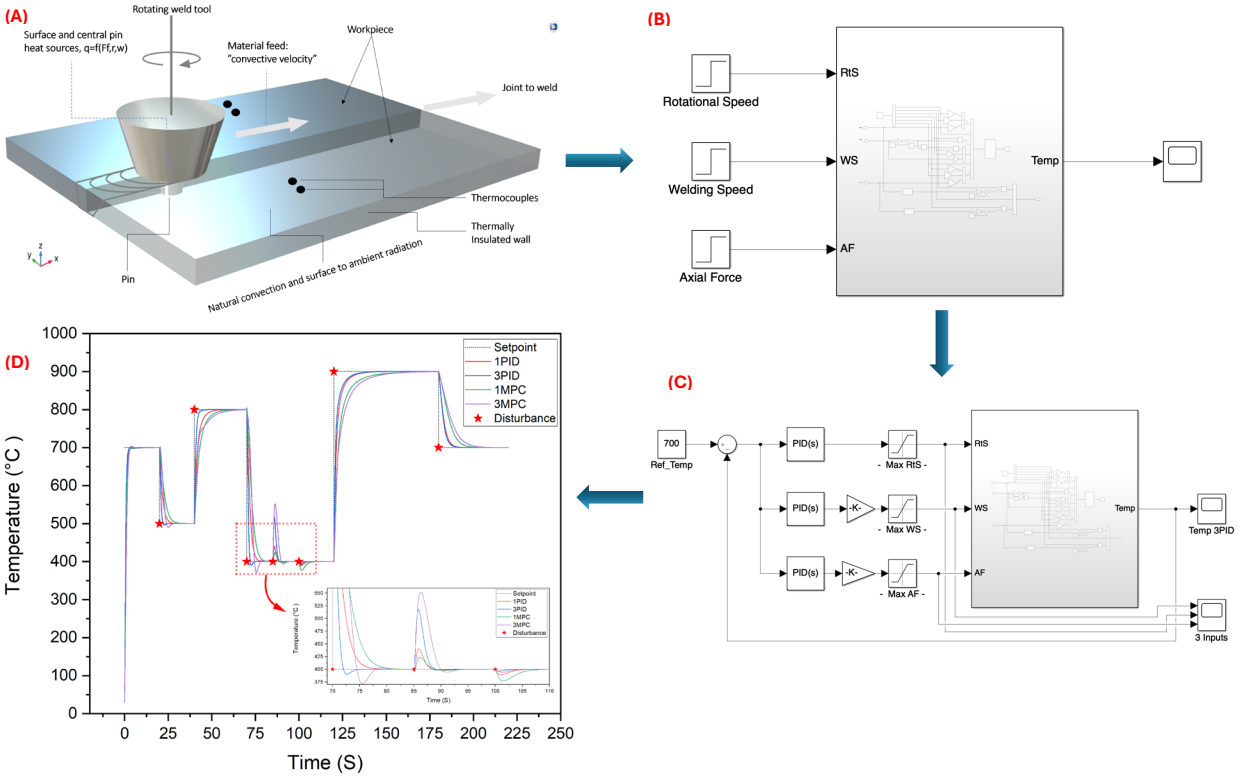

Figure 14: Schéma du diagramme pour la stratégie de contrôle développée, A) Croquis du modèle par éléments finis développé pour le processus FSW dans COMSOL Multiphysics, B) Diagramme de bloc du système FSW identifié, C) Stratégie de contrôle PID pour le processus FSW, D) Réponse des performances de contrôle des différentes stratégies de contrôle face aux perturbations.

Conclusion

Cette thèse examine de manière exhaustive l'optimisation des paramètres de soudage par friction-malaxage (FSW) pour les superalliages à base de nickel, en particulier l'Inconel 718, avec pour objectif d'améliorer les performances de soudage et les propriétés mécaniques. La recherche couvre diverses techniques analytiques, y compris la modélisation par éléments finis, l'analyse Taguchi, l'ANOVA et la régression non linéaire, afin de déduire des insights significatifs sur le processus FSW.

Le premier chapitre pose les bases en examinant l'état actuel de la technologie FSW, en particulier son application aux superalliages à base de nickel tels que l'Inconel 718. Il souligne les défis associés au soudage de matériaux à haute résistance et met en évidence le besoin de stratégies avancées de gestion thermique. La revue de la littérature, comprenant environ 275 références, offre un aperçu complet des connaissances existantes et identifie les lacunes que cette thèse vise à combler.

Le deuxième chapitre détaille le développement d'un modèle par éléments finis (FEM) qui simule avec précision le comportement thermomécanique du processus FSW. Le modèle couple les phénomènes thermiques et mécaniques pour prédire la distribution de température, l'évolution des contraintes et l'écoulement du matériau pendant le soudage. Le FEM a été validé à l'aide de données expérimentales publiées provenant d'essais de soudage sur l'alliage d'aluminium 6061-T6, puis étendu à l'Inconel 718. Les méthodologies statistiques, y compris l'analyse Taguchi et l'ANOVA, sont présentées avec des équations pertinentes, établissant un cadre solide pour l'optimisation des paramètres.

Dans le troisième chapitre, les effets de divers paramètres de FSW - force axiale, vitesse de rotation, vitesse de soudage, diamètre de l'épaule et diamètre de la broche - sur les performances de l'Al-T6 et de l'Inconel 718 sont analysés. Les résultats indiquent que des températures plus basses de la pièce conduisent à des structures de grain plus fines, une réduction de l'évolution des contraintes et une augmentation de la dureté. En particulier, il a été constaté que des forces axiales et des vitesses de rotation plus faibles, combinées à une vitesse de soudage plus élevée et à des diamètres d'épaule et de broche plus grands, optimisent les propriétés thermiques et mécaniques des soudures. De plus, le chapitre démontre que la force axiale et la vitesse de rotation sont les paramètres les plus influents. Les modèles de régression non linéaires introduits dans ce chapitre offrent des capacités prédictives, aidant à anticiper les résultats de performance en fonction des réglages des paramètres de FSW.

Le quatrième chapitre étend le FEM validé au soudage dissimilaire des alliages Inconel 718 et Ti-6Al-4V. L'étude paramétrique et l'analyse statistique révèlent les interactions complexes entre les paramètres de soudage et leurs effets sur la qualité des soudures. Les résultats soulignent l'importance d'un contrôle précis sur les variables de processus pour obtenir des résultats optimaux dans le soudage de matériaux dissemblables. Ce chapitre introduit également des modèles de régression qui offrent des capacités prédictives, aidant à anticiper les résultats de performance en fonction de réglages spécifiques des paramètres.

Les chapitres 3 et 4 explorent également des approches innovantes pour la gestion thermique lors du FSW, en se concentrant sur le préchauffage par induction et le refroidissement actif. L'introduction de ces stratégies améliore significativement l'efficacité du processus en permettant des vitesses de rotation et des forces axiales plus faibles, améliorant ainsi la dissipation de la chaleur et conduisant à des structures de grain plus fines. Enfin, le chapitre 5 propose une approche alternative et économique pour la gestion thermique à travers la mise en œuvre de stratégies de contrôle telles que le contrôle proportionnel-intégral-dérivé (PID) et le contrôle prédictif de modèle (MPC), démontrant leur efficacité dans le maintien des températures de soudage optimales et l'amélioration de la qualité globale des soudures.

La recherche présentée dans cette thèse apporte des insights précieux sur l'optimisation des paramètres de FSW pour l'Inconel 718. L'intégration de la modélisation par éléments finis avec l'analyse statistique et les méthodologies avancées de contrôle a conduit à une meilleure compréhension du comportement thermomécanique du processus FSW. Les principales conclusions incluent :

- Influence des paramètres: La force axiale et la vitesse de rotation sont les paramètres les plus critiques affectant la température de la pièce et, par conséquent, les propriétés mécaniques des soudures.
- Gestion thermique: Le préchauffage par induction et le refroidissement actif améliorent significativement la qualité des soudures en améliorant la dissipation de la chaleur et en permettant des structures de grain plus fines. De plus,

l'application d'une stratégie efficace de contrôle de processus maintient avec succès une température de pièce optimale.

- Modèles prédictifs: Les modèles de régression non linéaires développés offrent des capacités prédictives robustes, facilitant l'anticipation des résultats de soudage en fonction de réglages spécifiques des paramètres de FSW, principalement la vitesse de rotation.

Recommandations pour les travaux futurs

Les recherches futures devraient explorer les domaines suivants pour avancer davantage dans la compréhension et l'application du FSW pour les superalliages à base de nickel:

- Élargissement de la gamme de matériaux : Examiner l'applicabilité des modèles développés et des stratégies de contrôle à d'autres alliages à haute performance, y compris ceux utilisés dans les industries aérospatiale et nucléaire.
- Surveillance en temps réel : Développer des systèmes de surveillance et de contrôle en temps réel qui exploitent les modèles prédictifs pour ajuster dynamiquement les paramètres de soudage pendant le processus FSW.
- Études d'échelle : Réaliser des études d'échelle pour évaluer la faisabilité des paramètres optimisés de FSW et des stratégies de contrôle dans les applications industrielles, assurant la scalabilité et la reproductibilité.

En abordant ces domaines, les futures recherches peuvent capitaliser sur les conclusions de cette thèse, contribuant ainsi à l'avancement continu de la technologie FSW et à son application aux matériaux à haute performance.

Publications and Scientific Contributions:

Journal Paper	Abotaleb, A., Khraisheh, M., Remond, Y. et al. Parametric investigation of friction stir welding of aluminum alloy and Inconel 718 using finite element analysis. Discov Mechanical Engineering 3, 37 (2024). https://doi.org/10.1007/s44245-024-00076-1.
Journal Paper	A. Abotaleb, M. Al-Azba, M. Khraisheh, Y. Remond, S. Ahzi. Workpiece Temperature Control in Friction Stir Welding of Inconel 718 through Integrated Numerical Analysis and Process Control. Front. Control Eng., 30 October 2024 Sec. Control and Automation Systems Volume 5 - 2024 | https://doi.org/10.3389/fcteg.2024.1459399.
Journal Paper	M. Al-Azba, Z. Cen, A. Abotaleb. Solar Air Conditioning Case Studies for Qatar Climate Conditions. J. Eng. Sustain. Bldgs. Cities. Aug 2023, 4(3): 031001 (11 pages). https://doi.org/10.1115/1.4062840. Journal of Engineering for Sustainable Buildings and Cities- **ASME.**
Journal Paper	A. Abotaleb, M. Khraisheh, Y. Remond, S. Ahzi. Temperature and Stress Evolution in Friction Stir Welding of Dissimilar Materials: Inconel 718 and Ti-6Al-4V Alloy. (In Preparation)
Review Paper	A. Abotaleb, Y. Remond, M. Khraisheh, S. Ahzi. Friction Stir Welding of Inconel 718: A Review. (In Preparation)
Conference Paper	A. Abotaleb, Y. Remond, M. Khraisheh, S. Ahzi. Finite Element Analysis of Friction Stir Welding of Al Alloy and Inconel 718. COMSOL Conference 2023 Munich, 27-29 Oct 2023. https://www.comsol.com/paper/finite-element-analysis-of-friction-stir-welding-of-al-alloy-and-inconel-718-122311

Conference Paper	M. Al-Azba, A. Abotaleb. Efficient Geothermal Cooling in Harsh Environments: A Combined Experimental and Modelling Approach. COMSOL Conference 2023 Munich, 27-29 Oct 2023. https://www.comsol.com/paper/efficient-geothermal-cooling-in-harsh-environments-a-combined-experimental-and-m-122141
Conference Paper	A. Abotaleb, M. Al-Azba, Y. Remond, S. Ahzi. Enhancing Friction Stir Welding Quality of Inconel 718: An Approach of Numerical Modeling and Fuzzy Logic-Based Temperature Control. COMSOL Conference Florence 22–24 October 2024. https://www.comsol.com/paper/fsw-quality-of-inconel-718-numerical-modeling-and-fuzzy-logic-based-temperature-control-approach-134982
Oral Presentation	A. Abotaleb, Y. Remond, M. Khraisheh, S. Ahzi. Finite Element Analysis of Friction Stir Welding of Al Alloy and Inconel 718. COMSOL Conference 2023 Munich, 27-29 Oct 2023. https://www.comsol.com/paper/finite-element-analysis-of-friction-stir-welding-of-al-alloy-and-inconel-718-122311
Oral Presentation	M. Al-Azba, A. Abotaleb. Efficient Geothermal Cooling in Harsh Environments: A Combined Experimental and Modelling Approach. COMSOL Conference 2023 Munich, 27-29 Oct 2023. https://www.comsol.com/paper/efficient-geothermal-cooling-in-harsh-environments-a-combined-experimental-and-m-122141
Poster Presentation	A. Abotaleb, M. Al-Azba, Y. Remond, S. Ahzi. Enhancing Friction Stir Welding Quality of Inconel 718: An Approach of Numerical Modeling and Fuzzy Logic-Based Temperature Control. COMSOL Conference Florence 22–24 October 2024. https://www.comsol.com/paper/fsw-quality-of-inconel-718-

numerical-modeling-and-fuzzy-logic-based-temperature-control-approach-134982

Thesis Summary (in French and English)

Ahmed Abotaleb

Advanced modeling and optimization of the friction stir welding process: applications to Inconel 718 and high-performance alloys

Résumé

Cette étude se concentre sur le procédé de soudage par friction-malaxage (FSW), une technique de soudage en phase solide de plus en plus utilisée pour souder des matériaux métalliques similaires et dissemblables. La recherche vise à optimiser les paramètres de FSW pour l'Inconel 718 et le soudage dissemblable de l'Inconel 718 et des alliages Ti-6Al-4V en utilisant un modèle thermomécanique développé dans COMSOL Multiphysics v5.3. Le modèle, validé avec des données expérimentales pour l'aluminium 6061-T6, a été étendu à l'Inconel 718. Des paramètres de procédé clés tels que la vitesse de rotation, la vitesse de soudage, la force axiale, le diamètre de l'épaulement, le diamètre de la broche, le refroidissement actif et le préchauffage par induction ont été analysés à travers une étude paramétrique, une analyse Taguchi, une ANOVA et une régression non linéaire. Les résultats montrent que la force axiale et la vitesse de rotation ont un impact significatif sur le processus FSW. Le préchauffage par induction et le refroidissement actif ont amélioré la dissipation de la chaleur et les structures des grains. L'étude propose également des stratégies efficaces de contrôle de processus en utilisant les méthodes PID et MPC pour gérer les dynamiques thermiques, établissant un précédent pour l'optimisation du FSW dans les alliages de haute performance.

Mots-clés: **Soudage, Multiphysique, Modélisation, Inconel 718, Dissimilaire**

Résumé en anglais

This study focuses on the friction stir welding (FSW) process, a solid-state joining technique increasingly used for welding both similar and dissimilar metallic materials. The research aims to optimize FSW parameters for Inconel 718 and the dissimilar welding of Inconel 718 and Ti-6Al-4V alloys using a thermomechanical model developed in COMSOL Multiphysics v5.3. The model, validated with experimental data for 6061-T6 Aluminum, was extended to Inconel 718. Key process parameters such as rotational speed, welding speed, axial force, shoulder diameter, pin diameter, active cooling, and induction preheating were analyzed through parametric study, Taguchi analysis, ANOVA, and non-linear regression. Findings highlight that axial force and rotational speed significantly impact the FSW process. Induction preheating and active cooling improved heat dissipation and grain structures. The study also proposes effective process control strategies using PID and MPC methods to manage thermal dynamics, setting a precedent for optimizing FSW in high-performance alloys.

Keywords: Welding, Multiphysics, Modeling, Inconel 718, Dissimilar

References

Uncategorized References

1. Yunus, M. and M.S. Alsoufi, *Mathematical Modelling of a Friction Stir Welding Process to Predict the Joint Strength of Two Dissimilar Aluminium Alloys Using Experimental Data and Genetic Programming.* Modelling and Simulation in Engineering, 2018. **2018**: p. 4183816.
2. Pan, W., et al., *A new smoothed particle hydrodynamics non-Newtonian model for friction stir welding: Process modeling and simulation of microstructure evolution in a magnesium alloy.* International Journal of Plasticity, 2013. **48**: p. 189-204.
3. Barnes, S.J., et al., *Friction Stir Welding in HSLA-65 Steel: Part I. Influence of Weld Speed and Tool Material on Microstructural Development.* Metallurgical and Materials Transactions A, 2012. **43**(7): p. 2342-2355.
4. Franke, D., et al., *Understanding process force transients with application towards defect detection during friction stir welding of aluminum alloys.* Journal of Manufacturing Processes, 2020. **54**: p. 251-261.
5. Mishra, R.S., et al., *High strain rate superplasticity in a friction stir processed 7075 Al alloy.* Scripta Materialia, 1999. **42**(2): p. 163-168.
6. Yu, H.Z. and R.S. Mishra, *Additive friction stir deposition: a deformation processing route to metal additive manufacturing.* Materials Research Letters, 2021. **9**(2): p. 71-83.
7. Haghshenas, M. and A.P. Gerlich, *Joining of automotive sheet materials by friction-based welding methods: A review.* Engineering Science and Technology, an International Journal, 2018. **21**(1): p. 130-148.
8. Srivastava, M., et al., *A Review on Recent Progress in Solid State Friction Based Metal Additive Manufacturing: Friction Stir Additive Techniques.* Critical Reviews in Solid State and Materials Sciences, 2019. **44**(5): p. 345-377.
9. Khodabakhshi, F. and A.P. Gerlich, *Potentials and strategies of solid-state additive friction-stir manufacturing technology: A critical review.* Journal of Manufacturing Processes, 2018. **36**: p. 77-92.
10. Palanivel, S. and R.S. Mishra, *Building without melting: a short review of friction-based additive manufacturing techniques.* International Journal of Additive and Subtractive Materials Manufacturing, 2017. **1**(1): p. 82-103.
11. Mishra, R.S. and Z.Y. Ma, *Friction stir welding and processing.* Materials Science and Engineering: R: Reports, 2005. **50**(1): p. 1-78.
12. Reynolds, A.P., *Visualisation of material flow in autogenous friction stir welds.* Science and Technology of Welding and Joining, 2000. **5**(2): p. 120-124.

13. Baeslack, W.A., K.V. Jata, and T.J. Lienert, *Structure, properties and fracture of friction stir welds in a high-temperature Al-8.5Fe-1.3V–1.7Si alloy (AA-8009).* Journal of Materials Science, 2006. **41**(10): p. 2939-2951.

14. Colligan, K., *Material flow behavior during friction welding of aluminum.* Weld J, 1999. **75**(7): p. 229s-237s.

15. Xu, S., et al., *Finite element simulation of material flow in friction stir welding.* Science and Technology of Welding and Joining, 2001. **6**(3): p. 191-193.

16. Colegrove, P.A. and H.R. Shercliff, *Experimental and numerical analysis of aluminium alloy 7075-T7351 friction stir welds.* Science and Technology of Welding and Joining, 2003. **8**(5): p. 360-368.

17. McGlaun, J.M., S.L. Thompson, and M.G. Elrick, *CTH: A three-dimensional shock wave physics code.* International Journal of Impact Engineering, 1990. **10**(1): p. 351-360.

18. Stewart M.B., A.G.P., Nunes A.C., Romine P. , *Developments in Theoretical and Applied Mechanics* Florida Atlantic University, USA, 1998: p. pp. 472–484.

19. Tang, W., et al., *Heat Input and Temperature Distribution in Friction Stir Welding.* Journal of Materials Processing & Manufacturing Science - J MATER PROCESS MANUF SCI, 1998. **7**: p. 163-172.

20. W.J. Arbegast, i.Z.J., A. Beaudoin, T.A. Bieler, B. Radhakrishnan (Eds.), *Hot Deformation of Aluminum Alloys III.* TMS, Warrendale, PA, USA, 2003: p. 313.

21. International, A.S.M. and S. American Welding. *Trends in welding research : proceedings of the 5th international conference, Pine Mountain, Georgia, USA, June 1 - 5, 1998*. in *International Conference Trends in Welding Research ; 5*. 1999. Materials Park, Ohio, Pine Mountain, Ga.: ASM International;.

22. Benavides, S., et al., *Low-temperature friction-stir welding of 2024 aluminum.* Scripta Materialia, 1999. **41**(8): p. 809-815.

23. Humphreys, F.J. and M. Hatherly, *Chapter 12 - CONTROL OF RECRYSTALLIZATION*, in *Recrystallization and Related Annealing Phenomena*, F.J. Humphreys and M. Hatherly, Editors. 1995, Pergamon: Oxford. p. 393-415.

24. Humphreys, F.J. and M. Hatherly, *Chapter 3 - THE STRUCTURE AND ENERGY OF GRAIN BOUNDARIES*, in *Recrystallization and Related Annealing Phenomena*, F.J. Humphreys and M. Hatherly, Editors. 1995, Pergamon: Oxford. p. 57-83.

25. Humphreys, F.J. and M. Hatherly, *Chapter 9 - GRAIN GROWTH FOLLOWING RECRYSTALLIZATION*, in *Recrystallization and Related Annealing Phenomena*, F.J. Humphreys and M. Hatherly, Editors. 1995, Pergamon: Oxford. p. 281-325.

26. Humphreys, F.J. and M. Hatherly, *Chapter 6 - RECRYSTALLIZATION OF SINGLE-PHASE ALLOYS*, in *Recrystallization and Related Annealing*

Phenomena, F.J. Humphreys and M. Hatherly, Editors. 1995, Pergamon: Oxford. p. 173-220.

27. Field, D.P., et al., *Heterogeneity of crystallographic texture in friction stir welds of aluminum.* Metallurgical and Materials Transactions A, 2001. **32**(11): p. 2869-2877.

28. Jata, K.V., K.K. Sankaran, and J.J. Ruschau, *Friction-stir welding effects on microstructure and fatigue of aluminum alloy 7050-T7451.* Metallurgical and Materials Transactions A, 2000. **31**(9): p. 2181-2192.

29. Heinz, B. and B. Skrotzki, *Characterization of a friction-stir-welded aluminum alloy 6013.* Metallurgical and Materials Transactions B, 2002. **33**(3): p. 489-498.

30. Dalle Donne, C., et al., *Investigations on residual stresses in friction stir welds.* 2001.

31. Wang, X.-L., Feng, Z., David, S., Spooner, S., Hubbard, C.S. . *Neutron diffraction study of residual stresses in friction stir welds*. in *Proc. ICRS 6, IOM Communications*. 2000. London, UK

32. Peel, M., et al., *Microstructure, mechanical properties and residual stresses as a function of welding speed in aluminium AA5083 friction stir welds.* Acta Materialia, 2003. **51**(16): p. 4791-4801.

33. Sato, Y.S., et al., *Precipitation sequence in friction stir weld of 6063 aluminum during aging.* Metallurgical and Materials Transactions A, 1999. **30**(12): p. 3125-3130.

34. Sato, Y.S., et al., *Microtexture in the friction-stir weld of an aluminum alloy.* Metallurgical and Materials Transactions A, 2001. **32**(4): p. 941-948.

35. Svensson, L.E., et al., *Microstructure and mechanical properties of friction stir welded aluminium alloys with special reference to AA 5083 and AA 6082.* Science and Technology of Welding and Joining, 2000. **5**(5): p. 285-296.

36. Mishra, R., et al., *Mechanical properties of friction stir welded aluminum alloys.* Joining of Advanced and Specialty Materials, 2000: p. 157-159.

37. W.J. Arbegast, K.S.B., P.J. Hartley. *Proceedings of the Fifth International Conference on Trends in Welding Research,* . 1998. Pine Mountain, GA, USA,.

38. Reynolds, A.P., et al., *Structure, properties, and residual stress of 304L stainless steel friction stir welds.* Scripta Materialia, 2003. **48**(9): p. 1289-1294.

39. Iordachescu, M., E. Scutelnicu, and D. Iordachescu, *Microstructural Changes in Aluminium Alloys by Friction Stir Processing.* 2005.

40. Assidi, M., et al., *Friction model for friction stir welding process simulation: Calibrations from welding experiments.* International Journal of Machine Tools and Manufacture, 2010. **50**(2): p. 143-155.

41. Myung, D., et al., *Probing the Mechanism of Friction Stir Welding with ALE Based Finite Element Simulations and Its Application to Strength Prediction of Welded Aluminum.* Metals and Materials International, 2021. **27**(4): p. 650-666.

42. Hasan, A.F., C.J. Bennett, and P.H. Shipway, *A numerical comparison of the flow behaviour in Friction Stir Welding (FSW) using unworn and worn tool geometries.* Materials & Design, 2015. **87**: p. 1037-1046.

43. Jedrasiak, P. and H.R. Shercliff, *Small strain finite element modelling of friction stir spot welding of Al and Mg alloys.* Journal of Materials Processing Technology, 2019. **263**: p. 207-222.

44. He, X., F. Gu, and A. Ball, *A review of numerical analysis of friction stir welding.* Progress in Materials Science, 2014. **65**: p. 1-66.

45. Chen, G., et al., *Thermo-mechanical Analysis of Friction Stir Welding: A Review on Recent Advances.* Acta Metallurgica Sinica (English Letters), 2020. **33**(1): p. 3-12.

46. Colegrove, P.A. and H.R. Shercliff, *Two-dimensional CFD modelling of flow round profiled FSW tooling.* Science and Technology of Welding and Joining, 2004. **9**(6): p. 483-492.

47. Colegrove, P.A. and H.R. Shercliff, *3-Dimensional CFD modelling of flow round a threaded friction stir welding tool profile.* Journal of Materials Processing Technology, 2005. **169**(2): p. 320-327.

48. Zhang, S., et al., *Numerical analysis and analytical modeling of the spatial distribution of heat flux during friction stir welding.* Journal of Manufacturing Processes, 2018. **33**: p. 245-255.

49. Hasan, A.F., *CFD modelling of friction stir welding (FSW) process of AZ31 magnesium alloy using volume of fluid method.* Journal of Materials Research and Technology, 2019. **8**(2): p. 1819-1827.

50. Zhai, M., C. Wu, and H. Su, *Influence of tool tilt angle on heat transfer and material flow in friction stir welding.* Journal of Manufacturing Processes, 2020. **59**: p. 98-112.

51. Wu, W., A.M. Zhang, and M. Liu, *A cell-centered indirect Arbitrary-Lagrangian-Eulerian discontinuous Galerkin scheme on moving unstructured triangular meshes with topological adaptability.* Journal of Computational Physics, 2021. **438**: p. 110368.

52. Ansari, M.A., R. Abdi Behnagh, and A. Salvadori, *Numerical analysis of high-speed water jet spot welding using the arbitrary Lagrangian-Eulerian (ALE) method.* The International Journal of Advanced Manufacturing Technology, 2021. **112**(1): p. 491-504.

53. Schmidt, H. and J. Hattel, *A local model for the thermomechanical conditions in friction stir welding.* Modelling and Simulation in Materials Science and Engineering, 2005. **13**(1): p. 77.

54. Deng, X. and S. Xu, *Two-Dimensional Finite Element Simulation of Material Flow in the Friction Stir Welding Process.* Journal of Manufacturing Processes, 2004. **6**(2): p. 125-133.

55. Zhang, H.W., Z. Zhang, and J.T. Chen, *The finite element simulation of the friction stir welding process.* Materials Science and Engineering: A, 2005. **403**(1): p. 340-348.

56. Zhang, H.W., Z. Zhang, and J.T. Chen, *3D modeling of material flow in friction stir welding under different process parameters.* Journal of Materials Processing Technology, 2007. **183**(1): p. 62-70.

57. Zhang, Z., *Comparison of two contact models in the simulation of friction stir welding process.* Journal of Materials Science, 2008. **43**(17): p. 5867-5877.

58. Dialami, N., et al., *Enhanced friction model for Friction Stir Welding (FSW) analysis: Simulation and experimental validation.* International Journal of Mechanical Sciences, 2017. **133**: p. 555-567.

59. Dialami, N., et al., *Prediction of joint line remnant defect in friction stir welding.* International Journal of Mechanical Sciences, 2019. **151**: p. 61-69.

60. Dialami, N., M. Cervera, and M. Chiumenti, *Defect formation and material flow in Friction Stir Welding.* European Journal of Mechanics - A/Solids, 2020. **80**: p. 103912.

61. Andrade, D.G., et al., *Modelling torque and temperature in friction stir welding of aluminium alloys.* International Journal of Mechanical Sciences, 2020. **182**: p. 105725.

62. Andrade, D.G., et al., *Analysis of contact conditions and its influence on strain rate and temperature in friction stir welding.* International Journal of Mechanical Sciences, 2021. **191**: p. 106095.

63. Tongne, A., et al., *On material flow in Friction Stir Welded Al alloys.* Journal of Materials Processing Technology, 2017. **239**: p. 284-296.

64. Benson, D.J., *A mixture theory for contact in multi-material Eulerian formulations.* Computer Methods in Applied Mechanics and Engineering, 1997. **140**(1): p. 59-86.

65. Al-Badour, F., et al., *Coupled Eulerian Lagrangian finite element modeling of friction stir welding processes.* Journal of Materials Processing Technology, 2013. **213**(8): p. 1433-1439.

66. Chauhan, P., et al., *Modeling of defects in friction stir welding using coupled Eulerian and Lagrangian method.* Journal of Manufacturing Processes, 2018. **34**: p. 158-166.

67. Su, Y., et al., *Strengthening mechanism of friction stir welded alpha titanium alloy specially designed T-joints.* Journal of Manufacturing Processes, 2020. **55**: p. 1-12.

68. Akbari, M., P. Asadi, and R.A. Behnagh, *Modeling of material flow in dissimilar friction stir lap welding of aluminum and brass using coupled Eulerian and Lagrangian method.* The International Journal of Advanced Manufacturing Technology, 2021. **113**(3): p. 721-734.

69. Wang, X., et al., *Tool-workpiece stick-slip conditions and their effects on torque and heat generation rate in the friction stir welding.* Acta Materialia, 2021. **213**: p. 116969.

70. Darras, B.M., et al., *Friction stir processing of commercial AZ31 magnesium alloy.* Journal of Materials Processing Technology, 2007. **191**(1): p. 77-81.

71. Nassar, H.W. and M.K. Khraisheh, *Simulation of Material Flow and Heat Evolution in Friction Stir Processing Incorporating Melting.* Journal of Engineering Materials and Technology, 2012. **134**(4).

72. Aljoaba, S., et al., *Modeling the Effects of Coolant Application in Friction Stir Processing on Material Microstructure Using 3D CFD Analysis.* Journal of Materials Engineering and Performance, 2012. **21**(7): p. 1141-1150.

73. Albakri, A.N., et al., *Simulation of Friction Stir Processing with Internally Cooled Tool.* Advanced Materials Research, 2012. **445**: p. 560-565.

74. Aljoaba, S.Z., et al., *Modeling of friction stir processing using 3D CFD analysis.* International Journal of Material Forming, 2009. **2**(1): p. 315.

75. Darras, B.M. and M.K. Khraisheh, *Analytical Modeling of Strain Rate Distribution During Friction Stir Processing.* Journal of Materials Engineering and Performance, 2008. **17**(2): p. 168-177.

76. Hou, Z., et al., *Residual Stresses in Dissimilar Friction Stir Welding of AA2024 and AZ31: Experimental and Numerical Study.* Journal of Manufacturing Science and Engineering-transactions of The Asme, 2018. **140**: p. 051015.

77. Graf, A., *Chapter 3 - Aluminum alloys for lightweight automotive structures*, in *Materials, Design and Manufacturing for Lightweight Vehicles (Second Edition)*, P.K. Mallick, Editor. 2021, Woodhead Publishing. p. 97-123.

78. Torzewski, J., et al., *Microstructure and Mechanical Properties of Dissimilar Friction Stir Welded Joint AA7020/AA5083 with Different Joining Parameters.* Materials, 2022. **15**(5): p. 1910.

79. Grażyna, M.-N., et al., *Microstructure and Properties of As-Cast and Heat-Treated 2017A Aluminium Alloy Obtained from Scrap Recycling.* Materials, 2021. **14**(1): p. 89.

80. Zhu, L., N. Li, and P.R.N. Childs, *Light-weighting in aerospace component and system design.* Propulsion and Power Research, 2018. **7**(2): p. 103-119.

81. Ojo Sunday Isaac, F., P. Abimbola Patricia Idowu, and U. Nduka Ekene, *Effect of Alloying Element on the Integrity and Functionality of Aluminium-Based Alloy*, in *Aluminium Alloys*, S. Subbarayan, Editor. 2017, IntechOpen: Rijeka. p. Ch. 13.

82. Braun, R., *Nd:YAG laser butt welding of AA6013 using silicon and magnesium containing filler powders.* Materials Science and Engineering: A, 2006. **426**(1): p. 250-262.

83. Engler, O., K. Kuhnke, and J. Hasenclever, *Development of intermetallic particles during solidification and homogenization of two AA 5xxx series Al-Mg alloys with different Mg contents.* Journal of Alloys and Compounds, 2017. **728**: p. 669-681.

84. Ertuğ, B. and L.C. Kumruoğlu, *5083 type Al-Mg and 6082 type Al-Mg-Si alloys for ship building".* Am. J. Eng. Res., 2015. **4**(3): p. 146-150.

85. Liang, W.J., et al., *General aspects related to the corrosion of 6xxx series aluminium alloys: Exploring the influence of Mg/Si ratio and Cu.* Corrosion Science, 2013. **76**: p. 119-128.

86. Herbert, M.A., et al., *Investigation on microstructure and mechanical properties of Friction Stir Welded AA6061-4.5Cu-10SiC composite.* IOP Conference Series: Materials Science and Engineering, 2016. **114**(1): p. 012125.

87. Omer, K., C. Butcher, and M. Worswick, *Characterization and application of a constitutive model for two 7000-series aluminum alloys subjected to hot forming.* International Journal of Mechanical Sciences, 2020. **165**: p. 105218.

88. Saju, T. and M. Velu, *Review on welding and fracture of nickel based superalloys.* Materials Today: Proceedings, 2021. **46**: p. 7161-7169.

89. Antonio, M.M.G.a., *BLISK Fabrication by Linear Friction Welding*, in *Advances in Gas Turbine Technology*, B. Ernesto, Editor. 2011, IntechOpen: Rijeka. p. Ch. 18.

90. Lemos, G.V.B., et al., *Progress in friction stir welding of Ni alloys.* Science and Technology of Welding and Joining, 2017. **22**(8): p. 643-657.

91. Liu, S., et al., *Friction surface cladding: An exploratory study of a new solid state cladding process.* Journal of Materials Processing Technology, 2016. **229**: p. 769-784.

92. Choudhury, B. and M. Chandrasekaran, *Investigation on welding characteristics of aerospace materials – A review.* Materials Today: Proceedings, 2017. **4**(8): p. 7519-7526.

93. Loria, E.A., *Recent developments in the progress of superalloy 718.* JOM, 1992. **44**(6): p. 33-36.

94. Schafrik, R.E., D.D. Ward, and J.R. Groh, *Application of Alloy 718 in GE Aircraft Engines: Past, Present and Next Five Years.* Superalloys, 2001: p. 1-11.

95. deBarbadillo, J.J. and S.K. Mannan, *Alloy 718 for Oilfield Applications.* JOM, 2012. **64**(2): p. 265-270.

96. Sandhu, S.S. and A.S. Shahi, *Metallurgical, wear and fatigue performance of Inconel 625 weld claddings.* Journal of Materials Processing Technology, 2016. **233**: p. 1-8.

97. Pollock, T.M. and S. Tin, *Nickel-Based Superalloys for Advanced Turbine Engines: Chemistry, Microstructure and Properties.* Journal of Propulsion and Power, 2006. **22**(2): p. 361-374.

98. Devendranath Ramkumar, K., et al., *Influence of filler metals and welding techniques on the structure–property relationships of Inconel 718 and AISI 316L dissimilar weldments.* Materials & Design (1980-2015), 2014. **62**: p. 175-188.

99. Manikandan, S.G.K., D. Sivakumar, and M. Kamaraj, *1 - Physical metallurgy of alloy 718*, in *Welding the Inconel 718 Superalloy*, S.G.K. Manikandan, D. Sivakumar, and M. Kamaraj, Editors. 2019, Elsevier. p. 1-19.

100. Manikandan, S.G.K., D. Sivakumar, and M. Kamaraj, *3 - Microsegregation and interdendritic Laves phase*, in *Welding the Inconel 718 Superalloy*, S.G.K. Manikandan, D. Sivakumar, and M. Kamaraj, Editors. 2019, Elsevier. p. 47-52.

101. Muralidharan, B.G., V. Shankar, and T.P.S. Gill, *Weldability of Inconel 718 - a review*. 1996: India.

102. Lee, H.T., et al., *Dissimilar welding of nickel-based Alloy 690 to SUS 304L with Ti addition.* Journal of Nuclear Materials, 2004. **335**(1): p. 59-69.

103. Chamanfar, A., et al., *Cracking in fusion zone and heat affected zone of electron beam welded Inconel-713LC gas turbine blades.* Materials Science and Engineering: A, 2015. **642**: p. 230-240.

104. Iturbe, A., et al., *Mechanical characterization and modelling of Inconel 718 material behavior for machining process assessment.* Materials Science and Engineering: A, 2017. **682**: p. 441-453.

105. Raj, S. and P. Biswas, *Effect of induction preheating on microstructure and mechanical properties of friction stir welded dissimilar material joints of Inconel 718 and SS316L.* CIRP Journal of Manufacturing Science and Technology, 2023. **41**: p. 160-179.

106. *Weld Integrity and Performance*, ed. S. Lampman. 1997: ASM International.

107. David, S.A., et al., *Weldability and weld performance of candidate nickel base superalloys for advanced ultrasupercritical fossil power plants part I: fundamentals.* Science and Technology of Welding and Joining, 2015. **20**(7): p. 532-552.

108. Siefert, J.A., et al., *Weldability and weld performance of candidate nickel based superalloys for advanced ultrasupercritical fossil power plants Part II: weldability and cross-weld creep performance.* Science and Technology of Welding and Joining, 2016. **21**(5): p. 397-427.

109. Ye, F., et al., *Friction stir welding of Inconel alloy 600.* Journal of Materials Science, 2006. **41**(16): p. 5376-5379.

110. Ahmed, M.M.Z., B.P. Wynne, and J.P. Martin, *Effect of friction stir welding speed on mechanical properties and microstructure of nickel based super alloy Inconel 718.* Science and Technology of Welding and Joining, 2013. **18**(8): p. 680-687.

111. Hong, J.K., et al., *Microstructures and mechanical properties of Inconel 718 welds by CO2 laser welding.* Journal of Materials Processing Technology, 2008. **201**(1): p. 515-520.

112. Gobbi, S., et al., *High powder CO2 and Nd□YAG laser welding of wrought Inconel 718.* Journal of Materials Processing Technology, 1996. **56**(1): p. 333-345.

113. Huang, C.A., et al., *A study of the heat-affected zone (HAZ) of an Inconel 718 sheet welded with electron-beam welding (EBW).* Materials Science and Engineering: A, 2005. **398**(1): p. 275-281.

114. Chen, W., M.C. Chaturvedi, and N.L. Richards, *Effect of boron segregation at grain boundaries on heat-affected zone cracking in wrought INCONEL 718.* Metallurgical and Materials Transactions A, 2001. **32**(4): p. 931-939.

115. Song, K.H., H.S. Kim, and W.Y. Kim, *Precipitates formation and its impact in friction stir welded and post-heat-treated Inconel 718 alloy.* MRS Proceedings, 2011. **1363**: p. mrss11-1363-rr05-17.

116. Rule, J.R. and J.C. Lippold, *Physical Simulation of Friction Stir Welding and Processing of Nickel-Base Alloys Using Hot Torsion: Physical Metallurgical and Materials Science.* Metallurgical and Materials Transactions, 2013. **44**(8): p. 3649-3663.

117. Alexopoulos, N.D., et al., *Fatigue Behavior of Inconel 718 TIG Welds.* Journal of Materials Engineering and Performance, 2014. **23**(8): p. 2973-2983.

118. Song, K.H. and K. Nakata, *Microstructural and mechanical properties of friction-stir-welded and post-heat-treated Inconel 718 alloy.* Journal of Alloys and Compounds, 2010. **505**(1): p. 144-150.

119. Song, K.H., H. Fujii, and K. Nakata, *Effect of welding speed on microstructural and mechanical properties of friction stir welded Inconel 600.* Materials & Design, 2009. **30**(10): p. 3972-3978.

120. Sato, Y.S., et al., *Effect of microstructure on properties of friction stir welded Inconel Alloy 600.* Materials Science and Engineering: A, 2008. **477**(1): p. 250-258.

121. Song, K.H. and K. Nakata, *Effect of precipitation on post-heat-treated Inconel 625 alloy after friction stir welding.* Materials & Design, 2010. **31**(6): p. 2942-2947.

122. Song, K.H., T. Tsumura, and K. Nakata, *Development of Microstructure and Mechanical Properties in Laser-FSW Hybrid Welded Inconel 600.* MATERIALS TRANSACTIONS, 2009. **50**(7): p. 1832-1837.

123. Prado, R.A., et al., *Tool wear in the friction-stir welding of aluminum alloy 6061+20% Al2O3: a preliminary study.* Scripta Materialia, 2001. **45**(1): p. 75-80.

124. Raffo, P.L., *Yielding and fracture in tungsten and tungsten-rhenium alloys.* Journal of the Less Common Metals, 1969. **17**(2): p. 133-149.

125. Fall, A., et al., *Tool Wear Characteristics and Effect on Microstructure in Ti-6Al-4V Friction Stir Welded Joints.* Metals, 2016. **6**(11): p. 275.

126. Feng, Z., et al., *Friction Stir Spot Welding of Advanced High-Strength Steels - A Feasibility Study*. 2005, SAE International.

127. Meran, C., V. Kovan, and A. Alptekin, *Friction stir welding of AISI 304 austenitic stainless steel.* Materialwissenschaft und Werkstofftechnik, 2007. **38**(10): p. 829-835.

128. *Defects and Their Effects on Materials Properties*, in *Structure-Property Relations in Nonferrous Metals*. 2005. p. 18-27.

129. Selvam, S. *COMPARISON OF HEAVY ALLOY TOOL IN FRICTION STIR WELDING*. 2012.

130. Jasthi, B.K., W.J. Arbegast, and S.M. Howard, *Thermal Expansion Coefficient and Mechanical Properties of Friction Stir Welded Invar (Fe-36%Ni).* Journal of Materials Engineering and Performance, 2009. **18**(7): p. 925-934.

131. Wurster, S., B. Gludovatz, and R. Pippan, *High temperature fracture experiments on tungsten–rhenium alloys.* International Journal of Refractory Metals and Hard Materials, 2010. **28**(6): p. 692-697.

132. Mandel, K., et al., *The influence of stress state on the compressive strength of WC–Co with different Co contents.* International Journal of Refractory Metals and Hard Materials, 2014. **47**: p. 124-130.

133. Song, K.H., T. Tsumura, and K. Nakata. *Development of microstructure and mechanical properties in laser-FSW hybrid welded inconel 600*. in *Materials Transactions*. 2009.

134. Raj, S., P. Pankaj, and P. Biswas. *Microstructure and Mechanical Characterisation of Friction Stir Welded Inconel 718 Alloy*. in *Recent Advances in Mechanical Engineering*. 2021. Singapore: Springer Singapore.

135. Raj, S. and P. Biswas, *High-Frequency Induction-Assisted Hybrid Friction Stir Welding of Inconel 718 Plates.* Journal of Manufacturing Science and Engineering, 2021. **144**(4).

136. Raj, S., P. Pankaj, and P. Biswas, *Friction Stir Welding of Inconel-718 Alloy Using a Tungsten Carbide Tool.* Journal of Materials Engineering and Performance, 2022. **31**(3): p. 2086-2101.

137. Saha, R. and P. Biswas, *Temperature and Stress Evaluation during Friction Stir Welding of Inconel 718 Alloy Using Finite Element Numerical Simulation.* Journal of Materials Engineering and Performance, 2022. **31**(3): p. 2002-2011.

138. Song, K.H., W.Y. Kim, and K. Nakata, *Evaluation of microstructures and mechanical properties of friction stir welded lap joints of Inconel 600/SS 400.* Materials & Design, 2012. **35**: p. 126-132.

139. E, P., et al., *Investigate the welding of Inconel 718 and Inconel 600 in friction stir welding.* Materials Today: Proceedings, 2022. **60**: p. 1385-1388.

140. Threadgill, P.L., et al., *Friction stir welding of aluminium alloys.* International Materials Reviews, 2009. **54**(2): p. 49-93.

141. Rao, D., et al., *Asymmetric mechanical properties and tensile behaviour prediction of aluminium alloy 5083 friction stir welding joints.* Materials Science and Engineering: A, 2013. **565**: p. 44-50.

142. John N. DuPont, J.C.L., Samuel D. Kiser, *Weldability Testing*, in *Welding Metallurgy and Weldability of Nickel-Base Alloys*. 2009. p. 379-402.

143. Lohwasser, D. and Z. Chen, *Friction stir welding: From basics to applications*. 2009: Elsevier.

144. Podržaj, P., B. Jerman, and D. Klobčar, *Welding defects at friction stir welding.* Metalurgija, 2015. **54**(2): p. 387-389.

145. Kurt, A., I. Uygur, and H. Ates, *Effect of Porosity Content on the Weldability of Powder Metal Parts Produced by Friction Stir Welding.* Materials Science Forum, 2007. **534-536**: p. 789-792.

146. Murr, L.E., et al., *Friction-stir welding: microstructural characterization.* Materials Research Innovations, 1998. **1**(4): p. 211-223.

147. Lemos, G.V.B., et al., *Efeito da velocidade de rotação da ferramenta na soldagem por fricção e mistura mecânica da liga inconel 625.* Associação Brasileira de Metalurgia, Materiais e Mineração. Anais do, 2016. **71**: p. 27-29.

148. Crook, P., *Corrosion-resistant nickel alloys, Part 1: nickel alloys provide levels of corrosion resistance not possible with other alloys. This is part one of a three-part series about corrosion-resistant nickel alloys.* Advanced materials & processes, 2007. **165**(6): p. 37-40.

149. McCoy, S., B. Puckett, and E. Hibner, *High performance age-hardenable nickel alloys solve problems in sour oil and gas service.* Balance, 2002. **14**(5): p. 16-23.

150. Designation, A., *Standard test methods for pitting and crevice corrosion resistance of stainless steels and related alloys by use of ferric chloride solution.* ASTM International, 2009.

151. Bassiouni, M., et al. *Studies on the degree of sensitization of welded 2507 super duplex stainless steel using a modified DL-EPR test procedure*. in *Proceedings of the 50th Annual Conference of the Australasian Corrosion Association 2010: Corrosion and Prevention 2010*. 2010. Australasian Corrosion Association Inc.

152. Prohaska, M., et al. *Possibilities and limitations of replacing a conventional corrosion test with an electrochemical potentiokinetic reactivation method using*

the example of alloy 625. in *EUROCORR 2009, The European Corrosion Congress*. 2009.

153. Lackner, R., et al., *Sensitization of as Rolled and Stable Annealed Alloy 625.* BHM Berg- und Hüttenmännische Monatshefte, 2014. **159**(1): p. 12-22.

154. Peters, M., et al., *Titanium Alloys for Aerospace Applications*, in *Titanium and Titanium Alloys*. 2003. p. 333-350.

155. Muralimohan, C.H., et al., *Analysis and Characterization of the Role of Ni Interlayer in the Friction Welding of Titanium and 304 Austenitic Stainless Steel.* Metallurgical and Materials Transactions A, 2016. **47**(1): p. 347-359.

156. Welsch, G., R. Boyer, and E. Collings, *Materials properties handbook: titanium alloys*. 1993: ASM international.

157. Cheepu, M., V. Muthupandi, and S. Loganathan, *Friction Welding of Titanium to 304 Stainless Steel with Electroplated Nickel Interlayer.* Materials Science Forum, 2012. **710**: p. 620-625.

158. Fratini, L., et al., *A new fixture for FSW processes of titanium alloys.* CIRP Annals, 2010. **59**(1): p. 271-274.

159. Cheepu, M., M. Ashfaq, and V. Muthupandi, *A New Approach for Using Interlayer and Analysis of the Friction Welding of Titanium to Stainless Steel.* Transactions of the Indian Institute of Metals, 2017. **70**(10): p. 2591-2600.

160. Karna, S., et al., *Recent Developments and Research Progress on Friction Stir Welding of Titanium Alloys: An Overview.* IOP Conference Series: Materials Science and Engineering, 2018. **330**(1): p. 012068.

161. Rai, R., et al., *Review: Friction stir welding tools.* Science and Technology of Welding and Joining, 2011. **16**(4): p. 325-342.

162. Buffa, G., A. Ducato, and L. Fratini, *FEM based prediction of phase transformations during Friction Stir Welding of Ti6Al4V titanium alloy.* Materials Science and Engineering: A, 2013. **581**: p. 56-65.

163. Karna, S., et al. *Recent developments and research progress on friction stir welding of titanium alloys: an overview*. in *IOP Conference Series: Materials Science and Engineering*. 2018. IOP Publishing.

164. Zhang, Y., et al., *Stir zone microstructure of commercial purity titanium friction stir welded using pcBN tool.* Materials Science and Engineering: A, 2008. **488**(1): p. 25-30.

165. Wu, L.H., et al., *Tool wear and its effect on microstructure and properties of friction stir processed Ti–6Al–4V.* Materials Chemistry and Physics, 2014. **146**(3): p. 512-522.

166. Edwards, P. and M. Ramulu, *Effect of process conditions on superplastic forming behaviour in Ti–6Al–4V friction stir welds.* Science and Technology of Welding and Joining, 2009. **14**(7): p. 669-680.

167. Liu, H.J., L. Zhou, and Q.W. Liu, *Microstructural characteristics and mechanical properties of friction stir welded joints of Ti–6Al–4V titanium alloy.* Materials & Design, 2010. **31**(3): p. 1650-1655.

168. Zhou, L., H.J. Liu, and Q.W. Liu, *Effect of rotation speed on microstructure and mechanical properties of Ti–6Al–4V friction stir welded joints.* Materials & Design (1980-2015), 2010. **31**(5): p. 2631-2636.

169. Kitamura, K., et al., *Flexible control of the microstructure and mechanical properties of friction stir welded Ti–6Al–4V joints.* Materials & Design (1980-2015), 2013. **46**: p. 348-354.

170. Esmaily, M., et al., *Microstructural characterization and formation of α′ martensite phase in Ti–6Al–4V alloy butt joints produced by friction stir and gas tungsten arc welding processes.* Materials & Design, 2013. **47**: p. 143-150.

171. Su, J., et al., *Microstructure and mechanical properties of a friction stir processed Ti–6Al–4V alloy.* Materials Science and Engineering: A, 2013. **573**: p. 67-74.

172. Edwards, P.D. and M. Ramulu, *Material flow during friction stir welding of Ti-6Al-4V.* Journal of Materials Processing Technology, 2015. **218**: p. 107-115.

173. Zhang, Y., et al., *Microstructural characteristics and mechanical properties of Ti–6Al–4V friction stir welds.* Materials Science and Engineering: A, 2008. **485**(1): p. 448-455.

174. Ramulu, M., et al., *Tensile properties of friction stir welded and friction stir welded-superplastically formed Ti–6Al–4V butt joints.* Materials & Design, 2010. **31**(6): p. 3056-3061.

175. Schmidt, H.B. and J.H. Hattel, *Thermal modelling of friction stir welding.* Scripta Materialia, 2008. **58**(5): p. 332-337.

176. Chao, Y.J., X. Qi , and W. Tang, *Heat Transfer in Friction Stir Welding—Experimental and Numerical Studies.* Journal of Manufacturing Science and Engineering, 2003. **125**(1): p. 138-145.

177. Kamp, N., A. Sullivan, and J.D. Robson, *Modelling of friction stir welding of 7xxx aluminium alloys.* Materials Science and Engineering: A, 2007. **466**(1): p. 246-255.

178. Chen, C.M. and R. Kovacevic, *Finite element modeling of friction stir welding—thermal and thermomechanical analysis.* International Journal of Machine Tools and Manufacture, 2003. **43**(13): p. 1319-1326.

179. Chiumenti, M., et al., *Numerical modeling of friction stir welding processes.* Computer Methods in Applied Mechanics and Engineering, 2013. **254**: p. 353-369.

180. Buffa, G., et al., *Design of the friction stir welding tool using the continuum based FEM model.* Materials Science and Engineering: A, 2006. **419**(1): p. 381-388.

181. Buffa, G., et al., *Friction stir welding of lap joints: Influence of process parameters on the metallurgical and mechanical properties.* Materials Science and Engineering: A, 2009. **519**(1): p. 19-26.

182. PASTA, S. and A.P. REYNOLDS, *Residual stress effects on fatigue crack growth in a Ti-6Al-4V friction stir weld.* Fatigue & Fracture of Engineering Materials & Structures, 2008. **31**(7): p. 569-580.

183. W.B. Lee, Y.M.Y., S.B. Jung, in: K.V. Jata, M.W. Mahoney, R.S. Mishra, S.L. Semiatin, T. Lienert (Eds.). *Friction Stir Welding and Processing II,*. in *TMS, Warrendale,* . 2003. PA, USA, .

184. Lee, W.-B., Y.-M. Yeon, and S.-B. Jung, *The joint properties of dissimilar formed Al alloys by friction stir welding according to the fixed location of materials.* Scripta materialia, 2003. **49**(5): p. 423-428.

185. J. A. Baumann, R.J.L., D. R. Bolser, and R. Talwar, . *The Minerals, Metals & Materials Society*. in *Friction stir welding and processing II,* . March 2003. Warrendale, PA:.

186. Çam, G., *Friction stir welded structural materials: beyond Al-alloys.* International Materials Reviews, 2011. **56**(1): p. 1-48.

187. Saha, R. and P. Biswas, *Thermomechanical analysis of induction assisted friction stir welding of Inconel 718 alloy: A finite element approach.* International Journal of Pressure Vessels and Piping, 2022. **199**: p. 104731.

188. Sinclair, P.C., et al., *Heated Friction Stir Welding: An Experimental and Theoretical Investigation into How Preheating Influences Process Forces.* Materials and Manufacturing Processes, 2010. **25**(11): p. 1283-1291.

189. Chang, W.-S., et al., *Microstructure and Mechanical Properties of Hybrid Laser-Friction Stir Welding between AA6061-T6 Al Alloy and AZ31 Mg Alloy.* Journal of Materials Science & Technology, 2011. **27**(3): p. 199-204.

190. Wada, T., et al., *Friction Stir Welding of Medium Carbon Steel with Laser-Preheating.* ISIJ International, 2020. **60**(1): p. 153-159.

191. Xu, L., et al., *Experimental Study on Butt-joint TC4/GH4169 Dissimilar Metals Prepared by Double Laser Assisted FSW.* Journal of Physics: Conference Series, 2022. **2262**(1): p. 012010.

192. Chen, S., et al., *Mechanical properties of electric assisted friction stir welded 2219 aluminum alloy.* Journal of Manufacturing Processes, 2019. **44**: p. 197-206.

193. Amini, S. and M.R. Amiri, *Study of ultrasonic vibrations' effect on friction stir welding.* The International Journal of Advanced Manufacturing Technology, 2014. **73**(1): p. 127-135.

194. Strass, B., et al., *Realization of Al/Mg-Hybrid-Joints by Ultrasound Supported Friction Stir Welding - Mechanical Properties, Microstructure and Corrosion Behavior.* Advanced Materials Research, 2014. **966-967**: p. 521-535.

195. Mohan, D.G. and S. Gopi, *Induction assisted friction stir welding: a review.* Australian Journal of Mechanical Engineering, 2020. **18**(1): p. 119-123.

196. Cheon, J., et al., *Evaluation of a High-Frequency Induction Heating Assisted Friction Stir Welding Process on Carbon Steel Sheets.* J Weld Join, 2019. **37**(5): p. 501-507.

197. Álvarez, A.I., et al., *Evaluation of an induction-assisted friction stir welding technique for super duplex stainless steels.* Surface and Interface Analysis, 2014. **46**(10-11): p. 892-896.

198. Mohan, D.G., J. Tomków, and S. Gopi, *Induction Assisted Hybrid Friction Stir Welding of Dissimilar Materials AA5052 Aluminium Alloy and X12Cr13 Stainless Steel.* Advances in Materials Science, 2021. **21**(3): p. 17-30.

199. Kaushik, P. and D. Kumar Dwivedi, *Induction preheating in FSW of Al-Steel combination.* Materials Today: Proceedings, 2021. **46**: p. 1091-1095.

200. Daftardar, S., *Laser assisted friction stir welding: finite volume method and metaheuristic optimization*. 2009: Louisiana State University and Agricultural & Mechanical College.

201. Fei, X. and Z. Wu, *Research of temperature and microstructure in friction stir welding of Q235 steel with laser-assisted heating.* Results in Physics, 2018. **11**: p. 1048-1051.

202. Ahmad, B., A. Galloway, and A. Toumpis, *Numerical optimisation of laser assisted friction stir welding of structural steel.* Science and Technology of Welding and Joining, 2019. **24**(6): p. 548-558.

203. Long, X. and S.K. Khanna, *Modelling of electrically enhanced friction stir welding process using finite element method.* Science and Technology of Welding and Joining, 2005. **10**(4): p. 482-487.

204. Tiwari, A., et al., *CFD Modelling of Temperature Distribution and Material Flow Investigation During FSW of DH36 Shipbuilding Grade Steel.* Transactions of the Indian Institute of Metals, 2020. **73**(9): p. 2291-2307.

205. Pankaj, P., et al., *Plasma-Assisted Hybrid Dissimilar Friction Stir Welding for Joining of DH36 Steel and AISI 1008 Steel: Thermal Modelling and Experimental Analysis.* Arabian Journal for Science and Engineering, 2021. **46**(8): p. 7929-7952.

206. Shi, L., C.S. Wu, and Z. Sun, *An integrated model for analysing the effects of ultrasonic vibration on tool torque and thermal processes in friction stir welding.* Science and Technology of Welding and Joining, 2018. **23**(5): p. 365-379.

207. Sabry, I., A.-H.I. Mourad, and D.T. Thekkuden, *Vibration-Assisted Friction Stir Welding of AA 2024-T3 Plates*. 2021.

208. Pramod, R., et al., *Experimental studies on friction stir welding of aluminium alloy 5083 and prediction of temperature distribution using arbitrary Lagrangian–Eulerian-based finite element method.* Proceedings of the Institution of

Mechanical Engineers, Part L: Journal of Materials: Design and Applications, 2021. **236**(5): p. 1067-1076.

209. Examiner, P., and Stoner, K., U.S. Patent., Editor. 2004.

210. Sun, Y.F., et al., *Microstructure and mechanical properties of S45C steel prepared by laser-assisted friction stir welding.* Materials & Design, 2013. **47**: p. 842-849.

211. Yaduwanshi, D.K., S. Bag, and S. Pal, *Effect of Preheating in Hybrid Friction Stir Welding of Aluminum Alloy.* Journal of Materials Engineering and Performance, 2014. **23**(10): p. 3794-3803.

212. Mehta, K.P. and V.J. Badheka, *Hybrid approaches of assisted heating and cooling for friction stir welding of copper to aluminum joints.* Journal of Materials Processing Technology, 2017. **239**: p. 336-345.

213. Liu, X., S. Lan, and J. Ni, *Electrically assisted friction stir welding for joining Al 6061 to TRIP 780 steel.* Journal of Materials Processing Technology, 2015. **219**: p. 112-123.

214. Ji, S., et al., *Joint formation and mechanical properties of back heating assisted friction stir welded Ti–6Al–4V alloy.* Materials & Design, 2017. **113**: p. 37-46.

215. Vijendra, B. and A. Sharma, *Induction heated tool assisted friction-stir welding (i-FSW): A novel hybrid process for joining of thermoplastics.* Journal of Manufacturing Processes, 2015. **20**: p. 234-244.

216. Xu, N., et al., *Microstructure and tensile properties of rapid-cooling friction-stir-welded AZ31B Mg alloy along thickness direction.* Transactions of Nonferrous Metals Society of China, 2020. **30**(12): p. 3254-3262.

217. Liu, X.C., Y.F. Sun, and H. Fujii, *Clarification of microstructure evolution of aluminum during friction stir welding using liquid CO2 rapid cooling.* Materials & Design, 2017. **129**: p. 151-163.

218. Xu, W.-f., et al., *Effect of cooling conditions on corrosion resistance of friction stir welded 2219-T62 aluminum alloy thick plate joint.* Transactions of Nonferrous Metals Society of China, 2020. **30**(6): p. 1491-1499.

219. Xue, P., et al., *Achieving friction stir welded pure copper joints with nearly equal strength to the parent metal via additional rapid cooling.* Scripta Materialia, 2011. **64**(11): p. 1051-1054.

220. Sree Sabari, S., S. Malarvizhi, and V. Balasubramanian, *Characteristics of FSW and UWFSW joints of AA2519-T87 aluminium alloy: Effect of tool rotation speed.* Journal of Manufacturing Processes, 2016. **22**: p. 278-289.

221. Yi, D., et al., *Effect of cooling rate on microstructure of friction-stir welded AA1100 aluminum alloy.* Philosophical Magazine, 2016. **96**(18): p. 1965-1977.

222. Wu, L.H., et al., *Fabrication of high-quality Ti joint with ultrafine grains using submerged friction stirring technology and its microstructural evolution mechanism.* Acta Materialia, 2019. **166**: p. 371-385.

223. Tao, Y., et al., *Effect of post weld artificial aging and water cooling on microstructure and mechanical properties of friction stir welded 2198-T8 Al-Li joints.* Journal of Materials Science & Technology, 2022. **123**: p. 92-112.

224. Xie, G.M., et al., *Crystallography of the nugget zone of bainitic steel by friction stir welding in various cooling mediums.* Materials Characterization, 2021. **182**: p. 111523.

225. Elatharasan, G. and V.S.S. Kumar, *An Experimental Analysis and Optimization of Process Parameter on Friction Stir Welding of AA 6061-T6 Aluminum Alloy using RSM.* Procedia Engineering, 2013. **64**: p. 1227-1234.

226. Zhang, H. and H. Liu, *Mathematical model and optimization for underwater friction stir welding of a heat-treatable aluminum alloy.* Materials & Design, 2013. **45**: p. 206-211.

227. Venkateshkannan, M., et al., *Influences of Tool Geometry on Metallurgical and Mechanical Properties of Friction Stir Welded Dissimilar AA 2024 and AA 5052.* Procedia Engineering, 2014. **75**: p. 154-158.

228. Shojaeefard, M.H., et al., *Application of Taguchi optimization technique in determining aluminum to brass friction stir welding parameters.* Materials & Design (1980-2015), 2013. **52**: p. 587-592.

229. Silva, A.C.F., et al., *Friction stir welded T-joints optimization.* Materials & Design, 2014. **55**: p. 120-127.

230. Sadeesh, P., et al., *Studies on Friction Stir Welding of AA 2024 and AA 6061 Dissimilar Metals.* Procedia Engineering, 2014. **75**: p. 145-149.

231. Shojaeefard, M.H., et al., *Modelling and Pareto optimization of mechanical properties of friction stir welded AA7075/AA5083 butt joints using neural network and particle swarm algorithm.* Materials & Design, 2013. **44**: p. 190-198.

232. Mayfield, D.W. and C.D. Sorensen. *An improved temperature control algorithm for friction stir processing*. in *8th international friction stir welding symposium*. 2010. Timmendorfer Strand, Germany.

233. Fehrenbacher, A., et al., *Toward Automation of Friction Stir Welding Through Temperature Measurement and Closed-Loop Control.* Journal of Manufacturing Science and Engineering, 2011. **133**(5).

234. Fehrenbacher, A., et al., *Effects of tool–workpiece interface temperature on weld quality and quality improvements through temperature control in friction stir welding.* The International Journal of Advanced Manufacturing Technology, 2014. **71**(1): p. 165-179.

235. Fehrenbacher, A., et al., *Combined temperature and force control for robotic friction stir welding.* Journal of Manufacturing Science and Engineering, 2014. **136**(2).

236. Ross, K.A., *Investigation and implementation of a robust temperature control algorithm for friction stir welding*. 2012: Brigham Young University.

237. Chimbli, S., D. Medlin, and W. Arbegast, *Minimizing lack of consolidation defects in friction stir welds.* Friction Stir Welding IV, 2007: p. 135-142.

238. Cederqvist, L., et al., *Reliable sealing of copper canisters through cascaded control of power input and tool temperature.* Friction Stir Welding and Processing VI, 2011: p. 49-58.

239. Cederqvist, L., et al., *Cascade control of the friction stir welding process to seal canisters for spent nuclear fuel.* Control Engineering Practice, 2012. **20**(1): p. 35-48.

240. Ross, K. and C. Sorensen, *Advances in Temperature Control for FSP*, in *Friction Stir Welding and Processing VII*, R. Mishra, et al., Editors. 2016, Springer International Publishing: Cham. p. 301-310.

241. Marshall, D. and C. Sorensen, *System Parameter Identification for Friction Stir Processing*, in *Friction Stir Welding and Processing VII*, R. Mishra, et al., Editors. 2016, Springer International Publishing: Cham. p. 289-299.

242. Qin, W., et al., *Charge-Transfer Magnets: Multiferroicity of Carbon-Based Charge-Transfer Magnets (Adv. Mater. 4/2015).* Advanced Materials, 2015. **27**(4): p. 733-733.

243. García, C.E., D.M. Prett, and M. Morari, *Model predictive control: Theory and practice—A survey.* Automatica, 1989. **25**(3): p. 335-348.

244. Cortinovis, A., et al., *Experimental evaluation of MPC-based anti-surge and process control for electric driven centrifugal gas compressors.* Journal of Process Control, 2015. **34**: p. 13-25.

245. Ma, J., S.J. Qin, and T. Salsbury, *Application of economic MPC to the energy and demand minimization of a commercial building.* Journal of Process Control, 2014. **24**(8): p. 1282-1291.

246. Nielsen, I., O. Garpinger, and L. Cederqvist. *Simulation based evaluation of a nonlinear model predictive controller for friction stir welding of nuclear waste canisters*. in *2013 European Control Conference (ECC)*. 2013.

247. Cederqvist, L., et al., *Improved Temperature and Depth Control during FSW of Copper Canisters Using Feedforward Compensation*, in *Friction Stir Welding and Processing VIII*, R.S. Mishra, et al., Editors. 2016, Springer International Publishing: Cham. p. 69-76.

248. *Summary for Policymakers*, in *Climate Change 2013 – The Physical Science Basis: Working Group I Contribution to the Fifth Assessment Report of the Intergovernmental Panel on Climate Change*, C. Intergovernmental Panel on Climate, Editor. 2014, Cambridge University Press: Cambridge. p. 1-30.

249. Taysom, B.S., C.D. Sorensen, and J.D. Hedengren, *Dynamic modeling of friction stir welding for model predictive control.* Journal of Manufacturing Processes, 2016. **23**: p. 165-174.

250. Hedengren, J.D. and A.N. Eaton, *Overview of estimation methods for industrial dynamic systems.* Optimization and Engineering, 2017. **18**(1): p. 155-178.

251. Torić, N., et al., *Experimental Analysis of the Behaviour of Aluminium Alloy EN 6082AW T6 at High Temperature.* Metals, 2017. **7**(4): p. 126.

252. Payandeh, M., et al., *Mechanical and Thermal Properties of Rheocast Telecom Component Using Low Silicon Aluminium Alloy in As-Cast and Heat-Treated Conditions*, in *Light Metals 2015*, M. Hyland, Editor. 2016, Springer International Publishing: Cham. p. 209-214.

253. Deb, S., et al., *Establishing flow stress behaviour of Ti-6Al-4V alloy and development of constitutive models using Johnson-Cook method and Artificial Neural Network for quasi-static and dynamic loading.* Theoretical and Applied Fracture Mechanics, 2022. **119**: p. 103338.

254. Gangwar, K. and M. Ramulu, *Friction stir welding of titanium alloys: A review.* Materials & Design, 2018. **141**: p. 230-255.

255. Sbayti, M., et al., *Finite Element Analysis of hot Single Point Incremental forming of hip prostheses.* MATEC Web Conf., 2016. **80**: p. 14006.

256. Riahi, M. and H. Nazari, *Analysis of transient temperature and residual thermal stresses in friction stir welding of aluminum alloy 6061-T6 via numerical simulation.* The International Journal of Advanced Manufacturing Technology, 2011. **55**(1): p. 143-152.

257. Hernando, I., et al., *Inconel 718 laser welding simulation tool based on a moving heat source and phase change.* Procedia CIRP, 2018. **74**: p. 674-678.

258. Meyghani, B. and C. Wu, *Progress in Thermomechanical Analysis of Friction Stir Welding.* Chinese Journal of Mechanical Engineering, 2020. **33**(1): p. 12.

259. Jia, Z., et al., *Modified Johnson-Cook model of aluminum alloy 6016-T6 sheets at low dynamic strain rates.* Materials Science and Engineering: A, 2021. **820**: p. 141565.

260. Uhlmann, E., M.G. von der Schulenburg, and R. Zettier, *Finite Element Modeling and Cutting Simulation of Inconel 718.* CIRP Annals, 2007. **56**(1): p. 61-64.

261. Flores-Johnson, E.A., et al., *Numerical investigation of the impact behaviour of bioinspired nacre-like aluminium composite plates.* Composites Science and Technology, 2014. **96**: p. 13-22.

262. Bang, H., et al., *Joint properties of dissimilar Al6061-T6 aluminum alloy/Ti–6%Al–4%V titanium alloy by gas tungsten arc welding assisted hybrid friction stir welding.* Materials & Design, 2013. **51**: p. 544-551.

263. Xinjian, L., et al., *Optimization on the Johnson-Cook parameters of Ti-6Al-4V used for high speed cutting simulation.* Journal of Physics: Conference Series, 2020. **1653**(1): p. 012034.

264. Fraser, K.A., L. St-Georges, and L.I. Kiss, *Optimization of Friction Stir Welding Tool Advance Speed via Monte-Carlo Simulation of the Friction Stir Welding Process.* Materials, 2014. **7**(5): p. 3435-3452.

265. Chen, Q., et al., *Study on Wear Resistance of Ti-6Al-4V Alloy Composite Coating Prepared by Laser Alloying.* Applied Sciences, 2021. **11**(1): p. 446.

266. Soundararajan, V., S. Zekovic, and R. Kovacevic, *Thermo-mechanical model with adaptive boundary conditions for friction stir welding of Al 6061.* International Journal of Machine Tools and Manufacture, 2005. **45**(14): p. 1577-1587.

267. Holman, V., *INTRODUCTION.* Visual Resources, 1999. **15**(3): p. ix-x.

268. A Abotaleb, Y.R., M Khraisheh, S Ahzi, *Finite Element Analysis of Friction Stir Welding of Al Alloy and Inconel 718*, in *COMSOL Multiphysics* 2023: Munich.

269. Salloomi, K.N., F.I. Hussein, and S.N.M. Al-Sumaidae, *Temperature and Stress Evaluation during Three Different Phases of Friction Stir Welding of AA 7075-T651 Alloy.* Modelling and Simulation in Engineering, 2020. **2020**: p. 3197813.

270. Jain, R., S.K. Pal, and S.B. Singh, *A study on the variation of forces and temperature in a friction stir welding process: A finite element approach.* Journal of Manufacturing Processes, 2016. **23**: p. 278-286.

271. Schmidt, H., J. Hattel, and J. Wert, *An analytical model for the heat generation in friction stir welding.* Modelling and Simulation in Materials Science and Engineering, 2004. **12**(1): p. 143.

272. Meyghani, B., et al., *The Effect of Friction Coefficient in Thermal Analysis of Friction Stir Welding (FSW).* IOP Conference Series: Materials Science and Engineering, 2019. **495**(1): p. 012102.

273. Yu, Y., et al., *Dynamic softening mechanisms and Zener-Hollomon parameter of Al–Mg–Si–Ce–B alloy during hot deformation.* Journal of Materials Research and Technology, 2021. **15**: p. 6395-6403.

274. Salih, O.S., H. Ou, and W. Sun, *Heat generation, plastic deformation and residual stresses in friction stir welding of aluminium alloy.* International Journal of Mechanical Sciences, 2023. **238**: p. 107827.

275. Yuvaraj, K.P., et al., *Optimization of FSW tool parameters for joining dissimilar AA7075-T651 and AA6061 aluminium alloys using Taguchi Technique.* Materials Today: Proceedings, 2021. **45**: p. 919-925.

276. Jenarthanan, M.P., C. Varun Varma, and V. Krishna Manohar, *Impact of friction stir welding (FSW) process parameters on tensile strength during dissimilar welds of AA2014 and AA6061.* Materials Today: Proceedings, 2018. **5**(6, Part 2): p. 14384-14391.

277. C, S., S. P, and S.K. R, *Experimental Identification of Optimized Process Parameters for FSW of AZ91C Mg Alloy Using Quadratic Regression Models.* Strojniški vestnik - Journal of Mechanical Engineering, 2020.